UNIVERSITY OF SOUTHAMPTON

FACULTY OF ENGINEERING, SCIENCE AND MATHEMATICS

School of Chemistry

Characterising Catalyst Preparation: From Adsorbed Precursor Complex to Catalyst Particle

by

Katie Bethan Blaney

Thesis for degree of Doctor of Philosophy

June 2009

UNIVERSITY OF SOUTHAMPTON

ABSTRACT

FACULTY OF ENGINEERING, SCIENCE AND MATHEMATICS

SCHOOL OF CHEMISTRY

Doctor of Philosophy

CHARACTERISING CATALYST PREPARATION: FROM ADSORBED PRECURSOR COMPLEX TO CATALYST PARTICLE

by Katie Bethan Blaney

Catalyst performance can be enhanced by the high dispersion of precious metals onto supports. The deposition of metal particles and the structural arrangement they adopt once impregnated on a support is therefore of interest in determining the necessary conditions required for maximum catalyst efficiency. The details of the relationship between precursor and the final catalyst structure have not been extensively investigated; therefore it is the aim of this project to examine this relationship using techniques such as EXAFS, XRD and TEM.

A selection of Pt and Pd precursors has been deposited onto both Al_2O_3 and SiO_2 supports and the resulting materials examined using these characterisation methods. Bimetallic combinations of these precursors have also been prepared and characterised.

The EXAFS showed that the ligand stays intact during adsorption onto the support and that it is lost during heating. The type of support used had an effect on the dispersion of both the monometallic and bimetallic catalysts and also on the type of bimetallic particle formed. Al_2O_3 supported bimetallic particles consisted of a Pt rich core with a Pd outer shell whilst SiO_2 supported bimetallic particles were made up of a mixture of monometallic Pt and Pd particles and bimetallic Pt/Pd particles.

TABLE OF CONTENTS

DECLARATION OF AUTHORSHIP

I, **Katie Bethan Blaney** declare that the thesis entitled:

Characterising Catalyst Preparation: from Adsorbed Precursor Complex to Catalyst Particle

and the work presented in it are my own. I confirm that:

- This work was done wholly or mainly while in candidature for a research degree at this University;
- Where any part of this thesis has previously been submitted for a degree or any other qualification at this University or any other institution, this has been clearly stated;
- Where I have consulted the published work of others, this is always clearly attributed;
- Where I have quoted from the work of others, the source is always given. With the exception of such quotations, this thesis is entirely my own work;
- I have acknowledged all main sources of help;
- Where the thesis is based on work done by myself jointly with others, I have made clear exactly what was done by others and what I have contributed myself;

Signed: _____

Date: 2nd June 2009

ACKNOWLEDGEMENTS

Firstly, I would like to thank my supervisor Professor Andrea Russell for her advice, support and encouragement throughout my PhD and for the very long hours she put in at the NSLS. To those at Johnson Matthey who have made this work possible Dave Thompsett, Janet Fisher, Sarah Burton, Hoi Jobson, James McNaught and Dogan Ozkaya and in particular my industrial supervisor, Emma Schofield. For all their help at Daresbury, I would like to thank Ian Harvey and Chris Corrigan and at the NSLS, thanks go to Kumi Pandya and Bill O'Grady for their help with the collection of data and Jaimie Aichroth for keeping my glass topped up at the Brookhaven Center.

To the Russell group members both past and present who have made my PhD so enjoyable. Colin for helping me to settle into Southampton, Dave for teaching me not to judge a book by its cover, Peter for imparting his EXAFS knowledge to me and bringing a whole new meaning to "a large glass of Shiraz" and Suzanne for being a much welcomed female companion. To Jon who brightens up the work place and made my final year extremely entertaining, Steve who got stuck in and didn't hold seeing me at my worst against me, Anna who I only wish I'd been able to work with for longer, Gael who kept me going whenever the beam dumped and Praba, for working more night shifts than most – it didn't go un-noticed and I am very grateful. And to Fabrice, who has played a large part in getting me to this point and in whom I have found a true friend.

To my family who are always there when I need them. To my sisters, Felicity and Freya, who I can always rely on for an honest opinion and who I regard as my best friends. To Mum and Dad, who encouraged me to follow my dreams and have given me the opportunity to fulfil them. And finally to Tim, without whom I really wouldn't have been able to do this and who has lived this PhD with me, never failing in his patience or support. Thank you.

CHAPTER ONE: INTRODUCTION

This work is concerned with the characterisation of catalysts during the preparation process from the precursor complex adsorbed onto the catalytic support to the point at which the deposited metal is an active catalyst particle. In this chapter, what catalysts are and their relevance to environmental concerns of the modern day world will be introduced. Details will be given on the features of catalysts used in the reduction of toxic automotive emissions and the scope of this thesis will be outlined. Literature reviews relevant to the results collected in this study can be found at the start of the results chapters (Chapters Three and Four).

1. Catalysts

1.1. The History of Catalysis

As early as 1817, Humphry Davy presented a paper to the Royal Society describing heterogeneous catalytic oxidation[1] but it wasn't until 1836 that the term "catalysis" was used by Berzelius[2]. In the late 19th century, the work of Berzelius was continued by Ostwald and during a series of studies at that time, he confirmed that catalysts did indeed speed up reaction rates[3]. The use of catalysts in industrial processes developed in the early 20th century with processes such as the Haber process increasing in production[4]. During the inter-war years, industrial catalysis continued to advance with discoveries which would be of vital significance during World War II; most notably perhaps, the synthesising of hydrocarbons from carbon monoxide and hydrogen by Fischer and Tropsch in 1922 and the discovery of the catalytic cracking of petroleum in 1936 by Houdry[4].

After World War II, there was a significant rise in the number of automobiles purchased. The associated combustion of fossil fuels led to an increased release of harmful emissions into the atmosphere and this began to have a detrimental impact on the environment. Despite the first commercial automobile exhaust

after treatment being developed during the mid 1960s by Engelhard[5], the negative impact of exhaust gases continued to be heavily debated during the late 1960s and early 1970s. The development of exhaust gas catalysts has led to an enormous reduction in toxic emissions and the exhaust gas catalyst system is now the most common catalytic reactor in the world[4].

1.2. What is a Catalyst?

A catalyst is a substance that decreases the activation energy of a chemical reaction without itself undergoing any change. A catalyst has the action of lowering the activation energy of a reaction (Figure 1) and so more molecular collisions have the energy required to reach the transition state and convert from reactants into products.

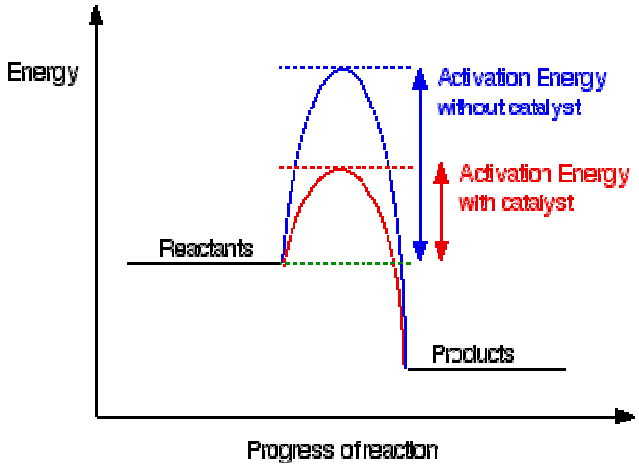

Figure 1 Schematic showing the effect a catalyst has on the activation energy in an exothermic reaction[6].

A catalyst can be either homogenous or heterogeneous. In homogenous catalysis, the reactants coordinate to the catalyst and are transformed into the product which is then released from the catalyst. In heterogeneous catalysis, the catalyst provides a surface whereby the reactants can become temporarily adsorbed. This weakens bonds in the substrate enough to facilitate the creation of new bonds. The bonds between the products and the catalyst are weak resulting in the products being released.

Exhaust catalysis is a well known example of heterogeneous catalysis; the catalytically active material is incorporated in the solid phase whereas the reactants and products are gaseous. This is shown schematically in Figure 2.

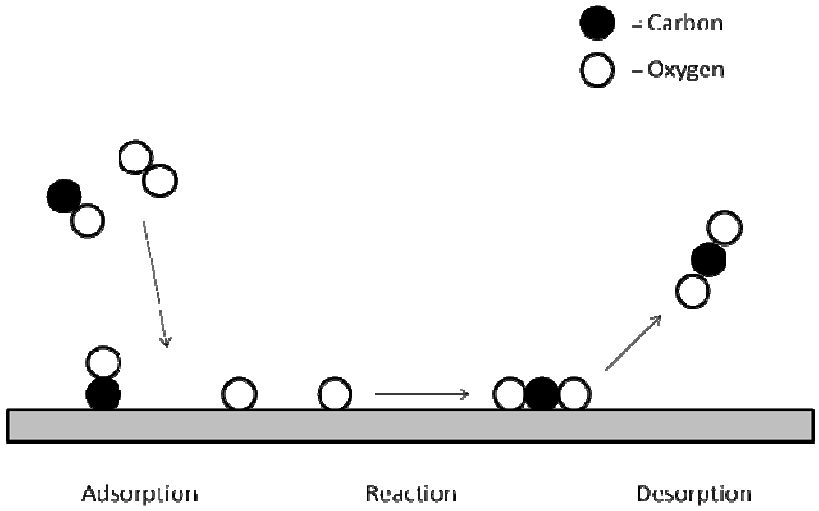

Figure 2 Schematic representation of the oxidation of carbon monoxide on a noble metal catalyst: $CO + ½ O_2 \rightarrow CO_2$.

The cycle presented in Figure 2 shows that during the reaction cycle, CO adsorbs associatively and O_2 dissociatively onto the surface of the catalyst. The CO molecule and the free O atom then combine to form an adsorbed CO_2 molecule. This molecule then desorbs from the surface of the catalyst and the reaction is complete.

1.3. Catalyst Preparation

Activity, stability, selectivity, and the ability to regenerate are all key attributes of a good catalyst. These factors can be related to the physical and chemical properties of the catalyst which, in turn, relates to the preparation methods[7]. An ideal preparation should result in a homogeneous distribution of metallic particles of a controlled size within a grain of support[8]. As Figure 2 indicated, catalysis occurs at the surface. It is therefore preferable for the surface to have a high fraction of surface atoms. This can be achieved by dispersing particles on porous supports – usually silica, alumina, titania or carbon.

The supports chosen for study in this work are γ-alumina and silica. The active exchange sites are, in the case of both supports, the surface hydroxyl groups. When referring to silica supports, these hydroxyl groups are often termed "silanol" groups.

Catalyst preparation involves two stages; the first is the deposition of a metal salt onto a porous support (impregnation) and the second is the conversion of the metal salt into a metallic or oxide state (calcination). Impregnation involves adding to the support a solution of the metal salt of sufficient concentration to give the required loading (metal wt %). The amount of solution added is enough to either fill or nearly fill the pore volume of the support particles resulting in a mixture which is then dried. This is referred to as "incipient wetness" as opposed to "wet" impregnation which involves using a large volume of metal solution (greater than the pore volume) and slurrying the mixture continuously during the drying step to ensure homogeneity[2]. Calcination is achieved by thermal treatment of the mixture (after drying) in either an inert atmosphere or an active one of either oxygen or hydrogen.

2. Automotive Emissions

2.1. Environmental Concerns

The combustion of fossil fuels in vehicles produces large amounts of gaseous emissions and particulate matter. These emissions contain toxic gases such as carbon monoxide (CO), nitrogen oxides (NO_x), and unburned hydrocarbons (HC) which have become a topic of public concern in recent years due to their pollutant nature. Their characteristics are outlined below:

a) Carbon Monoxide – a colourless, odourless gas which prevents the normal transport of oxygen in the blood leading to a decrease in the amount of oxygen supplied to the heart.

b) Nitrogen Oxides – these react in the presence of sunlight to form ground level ozone, a major constituent of smog. Mono-nitrogen oxides evolve into nitric acid, a component of acid rain.

c) Hydrocarbons – partially burned fuel molecules which react in the presence of nitrogen oxides and sunlight to form ground level ozone. They, along with particulate matter, are known to contain carcinogens.

In 1952, the great London smog killed thousands of people and lead to the introduction of a series of clean air acts in the UK. Since then, legislations on emissions into the atmosphere have continued to tighten and are in place all over the world. The first emission control devices were introduced in the 1970s[9] in the form of catalytic convertors which provide a chemical environment for a chemical reaction where toxic by-products are converted to less toxic gases. These convertors were introduced to comply with the newly tightened Environmental Protection Agency (EPA) on CO and NO_x emissions and it was estimated that as a result of these measures, by the year 2000, over 800 million tons of HC, CO and NOx had been prevented from entering the earth's atmosphere[10]. Table 1 shows how the permitted limits in automotive emissions have changed in the European Union since 1992.

Table 1 EU Emission Standards for Passenger Cars[11], g/km.

Tier	Date	CO	HC	HC + NO_x	NO_x	PM
Diesel						
Euro 1	Jul 1992	3.16		1.13		0.18
Euro 2	Jan 1996	1.0		0.7		0.08
Euro 3	Jan 2000	0.64		0.56	0.50	0.05
Euro 4	Jan 2005	0.50		0.30	0.25	0.025
Euro 5	Sept 2009	0.50		0.23	0.18	0.005
Euro 6	Sept 2014	0.50		0.17	0.08	0.005
Petrol						
Euro 1	Jul 1992	3.16		1.13		
Euro 2	Jan 1996	2.20		0.50		
Euro 3	Jan 2000	2.30	0.20		0.15	
Euro 4	Jan 2005	1.00	0.10		0.08	
Euro 5	Sept 2009	1.00	0.10		0.06	0.005
Euro 6	Sept 2014	1.00	0.10		0.06	0.005

As Table 1 shows, there has been a consistent reduction in limit between 1992 and 2009. New regulations due to be published later in 2009 and in 2014 are predicted to continue tightening the regulations on diesel emissions. There will also be an introduction of particulate matter regulations to petroleum powered passenger cars.

2.2. Catalytic Converters

The first catalytic converters consisted of pelleted catalysts in a radial flow-like reactor[12]. However, this system had limitations particularly as the pellets would move against each other as a result of the pulsating gas flow and the vibration of the engine and as a result would perish quite easily. In order to overcome these deficiencies an alternative structure was developed which made use of a ceramic monolithic honeycomb. The catalytic converter which resulted from these studies is shown in Figure 3.

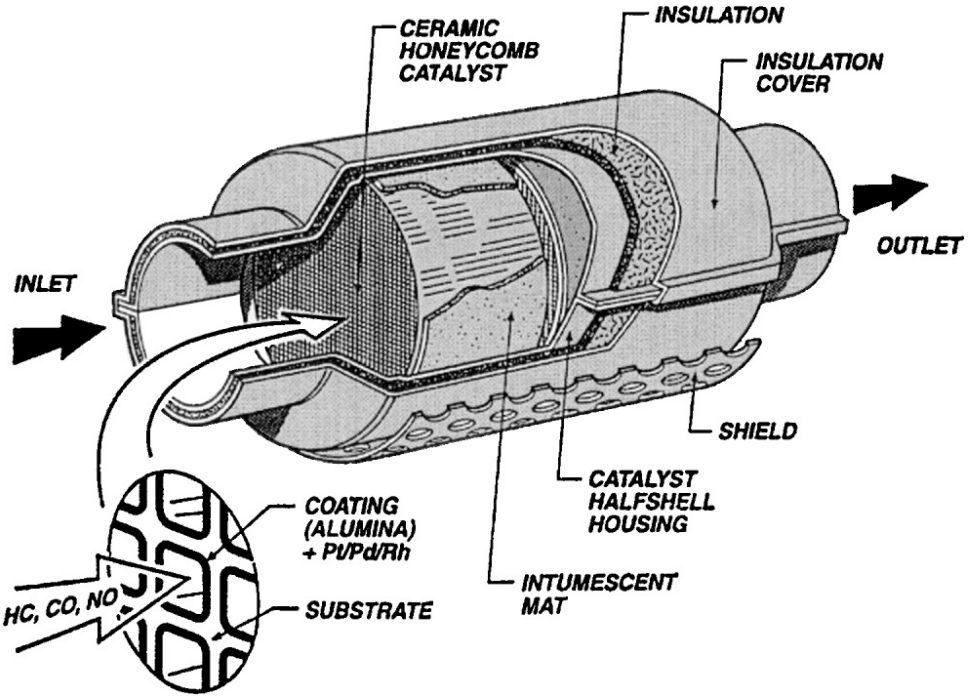

Figure 3 Automotive catalyst structural design including honeycomb support and mounting can[10].

The converter is made up of:

a) The core or substrate which is often a ceramic honeycomb and supports the catalyst.

b) The washcoat which is generally made of alumina or silica and when added to the core forms a rough surface and so increases the surface area. This in turn, creates more places for active precious metal sites.

c) The actual catalyst which is generally a precious metal.

2.2.1. Three-Way Catalysts

Early catalytic converters only oxidized CO and HC in a dual bed converter catalyst system[13]. However, around 1980, new NO_x standards were enforced leading to a rethink on the current structure[14]. By the mid 1980s there had been a switch to three-way catalysts, so called due to their task to promote three main reactions, the conversion of CO, HC and NO_x into the less toxic CO_2, H_2O and N_2 (Equations 1, 2 and 3).

$CO + \frac{1}{2}O_2 \rightarrow CO_2$ [1]

$HC + zO_2 \rightarrow nCO_2 + mH_2O$ [2]

$NO_x \rightarrow \frac{1}{2}N_2 + x/_2O_2$ [3]

Two types of reaction, oxidation and reduction, take place within a three-way catalyst in a two-stage process[12]. Oxidation catalysts oxidise the unburned carbon monoxide and hydrocarbons whilst the reduction catalyst is concerned with the reduction of NO_x.

The converters fitted today still use three-way catalysts but due to an increase in regulations since they were first introduced (Table 1), they have undergone many modifications and now contain multiple noble metals supported on different phases with various stabilisers and additives to ensure high performance and durability[14].

2.2.2. Diesel Oxidation Catalysts

Due to the increasing popularity of diesel engines and the tightening of the laws regarding diesel emissions (Table 1), a lot of interest is currently being concentrated on the control of diesel emissions[9,15-17]. Diesel combustion differs from petroleum combustion in that an excess of oxygen is present in the exhaust stream. This results in the oxidation of CO and HC into the less toxic CO_2 and H_2O occurring more readily than in petroleum engines.

Diesel combustion differs further from petroleum combustion as it produces solid, liquid and gaseous emission products. As a result of this, diesel oxidation catalysts have a slightly different design from the conventional three-way catalysts in that the monolith channels are slightly wider to accommodate the liquid waste and to prevent clogging the monolith pores[9].

Compression engines (diesel) work at much lower temperatures than spark ignition engines (petroleum) forcing the diesel oxidation catalyst to work at lower temperatures. To increase efficiency and compensate for the low working

temperatures, diesel oxidation catalysts often contain two or three times the amount of noble metal than a three-way catalyst[9].

Two other factors which need to be considered when reducing the detrimental impact on the environment caused by compression engines is the production of NO_x emissions and particulate matter. The amount of NO_x gases produced is relatively low when compared to spark emission engines[18]. However, under lean operating conditions, a suitable amount of NO_x reduction is not possible. The study of NO_x storage catalysts is of huge relevance at present as is the search for effective particulate matter filters[10,15,16,19-21].

Of the factors presented above, the main scope of this work is of platinum and palladium diesel oxidation catalysts. However, the characterisation of catalysts from precursor complex to catalyst particle could be attributed to any of the automotive catalysts discussed.

2.3. Precious Metals

The earliest record of the catalytic activity of platinum and palladium is thought to have been in 1817 by Humphry Davy[22]. However, it wasn't until World War I that platinum was first identified as a potential automotive catalyst[12]. With an awareness of economic impact, early studies into the feasibility of using base metals as automotive catalysts instead of platinum showed that they lacked the reactivity, durability and poison resistance that is required for automotive applications[23,24]. Therefore, there was a return to the more thermally stable noble metals where it was soon determined that as ruthenium, iridium and osmium all form volatile oxides, platinum (Pt) and palladium (Pd) were clear choices for oxidation catalysts[14].

As the catalysts used for oxidation had been determined, efforts were now turned to finding a suitable catalyst for NO_x reduction. A number of studies were carried out in the mid-1970s returning to ruthenium as a potential catalyst[24-28]. Although its stability was found to be good, the overall reduction of NO_x was sacrificed and so a ruthenium NO_x reduction catalyst was never produced.

Instead, rhodium (Rh) became the chosen metal as it is able to accommodate a high NO_x conversion which it retains in a lean situation[14].

Despite Pd being recognised as a good catalyst for oxidation and its relatively low cost, it did not feature in early three-way catalysts which used a mixture of Pt and Rh. This is because Pd experiences poisoning effects from lead and sulfur. Pd re-emerged as a good element for catalysis when the level of lead in fuel decreased.

Autocatalysts today are made from Pt, Pd and Rh. Frequently, two or more of the metals are used in combination. Three-way catalysts commonly contain Pd/Rh although Pt/Rh catalysts can still be found[12]. Diesel oxidation catalysts are generally Pt based but Pd is usually the chosen second metal in place of Rh[10,29].

3. Aims and Objectives

This review highlights the uses and application of catalysts with regards to automotive emission control. The work in this thesis involves the preparation and characterisation of various potential catalysts with an aim to understanding the interactions occurring on the support and the importance of the chosen precursor complex.

This project involves the synthesis of Pt and Pd complexes which have not previously been reported in literature as catalyst precursors and examining their changes in coordination chemistry during their transformation from precursor to catalyst. The aim is to use different ligand designs and many analytical techniques, concentrating on EXAFS, to determine the properties required for increased catalytic performance.

3.1. Precursor Complexes

The synthetic routes used for the preparation of the precursor complexes are outlined in detail in Chapter Two. In addition, two further precursor complexes were also used. The metals examined in this work were Pt and Pd. It has been well established that both Pt(II) and Pd(II) form an *N,O*-chelation with glycinate[30]. Studies by Wilson and Martin have confirmed that there are two nitrogen and two oxygen donors around the atom when the ligands were N-methyl-alanine, -valine and –glutamic acid with a molar ration (M:L) of 1:2[31,32]. The amino acid chosen for use as a ligand in this work was aspartic acid (asp). A [Pt(asp)$_2$] and a [Pd(asp)$_2$] complex were both synthesised. The structure of these complexes is shown below.

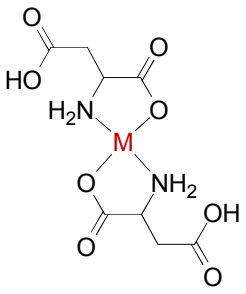

Figure 4 Structure of aspartic acid precursors where M = Pt or Pd.

Bearing in mind the *N,O*-chelation observed when an amino acid is complexed with a metal, a ligand containing similar nitrogen and oxygen donor groups was used to synthesise the other Pt and Pd precursors. The complex chosen for this study was 2,5-pyridinedicarboxylic acid (dcpy) and the donor atoms were the carboxy-oxygen of the 2-carboxylic acid and the nitrogen of the pyridine ring. The structure of these complexes is shown below.

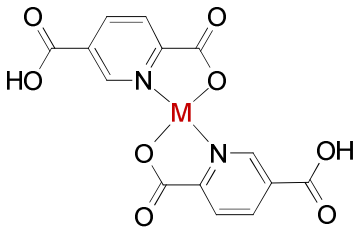

Figure 5 Structure of 2,5-pyridinedicarboxylic acid precursors where M = Pt or Pd.

To complete the sample of precursor complexes used, $[Pt(NH_3)_4](HCO_3)_2$ and $[Pd(NH_3)_4](HCO_3)_2$ were purchased from Alfa Aesar. The similarities in the precursor complexes are that they all contain one metal atom bonded to four donor atoms. They also all contain only M, carbon, nitrogen and oxygen (where M = Pt or Pd). However, they differ as they vary in size and, in the case of the $(dcpy)_2$ complexes, the ligand contains an aromatic functional group.

3.2. Catalyst Characterisation

The chemical properties of the precious metal precursor used in catalyst preparation play an important role in the interaction of the precious metal with the surface. Thus, knowledge concerning chemical properties and stability of the precious metal precursor is important to the catalyst preparation process[33]. A range of analytical techniques will be used in this study and these are as follows:

a) Infrared Spectroscopy;
b) Raman Spectroscopy;
c) Transmission Electron Microscopy (TEM);
d) X-Ray Diffraction (XRD);
e) Extended X-Ray Absorption Fine Structure (EXAFS);
f) Temperature Programmed Reduction (TPR).

The main technique that will be focussed on in this work is EXAFS. EXAFS is known to be a powerful tool to characterise metal supported catalysts. It is especially useful in determining the local environment around metal atoms[34].

The characteristics of each of these analytical methods and their applications to this study are described in detail in Chapter Two.

4. References

(1) Davy, H. *Philosophical Transactions of the Royal Society* **1817**, *107*, 77.

(2) Moulijn, J. A.; Leeuwen, P. W. M. N. v.; Staten, R. A. v. *Catalysis: An Intergrated Approach to Homogeneous, Heterogenoeous and Industrial Catalysis*; Elsevier: Amsterdam, **1993**.

(3) Somorjai, G. A.; McCrea, K. *Applied Catalysis A-General* **2001**, *222*, 3-18.

(4) Lindstrom, B.; Pettersson, L. J. *Cattech* **2003**, *7*, 130-138.

(5) Cohn, J. G. *Environmental Health Perspectives* **1975**, *10*, 159-164.

(6) http://www.chemguide.co.uk/physical/basicrates/catalyst.html Clarke, J. **2002**.

(7) Acres, G. J. K., Bird, A.J, Jenkins, J.W., King, F. *The Design and Preparation of Supported Catalysts*; RSC, **1981**; Vol. 4.

(8) Coq, B.; Figueras, F. *Coordination Chemistry Reviews* **1998**, *178-180*, 1753-1783.

(9) Haass, F., Fuess, H. *Advanced Engineering Materials* **2005**, *7*, 899.

(10) Heck, R. M.; Farrauto, R. J. *Applied Catalysis A-General* **2001**, *221*, 443-457.

(11) http://www.dieselnet.com/standards/eu/ld.php; Ecopoint Inc: **2007**; Vol. 2009.

(12) Twigg, M. V. *Catalysis Today* **2006**, *117*, 407-418.

(13) Shelef, M.; McCabe, R. W. In *Workshop on Building the Future of Catalysis*; Elsevier Science Bv: Egmond Zee, Netherlands, **1999**, p 35-50.

(14) Gandhi, H. S.; Graham, G. W.; McCabe, R. W. *Journal of Catalysis* **2003**, *216*, 433-442.

(15) Walker, A. P. *Topics in Catalysis* **2004**, *28*, 165-170.

(16) Gill, L. J.; Blakeman, P. G.; Twigg, M. V.; Walker, A. P. *Topics in Catalysis* **2004**, *28*, 157-164.

(17) Acres, G. J. K.; Harrison, B. *Topics in Catalysis* **2004**, *28*, 3-11.

(18) Zelenka, P.; Cartellieri, W.; Herzog, P. *Applied Catalysis B: Environmental* **1996**, *10*, 3-28.

(19) Belton, D. N.; Taylor, K. C. *Current Opinion in Solid State & Materials Science* **1999**, *4*, 97-102.

(20) Burch, R. In *13th ICC 2004 Conference*; Marcel Dekker Inc: Paris, FRANCE, **2004**, p 271-333.

(21) Maricq, M. M., Chase, R.E., Xu, N., Laing, P.M. *Environmental Science Technology* **2002**, *36*, 283-289.

(22) Robertson, A. J. B. *Platinum Metals Review* **1975**, *19*, 64-69.

(23) Kummer, J. T. *Journal of Physical Chemistry* **1986**, *90*, 4747-4752.

(24) Shelef, M. *Catalysis Reviews-Science and Engineering* **1975**, *11*, 1-40.

(25) Gandhi, H. S.; Stepien, H. K.; Shelef, M. *Materials Research Bulletin* **1975**, *10*, 837-845.

(26) Voorhoev.Rj; Remeika, J. P.; Trimble, L. E. *Materials Research Bulletin* **1974**, *9*, 1393-1404.

(27) Shelef, M.; Gandhi, H. S. *Abstracts of Papers of the American Chemical Society* **1974**, 93-93.

(28) Bauerle, G. L.; Pinkerto.Jd; Nobe, K. *Atmospheric Environment* **1974**, *8*, 217-219.

(29) Min., B. K., Santra, A.K., Goodman, D.W. *Catalysis Today* **2003**, *85*, 113-124.

(30) Appleton, T. G. *Coordination Chemistry Reviews* **1997**, *166*, 313-359.

(31) Wilson Jr, E. W.; Martin, R. B. *Inorganic Chemistry* **1970**, *9*, 528.

(32) Wilson Jr, E. W.; Martin, R. B. *Inorganic Chemistry* **1971**, *10*, 1197.

(33) Dawody, J.; Skoglundh, M.; Wall, S.; Fridell, E. *Journal of Molecular Catalysis A-Chemical* **2005**, *225*, 259-269.

(34) Borgna, A.; Le Normand, F.; Garetto, T. F.; Apesteguia, C. R.; Moraweck, B. *Catalyst Deactivation* **1999**, *126*, 179-186.

CHAPTER TWO: EXPERIMENTAL PROCEDURES

Chapter One details the relevance of precious metal catalysts at present and the importance in understanding the characteristics of the precursors used in catalyst preparation. This study began with the design of four novel precursors; two ligands were chosen, aspartic acid and 2,5-pyridinedicarboxylic acid and a platinum and palladium complex was synthesised using each. The aim was to use these catalyst precursors, along with known complexes $[Pt(NH_3)_4](HCO_3)_2$ and$[Pd(NH_3)_4](HCO_3)_2$ to determine the effect that the ligand structure has on the structure of the resulting catalyst particles. Various structural characterisation methods were then used. The synthetic route used in the preparation of these precursors and both the theory and practical aspects behind the characterisation methods are described in this chapter.

1. Reagents and Materials

Table 1 details the reagents and materials used in this study and their suppliers.

Table 1 List of reagents/materials used and their suppliers.

Reagent/Material	**Supplier**
2,5-pyridinedicarboxylic acid (98 %)	Sigma-Aldrich
γ-Alumina	Johnson Matthey
DL-aspartic acid (minimum 99 %)	Sigma-Aldrich
Nitric Acid (Lab reagent grade)	Fischer
Potassium tetrachloropalladate	Alfa Aesar
Potassium tetrachloroplatinate	Alfa Aesar
Silica	Johnson Matthey
Sodium Hydroxide (Lab reagent grade)	Fischer
Tetramethylammonium hydroxide (1.0 M)	Sigma-Aldrich
Tetrammine palladium hydrogen carbonate	Alfa Aesar
Tetrammine platinum hydrogen carbonate	Alfa Aesar
Water (18 MΩ cm)	Ondeo Pur1te Select Purifier

2. Synthesis

The platinum and palladium precursors designed for this work contain a central metal atom surrounded by four low molecular weight atoms. The ligands used act as bidentate chelates bonding to the metal atom through nitrogen and oxygen.

The ligands used are similar in their coordination to the metal atom but differ in that aspartic acid is aliphatic and 2,5-pyridinedicarboxylic acid contains a pyridine ring. Aspartic acid also coordinates to the metal atom through a terminal NH_2 group as opposed to the N of the pyridine ring as in the 2,5-pyridinedicarboxylic acid complexes. When the samples are prepared for impregnation on a catalytic support, base is added to render them negatively charged (and therefore soluble in water). With this in mind, $[Pt(NH_3)_4](HCO_3)_2$ and $[Pd(NH_3)_4](HCO_3)_2$ were selected as the fifth and sixth complexes in this study as when they are prepared for adsorption onto a catalytic support (by substitution of nitrogen for carbon in the counterion as a result of addition of HNO_3 to the complex), they are positively charged.

2.1 Physical Measurements

Elemental analyses were carried out at Medac Ltd, Teddington, UK for carbon, hydrogen and nitrogen. Mass Spectra were recorded on a Micromass Platform II HP1050 in the mass range 2 – 4000 Da. IR spectra were recorded on a Mattson Satellite FTIR Spectrometer with a Specac ATR in the 500 – 4000 wavenumbers range.

2.2 $[Pt(asp)_2]$

500 mL of an aqueous solution of aspartic acid (98 %, 26.62 g) and sodium hydroxide (98.8 %, 5.18 g) was warmed to 70 °C and stirred for 2 h. The resulting solution was filtered to remove the un-dissolved aspartic acid. Potassium tetrachloroplatinate (46.6 % metal, 21.27 g) was added to the filtrate and stirred for a further 4 h at 95 °C. The solution was left to stand overnight after which the suspension was slurried and washed with water until the

conductance reached 72.4 μS. The ensuing pale green solid was left to dry in the oven at 100 °C for 1 h.

Yield: 11.1 g (47 %). Anal. Calc. for $C_8H_{12}N_2O_8Pt$: C, 20.92; H, 2.63; N, 6.10. Found: C, 21.18; H, 2.65; N, 6.00. Electronegative electrospray m/z 458. Characteristic IR absorptions: 3264, 3215, 3121, 2925, 2356, 1673, 1560, 1402, 1307, 1159, 909, 854 cm^{-1}.

2.3 [Pd(asp)$_2$]

200 mL of an aqueous solution of aspartic acid (98 %, 12.6 g) and sodium hydroxide (98.8 %, 3.80 g) was warmed to 70 °C and stirred for 2 h at which time the reaction was complete and had yielded a colourless solution. Potassium tetrachloropalladate (32.2 % metal, 15.5 g) was added to the filtrate and stirred for a further 3 h at 60 °C. After this time, a pale yellow solid had formed. The solution was left to stand overnight after which the suspension was slurried and washed with water until a stable conductance was reached. The resulting solid was left to dry in a dessicator overnight.

Yield: 10.4 g (59.8 %). Anal. Calc. for $C_8H_{12}N_2O_8Pd$: C, 25.93; H, 3.26; N, 7.56. Found: C, 25.18; H, 3.25; N, 7.42. Electronegative electrospray m/z 369. Characteristic IR absorptions: 3235, 3137, 2958, 2358, 1698, 1592, 1545, 1396, 1286, 1129, 1051, 838 cm^{-1}.

2.4 [Pt(dcpy)$_2$]

Potassium tetrachloroplatinate (46.6 %, 21.45 g) and 2,5-pyridinedicarboxylic acid (98 %, 17.48 g) were dissolved in 500 mL of water and warmed to 55 °C giving a solution of pH 1.24. Tetramethylammonium hydroxide (2 molar equivalents) was added dropwise, during which the pH rose to 3.1 then immediately started dropping again. Most of the ligand went into the solution although there was still some yellow solid floating around in the orange solution. The reaction was left stirring at 80 °C for 3 h during which time the mixture went from cloudy orange to a clear yellow solution. The mixture was allowed to cool to 50 °C and was filtered to separate the solution from the bright yellow solid.

The insoluble solid was washed with water until a conductivity of 17 µS was reached before being left to dry in a fan oven at 100 °C overnight.

Yield: 18.7 g (69 %). Anal. Calc. for $C_{14}H_8N_2O_8Pt$: C, 31.89; H, 1.53; N, 5.31. Found: C, 32.04; H, 1.33; N, 5.28. MALDI m/z 528. Characteristic IR absorptions: 2902, 2767, 2595, 2360, 1733, 1604, 1390, 1243, 1118, 876, 817 cm^{-1}.

2.5 [Pd(dcpy)$_2$]

Sodium hydroxide (98.8 %, 3.75 g) and 2,5-pyridinedicarboxylic acid (98 %, 15.7 g) were added to 250 mL of water and stirred for 2 h until a cloudy lemon coloured solution was observed. Potassium tetrachloropalladate (32.6 %, 15.34 g) was dissolved in 100 mL water and added to the cloudy lemon solution. The pH at this point was recorded as being 2.44. The solution was a yellow/cream colour. The mixture was filtered and the ensuing solid washed until a stable conductivity was achieved. The cream solid was then dried in a fan oven at 100 °C overnight.

Yield: 11.2g, (54 %). Anal. Calc. for $C_{14}H_8N_2O_8Pd$: C, 38.33; H, 1.84; N, 6.38. Found: C, 37.57; H, 1.73; N, 6.38. Characteristic IR absorptions: 3079, 3040, 2883, 2751, 2589, 2358, 1733, 1596, 1476, 1385, 1338, 1280, 1241, 1161, 1118, 1049, 898, 864, 817 cm^{-1}.

3. Catalyst Preparation

Catalyst preparation involves two stages – loading the catalyst precursor onto the support followed by conversion of the supported metal salt to a metallic or oxide state. Precursors are loaded onto a support to achieve high dispersion and therefore highly active catalysts. This is of high relevance when using precious metal catalysts as less metal is needed than in bulk metal systems[1]. The chosen method of catalyst preparation for this work involves filling the pores of a support with a solution of the metal salt followed by evaporation of the solution

by heating in an oven. The catalysts were prepared by mixing the solution with the support in a concentration which ensured a pre-determined metal weight percentage was achieved. Two different supports were used, alumina (Al_2O_3 and silica (SiO_2). These supports differ in basicity (Al_2O_3 is more basic than SiO_2) and so may interact with the precursors in this study in different ways depending on whether the precursor is anionic or cationic. Once the precursor had been loaded onto the support the second stage of preparation (the conversion of the supported metal salt to an oxide state) was carried out as described below in Section 3.3.

3.1 Monometallic Catalysts

The theoretical metal loading of the monometallic catalysts prepared was 2.5 wt%. The required amount of sample was calculated and the weighed solid was dissolved in an appropriate solvent. Platinum and palladium tetrammine hydrogen carbonate dissolved in two molar equivalents of aqueous nitric acid (HNO_3). The complexes synthesised specifically for this study were soluble in two molar equivalents of aqueous tetramethylammonium hydroxide, (NMe_4OH). The resulting solutions were added to the catalyst support (Al_2O_3 or SiO_2) and the mixtures were stirred. Water was added if the amount of solution used was insufficient to produce a "cake-like" consistency. The resulting mixtures were dried in an oven at 100 ºC for 1 h. The subsequent catalysts were submitted for assay by ICP-OAS which was carried out by a technician at the Johnson Matthey Technology Centre.

3.2 Bimetallic Catalysts

The bimetallic catalysts were prepared for this study using two different methods; co-impregnation where the precursors are mixed before being added to the support and sequential impregnation where the first precursor is adsorbed onto the catalytic support which is then dried before the second precursor is applied. A total wt% of 2.5 was required so the appropriate weights of two metal precursors to yield 1.25 wt % of each metal on the supported catalyst were dissolved in 2 M equivalents of aqueous NMe_4OH and HNO_3 (depending on the precursor). In the case of the co-impregnated catalysts, these solutions were mixed before being added to the support and stirred until a "cake-like"

consistency was achieved. The sequentially impregnated catalysts were prepared by dissolving the first metal complex into a solution, mixing it with the support and then drying it at 100 ºC for 1 h followed by addition of the second metal complex solution and again mixing and drying. All catalysts were submitted for assay by ICP-OAS which was carried out by a technician at the Johnson Matthey Technology Centre.

3.3 Heat treatment of catalysts

A small amount of each of the catalysts prepared in the methods described above was calcined. The method of calcination in this study was to heat the catalyst to 500 ºC at a rate of 10 ºC per minute and to dwell at this temperature for 2 h.
In addition to this, thermogravimetric studies were carried out on the dried catalysts to determine the temperature at which the ligand is burnt off the support (as outlined later in this chapter). Small amounts of the catalysts were heated to this temperature in an oven for further EXAFS studies.

4. Vibrational Spectroscopy

4.1 Theoretical Aspects of Vibrational Spectroscopy

All molecules possess degrees of rotational and vibrational energy. Vibrations in molecules can be excited either by the absorption of photons (infrared spectroscopy), or by the scattering of photons (Raman spectroscopy), electrons (electron energy loss spectroscopy) or neutrons (inelastic neutron scattering)[2].
This study used Raman and Infrared spectroscopy.

Infrared spectroscopy originates from the transitions between two vibrational levels of the molecule in the electronic ground state and is observed as an absorption spectrum in the infrared region[3]. It has been shown that when a ligand complexes with a metal, infrared spectroscopy shows a shift in peaks[4]. To demonstrate the metal complexation in the samples prepared from this study, infrared spectra were collected of both the ligand and the prepared precursor complex.

In contrast to infrared spectroscopy where a molecule absorbs photons, Raman spectroscopy is due to the inelastic scattering of photons which lose energy by exciting vibrations in the sample. When a sample is exposed to monochromatic light, the majority of photons undergo Rayleigh scattering i.e. scattering without energy exchange[2] and electrons are excited into a virtual state. It is on relaxing from this state either into the first vibrational energy (Stokes) or if it has been excited from a vibrational state, into the ground state (Anti Stokes) that the scattered light exhibits intensity at a certain frequency. Stokes bands are observed far more than Anti Stokes bands and have a higher intensity. Figure 1 shows the Raman effect.

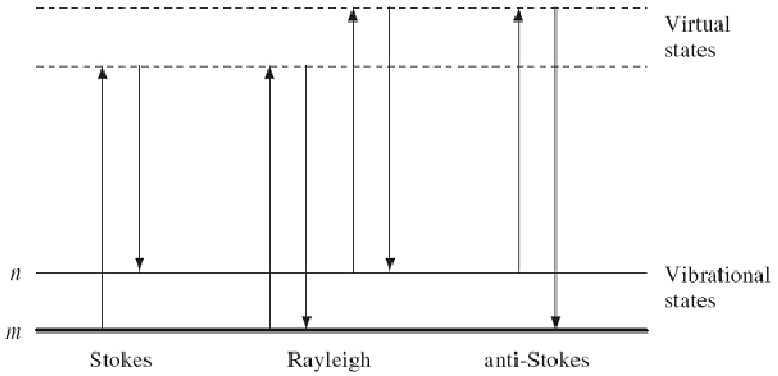

Figure 1 The Raman effect.

In this work, Raman spectroscopy was used to examine any changes in the structure of the precursor after it was adsorbed onto a support.

4.2 Experimental Aspects of Vibrational Spectroscopy

Infrared measurements were carried out at the University of Southampton on a Mattson Satellite FTIR instrument with a Specac ATR in the 500-4000 wavenumbers range. Samples were placed on a metal plate and scans were collected for 30 s.

Raman experiments were performed on a Renishaw 2000 operating in continuous scanning collection mode. The sample was placed on a clean microscope slide and the particles brought into focus under the microscope before the laser beam was applied. The slit width used was 50 μm. The laser wavelength was 633 nm

having a power of 2 mW. Spectra were obtained at a resolution of 4 cm^{-1}. Spectra were obtained from a 180 s scan over 2 accumulations.

5. Transmission Electron Microscopy (TEM) and Energy Dispersive X-Ray Analysis (EDX)

Information regarding the size and shape of particles of supported metal catalysts as well as the particle size distribution can be determined using TEM. EDX is a function that examines the proportions of the different components of the sample.

5.1 TEM and EDX

Transmission electron microscopy involves transmitting a beam of electrons through a very thin sample (less than 2000 Å) which the electrons then interact with. An electron microscope works by illuminating the sample, as opposed to conventional microscopes which use light, with an electron gun. A series of electromagnetic lenses focus the electron gun. The image can be viewed by looking at a fluorescent screen through a lead glass window or by a light sensitive sensor such as a camera. If a camera is used, it must work in the vacuum within the microscope[5]. These components are arranged into a vertical "microscope column".

Energy Dispersive X-ray analysis measures the X-rays emitted by the sample as a result of being hit by the electrons. The wavelengths of the X-rays emitted are characteristic to the sample and relate to the excitation of a core electron to a higher level. A spectrum of the energy versus relative counts of the detected X-rays can be obtained used to detect the proportion of each element present in the sample.

The TEM EDX data reported in this work was carried out by technicians at the Johnson Matthey Technology Centre.

6. X-ray Diffraction (XRD)

The correlation between the width of a peak observed in an X-ray diffraction pattern and particle size makes this technique an ideal method to combine with EXAFS. XRD data has been collected for all samples at the Johnson Matthey Technology Centre.

6.1 Theoretical Aspects of XRD

X-ray diffraction is the elastic scattering of X-ray photons by atoms in a periodic lattice. Powdered samples are measured with a stationary X-ray source which bombards the target with X-rays and a moveable detector which scans the intensity of the diffracted radiation as a function of the angle 2θ between the incoming and the diffracted beams. Scattering can occur either constructively or destructively. For constructive interference to occur, any of the powder particles have to be orientated in such a way that a crystal plane is at the correct angle, θ, to the incident beam. When this happens, a diffraction line appears. XRD patterns are usually plotted as intensity versus 2θ.

For a maximum diffracted intensity, the contribution of successive planes should be in phase (i.e. showing constructive interference). This condition can be expressed using Bragg's law:

$$n\lambda = 2dsin\theta \qquad [\mathbf{1}]$$

Where λ is the wavelength of the X-rays, d is the distance between the two lattice planes, θ is the angle between the incoming X-rays and the normal to the reflecting lattice plane and n is an integer called the order of reflection.

For a cubic structure, the intermolecular spacing, *d*, is determined using equation 2.

$$d = \frac{a}{\sqrt{h^2+k^2+l^2}} \qquad [\mathbf{2}]$$

Where, a is the lattice parameter and can be calculated using equation 3:

$$sin^2\theta_{hkl} = \frac{\lambda^2}{4a^2}(h^2 + k^2 + l^2) \quad [\mathbf{3}]$$

In cubic structures, some values of *hkl* are impossible. The indices must either be all odd or all even i.e. the first few diffraction lines are (111), (220), (220), (311) and (222). Using equation 3, the position of the diffraction lines for each lattice plane can be determined and structural information can be extracted from the pattern.

The width of the diffraction lines can be related to particle size. A diffraction line from a perfect crystal will be very narrow as opposed to the broadened line seen for crystallite sizes below 100 nm. Broadened lines are a result of incomplete destructive interference in scattering directions which occurs when the X-rays are out of phase. The Scherrer formula (equation 4) demonstrates how crystal size is related to line width.

$$L = \frac{0.9\,\lambda}{B_{2\theta}cos\theta} \quad [\mathbf{4}]$$

Where L is the average particle size, λ is the X-ray wavelength and $B_{2\theta}$ is the measured line broadening in radians.

7. X-ray Absorption Spectroscopy

X-ray absorption spectroscopy is a powerful tool in the characterisation of metal-supported catalysts, being especially useful for determining the local environment around metal atoms. An X-ray absorption spectrum consists of two parts, the X-Ray Absorption Near Edge Structure (XANES) and the Extended X-Ray Absorption Fine Structure (EXAFS). Both can be used to provide information describing the structural properties of catalysts. XANES can be used

to determine oxidation state whilst EXAFS is capable of detecting the type, number of, and distance to neighbouring atoms.

7.1 Theoretical Aspects of XAS

7.1.1 General Principles

When X-Rays travel through matter they interact with it resulting in a loss in intensity. This decay is a function of the path length (x) through the sample and the linear absorption coefficient (μ). This relationship can be expressed as shown below in equation 5 where I is the intensity of the transmitted X-rays and μ is the linear absorption coefficient, which is a function of photon energy, (E). Integrating over the path length gives rise to the Beer-Lambert equation (equation 6).

$$dI = -\mu I dx \quad [5]$$

$$I = I_0 e^{-\mu(E)x} \quad [6]$$

When the energy of the X-rays is increased, the adsorption of the material decreases until a critical energy is reached. Here, a sudden increase in absorbance is observed, which gives rise to the absorption edge. The increased absorbance corresponds to the elevation of a core electron of the absorber into an excited state or ejection into an excited state or into the continuum producing a photoelectron with kinetic energy, (E_k).

$$E_k = h\nu - E_{binding} \quad [7]$$

The intensity of the absorbance edge is determined by the X-ray absorption coefficient, μ. According to Fermi's golden rule (equation 8), the absorption coefficient is proportional to the probability of the absorption of a photon[6].

$$\mu \propto \sum_f \left|\langle \varphi_f | \boldsymbol{p}.\boldsymbol{A}(\boldsymbol{r}) | \varphi_i \rangle\right|^2 \delta(E_f - E_i - \hbar\omega) \quad [8]$$

Where ψ_i and ψ_f describe the initial and final states respectively, p represents the momentum operator and $A(r)$, the vector potential of the incident electromagnetic field. This process is termed the photoelectric effect. The principle quantum number of the orbital from which the core electron has ejected gives rise to the labelling of the adsorption edges. Excitation of an electron from the $1s(^2S_{1/2})$ is given the label K followed by L_I, L_{II} and L_{III} for electrons ejected from $2s(^2S_{1/2})$, $2p(^2P_{1/2})$ and $2p(^2P_{3/2})$ orbitals respectively (Figure 2).

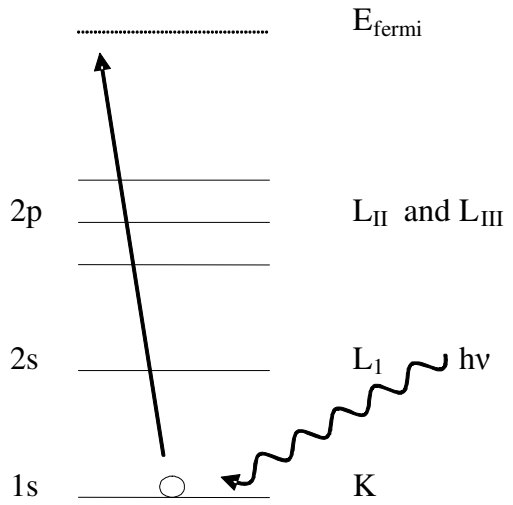

Figure 2 A representation of the photoelectric effect, illustrating the excitation of a 1s electron giving rise to the K absorption edge.

The ejected photoelectron can be described as a spherical wave with wave vector, k. This is illustrated in equation 9 where m_e is the mass of the electron, h is Planck's constant and E_0 is the zero point of energy in k-space which is usually taken to be the inflection point of the absorption edge.

$$\boldsymbol{k = \sqrt{\left(\frac{8\pi^2 m_e}{h^2}\right)(h\nu - E_0)}} \qquad [9]$$

A standard XAS Spectrum (Figure 3) can be split into three main regions. The first region is the pre-edge region. This corresponds to the energies where the photon energy is too low to excite or ionise the electron of the element of interest ($E<E_0$). The second region just below and above the absorption edge is referred

to as the XANES region. The XANES region displays features caused by electronic transitions from the core level to higher unfilled or partially filled orbitals ($s \rightarrow p$, or $p \rightarrow d$) and can extend up to 50 eV past the absorption edge. The XANES region displays effects such as multiple scattering and distortions of the excited state making this a complex region.

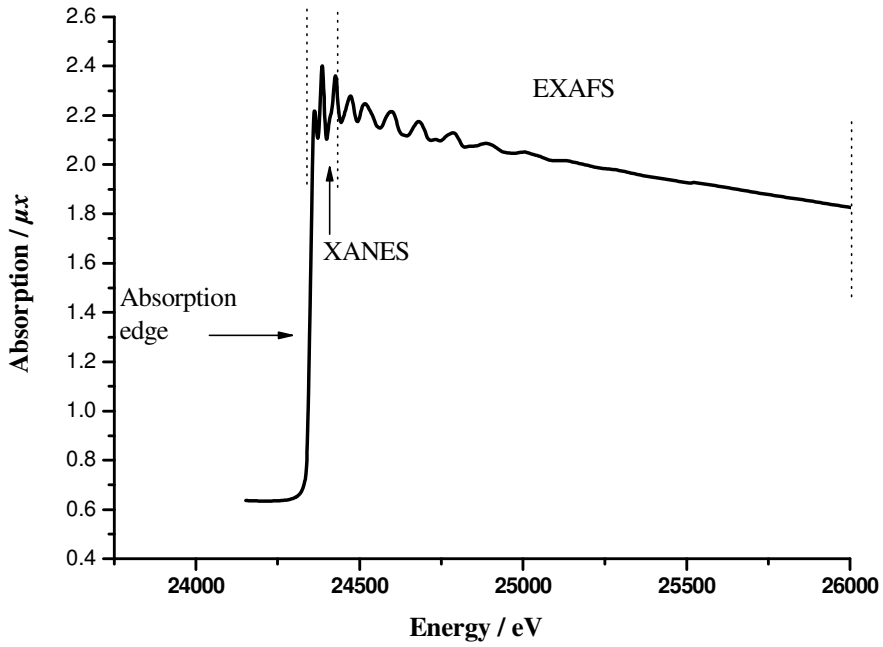

Figure 3 XAS spectrum of a Pd foil at the K absorption edge.

The third region, which begins ~50 eV past the absorption edge, is the EXAFS region. The photoelectrons in this area have high enough kinetic energy to leave the absorber atom and be scattered by neighbouring atoms. Single scattering by the nearest neighbour is the dominant feature. As the outgoing photoelectron scatters from the neighbouring atoms, a back-scattering wave is produced which can interact either constructively or destructively with the outgoing wave (Figure 4). The interaction between these waves as a function of the incident energy causes the oscillatory behaviour seen above the adsorption edge. These oscillations reflect the local structure surrounding the atom of interest.

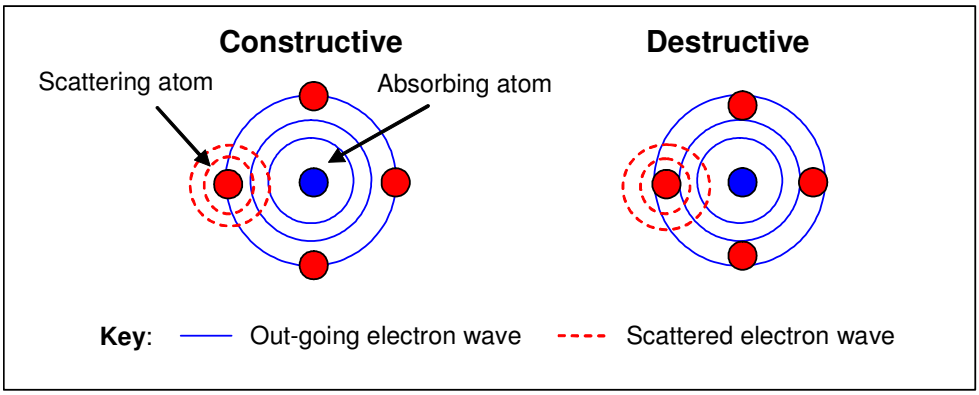

Figure 4 Schematic of the origin of the interference patterns in the final state wave-functions (The ring represents the maxima of the forward scattered (solid) and back scattered (dashed) waves).

The figure below (Figure 5) shows an XAS spectrum of a Pt foil. This spectrum essentially demonstrates the same characteristics of a Pd spectrum i.e. an absorption edge, a XANES region and an EXAFS region. However, the Pt edge is amongst a few edges which contain a large peak near the absorption edge known as the white line.

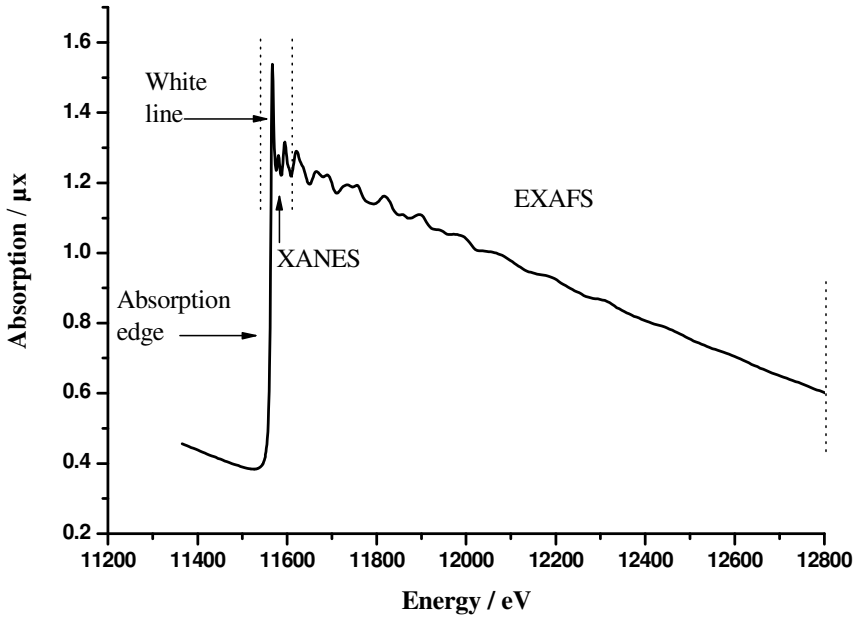

Figure 5 XAS Spectrum of a Pt foil at the L_{III} absorption edge.

The white line is the first peak after the absorption edge, within the XANES region, and is understood to be due to the presence of unoccupied d states at the Fermi energy[7].

The absorption coefficient above the absorption edge is defined in equation 10 where μ_0 is the background adsorption of a single atom as a result of elastic and inelastic scattering.

$$\mu_{tot} = \mu_0 (1 + \chi) \quad [\mathbf{10}]$$

The EXAFS oscillations are referred to as the function χ which can be extracted from the experimental data using equation 11. The oscillatory behaviour is given as a function of the wavevector, *k*.

$$\chi(k) = \frac{\mu_{tot}(k) - \mu_0(k)}{\mu_0(k)} \quad [\mathbf{11}]$$

The EXAFS region is of particular interest in this work as it can give information regarding the atomic number, distance to and coordination number of the neighbouring atoms around the absorbing atom.

7.1.2 The Origins of EXAFS

The first observation of fine structure in the X-ray absorption spectrum was in 1920 by Fricke *et al.*[8] However, it was not until the 1970s that EXAFS was recognised as a practical method for examining materials when Sayers *et al.*[9] reported that point scattering theory could be used to invert experimental data and provide structural information. Further work by Lee *et al.*[10] gave rise to point scattering plane wave approximation. This approximation assumes that the atomic radius of the central atom is much smaller than the distance to the neighbouring atom and, therefore, the spherical wave can be approximated as a plane wave. However, at *k* values less than 3 $Å^{-1}$, this theory breaks down and, as a result, more sophisticated spherical and curved wave theory simulations have been developed. Another assumption of the theory is that a photoelectron wave only scatters once before returning to the central atom when in reality, many systems experience multiple scattering (Figure 6) which affects the EXAFS.

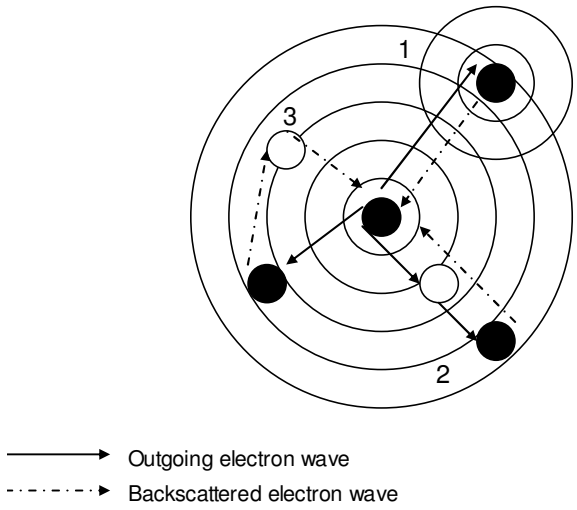

Figure 6 1) single scattering path; 2) and 3) multiple scattering paths.

It is vital that multiple scattering is considered when trying to extract structural information and nearest neighbour bond distances. The first quantitative treatments of multiple scattering effects were outlined by Lee *et al.*[10], work which has been expanded on more recently[6,11].

7.1.3 EXAFS Equations

The standard method for current analyses is still based on the quantitative work carried out by Sayers *et al*.[9] The EXAFS function, $\chi(k)$, is a summation of the sine waves produced from the outgoing photoelectron wavefunction, together with the backscattered wavefunction from each co-ordination shell, *j*.

$$\chi(k) = \sum_{j=1}^{shells} A_j\,(k) sin\delta_j(k) \qquad [\mathbf{12}]$$

The amplitude term, A_j can be described as shown in equation 13:

$$A_j\,(k) = \frac{N_j}{kR_j^2} S_0^2 F_j(k) e^{-2k^2\sigma_j^2} e^{\frac{-2R_j}{\lambda(k)}} \qquad [\mathbf{13}]$$

Where N_j is the number of atoms of type *j* at distance R_j from the absorber atom.

S_0 is an amplitude reduction factor, which describes multi-electron effects and central atom shake-up and shake-off observed after photo-ionisation due to relaxation processes[12]. F_j is the element specific backscattering amplitude from the jth atom extracted from reference compounds or calculated thoeretically[12]. $e^{-2k^2}\,\sigma_j^2$ is the Debye Waller factor and is partly due to atoms moving from their equilibrium atomic positions as a result of thermal effects. A similar effect is seen as a consequence of structural disorder and contributes to σ_2^j which is an exponential dampening term and therefore reduces the amplitude of χ at high k regions. $e^{\frac{-2R_j}{\lambda(k)}}$ describes the decay of the wave and therefore finite lifetime of the excited state where λ represents the mean free path of the photoelectron. The sine term defines the effects the inter-atomic distances and energy have on the oscillatory structure.

$$sin\delta(k) = \sin\left(2kR_j + \varphi_j(k)\right) \qquad [\mathbf{14}]$$

This function contains the interatomic distance R_j between the absorber atom and the backscattering atom as well as a phase factor $\varphi_j(k)$, which can be described as follows:

$$\varphi_j(k) = 2\varphi_{absorber}(k) + \varphi_{backscatterer}(k) \qquad [\mathbf{15}]$$

As shown in equation 15, the absorber contributes twice the amount to the phase factor as the back scattering atom. This is due to the photoelectron seeing the potential created by this atom twice. On the whole, the phase shift accounts for the differences which are typically a few tenths of an Å between the measured and geometric distances. As is also the case of F_j, the phase shift can be extracted from reference compounds or more typically is calculated theoretically.

7.1.4 Data Analysis

The Daresbury Suite of software (EXCALIB, EXBROOK and EXCURV98) was used to extract and fit the EXAFS data. The basic procedure is outlined below. The first step in data analysis is to read the raw data into EXCALIB; this

facilitates the conversion of the energy scale from millidegrees (analogous to the monochromator position) into energy. This program is also used to sum together a number of scans which can reduce noise levels.

EXBROOK involves the subtraction of the pre-edge background and the determination of E_0. To subtract the pre-edge background, two quadratics are fitted (one in the pre-edge region and one in the post-edge region) which are subsequently subtracted from the whole spectrum. The data is then normalised to give an edge jump of one (Figure 7). The edge jump is defined as the change between the linear pre-edge and smooth post-edge background extrapolated to E_0.

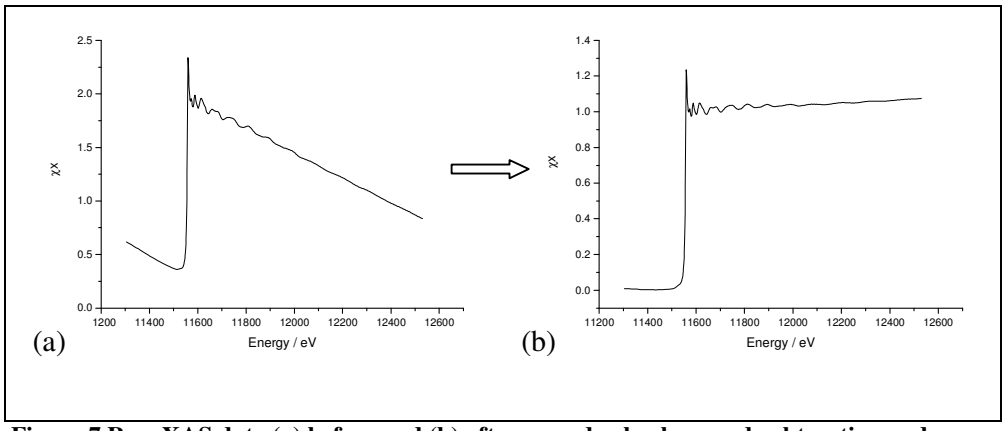

Figure 7 Raw XAS data (a) before and (b) after pre-edge background subtraction and normalisation.

E_0 is determined by taking the maximum in the first derivative; provided a sharp feature in the pre-edge region is not detected as this may give rise to more than one maximum, in which case the second maximum is taken. The energy scale is then set relative to E_0 i.e. the energy at E_0 is set at 0 eV (Figure 8).

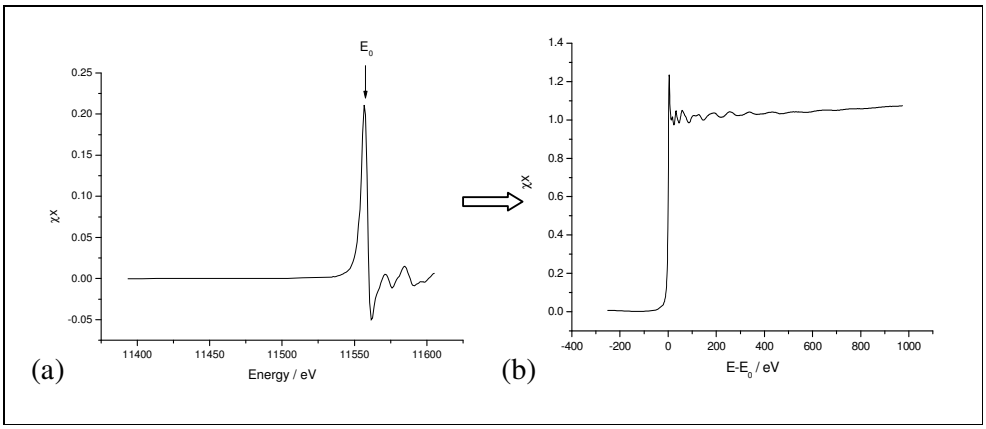

Figure 8 (a) Determination of E_0 from the derivative, (b) the re-scaled XAS spectrum.

The EXAFS region is then isolated and the post-edge background subtracted using EXBROOK. This second background subtraction separates the oscillatory EXAFS from the atomic part of the absorption, μ_0 (equation 11). A cubic spline is fitted to the data using the method developed by Cook and Sayers[13] ensuring care that the data isn't fitted too closely as this may result in some of the EXAFS features being removed with the background. This cubic spline technique is suitable for EXAFS background removal as there can be continued control of the degree of smoothing using a smoothing parameter, SM (equation 16)[13], which determines the spline function of the background, *BCK*. A weighting factor, *WE*, is also used to maximise the high *k* part of the spectrum.

$$\sum_{i=1}^{NPTS} \frac{(\mu_i - BCK_i)^2}{e^{-WEk_i^2}} \leq SM \qquad [16]$$

Background subtraction is started at approximately 50 eV above the edge position and the smoothing parameter can then be selected by examining the changes in the chi (EXAFS data) and Fourier transform plots. An ideal chi plot has evenly distributed amplitude above and below the axis (Figure 9) whilst an ideal Fourier Transform has its first peak between 1.8 and 3 $Å^{-1}$ when contributions below 1 $Å^{-1}$ are minimised.

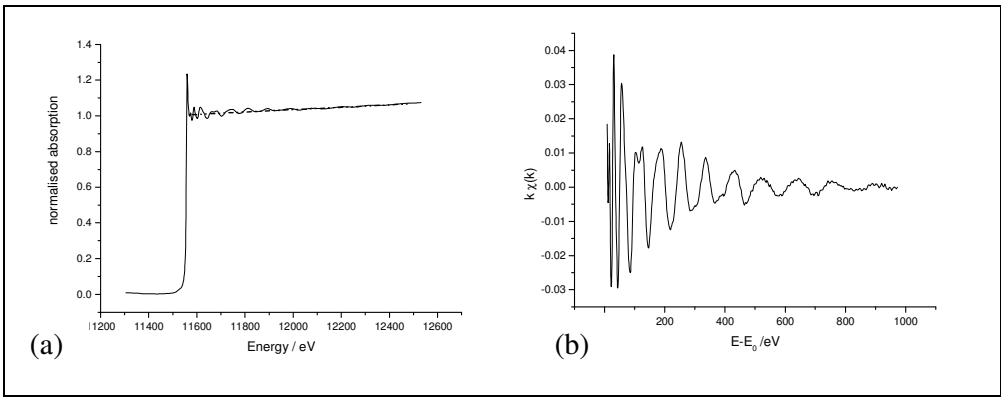

Figure 9 (a) Selection of cubic spline for post edge background removal, (b) the subsequent chi plot.

To fit the EXAFS data (chi file) obtained from EXBROOK, a program called EXCURV98 was used[14]. This program simulates EXAFS spectra using rapid curve wave theory[15] and Rehr and Alber's theory[6,16,17] from the parameters of the radial shells of atoms surrounding the central atom. The energy scale is converted from eV to *k* space, $Å^{-1}$, which evens out the amplitude. A chi plot and Fourier Transform as shown in Figure 10 can then be obtained.

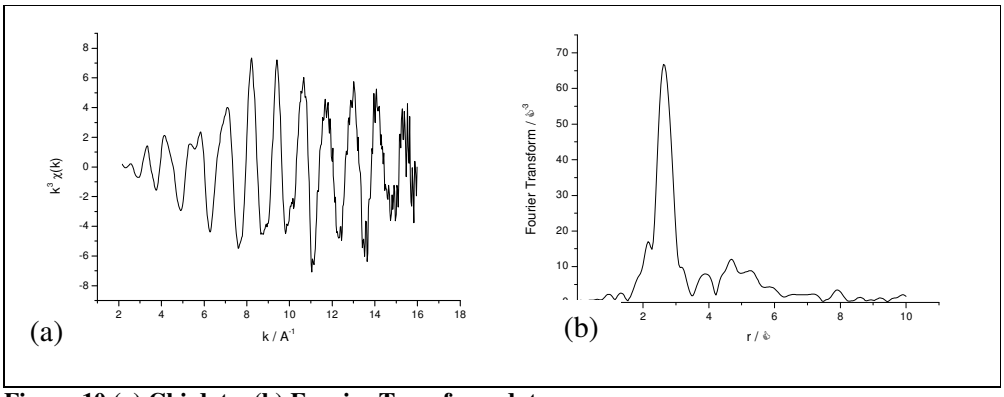

Figure 10 (a) Chi data, (b) Fourier Transform data.

Once this point has been reached, the probable values for coordination number (*N*), distance to the nearest neighbour, *R*, the Debye Waller factor ($2\sigma^2$) and the shift in Fermi energy (E_f) can be refined using a least-squares minimisation of the fit index. The integrity of the fit is defined by equation 17:

$$R_{EXAFS} = \sum_i^n 1 \Big/ \sigma^i\left(\left|\chi_i^{exp}(k) - \chi_i^{th}(k)\right|\right) \text{ x } 100\ \% \qquad [\mathbf{17}]$$

Where n is the number of data points, σ^i is the standard deviation for each data point i and $\chi_i^{\exp}(k)$ and $\chi_i^{th}(k)$ are the experimental and theoretical EXAFS, respectively. A fit is generally normally considered good if the R_{EXAFS} is 20 to 30 %. Errors in the parameters are estimated from standard deviations. The number of justified parameters, n_{max}, it is possible to fit can be estimated from the Nyqvist theorem (equation 18).

$$n_{max} = \frac{2\Delta k \Delta r}{\pi} + 1 \qquad [\mathbf{18}]$$

Where Δk and Δr are the widths in k- and r- space over which there is useful data.

The amplitude of the EXAFS oscillations varies with amplitude with respect to k with lower amplitude seen at high k space. If the EXAFS function is multiplied by k^i, where i = 1, 2, or 3, the emphasis of the chi plot is altered to favour high or low Z neighbours. For low Z neighbours, a weighting of 1 is used and a weighting of 3 is used for high Z neighbours. A compromise between high Z and low Z neighbours can be reached by using a weighting of 2.

7.2 Experimental Aspects of XAS

Two synchrotron sources were used in this study, the Synchrotron Radiation Source, Daresbury, UK and the National Synchrotron Light Source, Brookhaven, USA. The National Synchrotron Light Source is supported by the US Departmernt of Energy, Division of Material Sciences and Division of Chemical Sciences, under contract number DE-AC02-98CH10886. The beamline X11 is supported by the Office of Naval Research and contributions from Participating Research Team (PRT) members.

Synchrotron radiation is emitted when charged particles travel with a speed approaching that of light in curved paths in a magnetic field. One of the advantages of using synchrotron radiation is its high intensity. The radiation produced is generally 10^6 times more intense than that of conventional X-ray sources. Other advantages are the tunability that is possible over a wide energy range, high collimation and plane polarisation[18].

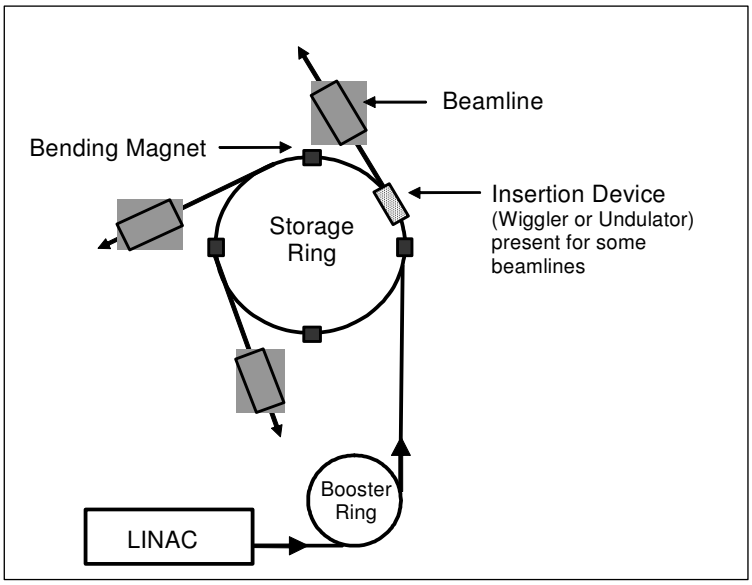

Figure 11 Schematic diagram of a Synchrotron Radiation Source[19] (not to scale and not all magnets shown).

Figure 12 Photograph of National Synchrotron Light Source (NSLS)[20]

Both synchrotrons utilised in this work produce an electron beam using a Linear Accelerator (LINAC). Pulses of these electrons are injected into the booster ring where they are accelerated by the application of radio frequency pulses causing the electrons to arrange in a series of microbunches. The electrons are accelerated further until they reach the required energy to be injected into the storage ring. Here, the electrons are subjected to a further boost of energy causing their velocity to be close to that of the speed of light. The beam is steered around the curve of the storage ring using a series of dipole bending

magnets. When the beam changes direction, a loss of energy is incurred in the form of electromagnetic radiation which emerges tangentially from the storage ring onto a beamline. To compensate for this loss in energy, fresh beam is injected approximately once every 24 hours. The SRS and NSLS have different ring energies. The SRS operates at a ring energy of 2 GeV with a maximum ring current of 250 mA. The NSLS has a ring energy of 2.8 GeV with a maximum current of 300 mA.

7.2.1 Experimental Station 9.3

Experiments conducted at the SRS, Daresbury Laboratory were measured on experimental station 9.3. The station is sourced by a Wiggler. Wigglers are insertion devices which enhance the flux and brightness of the light. They consist of a series of magnets which are designed to laterally deflect the beam. As the beam is deflected, synchrotron radiation is emitted, as with a bending magnet, but higher in intensity due to the large number of magnet poles in the wiggler. This station measures in the energy range 6 – 30 keV. The station is equipped with a "quick EXAFS" double crystal monochromator, with either Si(220) or Si(111) crystals. This system is water cooled. Station 9.3 also has a 13-element solid state detector for fluorescence experiments.

7.2.2 Experimental Stations X11A and X11B

Work carried out at the NSLS was on stations X11A and X11B. Both stations are sourced by a bending magnet. Station X11A is equipped with a 13 element Si-Li detector for fluorescence experiments. Station X11A has a channel-cut two-crystal monochromator containing Si(111) and Si(311) crystals allowing measurements in two energy ranges. Either an energy range of 4.5 – 26 keV can be measured (Si(111)crystal) or a range of 8 – 35 keV (Si(311) crystal). Station X11B has a channel-cut sinearm-driven double crystal monochromator containing a Si(111) crystal and can measure an energy range of 4.5–22 keV.

7.2.3 XAS Transmission Experiments

Two main modes are used for collection of XAS data, transmission and fluorescence with the simplest being transmission. An experiment set in transmission mode measures how the adsorption of the X-rays varies as the

energy of the incident photons is increased by a series of ionisation chambers (Figure 13).

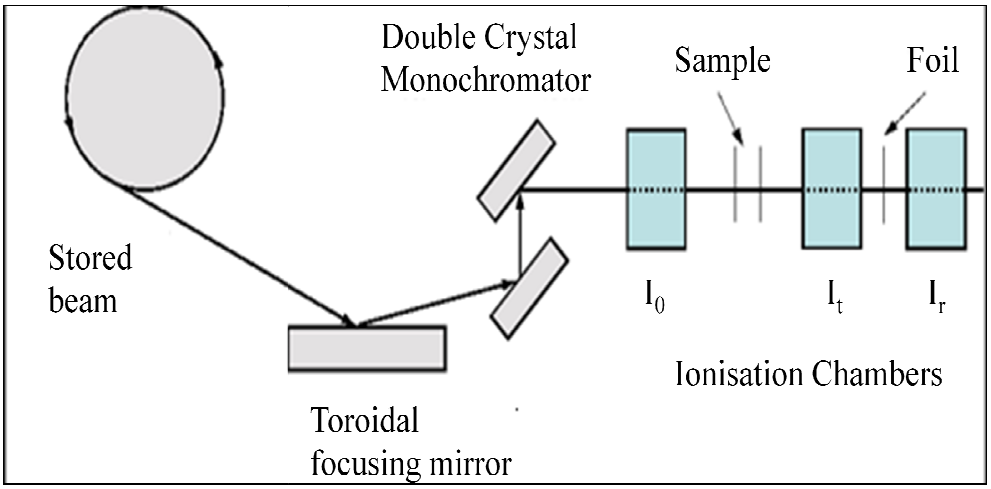

Figure 13 Set-up of an experiment in transmission mode.

As can be seen in Figure 13, the ion chambers are positioned both sides of the sample with I_0 measuring the incoming intensity and I_t measuring the transmitted intensity. The adsorption can then be measured as $ln(I_0/I_t)$. I_r is responsible for calibrating the energy once it has passed through a metal foil which is vital as fluctuations can cause an alteration in the position of the edge. I_0 is filled with a mixture of gases to absorb 20 % flux of the X-ray while I_t and I_r are filled with gases to absorb 80 % flux. Each ion chamber contains two metal plates so that when a constant voltage is applied across the chambers, ions are attracted to the negative plate and electrons to the positive plate and the resulting current is therefore proportional to the number of photons entering the chamber.

Transmission experiments are suitable for the collection of data of concentrated samples. Data collected on samples with a low concentration are likely to have a low signal to noise ratio as the X-ray absorption will be low. However, care must still be taken when preparing concentrated samples so the X-rays are not totally absorbed. An ideal value for absorbance edge, μx, being examined is between 0.3 and 1. The correct mass of sample required to achieve this absorbance can be calculated using equation 19.

$$mass = \frac{(\mu x)(area)}{\left(\mu/\rho\right)} \quad [19]$$

Where (μ/ρ) is the mass absorption coefficient of a sample with ρ being the density. Mass absorption coefficients used during this study are taken from calculations carried out by McMaster *et al*.[21].

As transmission experiments are the simplest experiments and produce very little statistical noise, they are preferred. Samples, however, must be completely homogeneous with care being taken to avoid pin holes in the prepared pellets which could result in leaking of the X-rays.

7.2.4 XAS Fluorescence Experiments

The less preferred fluorescence experiments are conducted when the sample is too dilute for transmission mode. A core hole is produced in an atom of the target element due to the photoelectric effect. An outer shell electron fills this hole and the energy difference between the outer shell and the inner shell is emitted as fluorescent radiation characteristic of the target element. The fluorescence EXAFS signal, I_f, consists of only a small fraction of the total absorption and is proportional to the incident intensity as follows:

$$\mu(E) = \frac{I_f}{I_0} \quad [20]$$

Fluorescence mode experiments (Figure 14) have a very similar set-up to transmission mode experiments; however the sample is aligned at 45º to the incident beam. This is to maximise the solid angle which helps minimise scattering (a main source of noise in this technique).

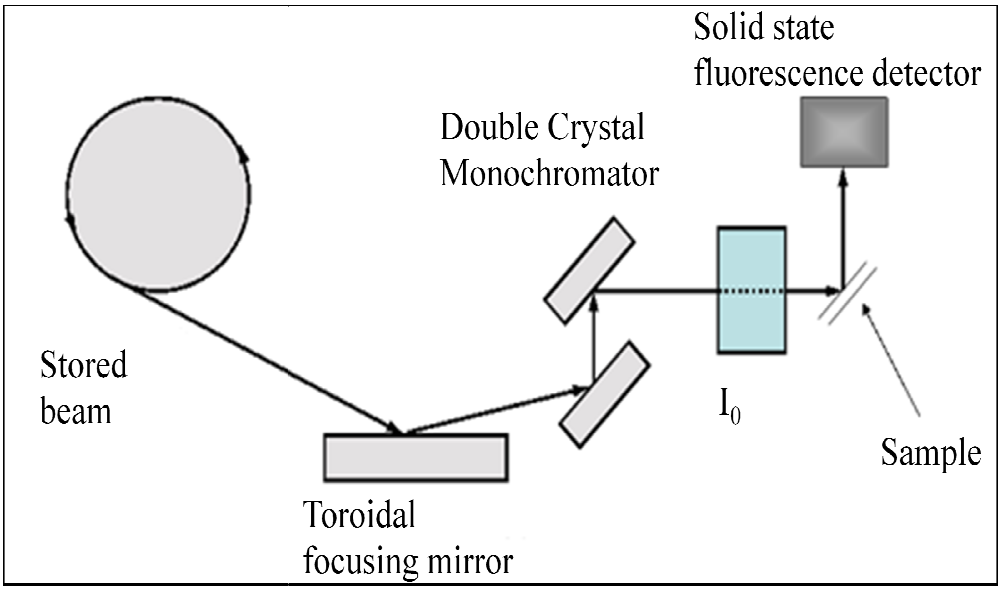

Figure 14 Set-up of an experiment in fluorescence mode.

Fluorescence radiation is detected using a solid state detector (Figure 14) which can discriminate between radiation at different energies and has resolution of around 100 eV. This detector is easily saturated due to background radiation being larger than fluorescence radiation so care must be taken when positioning the sample.

7.2.5 Gas Treatment Cell

Samples were placed in a gas treatment cell during experiments. The catalyst samples were studied as pellets which were prepared by grinding the sample into a very fine powder before compacting it into a pellet holder using a custom made press. The pellet holder containing the sample was the fixed into a "port" within the gas treatment cell (Figure 15).

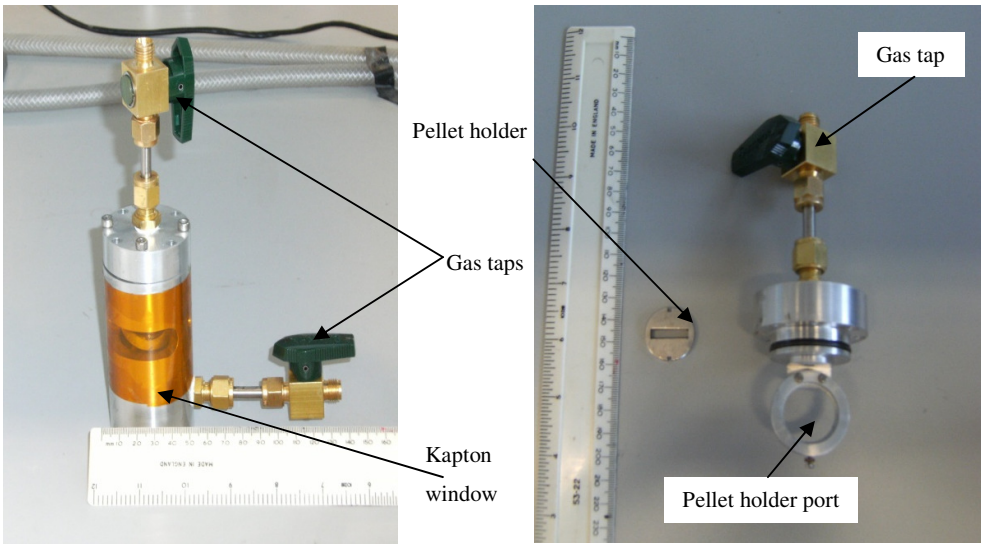

Figure 15 Gas cell and pellet holder.

The samples in this study were examined in both an air and hydrogen environment. When exposing the sample to a H_2 environment, laboratory grade $H_2(g)$ was flowed through the cell for at least 1 h. After this purge, the taps were closed. For safety reasons, this purge was carried out in a fume hood cupboard in a separate laboratory away from the beamline station. Frequent leak checks were carried out on the cell to prevent H_2 loss. After the experiment, the cell was purged with $N_2(g)$ for 30 mins before opening to air to re-passivate the reduced sample avoiding ignition upon exposure to air.

8. Temperature Programmed Techniques

Two forms of temperature programmed techniques were used during this study; thermogravimetric analysis to measure the weight loss of the catalysts during heating and temperature programmed reduction to predict the conditions at which the catalysts readily reduce.

8.1 Thermogravimetric Analysis

Thermogravimetric analysis (TGA) monitors the weight loss of a sample as a function of temperature and time. A small amount of sample is placed in a

furnace and as it is heated (to a pre-set temperature) the weight of the sample is continually recorded.

Measurements were carried out at the Johnson Matthey Technology Centre on an SDT 2960 Simultaneous DSC-TGA. A 20 mg sample of catalyst was weighed out and placed on a tared balance. A similar weight of calcined alumina was used as a reference. The furnace was closed and the sample was heated to 600 ºC at a rate of 10 ºC per minute. The weight of the sample was recorded throughout.

8.2 Temperature Programmed Reduction

Temperature Programmed Reduction (TPR) is a useful technique in the characterisation of metal oxide catalysts. It is based on the principle that the reduction of a catalyst will occur when Gibbs free energy, ΔG, has a negative value. Equation 21 shows how ΔG is dependent on pressures and temperatures[2].

$$\Delta G = \Delta G^0 + nRTln\left(\frac{p_{H_2O}}{p_{H_2}}\right) \quad [\mathbf{21}]$$

Where ΔG is the change in Gibbs free energy for the reduction, ΔG^0 is the same under standard conditions, n is the stoichiometric coefficient of reaction, R is the gas constant, T is the temperature and p is the partial pressure.

TPR is a valuable tool in the optimisation of catalyst pre-treatment and with regards to this study, was used to provide information on the temperatures needed for complete reduction of catalysts. This information was then correlated with the EXAFS data collected of these samples. During measurements, the catalyst was heated whilst being exposed to hydrogen. The difference between the inlet and outlet concentration of gases was then measured and the hydrogen uptakes determined. All TPR profiles reported in this work were collected at the Johnson Matthey Technology Centre by one of their scientists. The catalyst samples were heated to 500 ºC.

9. References

(1) Acres, G. J. K., Bird, A.J, Jenkins, J.W., King, F. *The Design and Preparation of Supported Catalysts*; RSC, **1981**; Vol. 4.

(2) Niemantsverdriet, J. W. *Spectroscopy in Catalysis - An Introduction*; Wiley: Weinheim, **2000**.

(3) Nakamoto, K. *Infrared and Raman Spectra of Inorganic and Coordination Compounds*; John Wiley and Sons, **1986**.

(4) Fujita, J., Martell, A.E., Nakomoto, K. *The Journal of Chemical Physics* **1962**, *36*, 324.

(5) Goodhew, P. J.; Humphreys, J.; Beanland, R. *Electron Microscopy and Analysis*; 3 ed., **2001**.

(6) Rehr, J. J.; Albers, R. C. *Reviews of Modern Physics* **2000**, *72*, 621-654.

(7) Brown, M.; Peierls, R. E.; Stern, E. A. *Physical Review B* **1977**, *15*, 738-744.

(8) Lytle, F. W. *Journal of Synchrotron Radiation* **1999**, *6*, 123-134.

(9) Sayers, D. E.; Stern, E. A.; Lytle, F. W. *Physical Review Letters* **1971**, *27*, 1204.

(10) Lee, P. A.; Pendry, J. B. *Physical Review B* **1975**, *11*, 2795-2811.

(11) Zabinsky, S. I.; Rehr, J. J.; Ankudinov, A.; Albers, R. C.; Eller, M. J. *Physical Review B* **1995**, *52*, 2995-3009.

(12) Russell, A. E.; Rose, A. *Chemical Review* **2004**, *104*, 4613-4635.

(13) Cook, J. W.; Sayers, D. E. *Journal of Applied Physics* **1981**, *52*, 5024-5031.

(14) Binsted, N. *EXCURV98: CCLRC Daresbury Laboratory computer program*, **1998**.

(15) Gurman, S. J.; Binsted, N.; Ross, I. *Journal of Physics C-Solid State Physics* **1984**, *17*, 143-151.

(16) Rehr, J. J.; Albers, R. C. *Physical Review B* **1990**, *41*, 8139-8149.

(17) Rehr, J. J.; Albers, R. C.; Zabinsky, S. I. *Physical Review Letters* **1992**, *69*, 3397-3400.

(18) Teo, B. K. *EXAFS: basic principles and data analysis*; Springer-Verlag, **1986**; Vol. 9.

(19) Rose, A. PhD Thesis, University of Southampton, **2004**.

(20) Courtesy of NSLS, B. N. L.

(21) McMaster, W. H. *National Bureau of Standards for Calculation of X-ray Cross Sections*.

CHAPTER THREE: MONOMETALLIC CATALYSTS

Chapter One gave an introduction into the use of precious metal catalysts in the reduction of automotive emissions. As stated, this work is concerned with the characterisation of these catalysts from the point at which a precursor complex is adsorbed onto the support to the state of being an active catalyst particle. Chapter Two introduced the characterisation methods used in this work. This chapter details the actual catalyst characterisation of a series of monometallic catalysts. The catalytic supports used were γ-alumina (Al_2O_3) and silica (SiO_2) and the metals of interest were platinum (Pt) and palladium (Pd). Characterisation of the precursor complexes is presented first with subsequent characterisation of the catalysts following on.

1. Introduction

The first step in the characterisation of the precursor complexes examined in this study is the measurement of the infrared spectra of both the precursor ligand and the precursor complex. According to X-ray analysis, two glycino ions coordinate to the metal by forming a trans-planar structure and the non-coordinating C=O groups are hydrogen bonded to the neighbouring molecule or water of crystallisation. Thus the $\upsilon(CO_2)$ stretches of amino acid complexes are affected by coordination as well as by intermolecular interactions[1]. Condrate and Nakomoto[2] carried out a normal coordinate analysis of the metal-glycino chelate ring. They found that the υ(C=O) stretching, $\upsilon(NH_2)$ rocking and υ(MN) and υ(MO) stretching bands are metal sensitive and shift to progressively higher frequencies as the metal is changed. Notably with regards to this study, Pd(II) complexes exhibited these bands at a lower frequency than the Pt(II) complexes.

The second step of this characterisation process is the characterisation of the catalyst samples immediately after adsorption and drying and also after a subsequent heat treatment. Precious metals deposited onto porous supports are used extensively as catalysts to reduce automotive emissions. The chemical

properties of the precious metal precursors used in the catalyst preparation play an important role in the interaction of the precious metal with the surface[3]. The interaction influences the precious metal particle size and distribution on the surface[4]. The characterisation methods used in this study were outlined in Chapter Two. Below is a review of other studies carried out in this area which incorporate the methods used in this work.

Dawody *et al*[4] demonstrated that a change in precursor can have an effect on the overall activity of a catalyst. Their study showed that there was a clear difference in catalytic activity between the four samples used despite the only difference between them being the precursor complex. In their study, the catalyst with the highest dispersion showed the highest activity.

A large proportion of the literature is based on hexachloroplatinic acid and other chloro-containing precursors and much attention has been focused on Pt/Al_2O_3. Processes such as the Pt/Al_2O_3 interaction, Pt complex decomposition during drying and calcination have been studied by many researchers[5-11]. Studies of the zeta potentials[9,12] show that the Al_2O_3 surface is positively charged at pH < 8, neutrally charged at pH 8-9 and negatively charged at pH > 9 meaning that a negatively charged Pt species will adsorb onto the support at pH < 8 and a positively charged species will adsorb at pH > 9 due to electrostatic interactions. Work by Schreier and Regalbuto[13] examined the uptake of cationic Pt complexes over negatively charged SiO_2 (high pH) and found the mechanism to be electrostatic in nature as with anionic chloroplatinate adsorption over alumina at low pH.

Halogenplatinate (IV) on SiO_2 has been studied by Boujday *et al*[14]. It was noted that the general trends for the interaction of the complex with SiO_2 are similar to those reported for Al_2O_3[5]. Further studies regarding the interaction of positive precursor complexes with a SiO_2 surface have also been investigated by Goguet *et al*[15]. They found that at temperatures around 200 ºC, about half the ligands are lost. It was also noted that at 300 ºC (under vacuum), the complex decomposed entirely to PtO.

Spieker *et al*[16] observed Pt complexes on Al_2O_3 with regards to the change in coordination chemistry of chloroaquohydroxy platinate complexes as they adsorb on the support. Comprehensive studies have also been carried out by Shelimov *et al*[5,6] on the characterisation of Pt/Al_2O_3 using various analytical techniques such as ^{195}Pt NMR, UV-Visible Spectroscopy, EXAFS and Raman Spectroscopy. Raman spectroscopy is not widely used for surface catalyst characterisation of supported metals[17]. Although this technique can provide useful information regarding the structure of the catalysts on their supports, it suffers from a major drawback in that it has a low sensitivity in the case of adsorbates.

Womes *et al*[8] studied the interaction of $[Pt(acac)_2]$ and Al_2O_3 surfaces using XAS. It had previously been reported that a 2-step decomposition mechanism took place in the preparation of Pt/Al_2O_3 catalysts from $[Pt(acac)_2]$ after drying, calcination and reduction steps at various temperatures[18]. This process involved the loss of one acac ligand at the drying stage and Pt bonded to two or three surface oxygen atoms followed by the loss of the second acac ligand during the calcination step. Similar mechanisms were proposed for $[Pd(acac)_2]$ on Al_2O_3[19] and also on SiO_2[20-22] although they were challenged by a model proposed by van Veen *et al*[23] where an immediate decomposition of $[Pd(acac)_2]$ and $[Pt(acac)_2]$ was proposed.

To prevent corrosion problems, use of non-chloride precious metal precursors is desirable[24]. As a result, the precursors examined in this work do not contain any chlorine. Furthermore, the precursors chosen for this study vary in size, charge and type of metal (Pt or Pd) and are deposited on both Al_2O_3 and SiO_2 supports for comparison.

It is clear from the brief review of the literature presented above that many attempts have been made to understand the mechanism by which a precious metal precursor adsorbs onto a catalytic support and the subsequent changes it undergoes with further heat and gas treatment. The work in this chapter aims to characterise this process with regards to the structure of the precursor complex and then catalyst precursor in an attempt to provide some information as to the

overall effect the nature of the precursor structure/metal/support used has on the final catalyst particle.

2. Experimental Procedures

2.1 Catalyst Preparation

Catalysts with a 2.5 theoretical metal weight percent (wt %) were prepared as outlined in Chapter Two, Section 3.1. Both Al_2O_3 and SiO_2 supported samples were prepared. Samples measured at this point will be referred to as "dried" for the remainder of this work. Metal content tests were performed by technicians at the Johnson Matthey Technology Centre and at Medac Ltd using Inductively Couples Plasma-Optical Emission Spectroscopy (ICP-OES).

A small amount of these samples was then taken and exposed to a pre-determined heat treatment in air. The samples were ramped to 500 °C at a rate of 10 °C per minute at which point they were left to dwell for 2 h. After 2 h the samples were cooled to room temperature at a rate of 20 °C per minute. Samples which have undergone this heat treatment will be referred to as "calcined" for the remainder of this work.

2.2 Vibrational Spectroscopy

Two forms of vibrational spectroscopy were used in this work; Infrared and Raman. The experimental set up used on both instruments is outlined in Chapter Two, Section 4.2. Infrared spectra were collected of the prepared precursor complex and its corresponding ligand to demonstrate complexation of the metal atom. Raman spectra were collected of the precursor complexes and of the monometallic catalyst compounds in their dried and calcined state to identify changes in bonding both when the precursor was adsorbed onto the support and when it was subjected to a heat treatment.

2.3 TEM and XRD

All samples for TEM and XRD were submitted to the Johnson Matthey Technology Centre for analysis. XRD was carried out on a Bruker AXS D-500 diffractometer with a 40 position samples changer. The radiation was Cu Kα (Ni filtered) and the scan range was $20^{o} \leq 2\theta \leq 100°$ with a 0.02° step size. A continuous scan rate of $0.25°min^{-1}$ was used.

TEM samples were measured in a Tecnai F20 Transmission Electron Microscope. The powder samples were crushed between two glass slides and the samples were positioned onto a lacey carbon coated 'finder' grid with the aid of a micro manipulator.

2.4 EXAFS

The absorption edges of interest in this study were Pt L_3 (11.564 keV) and Pd K (24.350 keV). Investigations were carried out on station 9.3 at the SRS, Daresbury Laboratory. Station 9.3 uses a double crystal monochromator with either Si(220) or Si(111) crystals as described in Chapter Two. The Wiggler I X-ray source permits experiments in the 6-30 keV range. EXAFS was collected in transmission mode. Pure complexes were prepared as BN pellets for EXAFS measurements (30 mg sample mixed with 30 mg BN). Catalyst samples were prepared as pellets (150 mg) without any dilution.

2.5 Sample Nomenclature

Samples will be referred to in terms of their precursor to avoid confusion. Therefore, it should be noted at this point that the following nomenclature applies throughout this chapter. Note, the counterion used in preparation of the samples will be omitted from the nomenclature.

a) "$M(L)_x$ as prepared" (where M = Pt or Pd and L = the relevant ligand) refers to the precursor complex before it has been deposited onto the support.
b) "$M(L)_x$ dried" refers to the catalyst samples after adsorption of the precursor and subsequent drying.
c) "$M(L)_x$ calcined" refers to the catalyst sample after heat treatment to 500 ºC in air.

3. Complex Characterisation

The infrared spectra obtained for the complexes Pt and [$Pd(asp)_2$] and the compound aspartic acid are shown in Figure 1. The data have been scaled as the intensity of the peaks is not of interest in this study. The figure shows that in comparison to the aspartic acid spectrum, Pt and [$Pd(asp)_2$] show N-H (denoted by [a]) and C=O stretching ([b]) at slightly higher frequencies confirming the complexation of the metal to the ligand at the proposed points on the structure. The shape of the C=O stretch has also changed, with a "shoulder" feature now being present at a slightly lower wavenumber than the C=O peak itself.

According to Condrate and Nakomoto[2], it would have been expected that the Pt N-H and C=O bands were found at higher frequencies than the Pd bands due to the increasing order of the metal-oxygen atom as the COO group becomes more asymmetrical as the metal-oxygen interaction becomes stronger[25]. However, in this case, although the Pt N-H stretch is found at a higher wavenumber than the Pd N-H stretch, the C=O stretch for [$Pt(asp)_2$] is found at a lower frequency. It is a broad peak in comparison to two distinct peaks seen for [$Pd(asp)_2$] and therefore the peak seen may represent both the C=O involved in the 5-membered chelate complexation of the metal and the C=O experiencing intermolecular interactions.

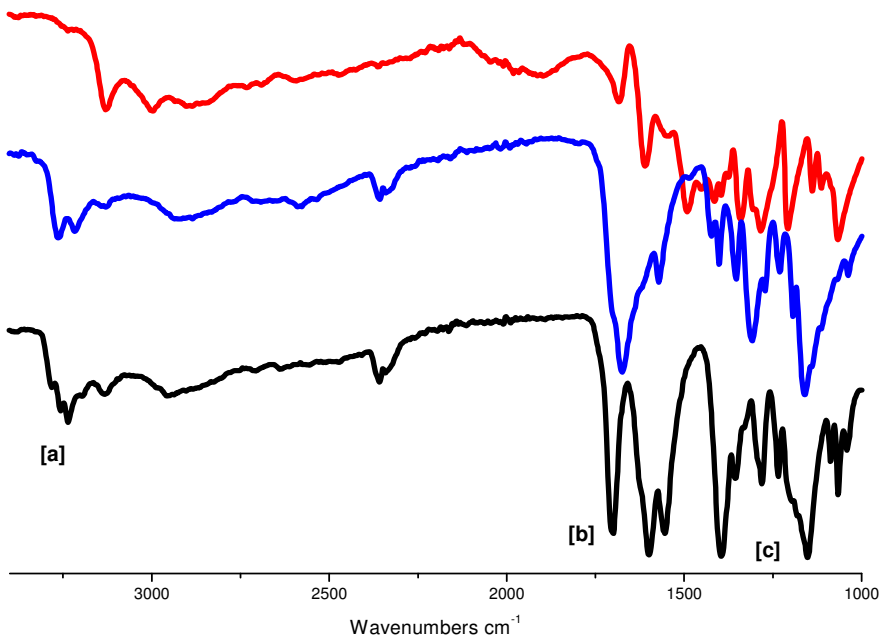

Figure 1 Infrared spectra of aspartic acid [red], [Pt(asp)$_2$] [blue] and [Pd(asp)$_2$] [black]. This data has been scaled.

Figure 2 shows the infrared spectra collected for 2,5-pyridinedicarboxylic acid (dcpy), [Pt(dcpy)$_2$] and [Pd(dcpy)$_2$]. Nakomoto[25] states that upon complex formation, pyridine vibrations in the high-frequency region are not shifted appreciably, a characteristic which is apparent in Figure 2 where the differences in the N-H ([a]) and C=O ([b]) peaks are less apparent than in Figure 1. However, there is also the appearance of a shoulder to the C=O peak when a metal is introduced as was seen in Figure 1 for the (asp)$_2$ complexes.

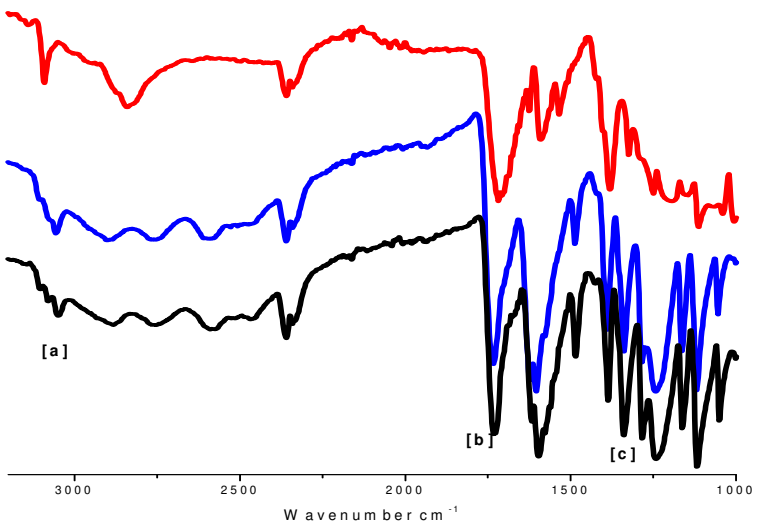

Figure 2 Infrared spectra of 2,5-pyridinedicarboxylic acid[red], [Pt(dcpy)$_2$] [blue] and [Pd(dcpy)$_2$] [black]. This data has been scaled.

An increase in the number of low frequency oscillations ([c]), which probably relate to the M-O and M-N bonds, is also seen which correlates with findings by Clark and Williams[26] who observed many low frequency oscillations when studying the infrared spectra of metal-pyridine complexes. A change in the peaks seen in the range of 1180-1360 cm^{-1} (C-N) may also suggest perturbation of the N atom of the pyridine ring.

4. Alumina Supported Catalysts

4.1 Catalyst Preparation

ICP-OAS was used to measure the metal weight percent (wt %) adsorbed onto the catalytic supports. The theoretical wt % is 2.5 for all the catalysts prepared in this study. Table 1 shows the actual wt % of metal present on the Al_2O_3 support after incipient wetness impregnation of the precursor complexes studied in this work.

Table 1 Actual metal wt % on Al_2O_3 support after adsorption of complex via incipient wetness and drying measured by ICP-OAS.

Precursor Complex	Metal	Actual wt %
$[Pt(asp)_2]$	Platinum	2.25
$[Pd(asp)_2]$	Palladium	2.40
$[Pt(dcpy)_2]$	Platinum	1.76
$[Pd(dcpy)_2]$	Palladium	1.45
$[Pt(NH_3)_4]$	Platinum	2.40
$[Pd(NH_3)_4]$	Palladium	2.38

Although the actual results are a little lower than the calculated theoretical wt %, all samples have a loading between 1.45 and 2.40 %. Interestingly, the overall loading is similar for samples with the same ligand agreeing with the suggestion that the chemical properties of the precursor play a role in the interaction of the precious metal with the support[4].

4.2 Raman

Raman spectra were collected of the $(asp)_2$ and the $(dcpy)_2$ samples as prepared complexes, dried onto the support and after calcining in order to compare the scattering variation between them. The Raman spectra of Pt and $[Pd(asp)_2]$ as a prepared complexes, dried onto Al_2O_3 and calcined are shown in Figure 4 below.

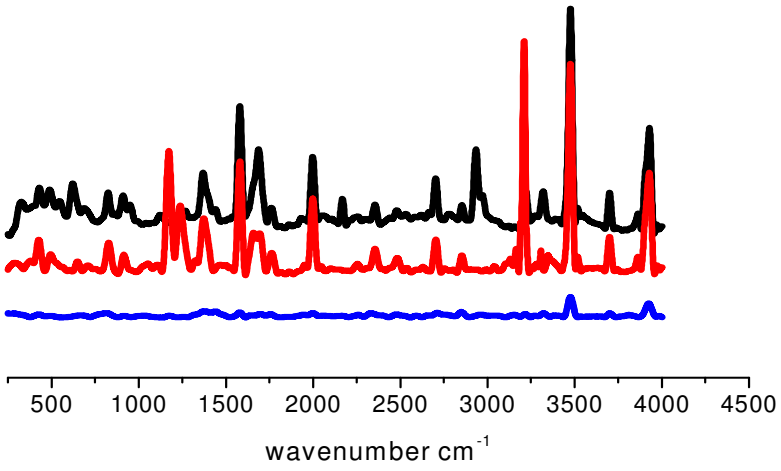

Figure 3 Raman spectra of [Pt(asp)$_2$] as a prepared complex (black), dried onto the support (red) and calcined (blue).

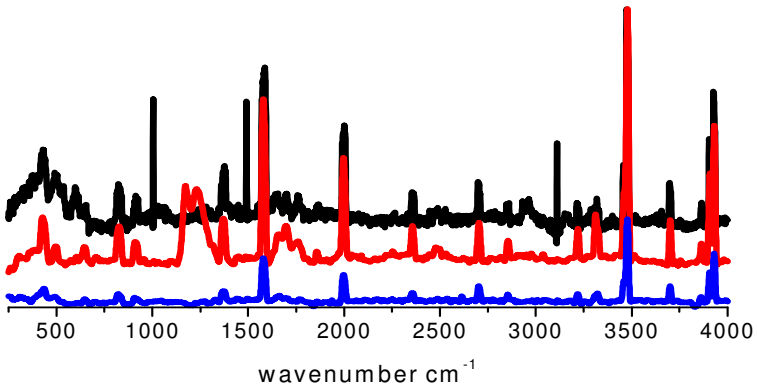

Figure 4 Raman spectra of [Pd(asp)$_2$] as a prepared complex (black), dried onto the support (red) and calcined (blue).

The spectra show that there is a correlation between the structure of the complex both before and after it is deposited onto the support. Peaks at ~1580, 2000 and 3500 cm^{-1} are attributed to $\delta(CH_2)$, υ(C=O) and υ(O-H)[27] respectively and are

noticeably less intense in the calcined sample, if they appear at all. Scattering caused by aliphatic chain vibrations in the region 600 – 1300 cm^{-1} does not appear when the calcined sample is measured. Both samples show an additional peak at ~ 1170 cm^{-1} after deposition onto the support. This could be due to interaction of the ligand with the newly introduced support. The similarity in the spectra of the samples as prepared complexes and dried onto the support indicates that the complex remains intact during deposition and that changes in the structure and loss of the ligand only occurs during heating.

The Raman spectra of Pt and $[Pd(dcpy)_2]$ are presented in Figure 5 and Figure 6 respectively. The complex and dried samples show many more peaks than the $(asp)_2$ complexes due to their larger ligand which contains a pyridine ring. Peaks in the region of 1600 – 1680 cm^{-1} are attributed to υ(CC) aromatic ring vibrations and υ(C=N) of the pyridine ring[27]. The contributions from CH_2, C=O and O-H vibrations are seen again for the complex and the dried samples indicating preservation of the ligand structure during deposition onto the support. These do not appear in the spectra collected of the calcined catalysts indicating that the ligand is burned off during heating.

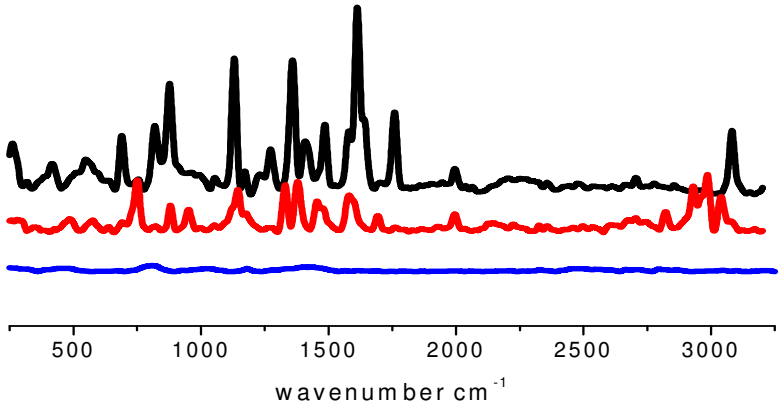

Figure 5 Raman spectra of $[Pt(dcpy)_2]$ as a prepared complex (black), dried onto the support (red) and calcined (blue).

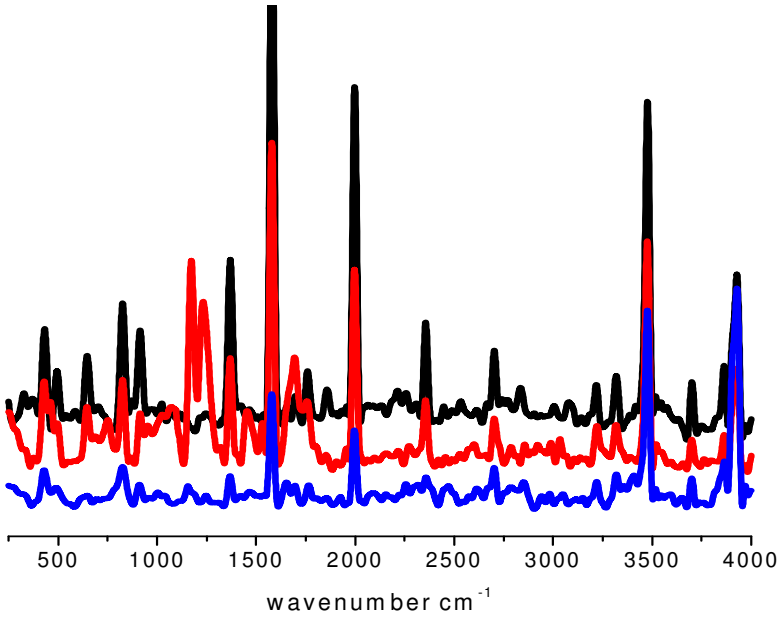

Figure 6 Raman spectra of [Pd(dcpy)$_2$] as a prepared complex (black), dried onto the support (red) and calcined (blue).

4.3 TEM

TEM gives a useful indication of the metal particle size and distribution. A series of micrographs collected for the catalyst samples prepared using [Pt(asp)$_2$] as the precursor complex are shown in Figure 7.

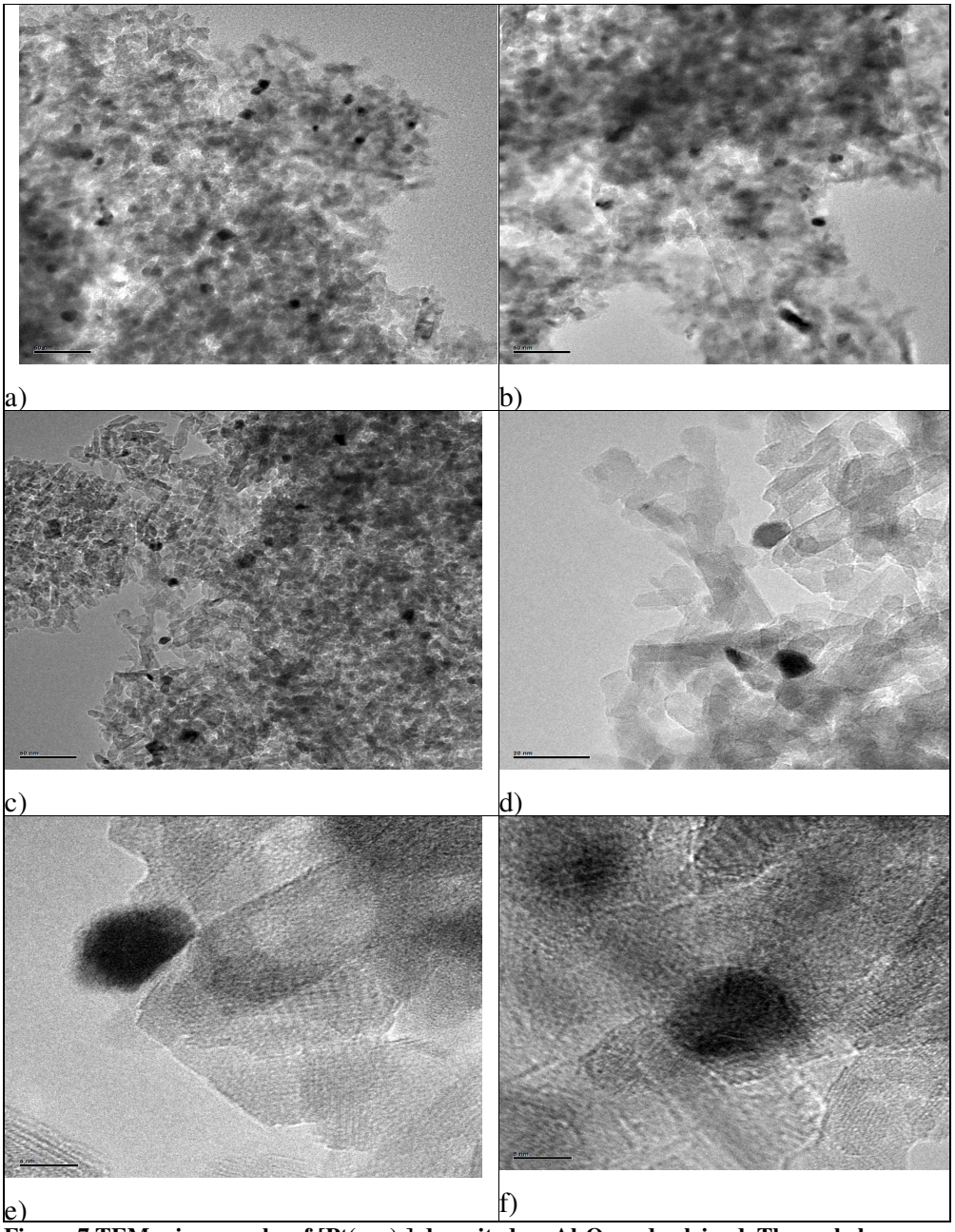

Figure 7 TEM micrographs of $[Pt(asp)_2]$ deposited on Al_2O_3 and calcined. The scale bars represent 50 nm (a, b and c), 20 nm (d) and 5 nm (e and f).

Similar micrographs of the other monometallic catalysts examined in this chapter can be found in reports T3282A and T3282B of the electronic appendix.

Figure 8 shows the particle sizes (with the average particle size quoted below) and distributions obtained by analysis of the TEM images for each of the catalysts following calcination.

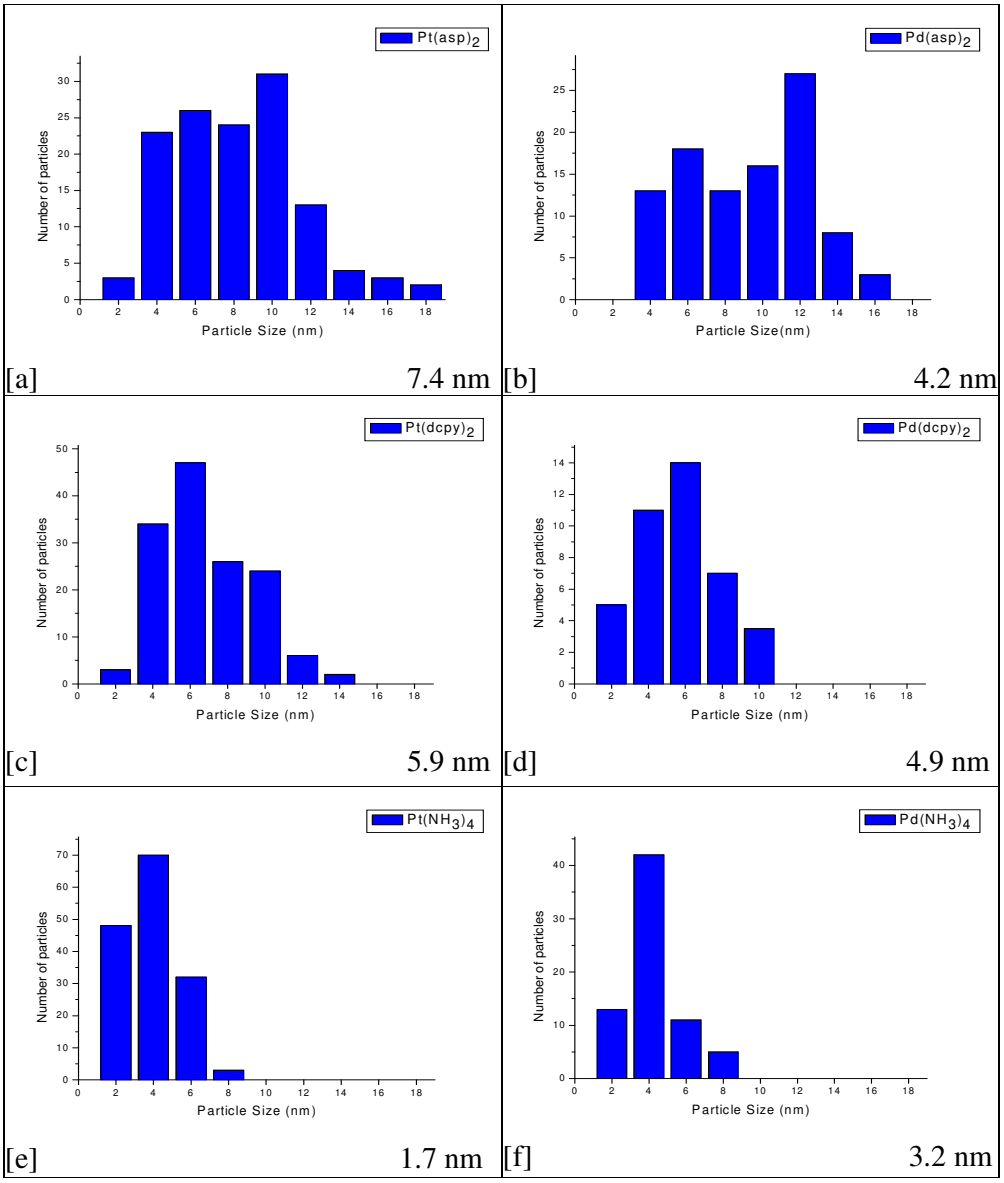

Figure 8 Particle size and distribution of[$Pt(asp)_2$] [a], [$Pd(asp)_2$] [b], [$Pt(dcpy)_2$] [c], [$Pd(dcpy)_2$] [d], [$Pt(NH_3)_4$] [e] and [$Pd(NH_3)_4$] [f] on Al_2O_3. All samples were analysed as calcined catalysts.

From the data, there is a clear relationship between the particle sizes and distributions and the identity of the ligand. The [$Pt(asp)_2$] sample has the largest particle size (7.4 nm) and a broad distribution (2 - 18 nm). [$Pd(asp)_2$] has a similar distribution but the average particle size is much lower at 4.2 nm. The $(NH_3)_4$ samples have the narrowest distribution (2 – 8 nm) and the smallest particle sizes (1.7 and 3.2 nm).

4.4 XRD

Figure 9 below shows the XRD patterns collected of the monometallic samples adsorbed on Al_2O_3 and calcined. A reference Al_2O_3 pattern is also shown. It can be seen from these patterns that all samples contain either cubic Pt or tetragonal PdO depending on the metal within the complex, as indicated by the vertical bars in the figures. No presence of bulk PtO_2 was detected which, considering the particle sizes seen in the TEM, suggests than any PtO_2 particles present are amorphous in character.

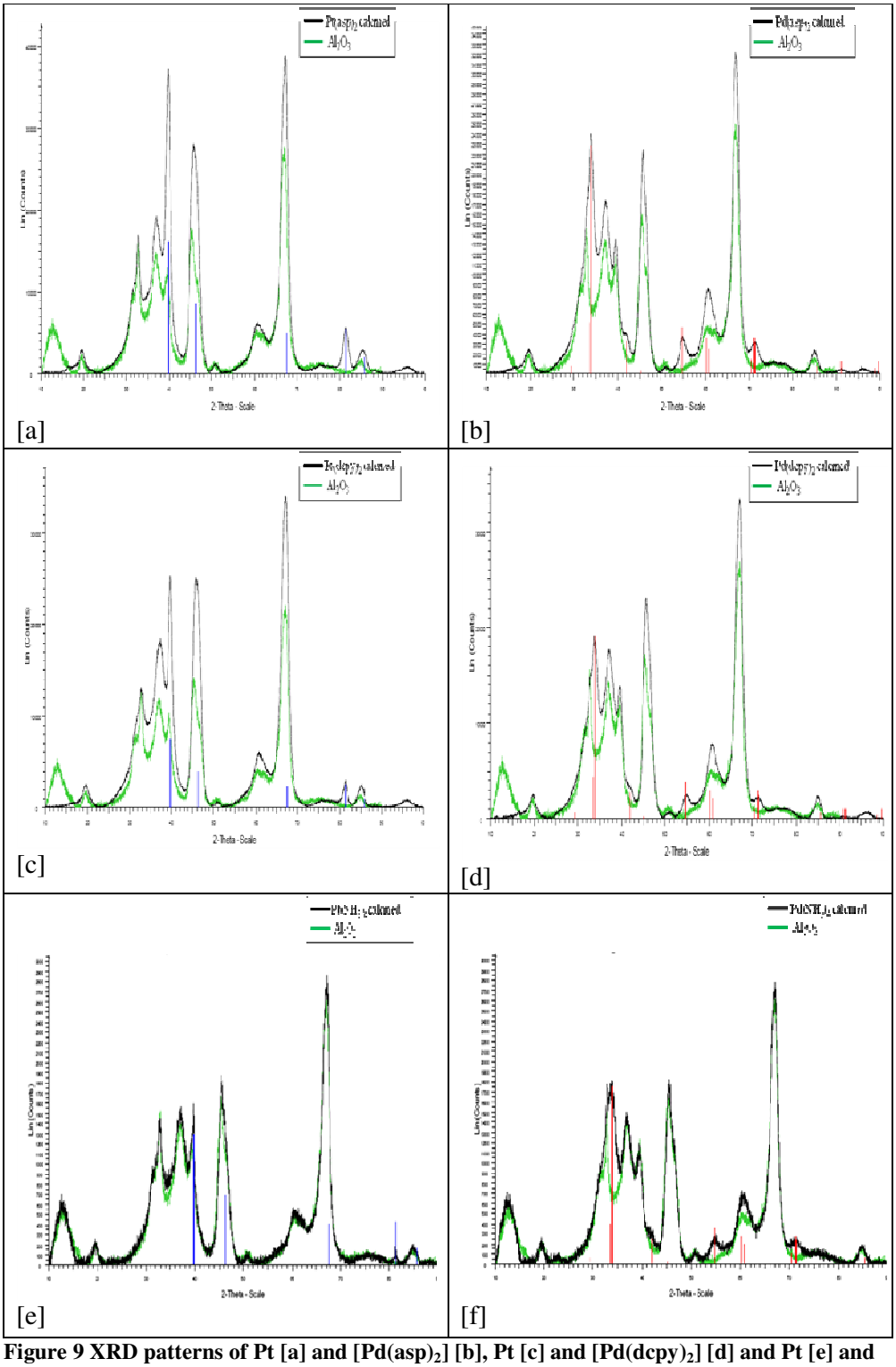

Figure 9 XRD patterns of Pt [a] and $[Pd(asp)_2]$ [b], Pt [c] and $[Pd(dcpy)_2]$ [d] and Pt [e] and $[Pd(NH_3)_4]$ [f]. All samples are calcined on Al_2O_3. ▮ refers to cubic Pt (PDF No 00-004-0802 a = 3.923 Å) and ▮ refers to tetragonal PdO (PDF No 00-046-1043 a = 3.890 Å).

4.5 EXAFS

The following sections display the EXAFS data collected of the monometallic samples on an Al_2O_3 support with the corresponding structural parameters. In some cases, features are seen in the Fourier Transform at longer distances (R) than the data is fitted. Fits of these higher shells were found to be of poor quality with high error values and so the fit was stopped at a shorter distance and the number of adjustable parameters restricted in accordance with Nyqvist's theorem (Chapter Two, Equation 18).

4.5.1 Pt and $Pd(asp)_2$ on Al_2O_3

The spectra in Figure 10 show the EXAFS data collected of the [$Pt(asp)_2$] sample both as a complex and dried onto Al_2O_3 and calcined. The dried sample was measured in an air environment. Calcined samples were measured in both air and a H_2 environment. The structural parameters obtained by analysis of this data are displayed in Table 2. The nature of the neighbour is shown as is the coordination number (N), the distance at which this atom is (R) and the Debye-Waller factor (A), with their corresponding error values. EXAFS is unable to distinguish between oxygen (O), carbon (C) and nitrogen (N) as neighbours. However, given the IR spectra presented above, it is reasonable to assume that the neighbours observed originate from the ligand structure and, thus, the neighbours have been labelled C and O as appropriate in the table.

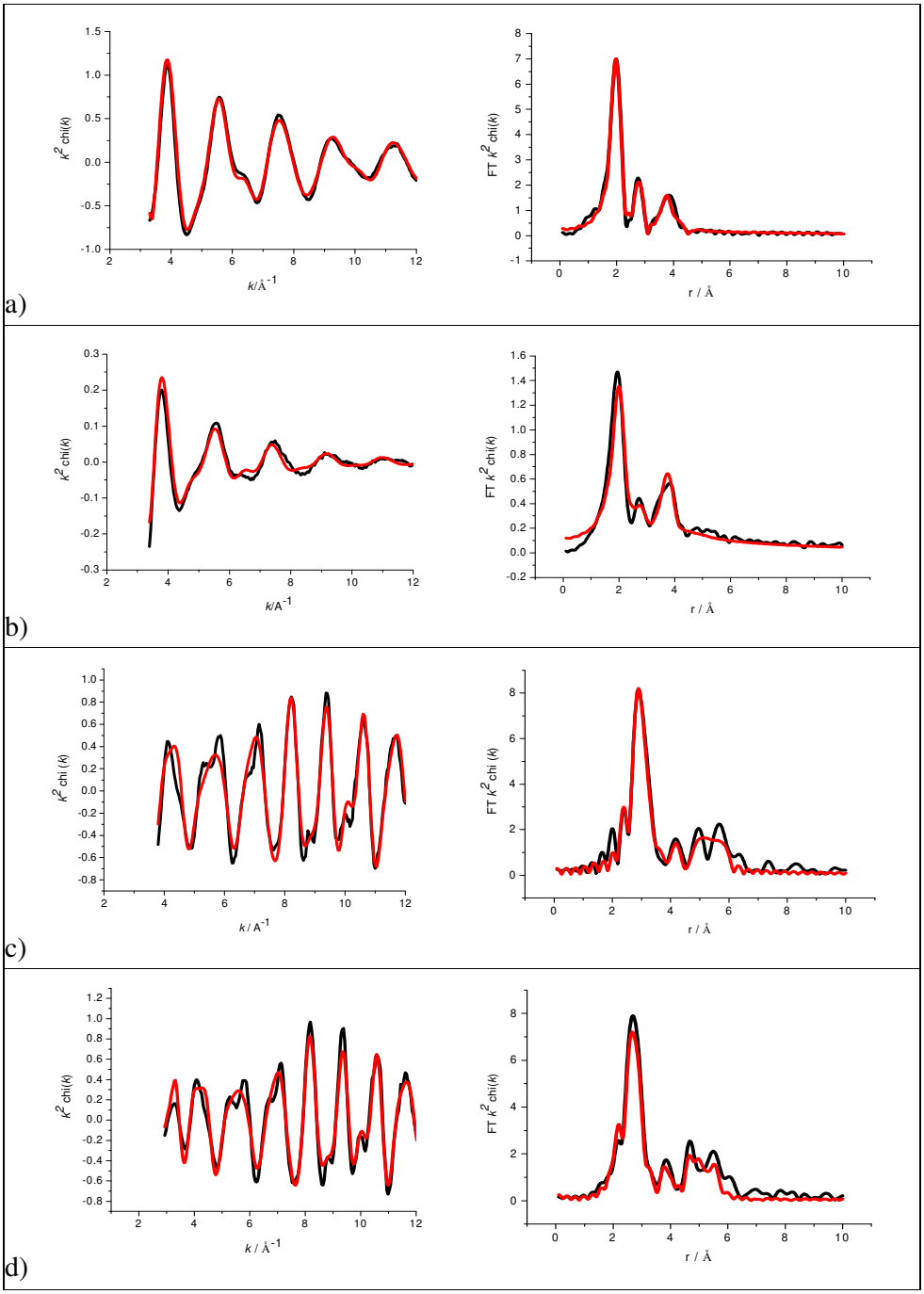

Figure 10 Experimental data (black lines) and fit (red lines) {left} and corresponding Fourier Transform {right} of $[Pt(asp)_2]$ as a prepared complex (a), dried on an Al_2O_3 support (b), after calcining at 500 ºC (c) and after calcining at 500 ºC followed by reduction at room temperature in H_2 (d). Data obtained at room temperature at the Pt L_3 edge in air (a, b, c) and H_2 (d). Data and Fourier Transforms are k^2 weighted.

Table 2 Structural parameters corresponding to the spectra presented in Figure 10.

Sample	Shell	N	R / Å	$2\sigma^2$/Å^2	E_f / eV	R_{exafs} / %
$Pt(asp)_2$ as prep	Pt-O	2.4 ± 0.1	2.01 ± 0.01	0.004 ± 0.001	-15.8 ± 0.3	17.97
	Pt-C	2.2 ± 0.1	2.85 ± 0.01	0.004 ± 0.001		
	Pt-C	6.2 ± 0.6	3.80 ± 0.01	0.016 ± 0.003		
	Pt-C	5.7 ± 1.1	4.38 ± 0.02	0.022 ± 0.007		
$Pt(asp)_2$ dried	Pt-O	1.7 ± 0.1	2.02 ± 0.00	0.005 ± 0.001	-15 2 ± 0.4	23.30
	Pt-C	1.6 ± 0.3	2.88 ± 0.02	0.016 ± 0.005		
	Pt-C	7.4 ± 0.6	3.76 ± 0.01	0.019 ± 0.003		
$Pt(asp)_2$ calcined (air)	Pt-O	0.6 ± 0.3	2.44 ± 0.03	0.009 ± 0.008	-10.4 ± 0.9	23.95
	Pt-Pt	7.0 ± 0.3	2.76 ± 0.01	0.012 ± 0.001		
	Pt-Pt	2.3 ± 0.6	3.87 ± 0.01	0.011 ± 0.002		
	Pt-Pt	5.4 ± 0.9	4.78 ± 0.01	0.009 ± 0.001		
	Pt-Pt	7.9 ± 1.4	5.42 ± 0.01	0.011 ± 0.001		
$Pt(asp)_2$ calcined (H_2)	Pt-Pt	6.5 ± 0.2	2.76 ± 0.01	0.012 ± 0.001	-12.2 ± 0.5	26.70
	Pt-Pt	2.0 ± 0.4	3.91 ± 0.01	0.010 ± 0.001		
	Pt-Pt	5.3 ± 0.7	4.80 ± 0.01	0.009 ± 0.001		
	Pt-Pt	9.5 ± 1.5	5.44 ± 0.01	0.014 ± 0.001		

The results are discussed in detail below in comparison to those collected for the [$Pd(asp)_2$] sample (Figure 11 and Table 3).

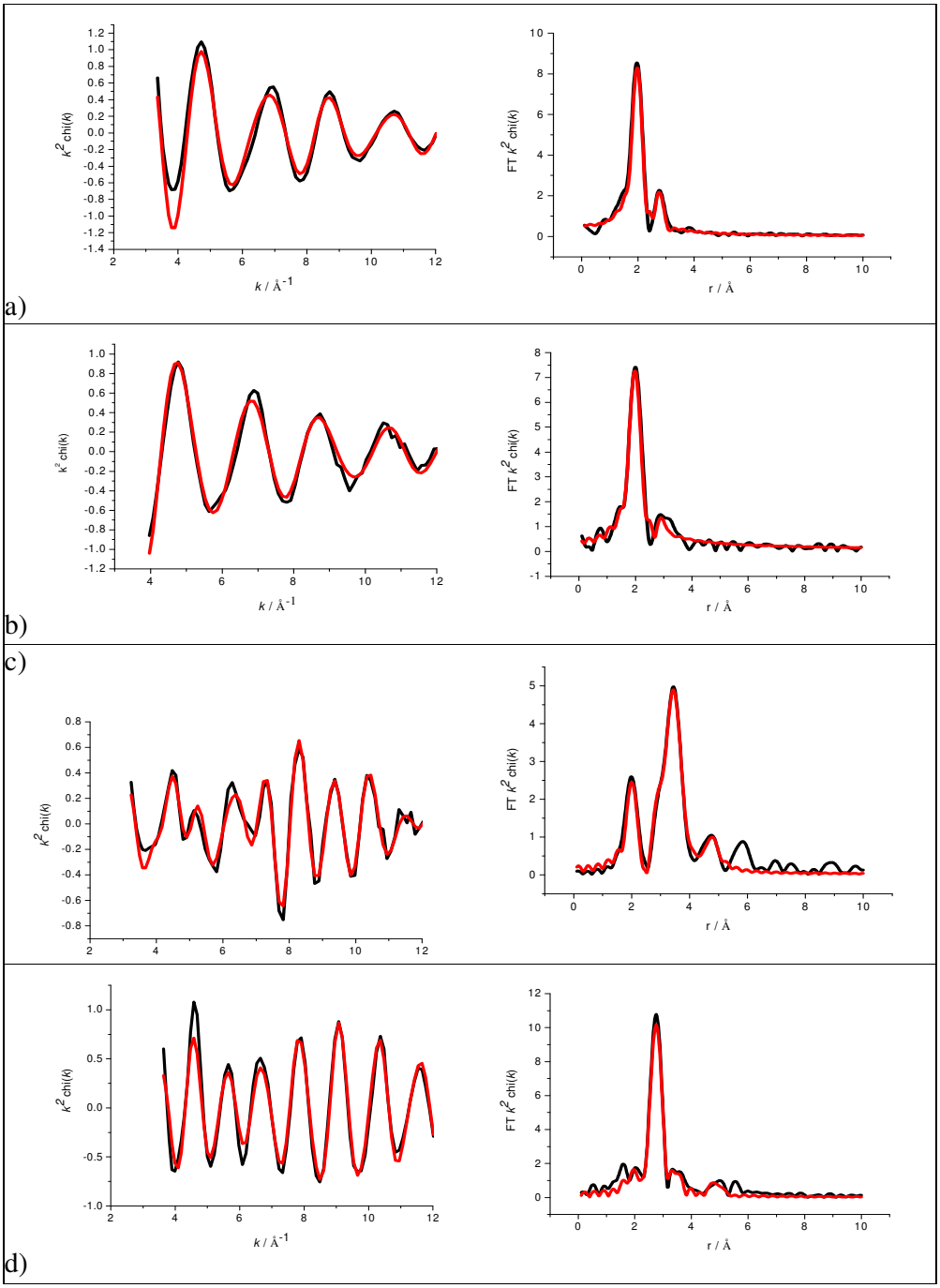

Figure 11 Experimental data (black lines) and fit (red lines) {left} and corresponding Fourier Transform {right} of $[Pd(asp)_2]$ as a prepared complex (a), dried on an Al_2O_3 support (b), after calcining at 500 ºC (c) and after calcining at 500 ºC followed by reduction at room temperature in H_2 (d). Data obtained at the Pd K edge at room temperature in air (a, b, c) and H_2 (d). Data and Fourier Transforms are k^2 weighted.

Table 3 Structural parameters corresponding to the spectra presented in Figure 11.

Sample	Shell	N	R / Å	$2\sigma^2/Å^2$	E_f / eV	R_{exafs} / %
$Pd(asp)_2$ as prep	Pd-O	2.8 ± 0.2	2.00 ± 0.01	0.003 ± 0.001	-4.6 ± 1.3	27.67
	Pd-C	1.9 ± 0.9	2.82 ± 0.04	0.003 ± 0.007		
$Pd(asp)_2$ dried	Pd-O	3.0 ± 0.2	2.00 ± 0.01	0.005 ± 0.001	-2.0 ± 1.1	20.20
	Pd-C	1.2 ± 0.6	2.87 ± 0.04	0.005 ± 0.009		
$Pd(asp)_2$ calcined (air)	Pd-O	0.7 ± 0.1	2.04 ± 0.01	0.001 ± 0.002	-2.9 ± 1.20	24.84
	Pd-Pd	2.7 ± 0.3	3.06 ± 0.01	0.013 ± 0.001		
	Pd-Pd	2.2 ± 0.3	3.44 ± 0.01	0.009 ± 0.001		
	Pd-Pd	3.2 ± 1.0	4.22 ± 0.03	0.012 ± 0.005		
	Pd-Pd	2.0 ± 0.8	4.37 ± 0.03	0.008 ± 0.006		
$Pd(asp)_2$ calcined (H_2)	Pd-Pd	4.8 ± 0.3	2.82 ± 0.01	0.011 ± 0.001	1.3 ± 0.9	21.10
	Pd-Pd	0.6 ± 0.5	3.51 ± 0.05	0.012 ± 0.010		
	Pd-Pd	2.2 ± 1.5	4.91 ± 0.03	0.011 ± 0.006		

The experimental data and corresponding chi plots shown in Figure 10 (a and b) and Figure 11 (a and b) which refer to the $(asp)_2$ complexes as prepared and dried on the Al_2O_3 support are very similar. In both cases only low *Z* neighbours are detected, a fact that is clearly supported by the decrease in the amplitudes of the oscillations at higher *k* in the chi plots. The distances at which these low *Z* neighbours are detected are 2.01, 2.35 and 3.80 Å for $[Pt(asp)_2]$ as prepared (Table 2) and 2.00 and 2.82 Å for $[Pd(asp)_2]$ (Table 3). These distance at 2 Å corresponds to those expected for the M-O and M-N bond in a 5-membered chelate ring as illustrated in Figure 12 and it is thought that the 2.8 Å distance could refer to the carbon atoms of the chelate.

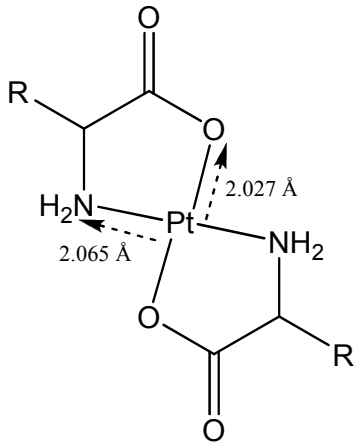

Figure 12 Schematic diagram of the inter-atomic distance from Pt to N or O in a 5 membered chelate[28].

The low *Z* atoms detected at longer range distances in Table 2 are attributed to atoms associated with the "R-group" of the ligand and the carbonyl oxygen atoms.

When the types of neighbouring atom (i.e. low *Z*) and the distances at which they are detected for the dried samples are compared to those of the complex, they are very similar. The distances of the atoms are still seen at 2.0 Å and 2.8 Å implying that when the complex is adsorbed onto the support, the ligand remains intact. $[Pt(asp)_2]$ exhibits a decrease in the coordination number of low *Z* atoms seen in shell 1 and shell 2 which could be due to partial decomposition of the complex or removal of water on drying.

Calcination should result in loss of the ligand and formation of metal nanoparticles on the support. The EXAFS data of the calcined samples confirms this by showing mainly metal (M) neighbours with a small amount of O present (Figure 10 [c], Table 2 and Figure 11 [c], Table 3). In the case of both $[Pt(asp)_2]$ calcined and $Pd(asp)_2$ calcined there has been a significant reduction in the number of low *Z* neighbours detected in shell 1 and in increase in M-O distance to 2.04 Å. Mansour et al[29] present a series of predicted models of Pt oxides and from this we conclude that the increased M-O distance indicates that the ligand has been burnt off and an oxide layer is now present on the surface of the metal particles. $[Pd(asp)_2]$ exhibits the presence of M-M neighbours at extended distances to what the literature predicts. This distance is between the shell radii

of the first and second shell in Pd metal and outside the range expected for Pd-Pd bonding suggesting that two Pd atoms are linked via a bridging oxygen atom[24]. Reduction of the sample in H_2 removes any surface oxide left by calcination and subsequent storage in air, giving a clearer idea of the metal particles present on the surface. Figure 10 (d) and Figure 11 (d) demonstrate a presence of high *Z* neighbours with the chi plots showing greater amplitude of the oscillations at high *k* compared to the data for the complex and dried catalysts[24]. The Fourier Transforms support the chi plots as a loss of the first shell peak at R = 2 Å and an increase in the size of the peak at around 2.7 Å, the standard Pt-Pt (2.77 Å) and Pd-Pd (2.75 Å) distances, are both seen.

Both Table 2 and Table 3 show that the data is well represented by metal atoms, with no low *Z* neighbours detected indicating full reduction of the catalyst samples. A smaller coordination number can often be attributed to smaller particle sizes[30]. Examining the first shell coordination numbers above, $[Pd(asp)_2]$ has a smaller number than $[Pt(asp)_2]$ indicating smaller particle sizes which is supported by the average particle sizes determined by TEM as shown in Figure 8.

4.5.2 Pt and $[Pd(dcpy)_2]$ on Al_2O_3

Figure 13 and Figure 14 present the EXAFS data collected of the $[Pt(dcpy)_2]$ and $[Pd(dcpy)_2]$ complexes and after deposition onto Al_2O_3, respectively. The catalyst was again measured as a dried sample (in air) and as a calcined sample (in air and H_2). The structural parameters obtained following analysis of the EXAFS are presented in Tables 4 and 5. As for the $(asp)_2$ complexes, the structures of the $(dcpy)_2$ complexes follow the same trend in development of the metal particles as the catalyst is dried, calcined, and then reduced.

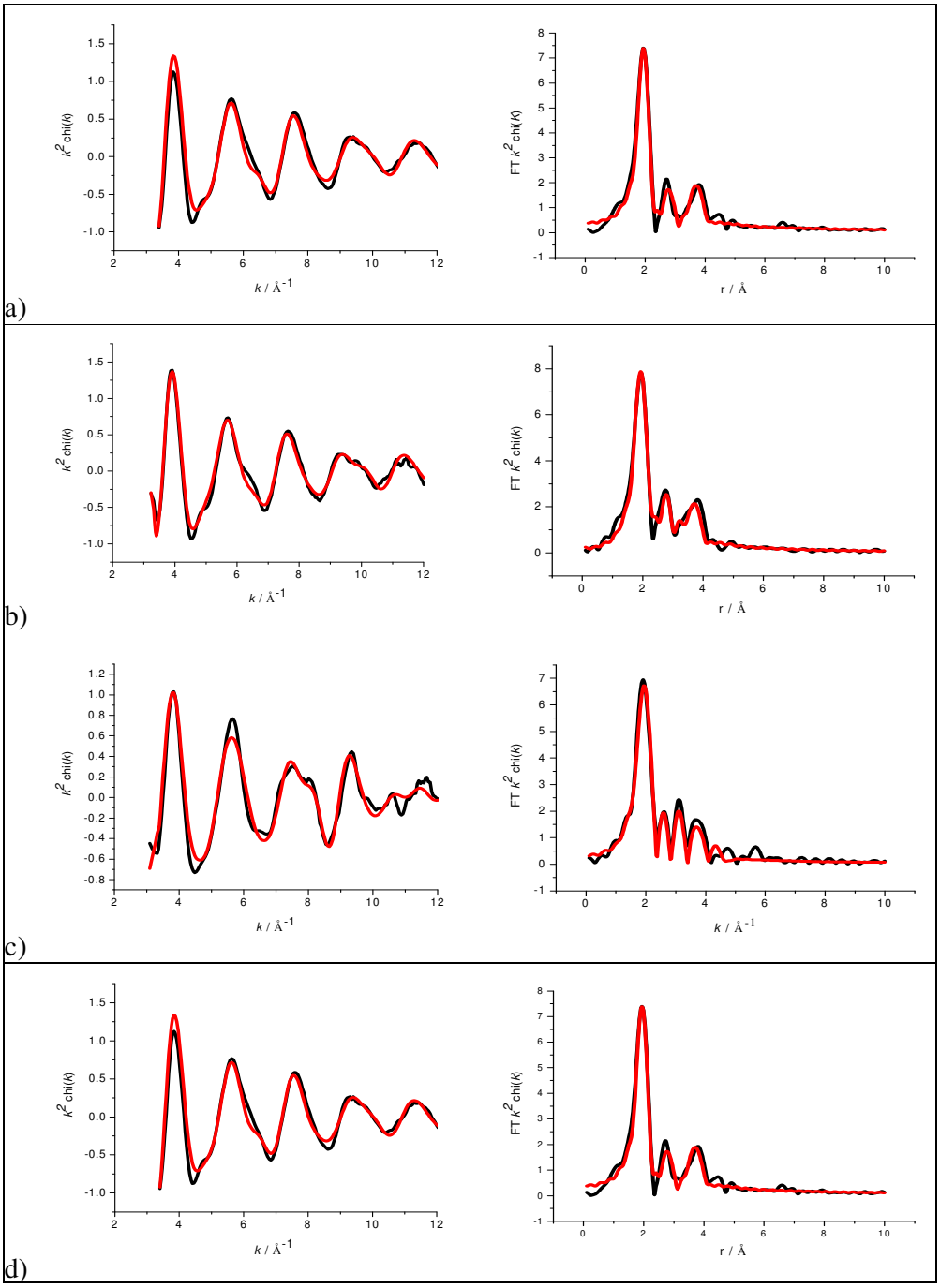

Figure 13 Experimental data (black lines) and fit (red lines) {left} and corresponding Fourier Transform {right} of [Pt(dcpy)$_2$] as a prepared complex (a), dried on a Al_2O_3 support (b), after calcining at 500 ºC (c) and after calcining at 500 ºC followed by reduction in H_2 (d). Data obtained at the Pt L_3 edge in an air (a, b, c) and H_2 (d). Data and Fourier Transforms are k^2 weighted.

Table 4 Structural parameters corresponding to the spectra presented in Figure 13.

Sample	Shell	N	R / Å	$2\sigma^2/Å^2$	E_f / eV	R_{exafs} / %
$Pt(dcpy)_2$ as prep	Pt-O	2.6 ± 0.1	1.99 ± 0.01	0.005 ± 0.001	-14.7 ± 0.6	24.76
	Pt-C	2.1 ± 0.6	2.86 ± 0.03	0.009 ± 0.005		
	Pt-C	9.5 ± 1.4	3.77 ± 0.02	0.019 ± 0.005		
$Pt(dcpy)_2$ dried	Pt-O	2.7 ± 0.1	1.98 ± 0.01	0.006 ± 0.001	-11.8 ± 0.5	19.28
	Pt-C	1.1 ± 0.0	2.84 ± 0.02	0.003 ± 0.001		
	Pt-C	7.3 ± 1.8	3.54 ± 0.02	0.035 ± 0.012		
	Pt-C	9.9 ± 1.5	3.76 ± 0.02	0.016 ± 0.004		
$Pt(dcpy)_2$ calcined (air)	Pt-O	3.0 ± 0.1	2.01 ± 0.01	0.009 ± 0.001	-15.9 ± 0.6	24.98
	Pt-Pt	1.0 ± 0.2	2.43 ±0.01	0.010 ± 0.002		
	Pt-Pt	1.7 ± 0.4	3.13 ± 0.02	0.015 ± 0.003		
	Pt-Pt	2.2 ± 0.8	3.89 ± 0.02	0.018 ± 0.006		
$Pt(dcpy)_2$ calcined (H_2)	Pt-Pt	4.1 ± 0.3	2.75 ± 0.01	0.013 ± 0.001	-10.4 ± 1.5	41.32
	Pt-Pt	1.3 ± 0.5	3.88 ± 0.02	0.009 ± 0.004		
	Pt-Pt	3.3 ± 1.0	4.78 ± 0.02	0.009 ± 0.002		
	Pt-O	0.5 ± 0.1	2.00 ± 0.03	0.006 ± 0.005		

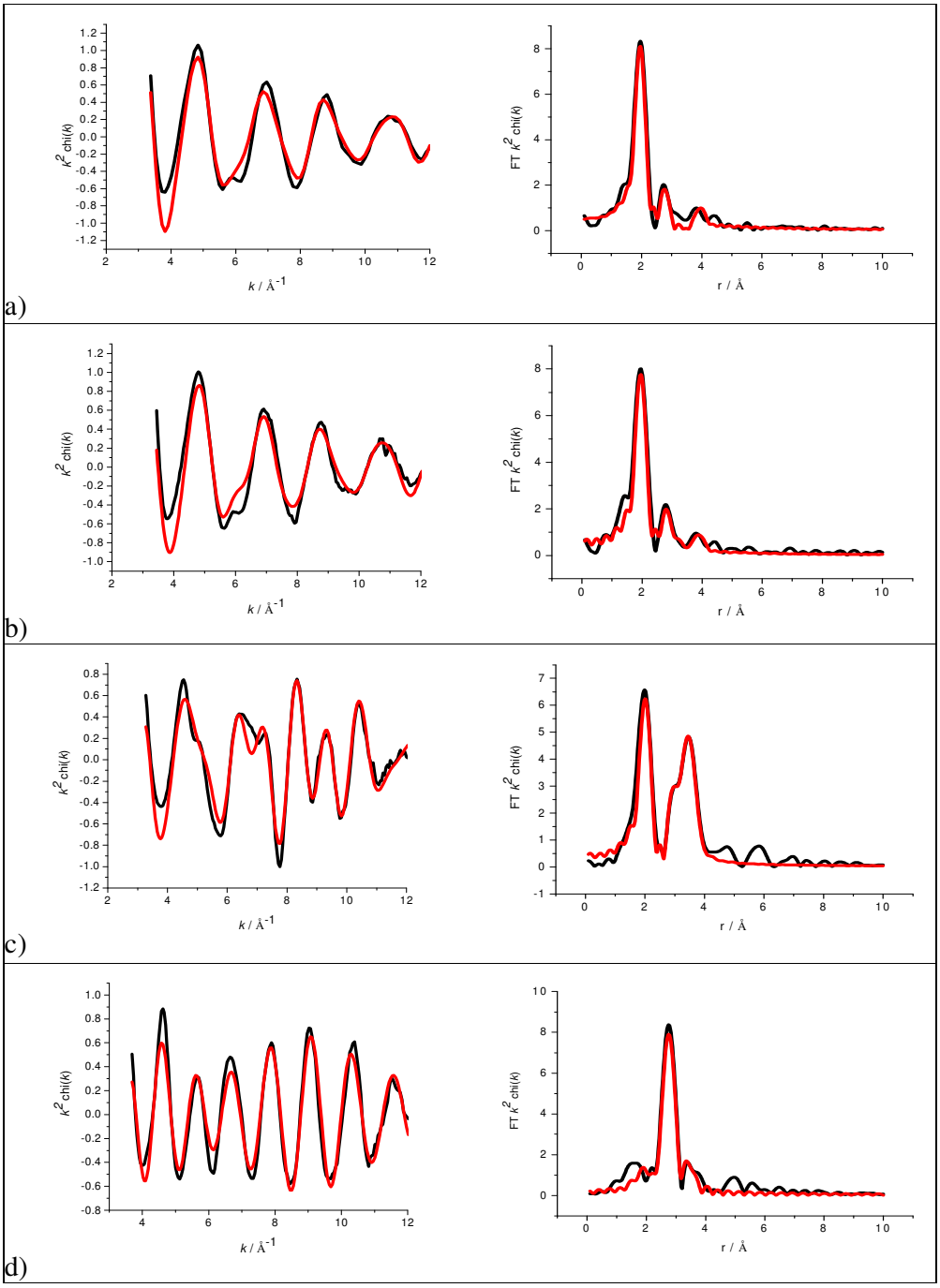

Figure 14 Experimental data (black lines) and fit (red lines) {left} and corresponding Fourier Transform {right} of [Pd(dcpy)$_2$] as a prepared complex (a), dried on a γ-Al$_2$O$_3$ support (b), after calcining at 500 ºC (c) and after calcining at 500 ºC followed by reduction in H$_2$ (d). Data obtained at the Pd K edge in an air (a, b, c) and H$_2$ (d). Data and Fourier Transforms are k^2 weighted.

Table 5 Structural parameters corresponding to the spectra presented in Figure 14.

Sample	Shell	N	R / Å	$2\sigma^2$/Å^2	E_f / eV	R_{exafs} / %
$Pd(dcpy)_2$ as prep	Pd-O	2.6 ± 0.2	1.99 ± 0.01	0.002 ± 0.001	-4.4 ± 1.3	31.41
	Pd-C	1.4 ± 0.9	2.81 ± 0.05	0.006 ± 0.001		
	Pd-C	5.7 ± 3.4	3.92 ± 0.05	0.015 ± 0.012		
$Pd(dcpy)_2$ dried	Pd-O	2.2 ± 0.2	1.99 ± 0.01	0.001 ± 0.001	-3.1 ± 1.2	35.11
	Pd-C	1.8 ± 0.9	2.83 ± 0.04	0.005 ± 0.007		
	Pd-C	3.2 ± 1.8	3.38 ± 0.05	0.022 ± 0.021		
	Pd-C	3.9 ± 2.4	3.88 ± 0.05	0.009 ± 0.012		
$Pd(dcpy)_2$ calcined (air)	Pd-O	1.8 ± 0.1	2.03 ± 0.01	0.001 ± 0.001	-5.0 ± 0.8	29.91
	Pd-Pd	2.5 ± 0.2	3.06 ± 0.01	0.010 ± 0.001		
	Pd-Pd	2.6 ± 0.4	3.45 ± 0.01	0.011 ± 0.002		
$Pd(dcpy)_2$ calcined (H_2)	Pd-Pd	4.4 ± 0.2	2.82 ± 0.01	0.013 ± 0.001	-0.9 ± 0.6	26.91
	Pd-Pd	0.6 ± 0.3	3.51 ± 0.03	0.010 ± 0.005		

The structural parameters of the as prepared and dried samples for both complexes indicate, again, that the complex is staying intact when it is adsorbed onto the support. Low *Z* neighbours are detected at distances on 1.99, 2.86 and 3.77 Å and 1.99, 2.81 and 3.92 Å for the $[Pt(dcpy)_2]$ and $[Pd(dcpy)_2]$ complexes respectively, the lower figure correlating directly with the measurements acquired from the Cambridge Structural Database as illustrated in Figure 12. The longer distances detected could again be attributed to the carbon atoms in the chelate various atoms in the remainder of the molecule.

When the complexes are adsorbed onto the Al_2O_3 support, the figures quoted in the above paragraph barely change leading to the conclusion that the complex is still intact. It is noted, however, in the case of both $[Pt(dcpy)_2]$ dried and $[Pd(dcpy)_2]$ dried that additional shells of low *Z* neighbours at 3.54 and 3.38 Å, respectively, were found. This may imply that some decomposition of the molecule has taken place and certainly the larger Debye-Waller values indicate that a certain amount of disorder is present in the samples. So although it can be

suggested that the 5-membered chelate surrounding the metal atom is still intact after adsorption onto the support, it is likely that the remainder of the complex has undergone some structural change.

Both the calcined $(dcpy)_2$ samples exhibit the characteristic traits of a calcined catalyst when measured in air. Oxygen neighbours are detected at 2.01 and 2.03 Å and the subsequent shells indicate only the presence of high *Z* neighbours. The $(dcpy)_2$ samples have a higher O coordination number than the $(asp)_2$ samples which may be due to the $(asp)_2$ samples existing mainly as metallic Pt and Pd after heat treatment and the $(dcpy)_2$ samples consisting of a higher proportion of PtO_2 and PdO particles. As with the $[Pt(asp)_2]$ sample however, any PtO_2 that is detected in the EXAFS must be amorphous as the XRD patterns show no trace of it. The inter-atomic distance of the second shell is unusual for both samples. $[Pt(dcpy)_2]$ calcined shows the presence of around one Pt atom (1.0 ± 0.2) at a Pt-Pt distance of 2.43 Å. It is difficult to explain this apparent bond contraction. It could be due to the presence of small clusters[31] which result in a small bond length due to the higher electron density between the atoms because of dehybridisation of the metal orbitals[32]. In contrast, $[Pd(dcpy)_2]$ exhibits the opposite behaviour with the first Pd-Pd distance detected at 3.06 Å. This distance is between the shell radii of the first and second shell in Pd metal and outside the range expected for Pd-Pd bonding suggesting that two Pd atoms are linked *via* a bridging oxygen atom[24].

When $[Pd(dcpy)_2]$ calcined was measured in a H_2 atmosphere, the Pd-Pd distance in the first shell was seen to decrease to 2.82 Å, a distance more typical of a Pd-Pd interaction. The bond distances in $[Pt(dcpy)_2]$ when measured in the H_2 environment were also seen to revert to more expected values for Pt-Pt interactions with the first shell having a bond distance of 2.75 Å. However, O atoms were also detected in this sample. At first, this was attributed to incomplete reduction, possibly caused by a leak in the gas cell. However, repeated purges with H_2 gas and separate replicate experiments yielded the same result. It was concluded that the low *Z* neighbour detected here could be an interaction between the Pt atom and the O atoms on the Al_2O_3 support. It should be noted that the Pt-O coordination number of $[Pt(dcpy)_2]$ calcined (H_2) is

significantly decreased from the Pt-O coordination number detected in $[Pt(dcpy)_2]$ calcined (air) (3.0 ± 0.1 and 0.5 ± 0.1 respectively). This, along with the increase in high *Z* neighbours detected indicated that reduction of the sample has taken place.

4.5.3 Pt and $[Pd(NH_3)_4]$ on Al_2O_3

The EXAFS data of the $[Pt(NH_3)_4]$ and $[Pd(NH_3)_4]$ samples collected under the same conditions as used above are presented in Figure 15 and Figure 16 and the corresponding structural parameters with error values are presented in Table 6 and Table 7 respectively.

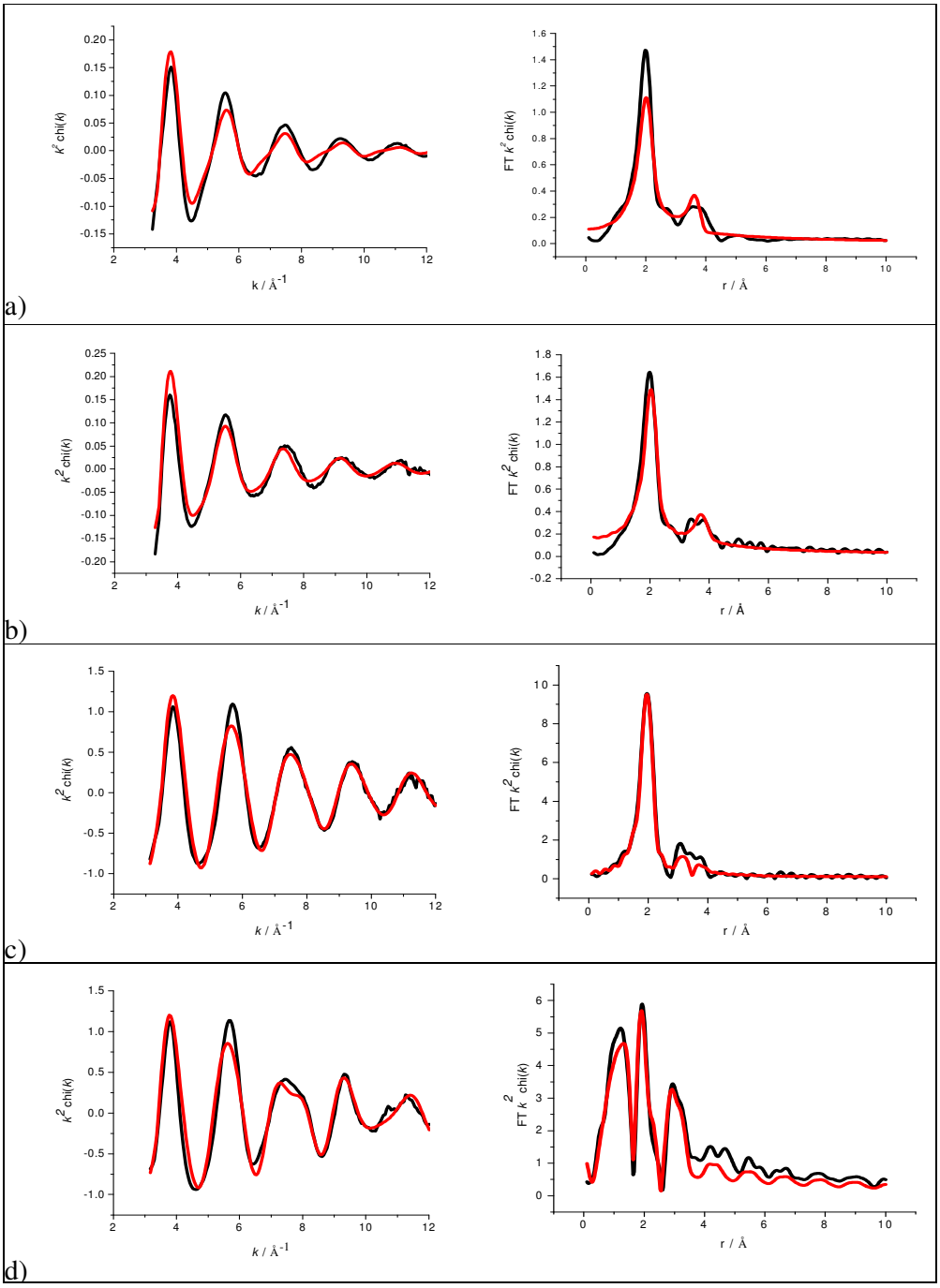

Figure 15 Experimental data (black lines) and fit (red lines) {left} and corresponding Fourier Transform {right} of $[Pt(NH_3)_4]$ as a prepared complex (a), dried on a Al_2O_3 support (c) after calcining at 500 ºC (e) and after calcining at 500 ºC followed by reduction in H_2 (d). Data obtained at the Pt L_3 edge in an air (a, b, c) and H_2 (d). Data and Fourier Transforms are k^2 weighted.

Table 6 Structural parameters corresponding to the spectra presented in Figure 15.

Sample	Shell	N	R / Å	$2\sigma^2$/Å^2	E_f / eV	R_{exafs} / %
$Pt(NH_3)_4$ as prep	Pt-N	2.2 ± 0.1	2.07 ± 0.01	0.006 ± 0.001	-14.6 ± 0.8	35.96
	Pt-N	2.7 ± 0.6	3.71 ± 0.03	0.017 ± 0.009		
$Pt(NH_3)_4$ dried	Pt-N	2.3 ± 0.1	2.09 ± 0.01	0.006 ± 0.001	-20.9± 0.9	35.20
	Pt-N	3.6 ± 0.8	3.80 ± 0.03	0.018 ± 0.010		
$Pt(NH_3)_4$ calcined (air)	Pt-O	3.4 ± 0.1	2.00 ± 0.00	0.005 ± 0.001	-18.4 ± 0.5	21.80
	Pt-Pt	2.2 ± 0.6	3.17 ± 0.02	0.028 ± 0.08		
$Pt(NH_3)_4$ calcined (H_2)	Pt-Pt	1.0 ± 0.3	2.77 ± 0.02	0.007 ± 0.002	-13.6 ± 0.7	27.33
	Pt-O	3.5 ± 0.2	2.01 ± 0.01	0.007 ± 0.001		
	Pt-Pt	2.6 ± 0.8	3.19 ± 0.02	0.023 ± 0.007		

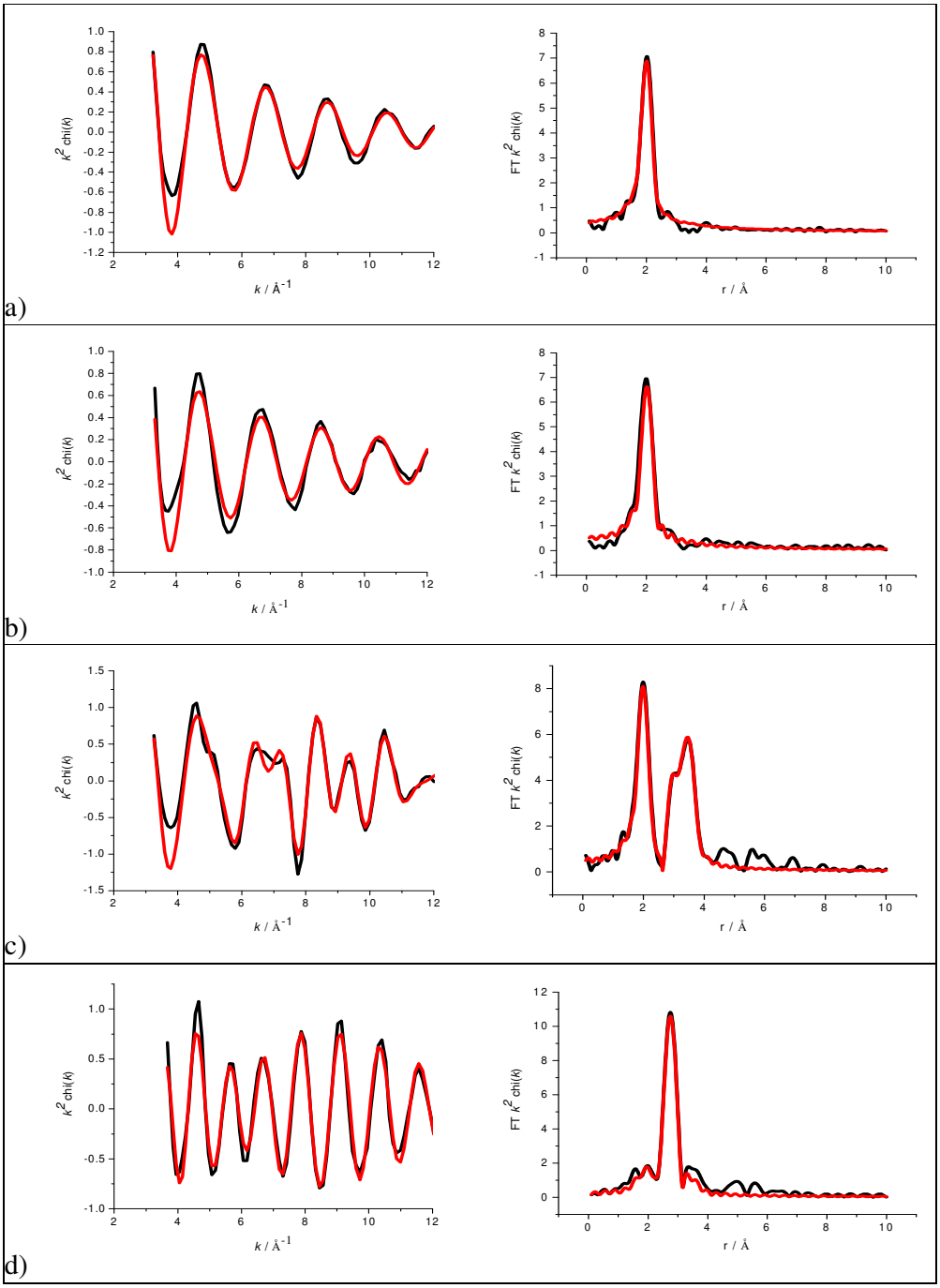

Figure 16 Experimental data (black lines) and fit (red lines) {left} and corresponding Fourier Transform {right} of $[Pd(NH_3)_4]$ as a prepared complex (a), dried on an Al_2O_3 support (b), after calcining at 500 ºC (c) and after calcining at 500 ºC followed by reduction in H_2 (d). Data obtained at the Pd K edge in an air (a, b, c) and H_2 (d). Data and Fourier Transforms are k^2 weighted.

Table 7 Structural parameters corresponding to the spectra in Figure 16.

Sample	Shell	N	R / Å	$2\sigma^2/Å^2$	E_f / eV	R_{exafs} / %
$Pd(NH_3)_4$ as prep	Pd-N	3.4 ± 0.2	2.04 ± 0.01	0.006 ± 0.001	-1.7 ± 1.1	20.13
$Pd(NH_3)_4$ dried	Pd-N	2.6 ± 0.2	2.05 ± 0.01	0.002 ± 0.001	-5.8 ± 1.2	31.03
$Pd(NH_3)_4$ calcined	Pd-O	2.3 ± 0.2	2.03 ± 0.01	0.001 ± 0.002	-5.0 ± 1.2	25.95
	Pd-Pd	3.0 ± 0.4	3.05 ± 0.01	0.011 ± 0.002		
	Pd-Pd	3.0 ± 0.6	3.44 ± 0.01	0.011 ± 0.003		
$Pd(NH_3)_4$ calcined (H_2)	Pd-Pd	5.3 ± 0.3	2.82 ± 0.01	0.013 ± 0.001	-5.4 ± 0.8	19.59
	Pd-Pd	0.6 ± 0.4	3.51 ± 0.05	0.011 ± 0.009		
	Pd-Pd	2.2 ± 1.4	4.91 ± 0.03	0.011 ± 0.006		

The data in Figure 15 confirms the presence of low *Z* neighbours in the as prepared and dried samples with Pt-N distances of 2.07 and 2.09 Å indicating that the complex retains its structure when adsorbed onto the support. A further shell of N atoms is detected at around 3.7 Å. As this shell is identified in both the as prepared and dried samples, it is not due to the low *Z*, O atoms of the Al_2O_3 support and so can possibly be attributed to the detection of atoms in neighbouring complexes adsorbed on the support. This effect isn't seen for the other precursors studied in this work, however, the $(NH_3)_4$ samples are much smaller in size and inter- as well as intra-molecular bond distances may be able to be detected. $[Pd(NH_3)_4]$ also shows a retention of its N atoms after adsorption onto the catalyst support with low Z neighbours detected at 2.04 Å in the as prepared sample and 2.05 Å in the dried.

Both the calcined samples measured in air contain a M-O interaction at ~2.0 Å and a M-M interaction at an increased length of ~3.0 Å. This distance is longer than would be expected and could be attributed to the presence of bridging bonds[24] as eluded to in the case of $[Pd(dcpy)_2]$ calcined. These samples follow the same trend as $[Pd(dcpy)_2]$ after reduction (i.e. removal of the O atoms and the M-M distance returning to a more likely interaction length). The Pt-Pt coordination number in the second shell of the calcined sample measured in air is smaller than the Pd-Pd coordination number for the same shell, a fact backed up

by the smaller average particle size in the Pt sample seen in the TEM data (Figure 8).

On reduction, $[Pd(NH_3)_4]$ contains only Pd neighbours however, full reduction of $[Pt(NH_3)_4]$ was not achieved – a factor which is discussed more thoroughly in Chapter Four. The bridging O atoms which were present in both samples before reduction have been lost as the first shell M-M distance is 2.77 and 2.82 Å for Pt and Pd respectively

5 Silica Supported Catalysts

5.1 Catalyst Preparation

ICP-OAS was used to measure the metal wt % adsorbed onto the catalytic support. The theoretical wt % was 2.5. Table 8 shows the actual wt % of metal present on the SiO_2 support after incipient wetness impregnation of the precursor complexes studied in this work.

Table 8 Actual metal wt % on SiO_2 support after adsorption of complex via incipient wetness and drying measured by ICP-OAS.

Precursor Complex	Metal	Actual wt %
$[Pt(asp)_2]$	Platinum	1.79
$[Pd(asp)_2]$	Palladium	2.47
$[Pt(dcpy)_2]$	Platinum	1.60
$[Pd(dcpy)_2]$	Palladium	1.75
$[Pt(NH_3)_4]$	Platinum	1.84
$[Pd(NH_3)_4]$	Palladium	1.43

The overall metal loadings seen here are less than for the alumina samples and again, less than the theoretical value, however, a loading in the range of 1.43-2.47 % is achieved. There is not a significant enough difference in the overall metal loadings to conclude that the nature of the support has an impact on the quantity of metal taken up during adsorption.

5.2 Raman

Raman spectra of the $(asp)_2$ and $(dcpy)_2$ samples as a prepared complexes, dried onto SiO_2 and calcined are shown in Figure 17 to Figure 20.

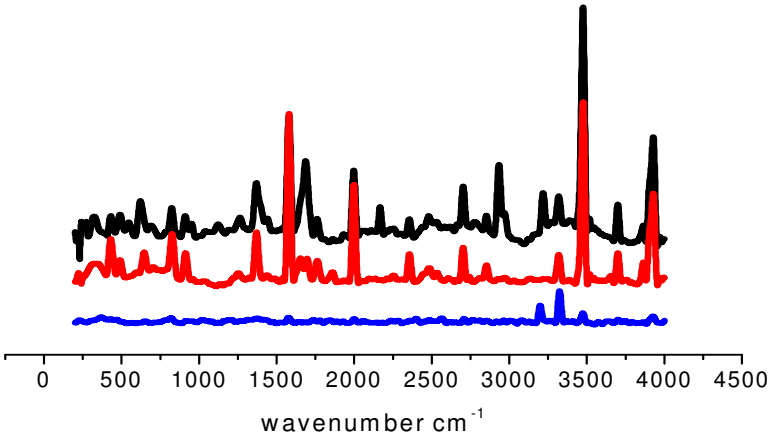

Figure 17 Raman spectra of $[Pt(asp)_2]$ as a prepared complex (black), dried onto SiO_2 support (red) and calcined (blue).

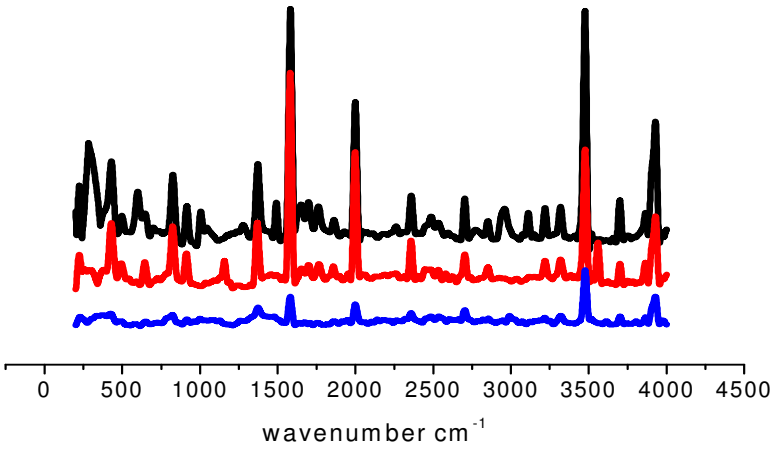

Figure 18 Raman spectra of [Pd(asp)$_2$] as a prepared complex (black), dried onto SiO$_2$ support (red) and calcined (blue).

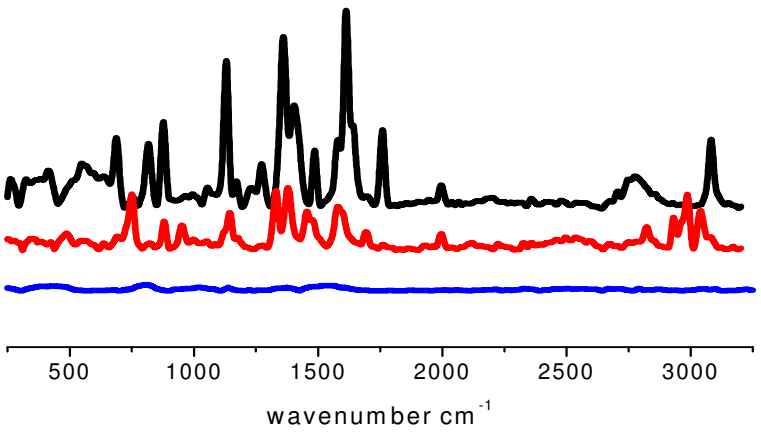

Figure 19 Raman spectra of[Pt(dcpy)$_2$] as a prepared complex (black), dried onto SiO$_2$ support (red) and calcined (blue).

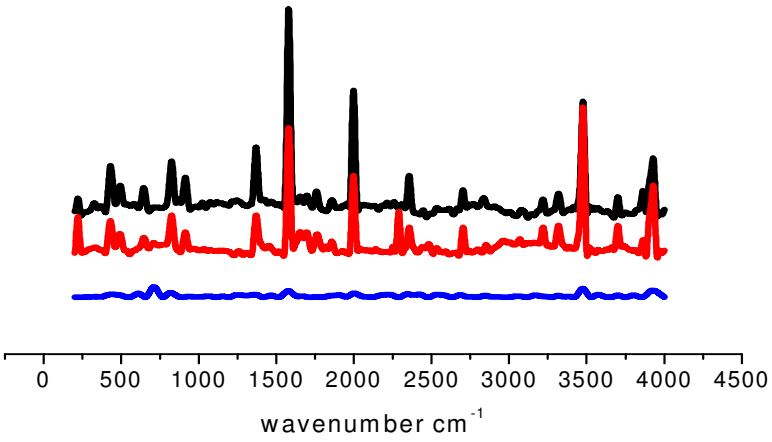

Figure 20 Raman spectra of [Pd(asp)$_2$] as a prepared complex (black), dried onto SiO_2 support (red) and calcined (blue).

The spectra show that for the Pd samples, although there is a slight change in the appearance of the spectra when the complex is measured dried as opposed to as prepared, there is a correlation between the peaks seen. Therefore, it can be suggested that the structure of the complex remains intact during adsorption and that any different characteristics observed in the dried spectra are due to interaction of the complex with the support. However, the Pt/SiO_2 samples show quite different spectra for the complex and dried samples. Although for the dried sample, vibrations are present to imply that parts of the ligand are still present, there are considerable shifts in the positions of the peaks indicating that the complex is interacting more with the support than the Pd/SiO_2 and both the Pt and Pd/Al_2O_3 samples.

All the graphs show that after the sample is calcined, very little is seen in the Raman spectra indicating that the ligands have been burnt off leaving metal oxide particles on the support.

5.3 TEM

TEM was carried out on the SiO_2 supported samples in the same way as the Al_2O_3 samples as outlined in Section 4.4. Micrographs were shown in Figure 7 to demonstrate the images collected during this study. Images at these scales were also taken of the SiO_2 catalyst samples and can be found in reports T3282A and T3282B in the electronic appendix. The particle size distributions obtained following analysis of the TEM images are shown in Figure 21 with the calculated average particle sizes.

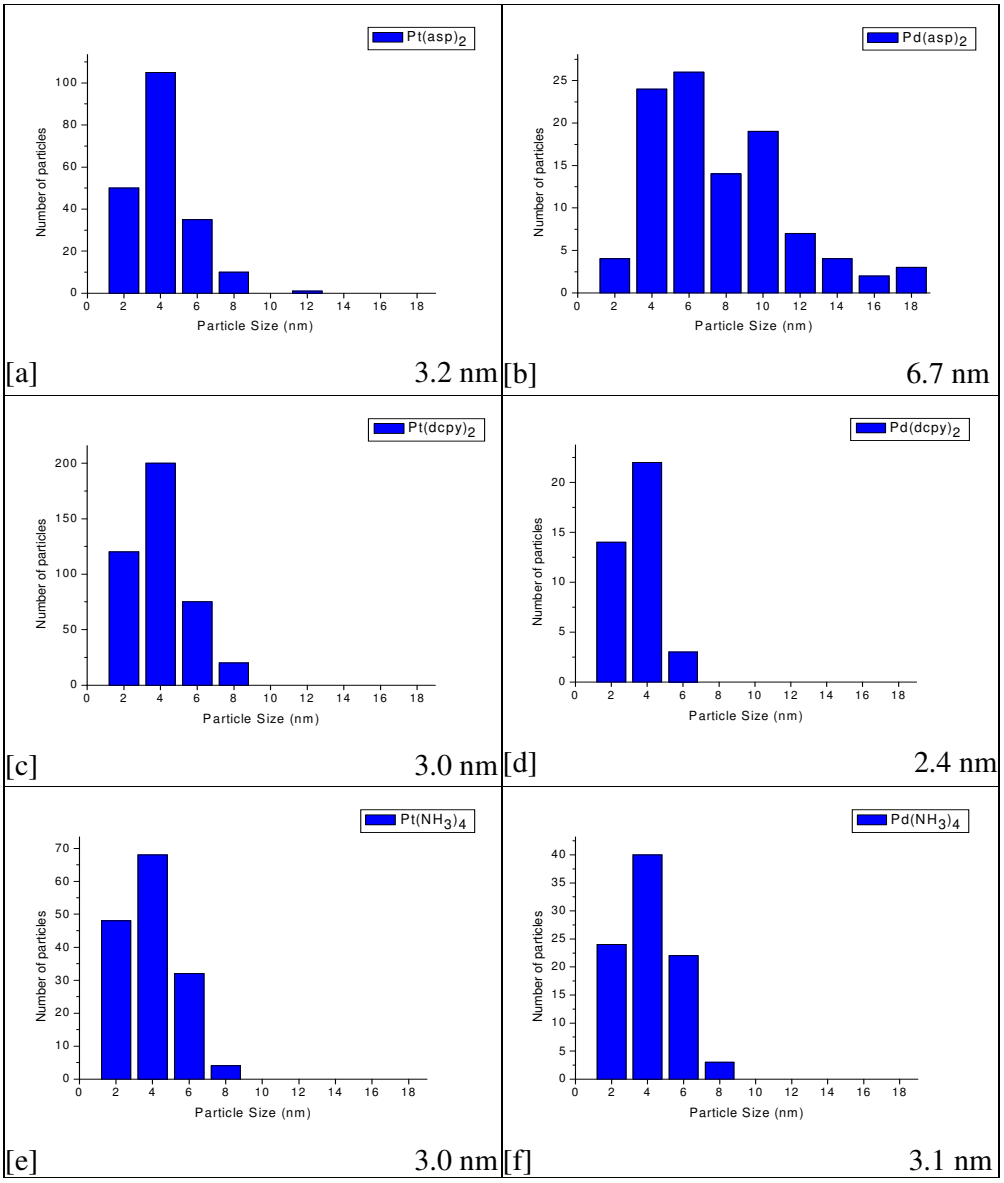

Figure 21 Particle size and distribution of [Pt(asp)$_2$] [a], [Pd(asp)$_2$] [b], [Pt(dcpy)$_2$] [c], [Pd(dcpy)$_2$] [d], [Pt(NH$_3$)$_4$] [e] and [Pd(NH$_3$)$_4$] [f] on SiO$_2$. All samples were analysed as calcined catalysts.

The (NH$_3$)$_4$ and (dcpy)$_2$ samples show the same trend for the distribution of particles size as their Al$_2$O$_3$ counterparts i.e. the distribution of particle sizes does not vary particularly between Pt and Pd catalysts prepared from the same ligand complex.

The [Pt(dcpy)$_2$] and [Pd(dcpy)$_2$] samples have a particle range of 2 – 8 and 2 – 6 nm respectively. This shows a loss of the larger particle sizes seen in the Al$_2$O$_3$

supported samples which could be due to the surface area of the support or the surface charge of the support. $[Pt(NH_3)_4]$ and $[Pd(NH_3)_4]$ samples have particle sizes in the range of 2 – 8 nm which is similar to those obtained for the corresponding Al_2O_3 supported samples. The average particle size of the $[Pt(NH_3)_4]$ particles is larger than for the Al_2O_3 complex but the Pd sample's particle size remains almost the same with a decrease of only 0.1 nm.

With regards to the $(asp)_2$ catalysts, $[Pd(asp)_2]$ on SiO_2 has a wide distribution of particle sizes and a large average particle size (6.7 nm), whilst$[Pt(asp)_2]$ shows a loss of large particle sizes with a particle size distribution ranging from only 2 – 12 nm.

5.4 XRD

Figure 22 below shows the XRD patterns collected of the monometallic samples adsorbed on SiO_2 and calcined. In this case, a reference pattern is not shown due to the amorphous nature of SiO_2. The large peak seen around $2\theta = 22$ in each pattern can be attributed to the support. As with the Al_2O_3 patterns, all samples contain either cubic Pt or tetragonal Pd depending on the metal within the complex and no bulk PtO_2 was detected.

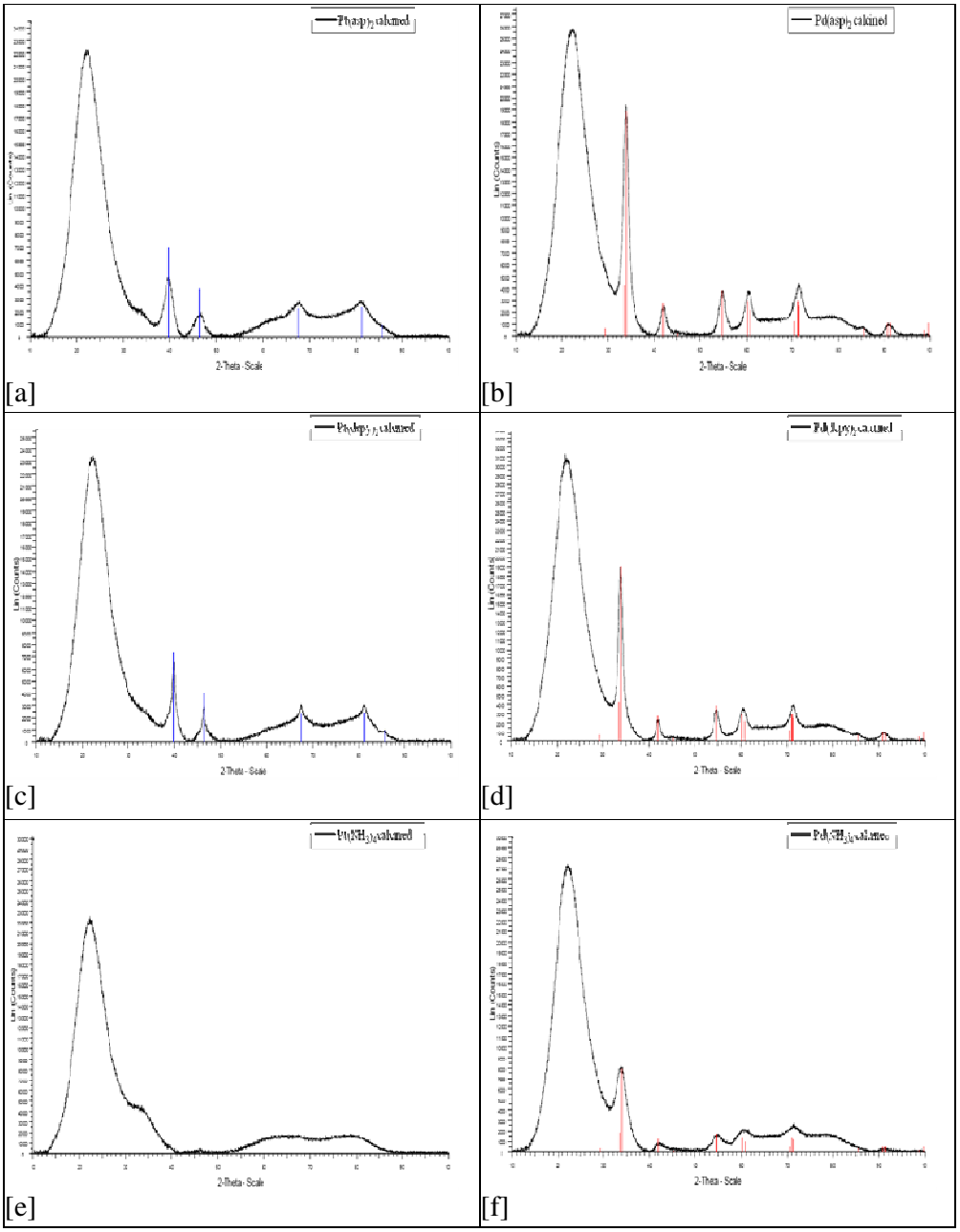

Figure 22 XRD patterns of Pt [a] and [Pd(asp)$_2$] [b], Pt [c] and [Pd(dcpy)$_2$] [d] and Pt [e] and [Pd(NH$_3$)$_4$] [f]. All samples are calcined on SiO$_2$. ▌ is cubic Pt (PDF No 00-004-0802 a = 3.923 Å) and ▌ is tetragonal PdO (PDF No 00-046-1043 a = 3.890 Å).

5.5 EXAFS

EXAFS were collected for the SiO_2 supported catalysts as reported in Section 4.3 for the Al_2O_3 catalysts. In each case, the dried, calcined (air) and calcined (H_2) spectra are reported. It became clear when discussing the samples prepared using an Al_2O_3 support that they all followed a similar trend, i.e. low *Z*

neighbours were detected when measuring the complexes and dried catalysts, and high *Z* neighbours for the calcined and reduced catalysts and this trend was observed for the data collected for the SiO_2 samples.

EXAFS data and the corresponding Fourier Transforms of the $(asp)_2$, $(dcpy)_2$ and $(NH_3)_4$ catalysts and the structural parameters obtained in the analysis are shown in Figure 23 - Figure 28 and Table 9 – Table 14.

5.5.1 Pt and [Pd(asp)$_2$] on SiO$_2$

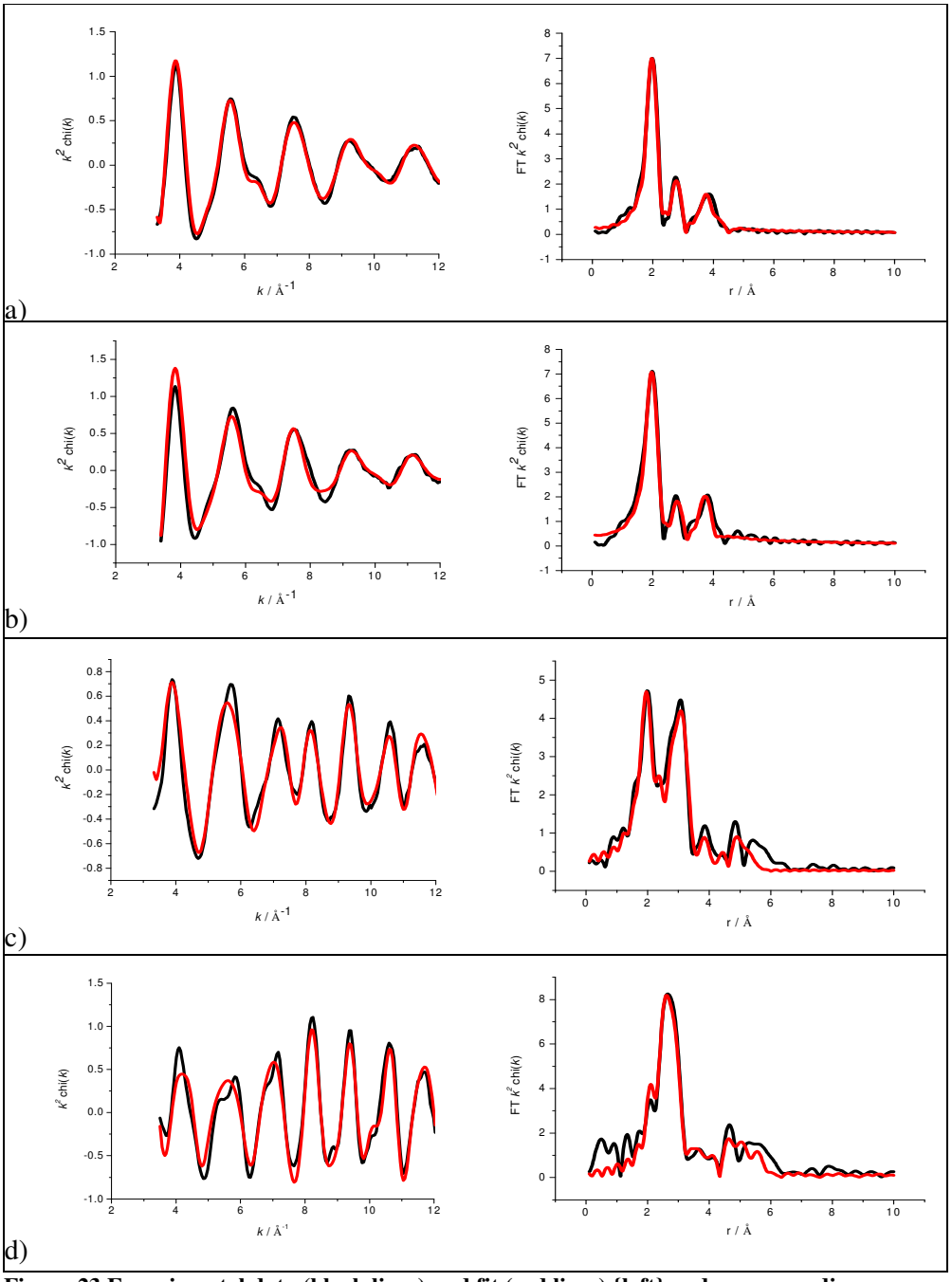

Figure 23 Experimental data (black lines) and fit (red lines) {left} and corresponding Fourier Transform {right} of [Pt(asp)$_2$] as a prepared complex (a), dried on a SiO$_2$ support (c), after calcining at 500 ºC (e) and after calcining at 500 ºC followed by reduction in H$_2$ (d). Data obtained at the Pt L$_3$ edge in an air (a, b, c) and H$_2$ (d). Data and Fourier Transforms are k^2 weighted.

Table 9 Structural parameters corresponding to spectra in Figure 23.

Sample	Shell	N	R / Å	$2\sigma^2/Å^2$	E_f / eV	R_{exafs} / %
$Pt(asp)_2$ as prep	Pt-O	2.4 ± 0.1	2.01 ± 0.01	0.004 ± 0.001	-15.8 ± 0.3	17.97
	Pt-C	2.2 ± 0.0	2.85 ± 0.01	0.004 ± 0.001		
	Pt-C	6.2 ± 0.6	3.80 ± 0.01	0.016 ± 0.003		
	Pt-C	5.7 ± 1.1	4.38 ± 0.02	0.022 ± 0.007		
$Pt(asp)_2$ dried	Pt-O	2.9 ± 0.8	2.02 ± 0.01	0.007 ± 0.001	-15.7 ± 0.7	28.87
	Pt-C	2.1 ± 0.7	2.89 ± 0.03	0.008 ± 0.005		
	Pt-C	8.3 ± 1.4	3.78 ± 0.02	0.014 ± 0.004		
$Pt(asp)_2$ calcined (air)	Pt-O	2.1 ± 0.1	2.02 ± 0.01	0.011 ± 0.001	-15.0 ± 0.9	26.11
	Pt-Pt	3.3 ± 0.2	2.76 ± 0.01	0.010 ± 0.001		
	Pt-Pt	2.1 ± 0.6	3.09 ± 0.02	0.022 ± 0.006		
	Pt-Pt	1.9 ± 0.8	3.89 ± 0.03	0.018 ± 0.007		
	Pt-Pt	2.6 ± 0.9	4.80 ± 0.02	0.010 ± 0.003		
$Pt(asp)_2$ calcined (H_2)	Pt-Pt	8.1 ± 0.4	2.75 ± 0.01	0.011 ± 0.001	-10.6 ± 0.8	28.92
	Pt-Pt	2.4 ± 0.8	3.87 ± 0.02	0.011 ± 0.004		
	Pt-Pt	4.7 ± 1.3	4.78 ± 0.02	0.010 ± 0.003		
	Pt-Pt	6.5 ± 2.1	5.40 ± 0.02	0.012 ± 0.007		

The results seen for $[Pt(asp)_2]$ on SiO_2 are very similar to those discussed for $[Pt(asp)_2]$ on Al_2O_3 with the distances calculated for $[Pt(asp)_2]$ dried being the same as the Al_2O_3 sample indicating that again, the precursor complex is intact after adsorption onto the support. Fewer Pt shells were required in fitting the EXAFS of the SiO_2 sample than for the Al_2O_3 sample. This agrees with the presence of smaller particles as found by analysis of the TEM data (Figure 21) collected for these samples.

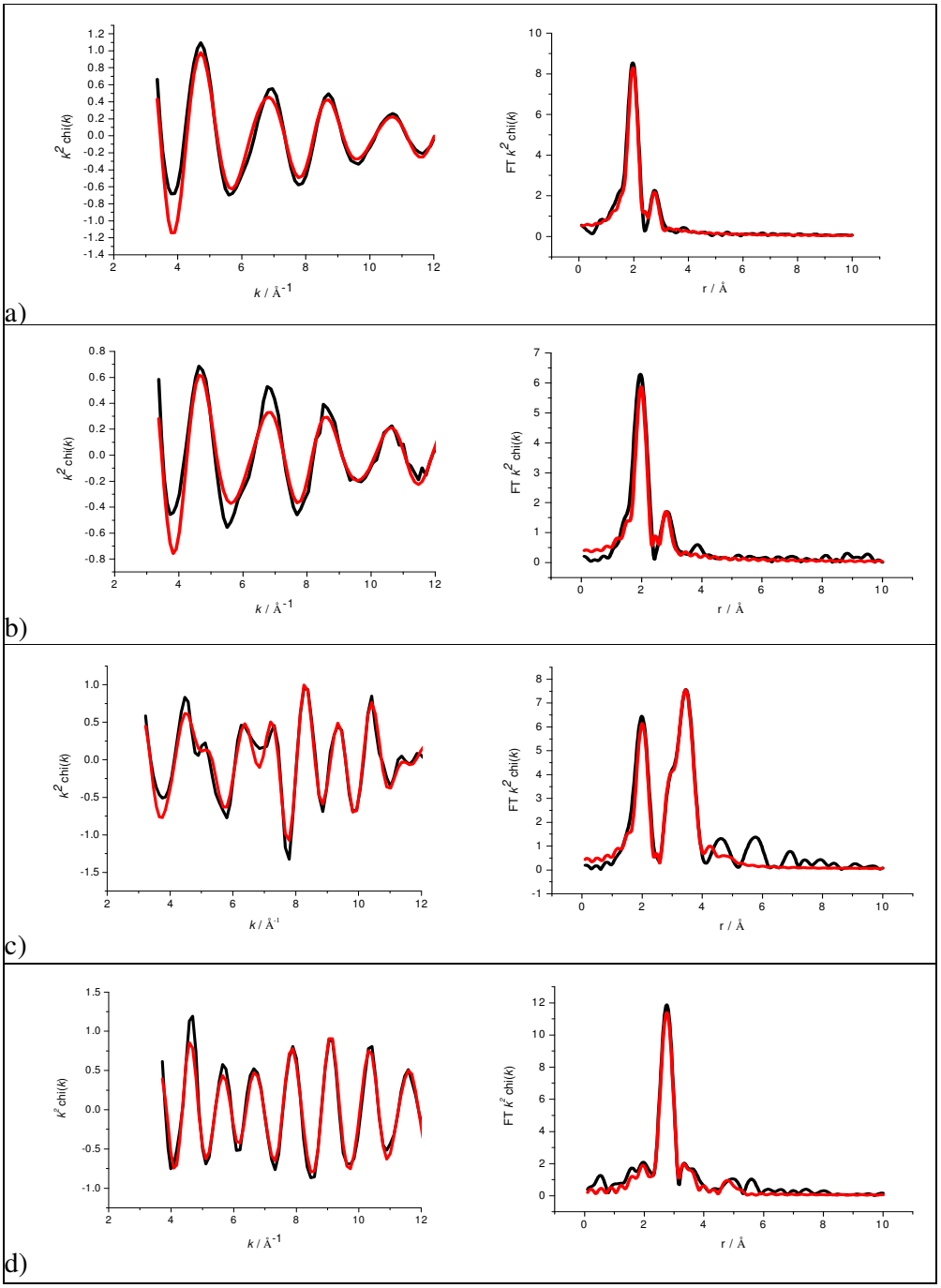

Figure 24 Experimental data (black lines) and fit (red lines) {left} and corresponding Fourier Transform {right} of $[Pd(asp)_2]$ as a prepared complex (a), dried on a SiO_2 support (b), after calcining at 500 °C (c) and after calcining at 500 °C followed by reduction in H_2 (d). Data obtained at the Pd K edge in an air (a, b, c) and H_2 (d). Data and Fourier Transforms are k^2 weighted.

Table 10 Structural parameters of corresponding to spectra presented in Figure 24.

Sample	Shell	N	R / Å	$2\sigma^2/Å^2$	E_f / eV	R_{exafs} / %
$Pd(asp)_2$ as prep	Pd-O	2.8 ± 0.2	2.00 ± 0.01	0.003 ± 0.001	-4.6 ± 1.3	27.67
	Pd-C	1.9 ± 0.9	2.82 ± 0.04	0.003 ± 0.007		
Pd(asp)2 dried	Pd-O	1.7 ± 0.2	2.01 ± 0.01	0.001 ± 0.002	-5.1 ± 1.4	34.75
	Pd-C	1.8 ± 0.8	2.87 ± 0.04	0.006 ± 0.009		
$Pd(asp)_2$ calcined (air)	Pd-O	2.9 ± 0.3	2.03 ± 0.02	0.004 ± 0.002	-4.7 ± 1.5	29.48
	Pd-Pd	3.6 ± 0.5	3.05 ± 0.01	0.011 ± 0.002		
	Pd-Pd	4.0 ± 0.7	3.44 ± 0.01	0.010 ± 0.002		
$Pd(asp)_2$ calcined (H_2)	Pd-Pd	5.9 ± 0.3	2.82 ± 0.01	0.013 ± 0.001	-6.3 ± 0.8	18.81
	Pd-Pd	1.3 ± 1.0	3.50 ± 0.05	0.022 ± 0.012		
	Pd-Pd	2.3 ± 1.5	4.90 ± 0.04	0.011 ± 0.006		

The data presented here differs from the data collected for $[Pt(asp)_2]/SiO_2$ quite significantly. Only two shells were detected when the dried sample was analysed suggesting that some deterioration of the ligand had taken place. However, looking at the distances of 2.01 and 2.87 Å, it is likely that the five-membered metal chelate has remained intact during adsorption. Furthermore, less Pd-Pd than Pt-Pt shells are detected for the calcined samples although the Pd-Pd distances observed for the calcined (air) sample are the same as those for the $[Pd(asp)_2]/Al_2O_3$ catalyst at this point.

$[Pd(asp)_2]/SiO_2$ calcined (H_2) contains one Pd-Pd shell with a large number of neighbours (6.61 ± 0.34) at a distance of 2.82 Å. This is in contrast to the results seen for the $[Pd(asp)_2]/Al_2O_3$ catalyst where two Pd-Pd shells were observed at distances slightly less and slightly greater (2.57 and 2.92 Å) than the distance calculated here. The large coordination number agrees well with the large average particle size seen in the TEM.

5.5.2 Pt and $[Pd(dcpy)_2]$ on SiO_2

The main difference from the $(asp)_2$ samples is the appearance of more peaks at greater distances than 2 Å as seen in the Fourier Transform plots, Figure 25 and Figure 26. Such differences were also found for the Al_2O_3 samples and were attributed to the precursor having a larger structure. This provides evidence that

the ligand is still intact after adsorption onto the support and is further supported by the low *Z* neighbour shells at distances of 1.99, 2.87 and 3.76 Å.

In contrast to the calcined Al_2O_3 samples, the short Pt-Pt distance is not observed when SiO_2 is the support for the [$Pt(dcpy)_2$] complex. Instead, a Pt-Pt bond of 2.76 Å is detected, at a length which agrees well with the literature values of supported Pt nanoparticles. This sample contains only high *Z* neighbours after reduction in H_2 with retention of the first shell Pt-Pt distance but an increase in the second shell Pt-Pt distance and a large increase in the coordination numbers in both cases.

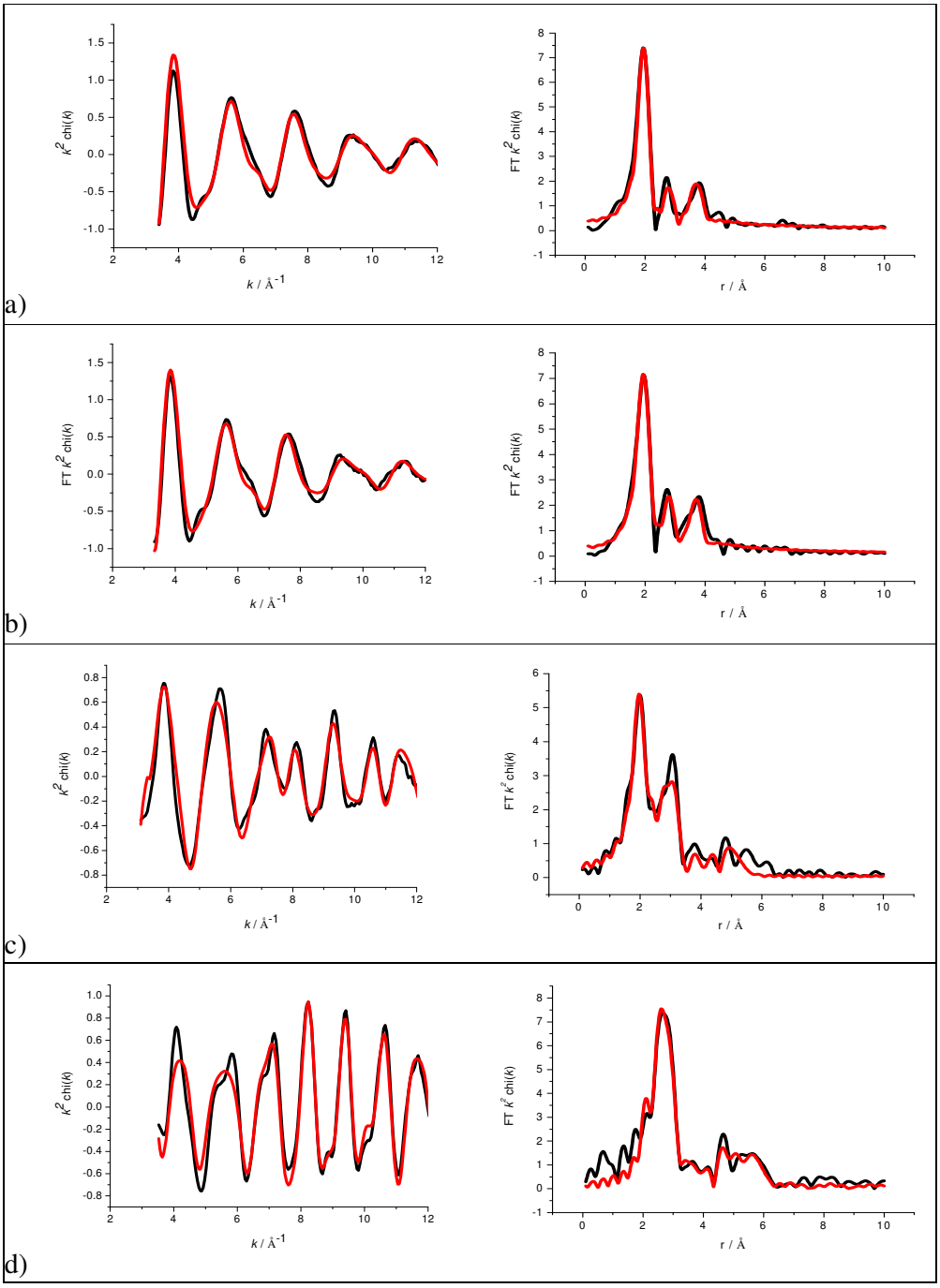

Figure 25 Experimental data (black lines) and fit (red lines) {left} and corresponding Fourier Transform {right} of [Pt(dcpy)$_2$] as a prepared complex (a), dried on a SiO_2 support (b), after calcining at 500 ºC (c) and after calcining at 500 ºC followed by reduction in H_2 (d). Data obtained at the Pt L_3 edge in an air (a, b, c) and H_2 (d). Data and Fourier Transforms are k^2 weighted.

Table 11 Structural parameters corresponding to the spectra presented in Figure 25.

Sample	Shell	N	R / Å	$2\sigma^2/Å^2$	E_f / eV	R_{exafs} / %
$Pt(dcpy)_2$ as prep	Pt-O	2.6 ± 0.1	1.99 ± 0.01	0.005 ± 0.001	-14.8 ± 0.6	24.76
	Pt-C	2.1 ± 0.6	2.86 ± 0.03	0.009 ± 0.005		
	Pt-C	0.5 ± 1.4	3.77 ± 0.02	0.019 ± 0.005		
$Pt(dcpy)_2$ dried	Pt-O	2.8 ± 0.1	1.99 ± 0.01	0.008 ± 0.001	-13.6 ± 0.6	25.38
	Pt-C	2.6 ± 0.5	2.87 ± 0.02	0.009 ± 0.004		
	Pt-C	8.2 ± 1.1	3.76 ± 0.02	0.016 ± 0.004		
$Pt(dcpy)_2$ calcined (air)	Pt-O	2.3 ± 0.1	2.94 ± 0.01	0.010 ± 0.001	-16.0 ± 0.7	28.62
	Pt-Pt	2.2 ± 0.2	2.79 ± 0.01	0.008 ± 0.001		
	Pt-Pt	1.8 ± 0.7	3.93 ± 0.02	0.016 ± 0.006		
	Pt-Pt	2.9 ± 1.1	4.81 ± 0.02	0.010 ± 0.003		
$Pt(dcpy)_2$ calcined (H_2)	Pt-Pt	7.3 ± 0.3	2.75 ± 0.01	0.011 ± 0.001	-10.7 ± 0.9	26.05
	Pt-Pt	2.3 ± 0.8	3.88 ± 0.02	0.012 ± 0.003		
	Pt-Pt	5.0 ± 1.1	4.78 ± 0.01	0.009 ± 0.002		
	Pt-Pt	7.8 ± 2.1	5.39 ± 0.02	0.012 ± 0.003		
	Pt-Pt	5.4 ± 2.3	5.80 ± 0.02	0.012 ± 0.005		

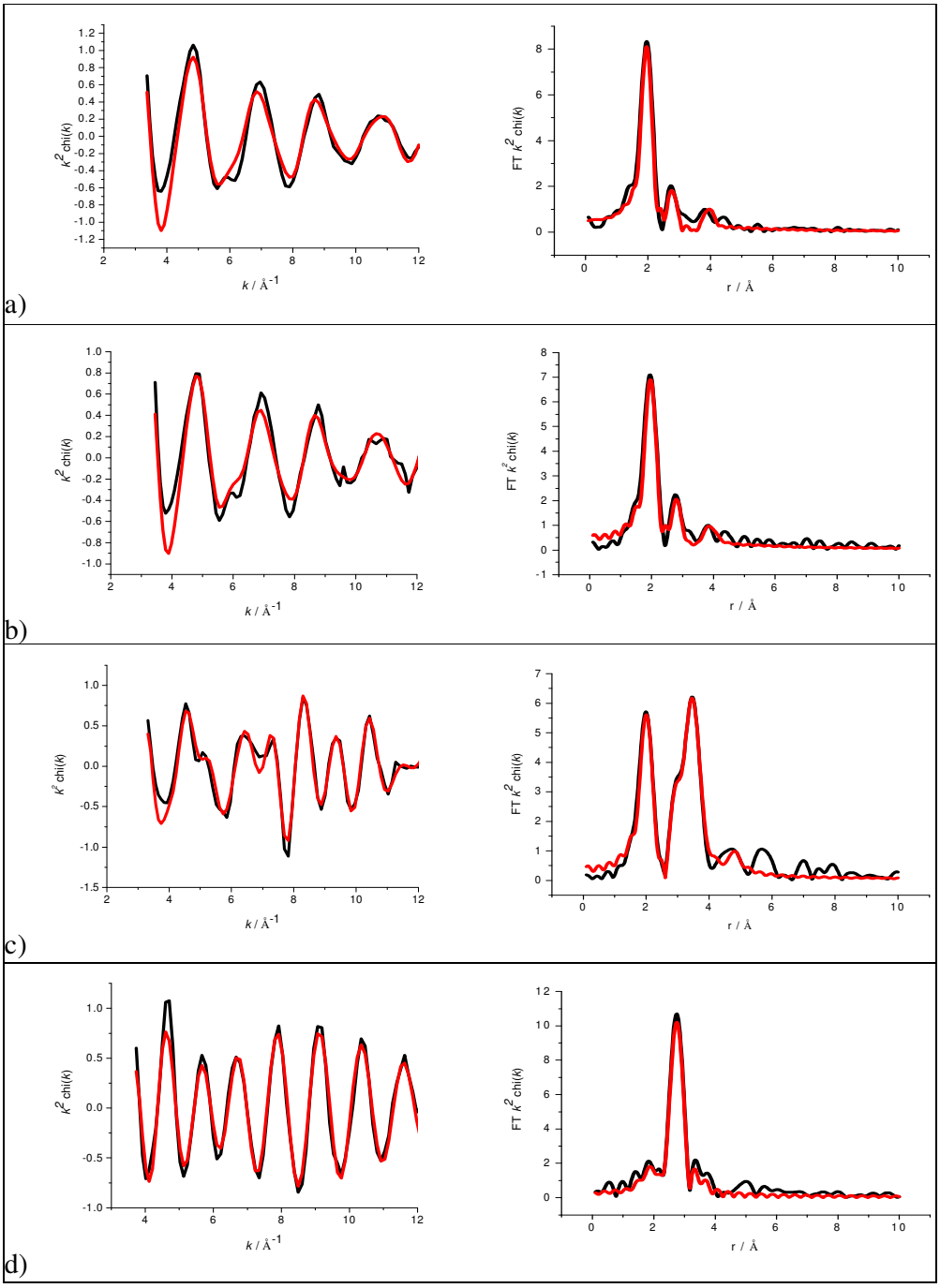

Figure 26 Experimental data (black lines) and fit (red lines) {left} and corresponding Fourier Transform {right} of [Pd(dcpy)$_2$] as a prepared complex (a), dried on a SiO$_2$ support (b), after calcining at 500 ºC (c) and after calcining at 500 ºC followed by reduction in H$_2$ (d). Data obtained at the Pd K edge in an air (a, b, c) and H$_2$ (d). Data and Fourier Transforms are k^2 weighted.

Table 12 Structural parameters corresponding to spectra presented in Figure 26.

Sample	Shell	N	R / Å	$2\sigma^2/Å^2$	E_f / eV	R_{exafs} / %
$Pd(dcpy)_2$ as prep	Pd-O	2.6 ± 0.2	1.99 ± 0.01	0.002 ± 0.001	-4.4 ± 1.3	31.41
	Pd-C	1.4 ± 0.9	2.81 ± 0.05	0.006 ± 0.001		
	Pd-C	5.7 ± 3.4	3.92 ± 0.05	0.015 ± 0.012		
$Pd(dcpy)_2$ dried	Pd-O	2.0 ± 0.2	2.00 ± 0.01	0.001 ± 0.001	-5.1 ± 1.6	34.21
	Pd-C	2.2 ± 1.0	2.83 ± 0.04	0.005 ± 0.008		
	Pd-C	6.0 ± 3.5	3.95 ± 0.05	0.012 ± 0.011		
$Pd(dcpy)_2$ calcined (air)	Pd-O	1.9 ± 0.1	2.04 ± 0.01	0.002 ± 0.001	-5.6 ± 1.1	25.29
	Pd-Pd	3.1 ± 0.4	3.05 ± 0.01	0.012 ± 0.001		
	Pd-Pd	4.1 ± 0.5	3.44 ± 0.01	0.009 ± 0.001		
	Pd-Pd	3.2 ± 1.6	4.22 ± 0.05	0.013 ± 0.010		
	Pd-Pd	2.4 ± 1.4	4.36 ± 0.05	0.011 ± 0.009		
$Pd(dcpy)_2$ calcined (H_2)	Pd-Pd	6.1 ± 0.4	2.82 ± 0.01	0.014 ± 0.001	-5.5 ± 0.9	22.97

The results of $[Pd(dcpy)_2]/SiO_2$ measured as a dried catalyst and after a subsequent heat treatment show almost exactly the same traits as the data collected for the same precursor complex adsorbed on Al_2O_3. Low *Z* neighbours at distances that correlate well with the model (Figure 12) are seen for the dried complex with a clear indication that the ligand is still present after adsorption onto the support. There is also the presence of high *Z* neighbours once the sample is calcined with oxygen neighbours at a distance consistent with oxide formation, which are subsequently removed after reduction in H_2. There are no Pd-Pd neighbours detected at the literature value of 2.75 Å, the first shell of high *Z* neighbours being seen at 3.05 Å indicating that the calcined sample is characterised by bridging of the O atoms. The Pd-Pd distance decreases after reduction to a value closer to that expected of metal nanoparticles.

5.5.3 Pt and $[Pd(NH_3)_4]$ on SiO_2

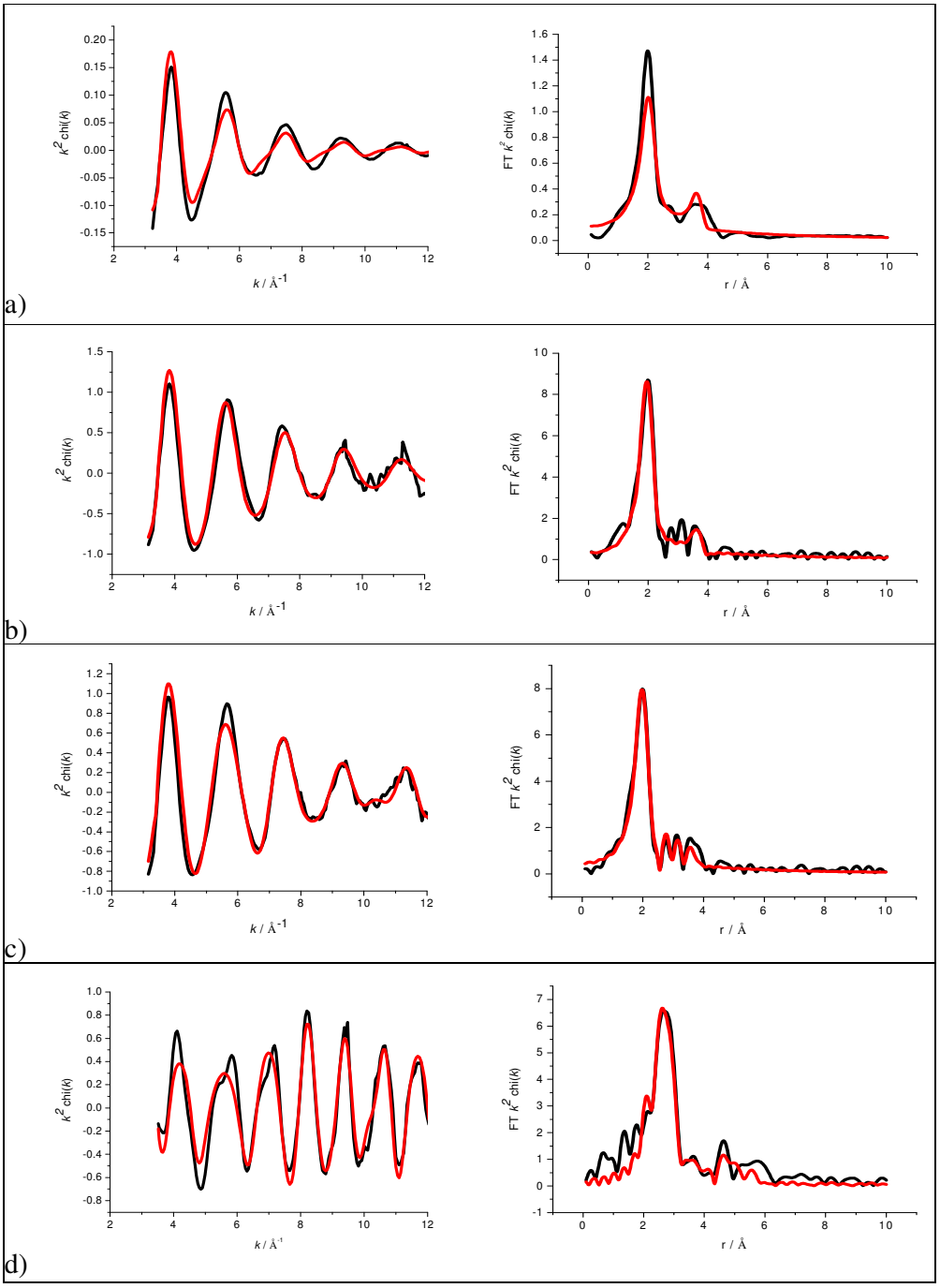

Figure 27 Experimental data (black lines) and fit (red lines) {left} and corresponding Fourier Transform {right} of $[Pt(NH_3)_4]$ as a prepared complex (a), dried on a SiO_2 support (b), after calcining at 500 °C (c) and after calcining at 500 °C followed by reduction in H_2 (d). Data obtained at the Pt L_3 edge in an air (a, b, c) and H_2 (d). Data and Fourier Transforms are k^2 weighted.

Table 13 Structural parameters corresponding to spectra presented in Figure 27.

Sample	Shell	N	R / Å	$2\sigma^2/Å^2$	E_f / eV	R_{exafs} / %
$Pt(NH_3)_4$ as prep	Pt-N	2.7 ± 0.1	2.07 ± 0.01	0.006 ± 0.001	-14.6 ± 0.8	35.96
	Pt-N	2.7 ± 0.6	3.71 ± 0.30	0.017 ± 0.009		
$Pt(NH_3)_4$ Dried	Pt-N	3.6 ± 0.2	2.01 ± 0.01	0.009 ± 0.001	-11.3 ± 0.7	28.27
	Pt-N	2.7 ± 0.8	3.69 ± 0.03	0.012 ± 0.009		
$Pt(NH_3)_4$ calcined	Pt-O	3.5 ± 0.1	2.02 ± 0.01	0.009 ± 0.001	-15.4 ± 0.6	23.29
	Pt-Pt	0.7 ± 0.2	2.54 ± 0.02	0.010 ± 0.003		
	Pt-Pt	1.4 ± 0.3	3.09 ± 0.01	0.012 ± 0.003		
$Pt(NH_3)_4$ calcined (H_2)	Pt-Pt	6.4 ± 0.3	2.75 ± 0.01	0.011 ± 0.001	-10.1 ± 0.9	30.57
	Pt-Pt	1.8 ± 0.7	3.86 ± 0.02	0.011 ± 0.004		
	Pt-Pt	3.5 ± 1.3	4.77 ± 0.02	0.010 ± 0.003		
	Pt-Pt	3.0 ± 1.8	5.37 ± 0.03	0.012 ± 0.007		

As has been observed before when this sample was measured on Al_2O_3 (Table 6), Pt-N neighbours are detected for the dried catalyst. Upon heat treatment, an oxide layer is formed and Pt neighbours are seen at distances of 2.54 Å and 3.09 Å. This value at 2.54 Å is slightly lower than would be expected although it is clear that this sample is not characterised by bridging ligands as were seen for the same precursor deposited on Al_2O_3. This short Pt-Pt distance does return to a value closer to the literature at 2.75 Å after reduction, implying that it is the oxide layer which is causing this effect.

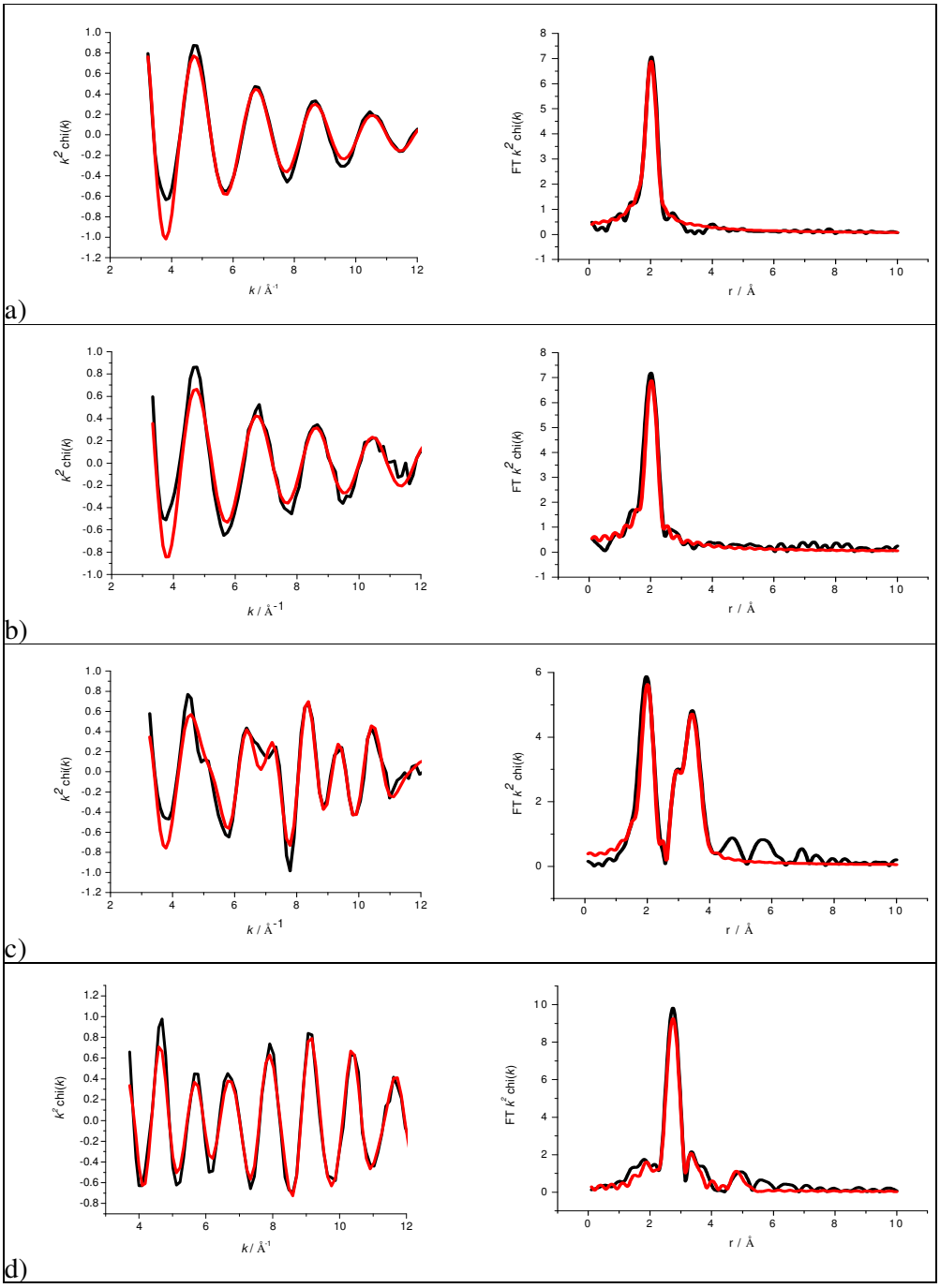

Figure 28 Experimental data (black lines) and fit (red lines) {left} and corresponding Fourier Transform {right} of $[Pd(NH_3)_4]$ as a prepared complex (a), dried on a SiO_2 support (b), after calcining at 500 ºC (c) and after calcining at 500 ºC followed by reduction in H_2 (d). Data obtained at the Pd K edge in an air (a, b, c) and H_2 (d). Data and Fourier Transforms are k^2 weighted.

Table 14 Structural parameters corresponding to spectra presented in Figure 28.

Sample	Shell	N	R / Å	$2\sigma^2/Å^2$	E_f / eV	R_{exafs} / %
$Pd(NH_3)_4$ as prep	Pd-N	3.4 ± 0.2	2.04 ± 0.01	0.006 ± 0.001	-1.7 ± 1.1	20.13
$Pd(NH_3)_4$ dried	Pd-N	2.8 ± 0.2	2.05 ± 0.01	0.002 ± 0.001	-2.8 ± 1.3	34.19
$Pd(NH_3)_4$ calcined (air)	Pd-O	1.9 ± 0.2	2.03 ± 0.01	0.004 ± 0.002	-5.3 ± 1.3	29.96
	Pd-Pd	2.5 ± 0.4	3.05 ± 0.01	0.011 ± 0.002		
	Pd-Pd	2.5 ± 0.5	3.44 ± 0.01	0.011 ± 0.003		
$Pd(NH_3)_4$ calcined (H_2)	Pd-Pd	4.9 ± 0.3	2.81 ± 0.01	0.013 ± 0.001	-5.7 ± 0.9	20.54
	Pd-Pd	0.8 ± 0.5	3.48 ± 0.04	0.012 ± 0.008		
	Pd-Pd	2.0 ± 1.2	4.92 ± 0.04	0.008 ± 0.005		

$[Pd(NH_3)_4]/SiO_2$ is very similar to $[Pd(NH_3)_4]/Al_2O_3$ with the presence of two shells of Pd-Pd neighbours in the calcined sample with similar coordination numbers. This sample does differ quite significantly from its Pt equivalent however with only one low *Z* neighbour shell being detected for the as a prepared complex and the dried catalyst indicating that neighbouring molecules cannot be seen. This may imply that the Pd sample is more dispersed than the Pt sample, with greater distances between neighbouring adsorbed complex molecules.

6 Discussion

This chapter began with the infrared measurements of the catalyst samples described in Chapter Two. The infrared showed a shift in $\upsilon(NH_2)$ to higher frequencies and a change in shape of the $\upsilon(C=O)$ peak confirming the ligand and the metal had complexed. These samples were then adsorbed onto Al_2O_3 and SiO_2 and a range of methods were used to characterise them as they were heat treated to produce catalyst nanoparticles.

The Raman spectra indicated that there were similarities between structure of the complex and the species present after adsorption onto the support. $[Pt(dcpy)_2]/SiO_2$ was found to have the largest interaction with the support with

the greatest perturbation of the peaks being seen when the dried sample was measured in comparison to the as prepared sample. The observation that the complex structure remains intact after adsorption was verified by EXAFS measurements of the as prepared and dried samples which showed little, if any change in both types of neighbours and the distances at which they were found.

Calcination should result in the loss of the ligand and this was shown for all the samples in this chapter as the only detectable M-O neighbour identified was found generally at a longer distance than the ligand low *Z* neighbour indicating an oxide layer had formed on the metal particle. M-M distances were sometimes varied with shorter distances indicating the presence of clusters and longer distances implying that bonding was occurring *via* a bridging O atom. In all cases, after reduction, the M-M distance reverted to the literature value. TEM measurements at this point showed variation in size with regards to ligand and support type for the $(dcpy)_2$ and $(NH_3)_4$ samples but little variation between Pt and Pd samples. The $(asp)_2$ samples however, varied considerably in particle size. $[Pt(asp)_2]/Al_2O_3$ and $[Pd(asp)_2]/SiO_2$ both showed large average particle sizes in the TEM, an observation supported by a large $N_{Pt\text{-}Pt}$ and $N_{Pd\text{-}Pd}$ coordination numbers respectively, after reduction.

The SiO_2 supported catalysts had smaller particle sizes on average than the Al_2O_3 supported catalysts, implying that a change in the characteristics of the support can have an effect on the dispersion of the catalysts. The characteristics which are most likely to have an effect on dispersion are surface area and surface charge. Indeed, Schreier and Regalbuto[13] found that for Pt/SiO_2, deposition at an optimal pH could yield reduced metal particles with 100 % dispersion. This feature confirms that a change in support can affect the overall activity of the catalyst as it has been found that catalysts which are more dispersed show a higher catalytic activity[33].

XRD measurements of the calcined catalysts consistently failed to detect PtO_2. This could have been due to the metal oxide particles being too small. However, in light of the average particle size measurements in the TEM, and the fact that

oxide neighbours are clearly seen in the EXAFS, it is concluded that the PtO_2 in these cases is amorphous and therefore undetectable by XRD.

When the sample was reduced, the low Z neighbours were removed leaving M-M neighbours. Generally, the coordination numbers of these neighbours agree with the TEM with a smaller average particle size correlating with a smaller coordination number.

7 References

(1) Stosick, A. J. *Journal of the American Chemical Society* **1945**, *67*, 365.

(2) Condrate, R. A., Nakomoto, K. *Journal of Chemical Physics* **1965**, *42*, 2590.

(3) Min, B. K., Santra, A.K., Goodman, D.W. *Catalysis Today* **2003**, *85*, 113-124.

(4) Dawody, J.; Skoglundh, M.; Wall, S.; Fridell, E. *Journal of Molecular Catalysis a-Chemical* **2005**, *225*, 259-269.

(5) Shelimov, B.; Lambert, J.-F.; Che, M.; Didillon, B. *Journal of Catalysis* **1999**, *185*, 462-478.

(6) Shelimov, B. N., Lambert, J-F., Che, M., Didillon, B. *Journal of Molecular Catalysis A: Chemical* **2000**, *158*, 91-99.

(7) Womes, M., Cholley, T., Le Peltier, F., Morin, S., Didillon, B., Szydlowski-Schildknecht, N. *Applied Catalysis A: General* **2005**, *283*, 9-22.

(8) Womes, M.; Lynch, J.; Bazin, D.; Le Peltier, F.; Morin, S.; Didillon, B. *Catalysis Letters* **2003**, *85*, 25-31.

(9) Brunelle, J. P. *Pure and Applied Chemistry* **1978**, *50*, 1211-1229.

(10) Regalbuto, R., Navada, A., Shadid, S., Briecker, M.L., Chen, Q. *Journal of Catalysis* **1999**, *184*, 335-348.

(11) Munozpaez, A.; Koningsberger, D. C. *Journal of Physical Chemistry* **1995**, *99*, 4193-4204.

(12) Olsbye, U.; Wendelbo, R.; Akporiaye, D. *Applied Catalysis a-General* **1997**, *152*, 127-141.

(13) Schreier, M., Regalbuto, J. *Journal of Catalysis* **2004**, *225*, 190-202.

(14) Boujday, S.; Lehman, J.; Lambert, J. F.; Che, M. *Catalysis Letters* **2003**, *88*, 23-30.

(15) Goguet, A.; Aouine, M.; Aires, F.; De Mallmann, A.; Schweich, D.; Candy, J. P. *Journal of Catalysis* **2002**, *209*, 135-144.

(16) Spieker, W. A.; Liu, J.; Hao, X.; Miller, J. T.; Kropf, A. J.; Regalbuto, J. R. *Applied Catalysis a-General* **2003**, *243*, 53-66.

(17) Mamede, A.-S.; Leclercq, E.; Payen, E.; Granger, P.; Grimblot, J. *Journal of Molecular Structure* **2003**, *651-653*, 353-364.

(18) Berdala, J., Freund, E., Lynch, J.P. *Journal de Physique* **1986**, *47*, C8-269.

(19) Lesagerosenberg, E.; Vlaic, G.; Dexpert, H.; Lagarde, P.; Freund, E. *Applied Catalysis* **1986**, *22*, 211-219.

(20) Kenvin, J. C.; White, M. G. *Journal of Catalysis* **1991**, *130*, 447-458.

(21) Kenvin, J. C.; White, M. G.; Mitchell, M. B. *Langmuir* **1991**, *7*, 1198-1205.

(22) Mitchell, M. B.; Chakravarthy, V. R.; White, M. G. *Langmuir* **1994**, *10*, 4523-4529.

(23) Vanveen, J. A. R.; Jonkers, G.; Hesselink, W. H. *Journal of the Chemical Society-Faraday Transactions I* **1989**, *85*, 389-413.

(24) Dou, D.; Liu, D. J.; Williamson, W. B.; Kharas, K. C.; Robota, H. J. *Applied Catalysis B-Environmental* **2001**, *30*, 11-24.

(25) Nakamoto, K. *Infrared and Raman Spectra of Inorganic and Coordination Compounds*; John Wiley and Sons, 1986.

(26) Clark, R. J. H., Williams, C. S. *Inorganic Chemistry* **1965**, *4*, 350.

(27) http://www.jobinyvon.com/usadivisions/Raman/applications/bands.pdf, J.-Y.; Vol. 2008.

(28) Krylova, L. F., Mateeva, L.M., Romanenko, G.V. *Zh. Strukt. Khim (Russ.) (J. Struct. Chem.)* **2006**, *47*, 670.

(29) Mansour, A. N.; Sayers, D. E.; Cook, J. W.; Short, D. R.; Shannon, R. D.; Katzer, J. R. *Journal of Physical Chemistry* **1984**, *88*, 1778-1781.

(30) Russell, A. E., Maniguet, S., Mathew, R.J., Yao, J., Roberts, M.A., Thompsett, D. *Journal of Power Sources* **2001**, *96*, 226-232.

(31) Bus, E.; Miller, J. T.; Kropf, A. J.; Prins, R.; van Bokhoven, J. A. *Physical Chemistry Chemical Physics* **2006**, *8*, 3248-3258.

(32) Delley, B.; Ellis, D. E.; Freeman, A. J.; Baerends, E. J.; Post, D. *Physical Review B* **1983**, *27*, 2132-2144.

(33) Schmitt, D., Fuess, H., Klein, H., Neuhausen, U., Lox, E.S. *Topics in Catalysis* **2001**, *16/17*, 355.

CHAPTER FOUR: BIMETALLIC CATALYSTS

Chapter Three was concerned with the characterisation of monometallic catalysts. This chapter deals with the characterisation of bimetallic catalysts. The monometallic precursors prepared in Chapter Two and characterised in Chapter Three were used to prepare the bimetallic catalysts presented here. All catalysts contain both Pt and Pd and Al_2O_3 and SiO_2 supports are used once again.

1 Introduction

The study of bimetallic Pt/Pd catalysts is of interest for many reasons, one of which is cost. If the same catalytic efficiency can be achieved using less Pt, this has an overall effect on the economy of diesel catalysts. It is well know that bimetallic catalysts often show properties that are distinctly different from those of the corresponding metallic catalyst[1]. Another reason is the behaviour of Pt after aging at high operating temperatures[2]. For example, it was reported by Chen and Schmidt[3] that Pt/Pd alloys sinter much more slowly in oxidative atmospheres than pure Pt does. Another is their sulfur tolerance; sulfur tolerant bimetallic Pt/Pd catalysts are likely to become a candidate for aromatic saturation[4]. However, the sulfur tolerance of these bimetallic catalysts is influenced by numerous factors such as the preparation details, degree of Pt/Pd alloy formation, Pt/Pd particle sizes and interactions between the particles and the supports etc[5]. This study aims to characterise a series of Pt/Pd bimetallic catalysts using EXAFS, TGA, TEM and XRD.

The study of bimetallic supported catalysts using analytical techniques such as EXAFS, TEM and TPR is well documented[1,2,6-13]. Morlang et al[2] used EXAFS to demonstrate that monometallic Pd catalysts behave differently from bimetallic Pt/Pd catalysts in that the monometallic catalyst is entirely oxidised after calcination and shows metallic character only after reduction. Pt/Pd catalysts, in

contrast, contain Pd in metallic form alongside Pd in oxidised form following calcination.

Fujikawa et al[14] investigated the high sulfur tolerance of Pt/Pd catalysts on an acidic support (such as Al_2O_3 or SiO_2) with regards to high aromatic hydrogenation in diesel fuel. Their aim was to determine why the Pt/Pd system had much more activity than the monometallic Pt system. They discovered that a bimetallic Pt/Pd system does not improve sulfur tolerance in comparison to a Pt or Pd monometallic system but a bimetallic system significantly enhances the intrinsic catalytic activity for aromatic hydrogenation. Further to this, they noticed the presence of Pt-Pt bonds within the catalyst samples, which indicated that the catalyst consisted of both Pt and Pd particles, rather than mixed Pt/Pd bimetallic particles[14].

It has been shown that the coordination number of the Pt-Pt bonds in bimetallic catalysts often exceeds that of the Pd-Pd bonds. This observation was attributed to segregation of Pd to the surface of the bimetallic particle by Hansen et al[15]. Similarly, Toshima et al[16-18] and Harada et al[19] reported results of analysis of bimetallic particles using X-ray photoelectron spectroscopy (XPS), XRD and EXAFS and found further evidence for core-shell structures where the Pd atoms are on the surface of the cluster with the Pt atoms in the core (Figure 1).

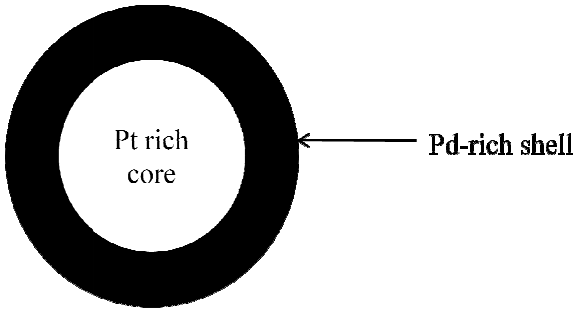

Figure 1 Schematic illustration of the Pt/Pd bimetallic "core shell structure" catalyst model.

Formation of bimetallic particles with a core-shell like structure has been reported in several other systems[1,7,11,20,21]. In contrast, Bando et al[22] showed that Pt/Pd metal particles on SiO_2 formed relatively uniform (well mixed) metal particles as opposed to on Al_2O_3 where segregated fine particles were formed.

Further studies of SiO_2 and Al_2O_3 supported Pt/Pd catalysts have been performed under high pressure and high liquid phase conditions[23] and showed again that the SiO_2 supported metals formed uniform particles as opposed to the segregated structure demonstrated by the Al_2O_3 catalyst.

The purpose of this chapter is to explore the role of the ligand, type of support and method of deposition on the structure of the resulting bimetallic Pt/Pd catalysts.

2 Experimental

2.1 Catalyst Preparation

Catalysts were prepared as outlined in Chapter Two, Section 3.2 and loadings were chosen to have a total metal weight percent (wt %) of 2.5 wt % comprising of 1.25 wt % of each metal compound. Bimetallic samples were prepared on both alumina and silica supports (as in Chapter Three). The key variables in preparation of the bimetallic catalysts were the precursor ligand and overall charge of the precursor. The actual metal content was measured using ICP-OAS by the Analytical Department at the Johnson Matthey Technology Centre.

As with the previous chapter, samples adsorbed onto the support and dried will be referred to as "dried" samples. Samples which are a result of a subsequent heat treatment in air involving a ramp to 500 ºC at a rate of 10 ºC per minute and left to dwell for 2 h will be referred to as "calcined".

2.2 TGA and TPR

Thermogravimetric measurements were carried out at the Johnson Matthey Technology Centre on an SDT 2960 Simultaneous DSC-TGA. A 20 mg sample of catalyst was weighed out and placed on a tared balance. A similar weight of calcined alumina was used as a reference. The furnace was closed and the sample was heated to 600 ºC at a rate of 10 ºC per minute. The weight of the sample was recorded throughout.

The TPR profiles reported in this chapter were collected at the Johnson Matthey Technology Centre by one of their scientists. The catalyst samples were heated to 500 ºC at 10 ºC per minute.

2.3 TEM and EDX

All samples for TEM and EDX were submitted to the Johnson Matthey Technology Centre for analysis. TEM samples were measured in a Tecnai F20 Transmission Electron Microscope. The powder samples were crushed between two glass slides and the samples were positioned onto a lacey carbon coated 'finder' grid with the aid of a micro manipulator.

2.4 XRD

All samples for XRD were submitted to the Johnson Matthey Technology Centre for analysis. XRD was carried out on a Bruker AXS D-500 diffractometer with a 40 position samples changer. The radiation was Cu Kα (Ni filtered) and the scan range was 20 to 100 °2θ with a 0.02° step size. A continuous scan rate of 0.25 °2θ per minute was used.

2.5 EXAFS

The adsorption edges of interest in this study were Pt L_3 (11.564 keV) and Pd K (24.350 keV). Bimetallic catalyst analysis was carried out at the National Synchrotron Light Source (NSLS) on stations X11A and X11B. Both stations are sourced by a bending magnet. Station X11A is equipped with a 13 element Si-Li detector for fluorescence experiments. Station X11A has a channel-cut two-crystal monochromator containing Si(111) and Si(311) crystals allowing measurements in two energy ranges. Either an energy range of 4.5 – 26 keV can be measured (Si(111)crystal) or a range of 8 – 35 keV (Si(311) crystal). Station X11B has a channel-cut sinearm-driven double crystal monochromator containing a Si(111) crystal and can measure an energy range of 4.5–22 keV.

2.6 Nomenclature

To ease comparisons in this chapter a nomenclature will be adopted to identify the catalyst samples by their ligands and the order in which they were adsorbed onto the support. Samples labelled $M_x(L_y)_2$+$M_a(L_b)_2$ indicate that metals M_x and

M_a with their respective ligands, L_y and L_b, were co-impregnated (+) onto the catalyst support. When the plus sign is replaced by a colon, $M_x(L_y)_2$**:**$M_a(L_b)_2$, it should be taken that $M_x(L_y)_2$ was deposited first followed by $M_a(L_b)_2$.

3 Alumina Supported Catalysts

3.1 Catalyst Preparation

ICP-OAS was used to measure the metal weight percent (wt %) adsorbed onto the catalytic supports. The overall theoretical loading was 2.5 wt % (1.25 wt % of Pt and Pd). The actual loading of metal on the Al_2O_3 support after incipient wetness impregnation of the precursor complexes studied in this chapter are presented in Table 1.

Table 1 Precursor complexes used for preparation of bimetallic catalyst samples, method of preparation and subsequent metal wt %.

Precursor 1	Precursor 2	Preparation Method	wt % Pt	wt % Pd	Total wt %
$[Pt(NH_3)_4]$	$[Pd(NH_3)_4]$	co-impregnation	0.65	0.70	1.35
$[Pd(NH_3)_4]$	$[Pt(NH3)_4]$	sequential	0.83	0.69	1.52
$[Pt(NH_3)_4]$	$[Pd(NH_3)_4]$	sequential	0.72	0.78	1.50
$[Pd(dcpy)_2]$	$[Pt(dcpy)_2]$	co-impregnation	0.67	0.75	1.42
$[Pt(dcpy)_2]$	$[Pd(dcpy)_2]$	sequential	0.73	0.69	1.42
$[Pd(dcpy)_2]$	$[Pt(dcpy)_2]$	sequential	0.67	0.75	1.42
$[Pd(NH_3)_4]$	$[Pt(asp)_2]$	sequential	0.78	0.86	1.64
$[Pt(asp)_2]$	$[Pd(NH_3)_4]$	sequential	0.90	0.90	1.80
$[Pd(dcpy)_2]$	$[Pt(NH_3)_4]$	sequential	0.82	0.75	1.57
$[Pt(NH_3)_4]$	$[Pd(dcpy)_2]$	sequential	0.89	0.86	1.75
$[Pd(NH_3)_4]$	$[Pt(dcpy)_2]$	sequential	0.85	0.93	1.78
$[Pt(dcpy)_2]$	$[Pd(NH_3)_4]$	sequential	0.81	0.84	1.65
$[Pt(asp)_2]$	$[Pd(dcpy)_2]$	sequential	0.72	0.79	1.51
$[Pd(dcpy)_2]$	$[Pt(asp)_2]$	sequential	0.80	0.77	1.57

None of the samples attained the theoretical wt %, however, the actual loadings for each sample are very similar. The Pt uptake for all samples was between 0.65 and 0.90 % and the total Pd uptake was between 0.69 and 0.93 %. This

implies that there is no difference in uptake between Pt and Pd metal as a function of the identity of the precursors and indicates that the nature of catalyst preparation (incipient wetness via co-impregnation or sequential impregnation) had no overall effect on the amount of metal adsorbed on the support. A similarity in the wt % of each metal adsorbed in each individual sample perhaps suggests that it is the combination of precursors which affects the metal uptake although no particular ligand combination has a significantly better uptake than another. This implies that the nature of the ligand i.e. charge, size etc had no effect on its adsorption properties.

3.2 Thermogravimetric Studies

Two types of thermogravimetric study were used in this work, thermogravimetric analysis (TGA) and temperature programmed reduction (TPR). TGA was used to determine the temperature at which the ligands are lost when the catalyst is calcined. This temperature was then used for EXAFS analysis. Dried samples were heated to the temperature at which the ligands are lost and the EXAFS was measured to determine the local structure of the atoms during this transition.

TPR was only measured for 4 samples. $[Pt(NH_3)_4]/Al_2O_3$ (from Chapter 3) and the catalysts containing only $(NH_3)_4$ ligands on Al_2O_3. This was because the EXAFS data for these particular samples did not indicate full reduction at room temperature under flowing H_2.

3.2.1 TGA

The TGA data are shown in Figure 2. The samples were measured individually from room temperature to 600 ºC at a ramp rate of 10 ºC per minute. The results have been grouped by ligand to aid comparison.

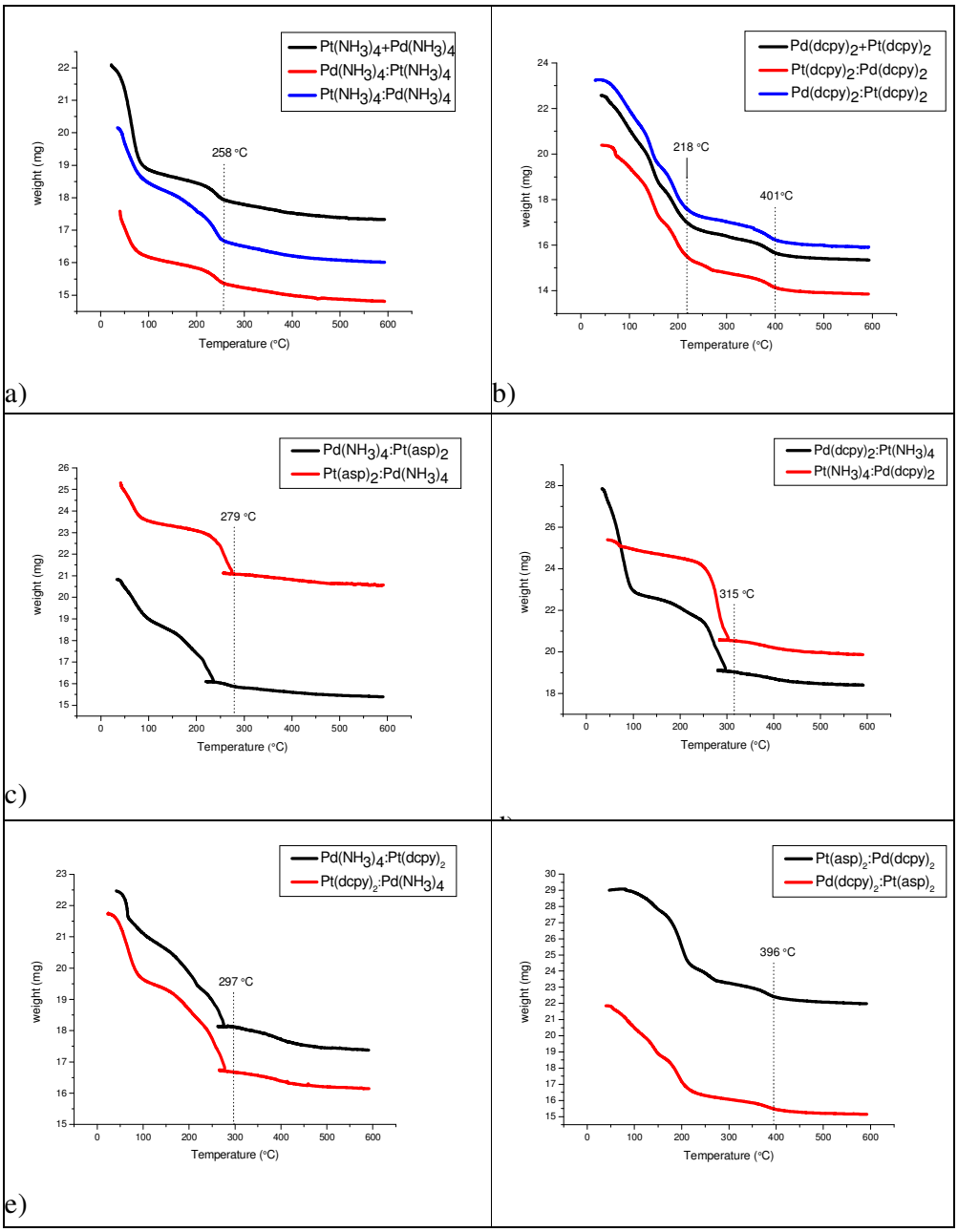

Figure 2 Weight loss (TGA) of catalyst on Al_2O_3 as the support during heating to 600 ºC in air. The vertical dashed lines indicate significant temperature points.

The TGA results show that although the temperature at which the ligands are lost varies slightly from sample to sample, the weight loss profile of catalyst samples containing the same precursors remains the same regardless of the order in which they are put onto the support. The $(NH_3)_4$ based catalysts shown in panel (a) all exhibit very similar profiles with the overall weight loss being complete at around 250 ºC. A large drop in weight is seen around 100 ºC, which is attributed

to water loss. With this taken into account it can be noted that the tetrammine ligand starts to burn off around 200 ºC and the process is very quick with a temperature range of only 50 ºC. In contrast, the $(dcpy)_2$ catalysts appear to have a two stage weight loss with a large amount of ligand lost before 200 ºC followed by a small loss in weight at around 400 ºC. It is worth noting at this point that the 2,5-pyrdinedicarboxylic acid ligand is much larger and more organic than the tetrammine ligand which could account for both the increased steepness of the weight loss and the higher temperature needed to burn off the ligands.

The mixed $(NH_3)_4$ catalysts (panels c, d and e) all contain a feature where the plot has doubled back on itself. This is due to an exothermic runaway where the heat of the ligand being burned off the support is higher than the temperature at which the furnace is programmed. This causes the furnace to cool and results in the feature seen on these graphs after the steep drop in weight. These three sets of samples all follow a similar profile where a steep loss in organic matter is seen until this feature is reached when weight loss appears to have stopped as the graph reaches a plateau.

The mixed $[Pt(asp)_2]$, $[Pd(dcpy)_2]$ samples in panel (f) have a similar profile, however, the loss of ligands is not as steep and therefore the feature described above is not observed. In fact, the nature of the catalysts measured and the rate at their loss of ligand can be directly associated with the presence of tetrammine in the sample. The samples containing this ligand exhibit a much quicker weight loss than those without a characteristic which can be attributed to the smaller size of the tetrammine ligand and its relative ease of combustion.

3.2.2 TPR

The reducibility of the calcined $(NH_3)_4$ catalysts and their reduction profiles are shown in Figure 3 as well as the profile of $[Pt(NH_3)_4]$ on Al_2O_3. The TPR profiles for these samples were measured as there was difficulty in reducing $[Pt(NH_3)_4]$ on Al_2O_3 during the studies described in Chapter Three and it was observed that they showed varying levels of reduction after exposure to H_2 in preparation for EXAFS analysis.

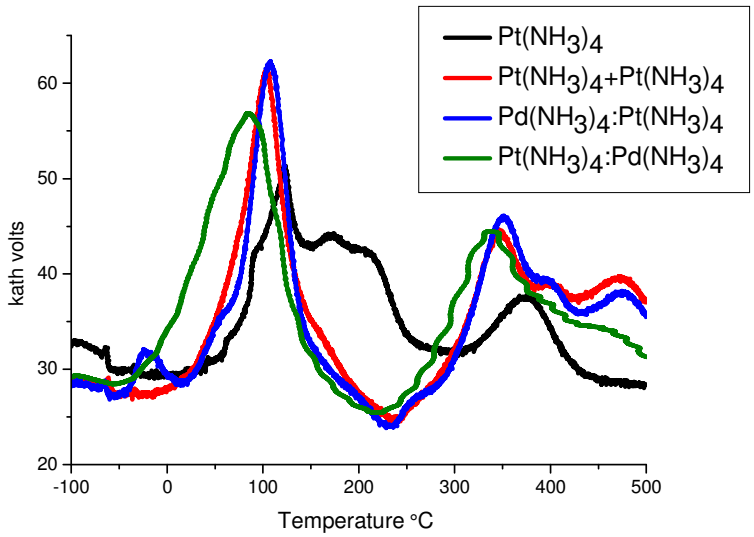

Figure 3 Temperature Programmed Reduction of calcined $[Pt(NH_3)_4]$, and $(NH_3)_4$ containing bimetallic catalysts.

For the bimetallic catalysts, two distinct reduction peaks are seen around 100 ºC and 350 ºC. These can be attributed to the successive reduction of PtO_2 to PtO and then Pt. The $H^{\bullet}$ uptakes are shown below in Table 2.

Table 2 $H^{\bullet}$ uptakes of samples determined from the TPR profiles shown in Figure 3.

Sample	$H^{\bullet}$ uptake (mmol $H^{\bullet}$/g)
$[Pt(NH_3)_4]$	0.47
$[Pt(NH_3)_4]+[Pd(NH_3)_4]$	0.90
$[Pd(NH_3)_4]:[Pt(NH_3)_4]$	0.68
$[Pt(NH_3)_4]:[Pd(NH_3)_4]$	0.74

As can be seen, the reduction peaks occur at higher temperatures for the monometallic sample, which also has the smallest hydrogen uptake. Hydrogen can be absorbed by Pd particles as well as adsorbed. The increased hydrogen uptake by the bimetallic catalysts is thus attributed to absorption. The reduction profiles of the bimetallic catalysts are all similar with that of the $[Pt(NH_3)_4]:[Pd(NH_3)_4]$ occurring at a slightly lower temperature and reduction for all samples starting at room temperature.

3.3 TEM

TEM gives a useful indication of the particle size and distribution on the catalyst samples. The average particle sizes and distributions were obtained by analysing TEM images (see reports T3050 and T3228A in the electronic appendix). The results are presented in Figure 4. Data has been grouped by ligand type to aid comparison.

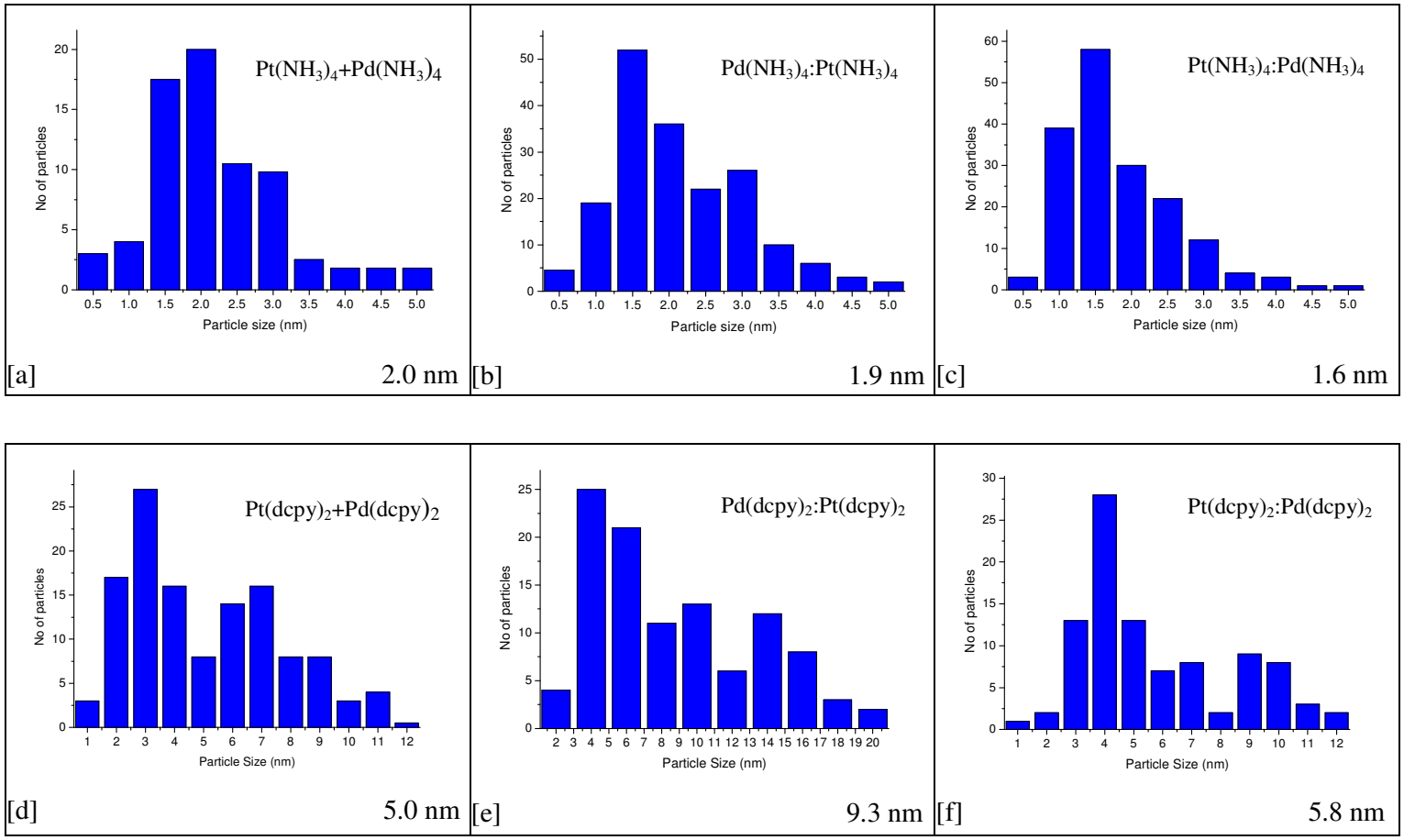

Figure 4 Particle size and distribution of bimetallic catalyst on Al_2O_3. All samples were analysed as calcined catalysts.

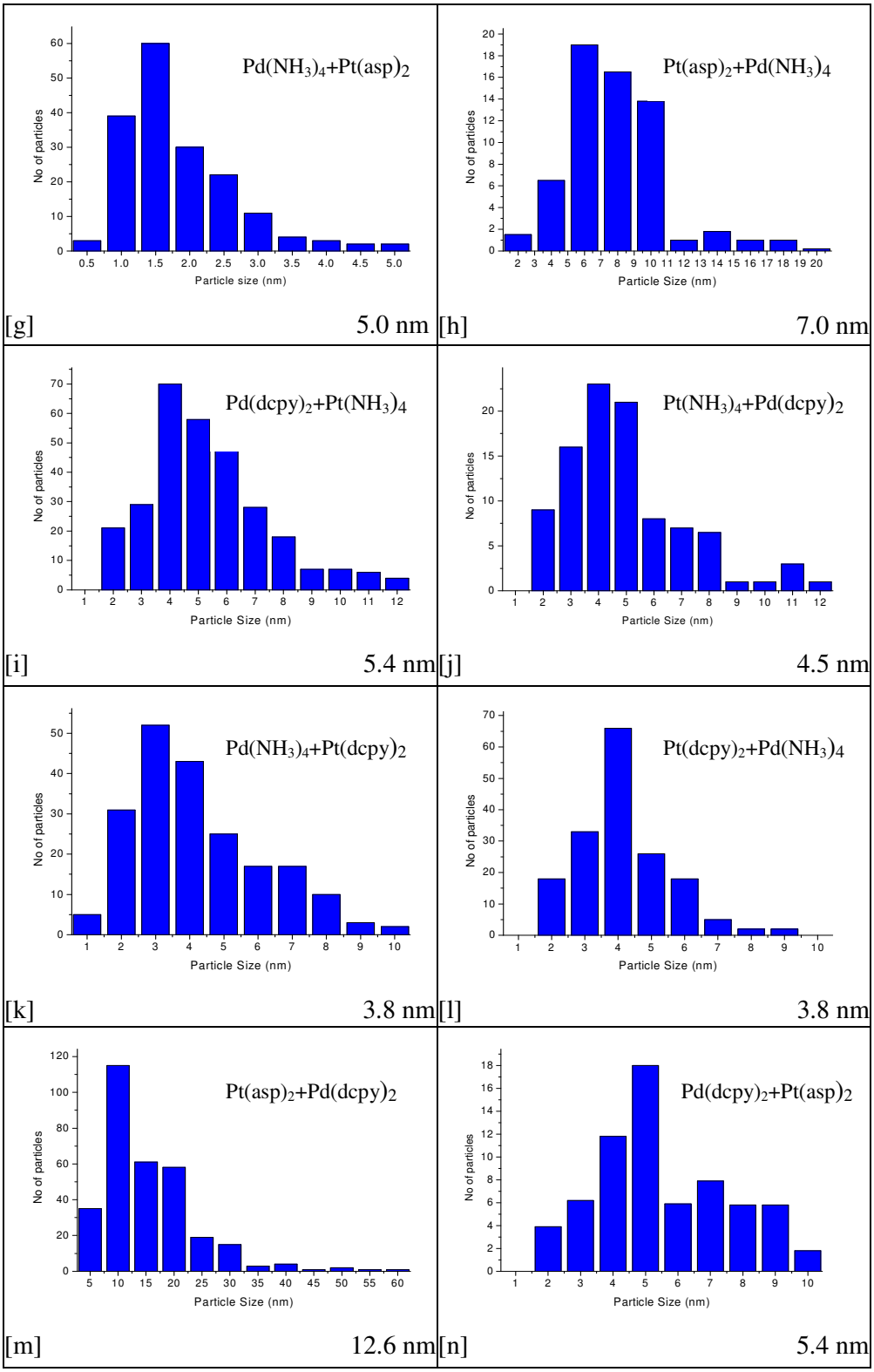

Figure 4 continued.

Panels [a] –[c] demonstrate that irrespective of the method and order in which the $(NH_3)_4$ precursor complexes are deposited onto the support, the average

particle size and distribution once the catalyst has been calcined remain very similar. The $(dcpy)_2$ complexes agree with this as far as the method is concerned. However, a much larger particle size exhibited by $[Pd(dcpy)_2]$:$[Pt(dcpy)_2]$ than the other two $(dcpy)_2$ samples (panels [d] – [f]), indicating that in this case the absence of Pt in the initial deposition step is important. Similar results were found for the $(NH_3)_4$ containing mixed catalyst samples (in panels [g] – [l]). Use of an $(asp)_2$ or $(dcpy)_2$ ligand containing complex resulted in a larger average particle size than is seen in panels [a] – [c]. However, the average particle size is smaller if the $(NH_3)_4$ ligand is adsorbed first indicating the order in which the precursor complexes are adsorbed can have an effect on the overall dispersion and by implication, the activity of the catalyst.

The samples prepared with the $[Pt(asp)_2]$ precursor complex exhibit the largest average particle sizes (7.0 and 12.6 nm in panels [h] and [m] respectively). This is not surprising considering the large particle sizes seen in the monometallic sample in Chapter Three and indicates that $[Pt(asp)_2]$ forms aggregates and that these samples may contain a mixture of monometallic Pt and Pd clusters[18].

3.4 XRD

The XRD patterns collected in this study of the Al_2O_3 supported samples are presented below in Figure 5 and provide information regarding the presence of different metal and oxide phases. The patterns are grouped by ligand type to aid comparison.

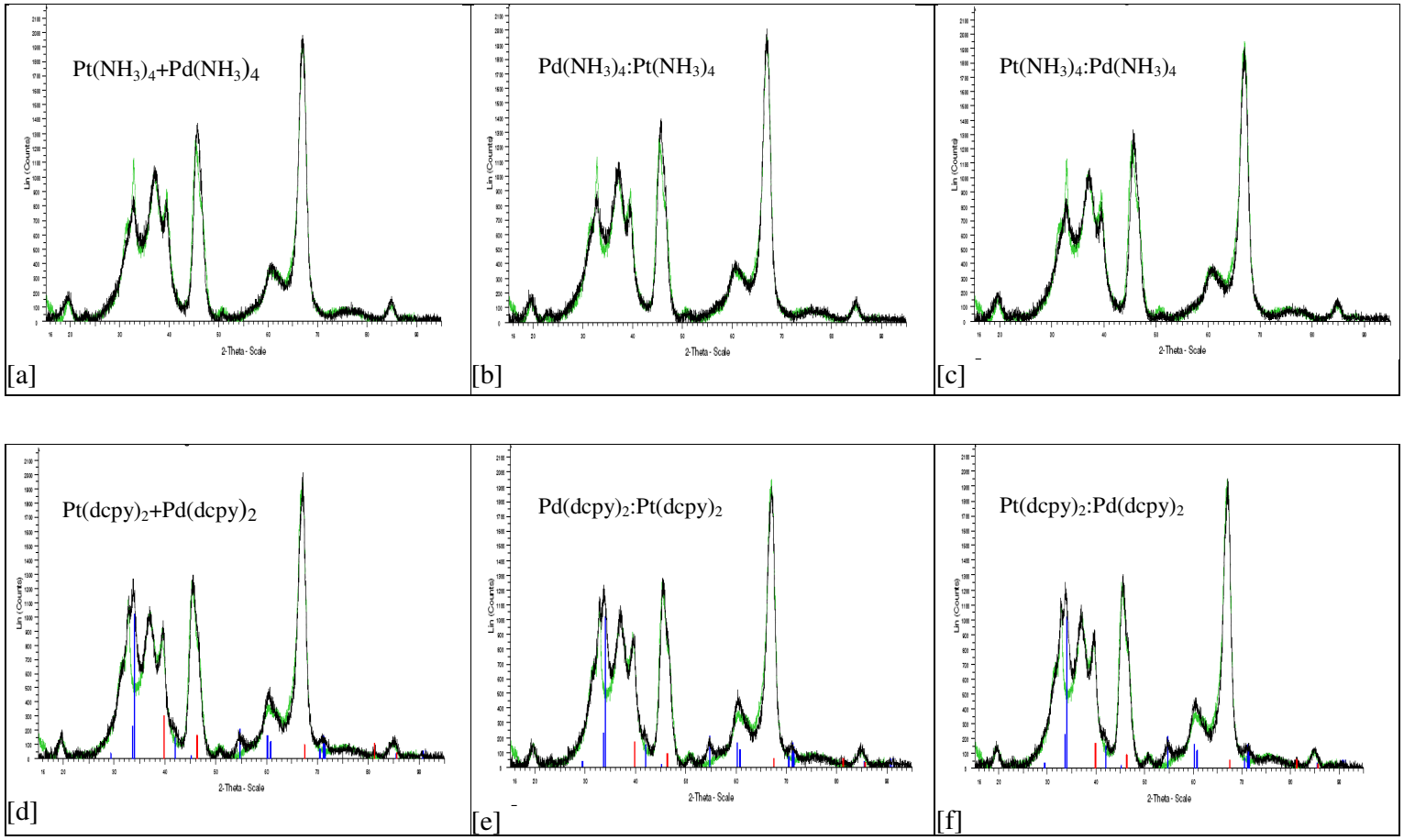

Figure 5 XRD patterns of the bimetallic samples calcined and supported on Al_2O_3. ▮ is tetragonal PdO (PDF No 00-046-1043), ▮ is cubic Pt (PDF No 00-004-0802) and ▮ is cubic Pd.

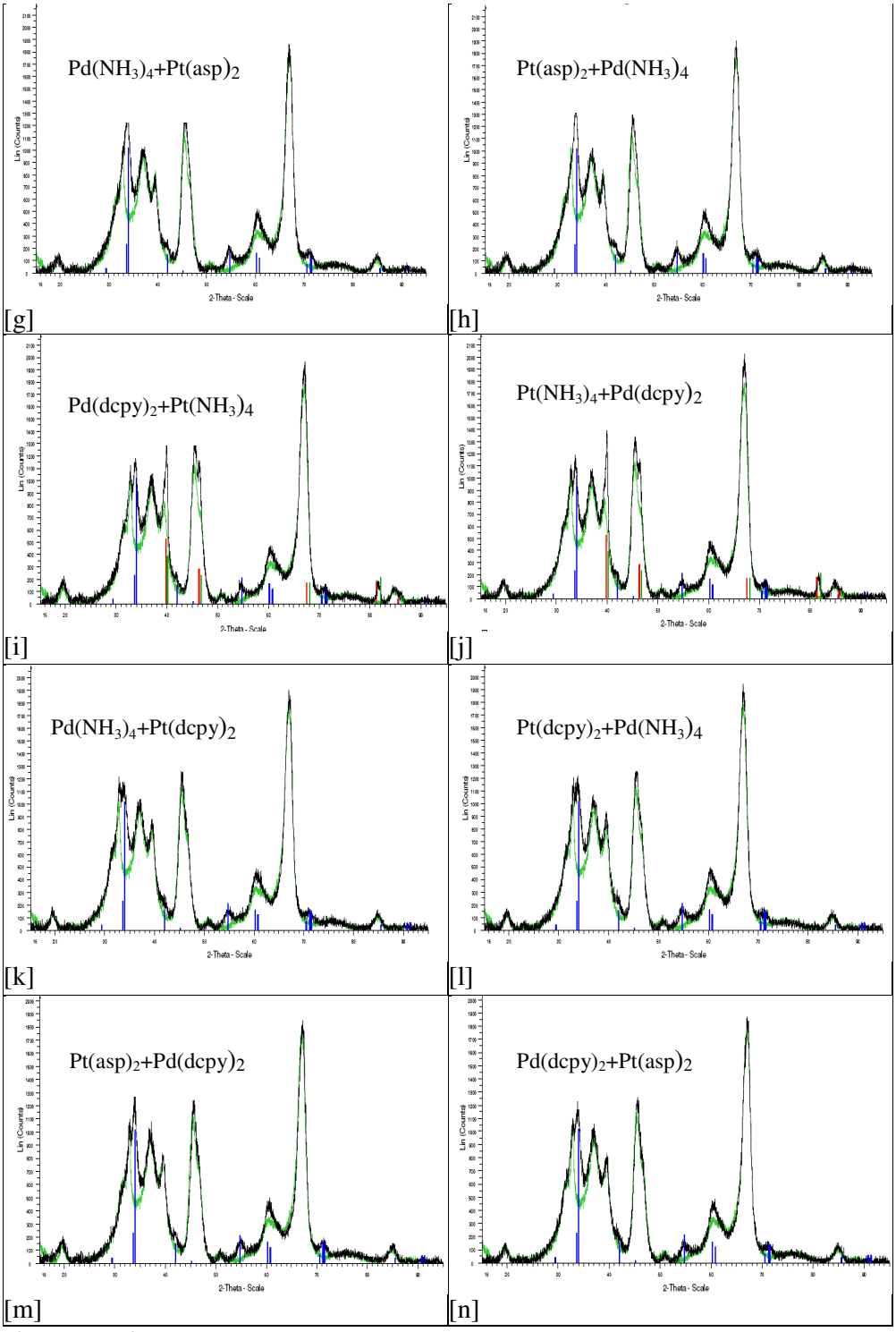

Figure 5 continued.

In contrast to the other samples, the XRD analysis of the Pt/Pd Al_2O_3 supported calcined catalysts show that tetrammine based catalysts do not contain any Pt or Pd crystalline reflections. This indicates the presence of small and poorly

crystalline metal particles, with a weak internal organisation[24]. This result agrees well with the smaller average mean particle sizes for these catalysts obtained by TEM.

A mixture of tetragonal PdO and cubic Pt is seen in the $(dcpy)_2$ based catalysts supporting the presence of a bimetallic system. However, samples containing $[Pd(NH_3)_4]$ and either $[Pt(asp)_2]$ or $[Pt(dcpy)_2]$ shown in panels [g], [h] and [k] – [n] only display crystalline phases of tetragonal PdO. As it is known from other forms of analysis that Pt is present in these samples, the absence of cubic Pt reflections may be due to the Pt crystallites being very small, < 2 nm, or amorphous in nature.

Samples $[Pt(NH_3)_4]$:$[Pd(dcpy)_2]$ and $[Pd(dcpy)_2]$: $[Pt(NH_3)_4]$ contain both tetragonal PdO and cubic Pt and also display an additional phase of cubic Pd indicating that the calcined sample exists in both the metallic and oxidised state. This shows that for a catalyst prepared using $[Pd(dcpy)_2]$, as a precursor, the oxidative behaviour of the Pd in the presence of Pt differs significantly from that of a monometallic Pd catalyst. In the bimetallic Pt/Pd catalyst, irrespective of the order in which the precursors are adsorbed onto the support, Pd exists in both metallic and oxidised form after calcination. The XRD pattern of the monometallic Pd catalyst shown in Chapter Three corresponds to the PdO phase. This phenomena has also be observed in other studies[2,3] but interestingly in this work, the effect is only observed when the $[Pd(dcpy)_2]$ ligand is paired with $[Pt(NH_3)_4]$.

3.5 EXAFS

EXAFS was collected of all Al_2O_3 samples as dried catalysts, heated catalysts in air and H_2 and calcined catalysts in air and H_2. The samples of most interest were chosen for presentation in this chapter and can be found in the sections below. Data for the samples not presented can be found in the electronic appendix. In all cases, the data was not fitted beyond R = 5 Å.

The data for the dried catalysts can be found in the electronic appendix and was all consistent with the spectra obtained for the monometallic samples indicating

that the intact precursor complexes were adsorbed and no formation of bimetallic species was found.

3.5.1 Heated Al_2O_3 supported catalysts

The spectra in Figure 6 (a-n) show the experimental data (black lines) and fit (red lines) {left} and corresponding Fourier Transform {right} of bimetallic catalysts on an Al_2O_3 support and heated to a temperature indicated within the panel. The data was obtained at the Pt L_3 edge. The data and Fourier Transforms are k^2 weighted.

Similarly, Figure 7 (a-n) shows the experimental data (black lines) and fit (red lines) {left} and corresponding Fourier Transform {right} of bimetallic catalysts on an Al_2O_3 support and heated to a temperature indicated within the panel at the Pd K edge. Again the data and Fourier Transforms are k^2 weighted.

The temperature to which the catalysts were heated to was the temperature required to remove the ligands as determined by the TGA measurements (Figure 2). The samples were measured at room temperature in air. The calculated structural parameters obtained by analysis of this data are presented in Table 3 (a-n) and Table 4 (a-n). In these tables, the nature of the neighbour is shown as is the coordination number (N), the distance (R) at which the atom is found and the Debye Waller factor ($2\sigma^2$), each with corresponding errors. For ease of interpretation, the tables and figures have been merged.

Figure 6a PtL_3

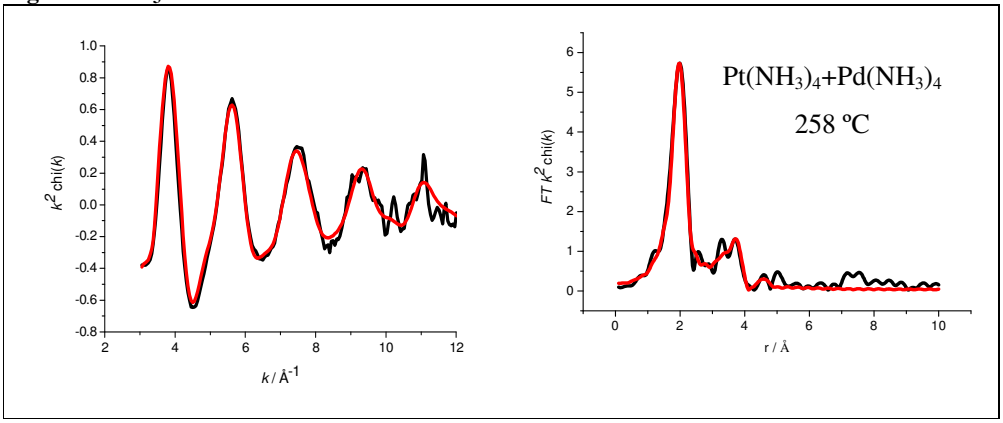

Figure 7a Pd K

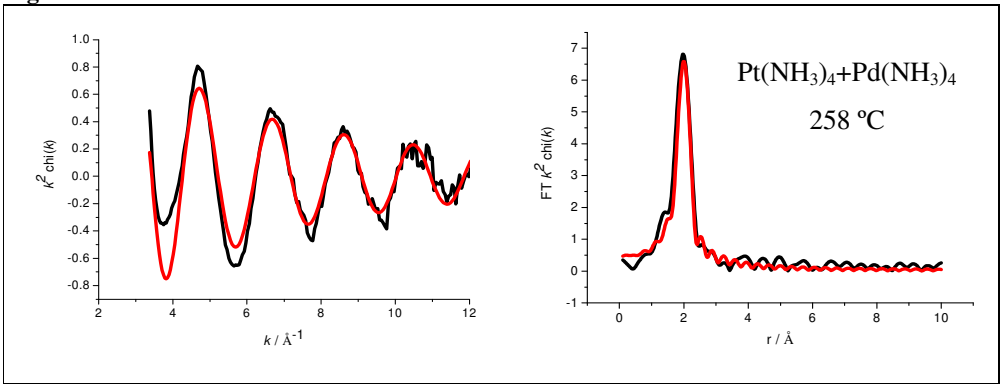

Table 3a Pt L_3

Sample	Shell	N	R / Å	$2\sigma^2$/Å^2	E_f / eV	R_{exafs} / %
$Pt(NH_3)_4$+$Pd(NH_3)_4$	Pt-O	2.3 ± 0.1	2.02 ± 0.01	0.009 ± 0.001	-13.1	21.78
	Pt-Pt	1.2 ± 0.6	2.78 ± 0.03	0.022 ± 0.011	±	
	Pt-Pd	0.8 ± 0.3	3.64 ± 0.02	0.015 ± 0.001	0.6	
	Pt-O	3.3 ± 0.4	3.67 ± 0.02	0.013 ± 0.001		

Table 4a Pd K

Sample	Shell	N	R / Å	$2\sigma^2$/Å^2	E_f / eV	R_{exafs} / %
$Pt(NH_3)_4$+$Pd(NH_3)_4$	Pd-O	2.1 ± 0.1	2.03 ± 0.01	0.002 ± 0.001	-1.6 ±	36.97
					1.1	

Figure 6b Pt L_3

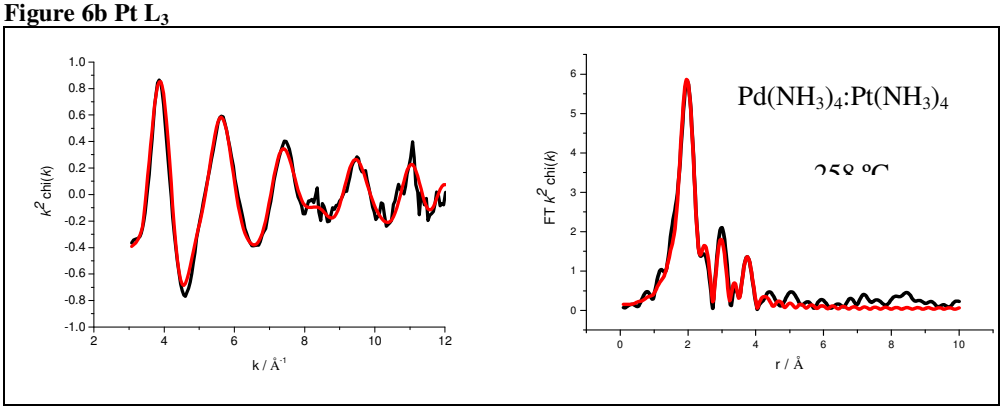

Figure 7b Pd K

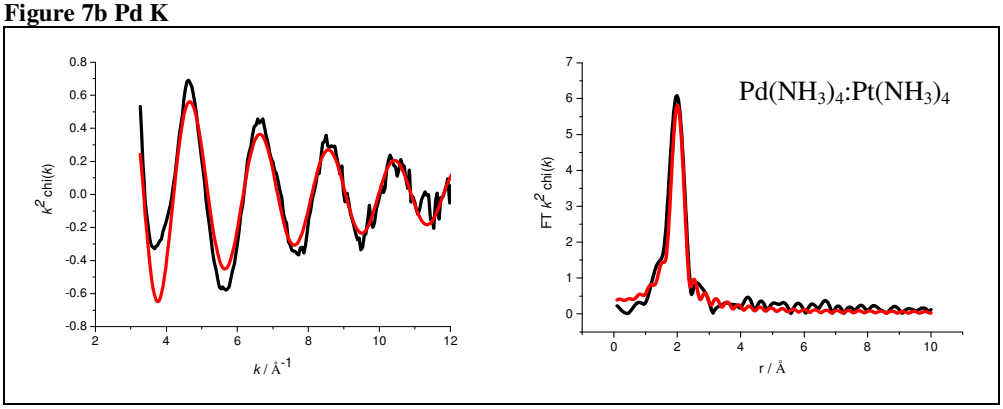

Table 3b Pt L_3

$Pd(NH_3)_4$:$Pt(NH_3)_4$	Pt-O	2.2 ± 0.1	2.01 ± 0.01	0.008 ± 0.001	-12.3	22.43
	Pt-O	1.7 ± 1.2	2.67 ± 0.05	0.019 ± 0.006	±	
	Pt-Pd	0.8 ± 0.1	2.79 ± 0.01	0.013 ± 0.002	1.1	
	Pt-Pt	0.6 ± 0.4	3.72 ± 0.03	0.005 ± 0.004		
	Pt-Pd	0.5 ± 0.2	3.63 ± 0.02	0.005 ± 0.004		
	Pt-O	2.5 ± 0.6	3.68 ± 0.03	0.011 ± 0.008		

Table 4b Pd K

$Pd(NH_3)_4$:$Pt(NH_3)_4$	Pd-O	1.8 ± 0.1	2.03 ± 0.1	0.002 ± 0.001	-5.6 ±	37.59
					1.0	

Figure 6c Pt L_3

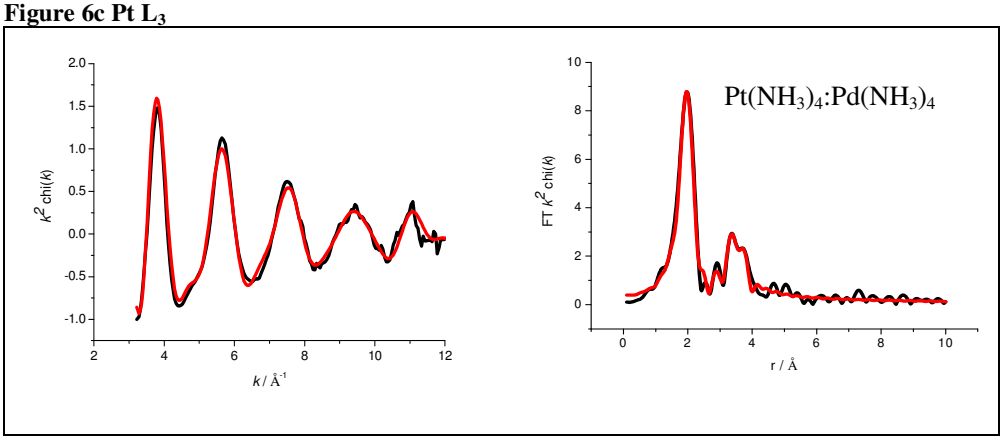

Figure 7c Pd K

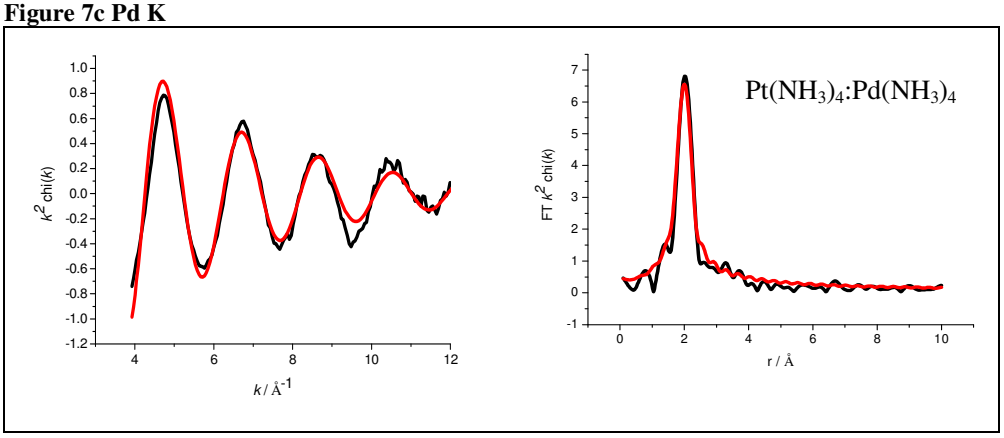

Table 3c Pt L_3

$Pt(NH_3)_4$:$Pd(NH_3)_4$	Pt-O	3.5 ± 0.1	2.02 ± 0.01	0.008 ± 0.001	-11.3 ± 0.1	19.39
	Pt-Pt	2.2 ± 0.6	3.13 ± 0.04	0.008 ± 0.004		
	Pt-Pd	3.3 ± 0.7	3.39 ± 0.03	0.010 ± 0.004		
	Pt-O	9.8 ± 1.0	3.70 ± 0.01	0.010 ± 0.003		

Table 4c Pd K

$Pt(NH_3)_4$:$Pd(NH_3)_4$	Pd-O	2.7 ± 0.1	2.02 ± 0.01	0.005 ± 0.001	-1.6 ± 0.6	17.69
	Pd-Pd	0.3 ± 0.1	2.56 ± 0.02	0.009 ± 0.003		
	Pd-Pt	0.6 ± 0.2	2.60 ± 0.02	0.011 ± 0.003		
	Pd-Pd	0.2 ± 0.1	3.21 ± 0.03	0.007 ± 0.004		

Figure 6d Pt L_3

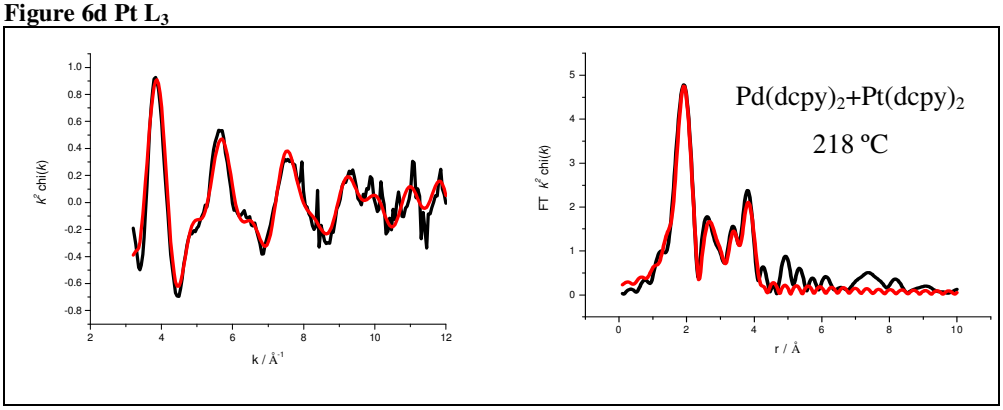

Figure 7d Pd K

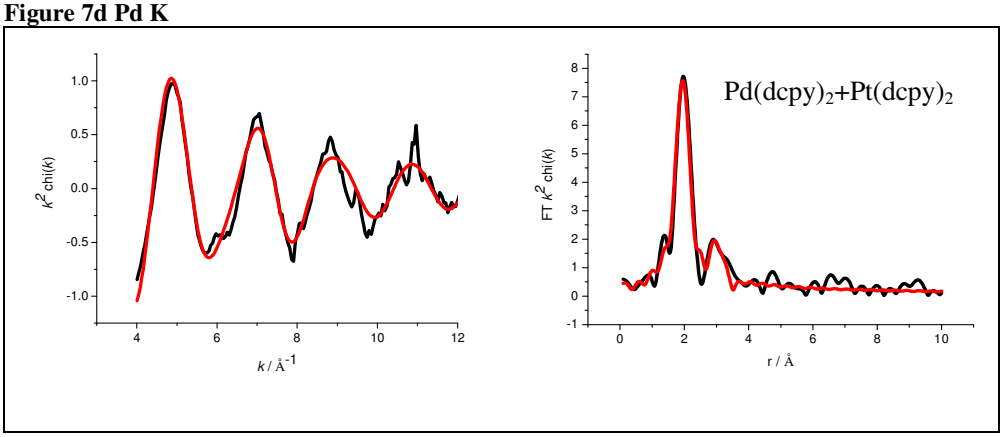

Table 3d Pt L_3

$Pd(dcpy)_2+Pt(dcpy)_2$	Pt-O	1.9 ± 0.1	1.99 ± 0.01	0.008 ± 0.001	-13.6	31.98
	Pt-Pt	3.3 ± 1.3	2.98 ± 0.03	0.041 ± 0.015	±	
	Pt-Pd	3.1 ± 0.5	2.95 ± 0.02	0.022 ± 0.004	0.8	
	Pt-Pt	1.8 ± 0.4	3.12 ± 0.02	0.014 ± 0.004		
	Pt-Pd	1.9 ± 0.5	3.50 ± 0.01	0.008 ± 0.002		

Table 4d Pd K

$Pd(dcpy)_2+Pt(dcpy)_2$	Pd-O	3.1 ± 0.2	1.97 ± 0.01	0.006 ± 0.001	3.0	25.32
	Pd-C	0.8 ± 0.5	2.84 ± 0.04	0.001 ± 0.007	±	
	Pd-C	3.1 ± 1.2	3.28 ± 0.03	0.013 ± 0.008	0.2	

Figure 6e Pt L_3

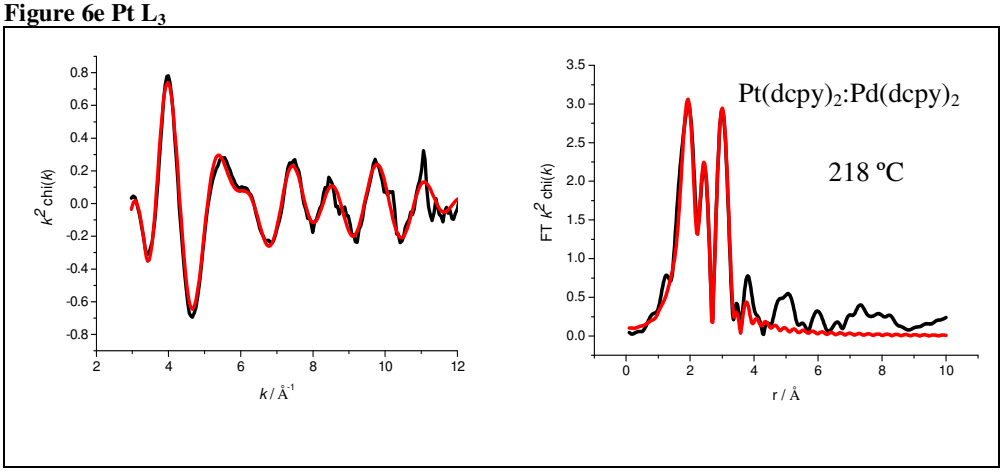

Figure 7e Pd K

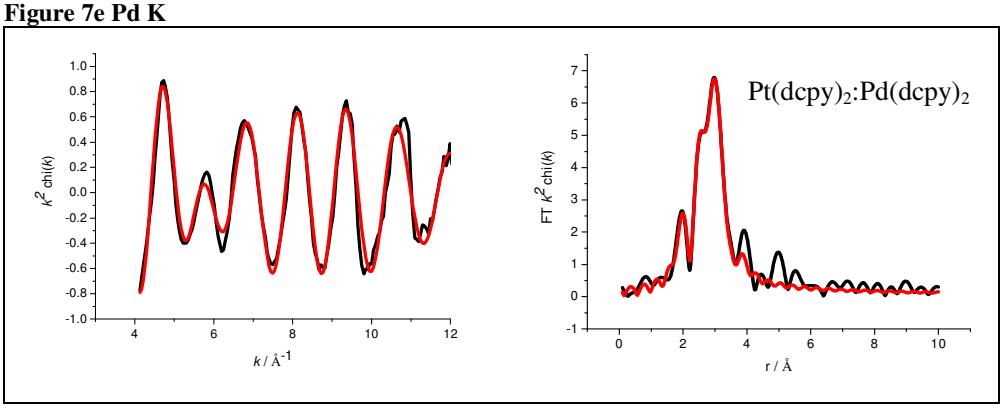

Table 3e Pt L_3

$Pt(dcpy)_2$:$Pd(dcpy)_2$	Pt-O	1.2 ± 0.7	1.98 ± 0.01	0.010 ± 0.002	-13.8 ± 0.7	25.86
	Pt-Pt	2.8 ± 0.4	2.77 ± 0.01	0.019 ± 0.003		
	Pt-Pd	1.7 ± 0.1	2.74 ± 0.01	0.015 ± 0.001		
	Pt-Pt	3.8 ± 0.5	2.97 ± 0.01	0.016 ± 0.002		
	Pt-Pd	1.9 ± 0.6	3.29 ± 0.01	0.016 ± 0.003		
	Pt-O	2.8 ± 0.6	3.65 ± 0.02	0.016 ± 0.008		

Table 4e Pd K

$Pt(dcpy)_2$:$Pd(dcpy)_2$	Pd-O	0.7 ± 0.1	1.99 ± 0.01	0.004 ± 0.002	-0.1 ± 0.6	17.53
	Pd-Pd	3.9 ± 0.2	2.72 ± 0.01	0.012 ± 0.001		
	Pd-Pt	1.6 ± 0.5	2.69 ± 0.02	0.020 ± 0.006		
	Pd-Pd	1.0 ± 0.3	3.81 ± 0.02	0.013 ± 0.004		
	Pd-Pd	2.5 ± 0.6	4.74 ± 0.01	0.011 ± 0.002		

Figure 6f Pt L_3

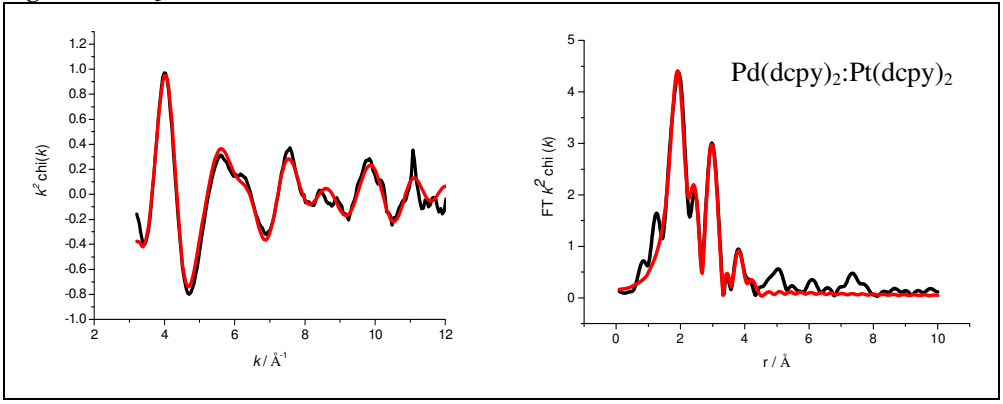

Figure 7f Pd K

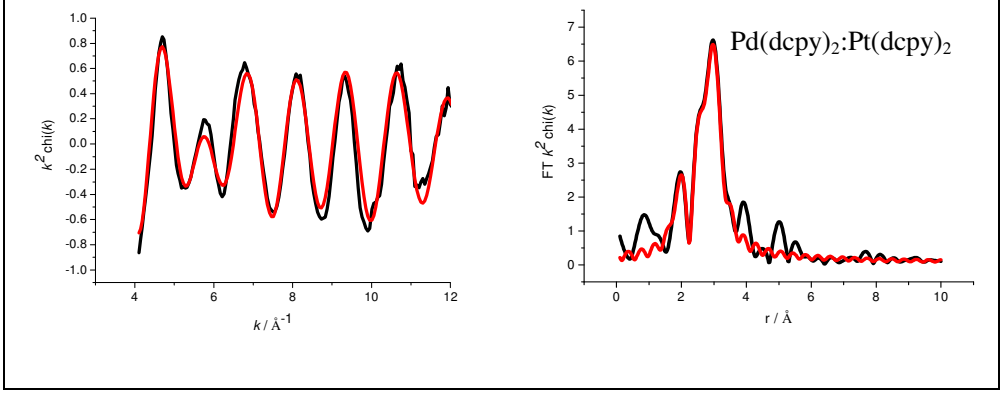

Table 3f Pt L_3

$Pd(dcpy)_2$:$Pt(dcpy)_2$	Pt-O	1.9 ± 0.1	1.96 ± 0.01	0.013 ± 0.001	-12.0	24.15
	Pt-Pt	2.4 ± 0.6	2.97 ± 0.01	0.021 ± 0.004	±	
	Pt-Pd	1.3 ± 0.3	2.72 ± 0.01	0.018 ± 0.002	0.9	
	Pt-O	1.7 ± 0.4	2.64 ± 0.03	0.022 ± 0.008		
	Pt-Pt	0.8 ± 0.5	3.68 ± 0.04	0.012 ± 0.007		
	Pt-Pd	1.1 ± 0.3	3.62 ± 0.02	0.014 ± 0.004		

Table 4f Pd K

$Pd(dcpy)_2$:$Pt(dcpy)_2$	Pd-O	0.8 ± 0.1	1.99 ± 0.01	0.003 ± 0.002	-0.1 ±	21.68
	Pd-Pd	3.9 ± 0.2	2.74 ± 0.01	0.012 ± 0.001	0.7	
	Pd-Pt	0.5 ± 0.3	2.72 ± 0.05	0.017 ± 0.019		
	Pd-Pd	0.8 ± 0.4	3.83 ± 0.03	0.012 ± 0.005		
	Pd-Pd	1.9 ± 0.7	4.77 ± 0.02	0.012 ± 0.004		

Figure 6g Pt L_3

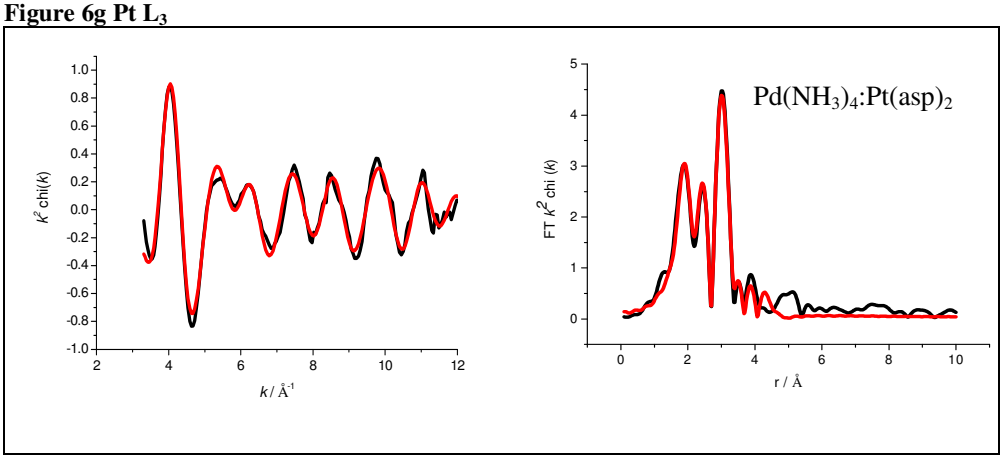

Figure 7g Pd K

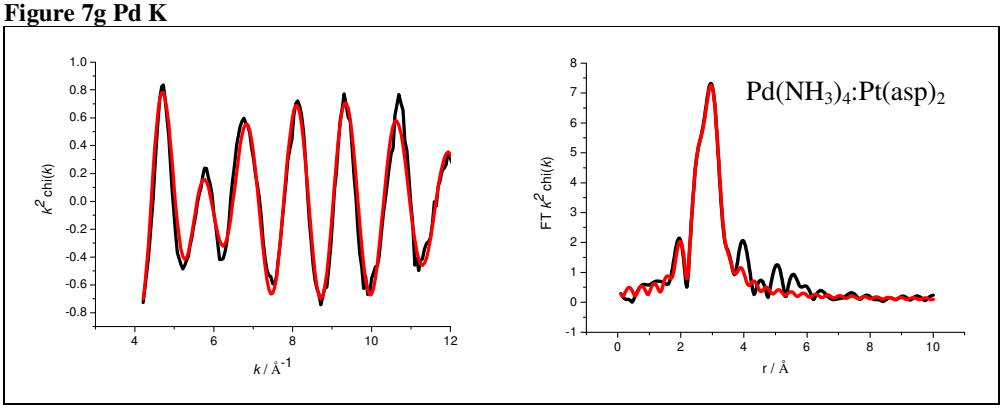

Table 3g Pt L_3

$Pd(NH_3)_4$:$Pt(asp)_2$	Pt-O	1.1 ± 0.1	1.96 ± 0.01	0.010 ± 0.001	-14.4	23.43
	Pt-Pt	0.9 ± 0.3	2.69 ± 0.02	0.008 ± 0.002	±	
	Pt-Pd	2.4 ± 0.2	2.74 ± 0.01	0.014 ± 0.001	0.8	
	Pt-O	1.9 ± 0.2	2.75 ± 0.02	0.004 ± 0.003		
	Pt-Pt	1.9 ± 0.4	3.74 ± 0.01	0.014 ± 0.003		
	Pt-Pd	1.0 ± 0.2	3.67 ± 0.01	0.013 ± 0.003		

Table 4g Pd K

$Pd(NH_3)_4$:$Pt(asp)_2$	Pd-O	0.5 ± 0.1	2.01 ± 0.02	0.004 ± 0.004	0.3	18.47
	Pd-Pd	4.1 ± 0.2	2.74 ± 0.01	0.011 ± 0.001	±	
	Pd-Pt	1.1 ± 0.3	2.73 ± 0.02	0.012 ± 0.004	0.7	
	Pd-Pd	0.8 ± 0.3	3.85 ± 0.02	0.011 ± 0.004		
	Pd-Pd	2.3 ± 0.6	4.77 ± 0.02	0.012 ± 0.003		

Figure 6h Pt L_3

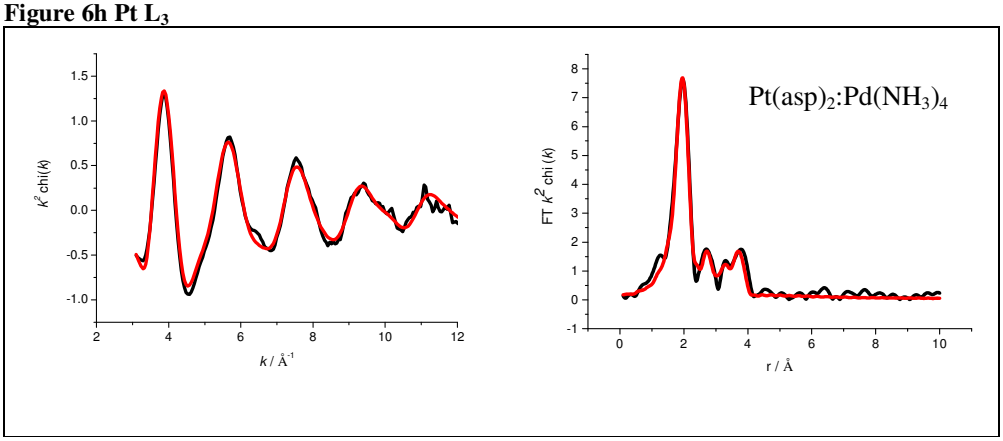

Figure 7h Pd K

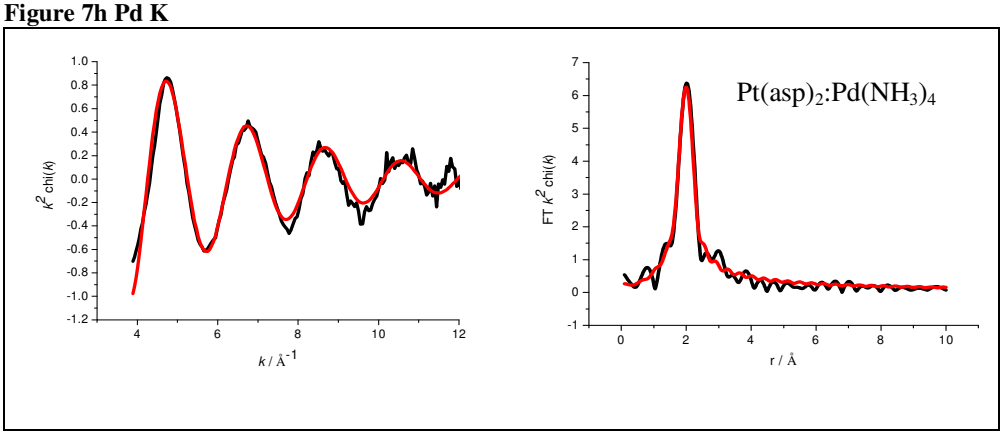

Table 3h Pt L_3

$Pt(asp)_2:Pd(NH_3)_4$	Pt-O	2.9 ± 0.1	2.00 ± 0.01	0.007 ± 0.001	-12.2	19.90
	Pt-O	0.7 ± 0.2	2.79 ± 0.03	0.006 ± 0.005	±	
	Pt-O	3.4 ± 0.7	3.53 ± 0.02	0.019 ± 0.007	0.5	
	Pt-O	4.7 ± 0.8	3.72 ± 0.02	0.011 ± 0.004		

Table 4h Pd K

$Pt(asp)_2:Pd(NH_3)_4$	Pd-O	3.2 ± 0.1	2.01 ± 0.01	0.009 ± 0.001	1.7	17.48
	Pd-Pd	0.7 ± 0.1	2.54 ± 0.01	0.014 ± 0.002	±	
	Pd-Pt	1.0 ± 0.2	2.58 ± 0.01	0.015 ± 0.003	0.9	
	Pd-Pd	0.4 ± 0.2	3.83 ± 0.03	0.007 ± 0.004		

Figure 6i Pt L_3

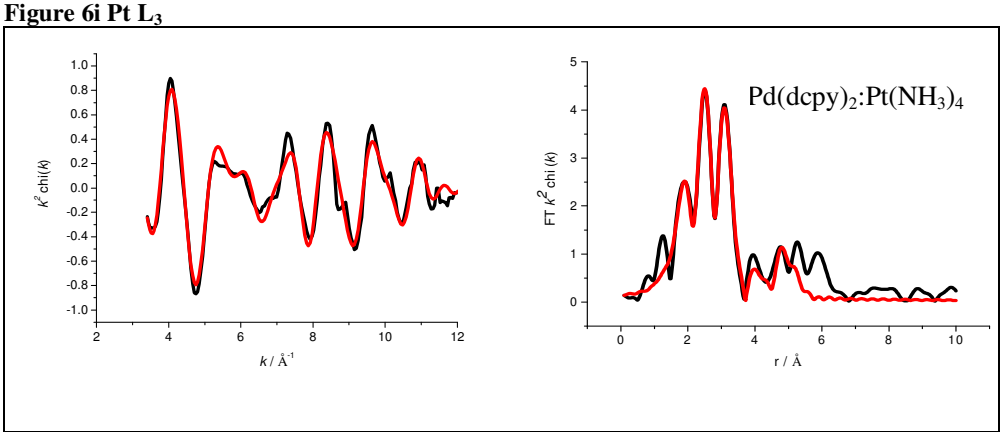

Figure 7i Pd K

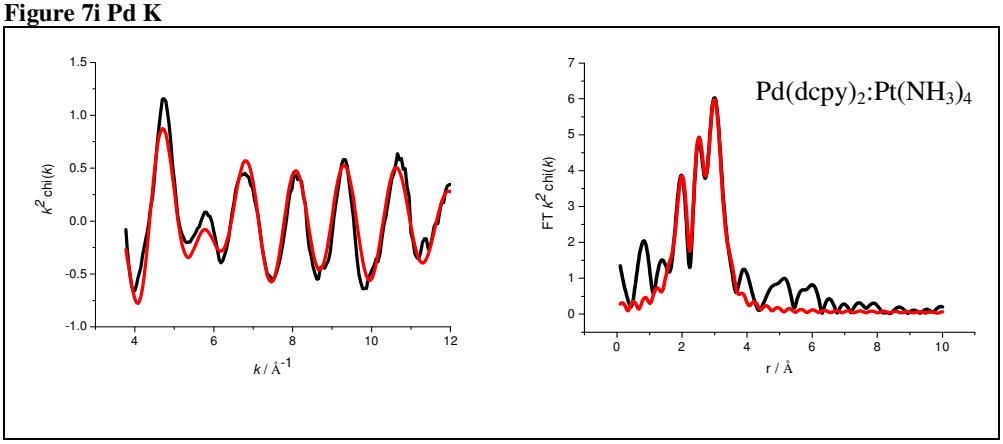

Table 3i Pt L_3

$Pd(dcpy)_2:Pt(NH_3)_4$	Pt-O	1.0 ± 0.1	1.95 ± 0.1	0.013 ± 0.003	-11.4	27.40
	Pt-Pt	2.6 ± 0.3	2.72 ± 0.01	0.011 ± 0.001	±	
	Pt-Pd	2.3 ± 0.2	2.73 ± 0.01	0.011 ± 0.001	0.8	
	Pt-O	1.2 ± 0.3	2.72 ± 0.03	0.011 ± 0.007		
	Pt-Pt	1.4 ± 0.6	3.81 ± 0.02	0.010 ± 0.008		
	Pt-Pt	3.4 ± 0.8	4.69 ± 0.01	0.014 ± 0.005		

Table 4i Pd K

$Pd(dcpy)_2:Pt(NH_3)_4$	Pd-O	1.5 ± 0.1	2.01 ± 0.01	0.009 ± 0.002	-0.6	27.64
	Pd-Pd	3.1 ± 0.2	2.74 ± 0.01	0.009 ± 0.001	±	
	Pd-Pt	0.6 ± 0.2	2.75 ± 0.03	0.006 ± 0.004	0.9	
	Pd-Pd	0.8 ± 0.4	3.84 ± 0.02	0.014 ± 0.007		
	Pd-Pd	2.4 ± 0.8	4.77 ± 0.02	0.012 ± 0.004		

Figure 6j Pt L_3

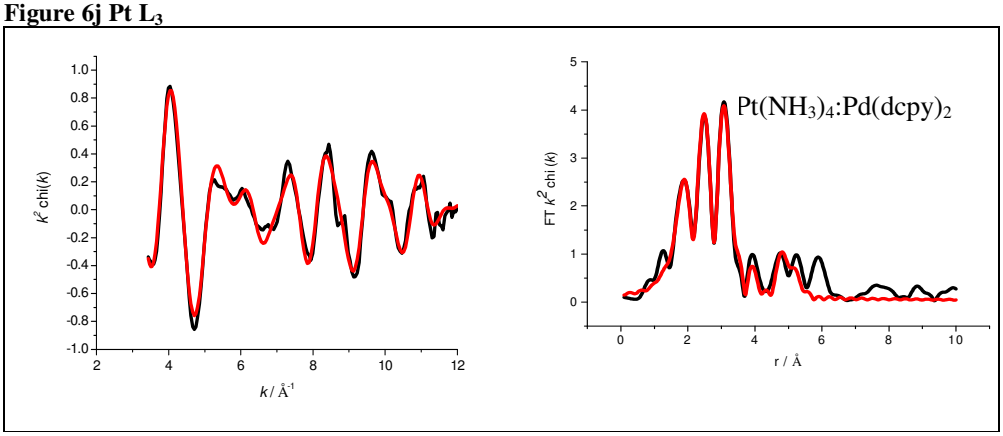

Figure 7j Pd K

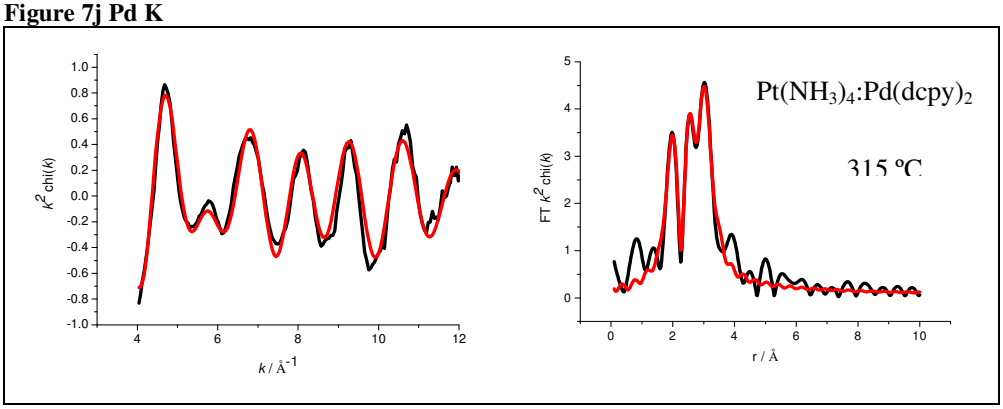

Table 3j Pt L_3

$Pt(NH_3)_4$:Pd(dcpy)$_2$	Pt-O	2.2 ± 0.3	1.94 ± 0.10	0.011 ± 0.002	-12.7	24.35
	Pt-Pt	2.1 ± 0.1	2.72 ± 0.01	0.010 ± 0.005	±	
	Pt-Pd	1.8 ± 0.3	2.74 ± 0.01	0.011 ± 0.001	0.7	
	Pt-O	1.2 ± 0.3	2.74 ± 0.02	0.012 ± 0.005		
	Pt-Pt	1.2 ± 0.5	3.78 ± 0.02	0.012 ± 0.005		
	Pt-Pt	3.3 ± 0.7	4.69 ± 0.01	0.011 ± 0.002		
	Pt-Pd	0.5 ± 0.2	3.66 ± 0.03	0.011 ± 0.006		

Table 4j Pd K

$Pt(NH_3)_4$:Pd(dcpy)$_2$	Pd-O	1.3 ± 0.1	2.01 ± 0.01	0.005 ± 0.001	-1.7	23.44
	Pd-Pd	2.7 ± 0.2	2.75 ± 0.01	0.011 ± 0.001	±	
	Pd-Pt	0.7 ± 0.3	2.77 ± 0.03	0.013 ± 0.006	0.7	
	Pd-Pt	0.7 ± 0.5	3.76 ± 0.03	0.013 ± 0.007		
	Pd-Pd	1.2 ± 0.6	4.79 ± 0.03	0.012 ± 0.005		

Figure 6k Pt L_3

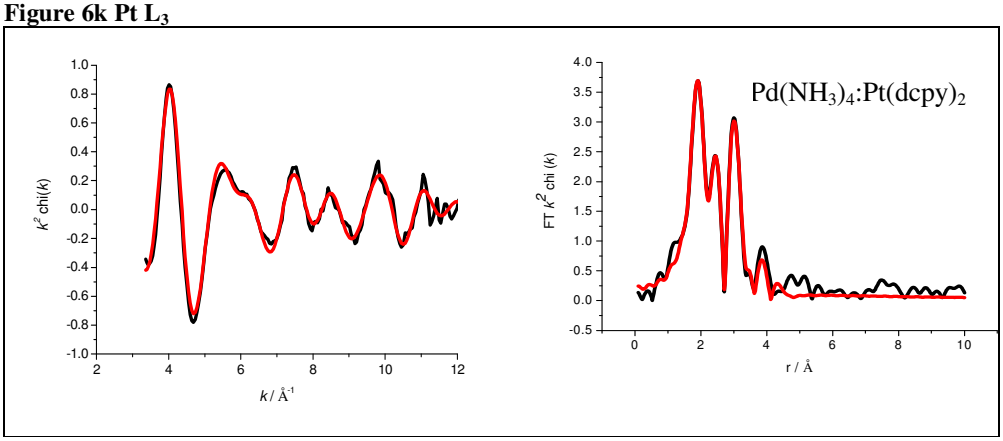

Figure 7k Pd K

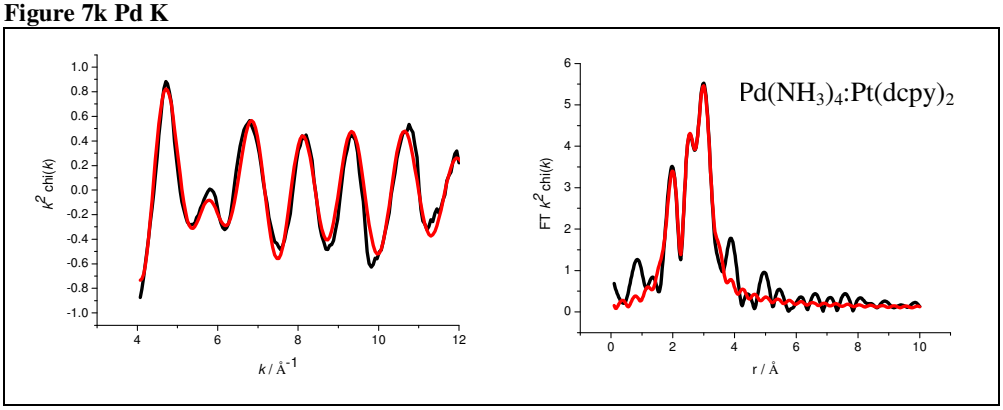

Table 3k Pt L_3

$Pd(NH_3)_4$:$Pt(dcpy)_2$	Pt-O	1.3 ± 0.1	1.96 ± 0.01	0.009 ± 0.001	-14.0	21.76
	Pt-Pt	1.2 ± 0.3	2.69 ± 0.01	0.011 ± 0.002	±	
	Pt-Pd	1.2 ± 0.1	2.72 ± 0.01	0.011 ± 0.001	0.8	
	Pt-O	2.3 ± 0.2	2.74 ± 0.02	0.015 ± 0.003		
	Pt-Pt	1.4 ± 0.4	3.77 ± 0.02	0.019 ± 0.006		
	Pt-Pd	0.6 ± 0.2	3.66 ± 0.02	0.013 ± 0.005		

Table 4k Pd K

$Pd(NH_3)_4$:$Pt(dcpy)_2$	Pd-O	1.5 ± 0.1	2.02 ± 0.01	0.009 ± 0.001	-0.8	20.52
	Pd-Pd	2.9 ± 0.2	2.74 ± 0.01	0.011 ± 0.001	±	
	Pd-Pt	0.4 ± 0.2	2.72 ± 0.04	0.010 ± 0.007	0.7	
	Pd-Pt	0.6 ± 0.4	3.72 ± 0.04	0.007 ± 0.004		
	Pd-Pd	1.5 ± 0.6	4.75 ± 0.02	0.011 ± 0.003		

Figure 6l Pt L_3

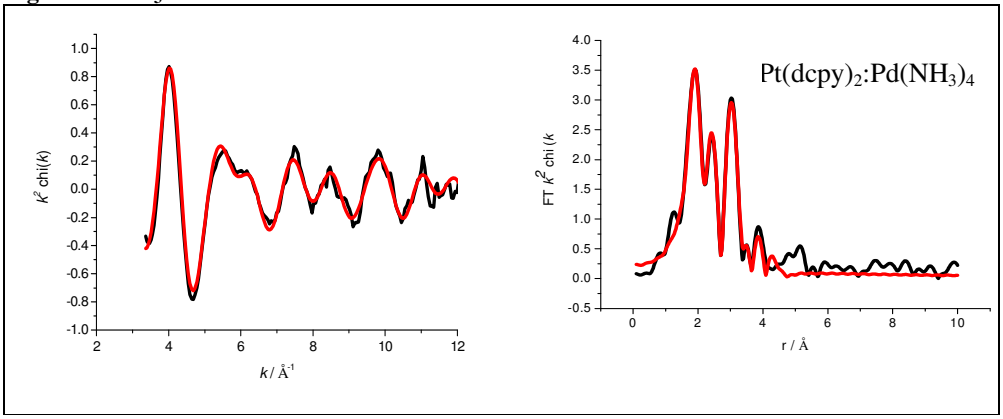

Figure 7l Pd K

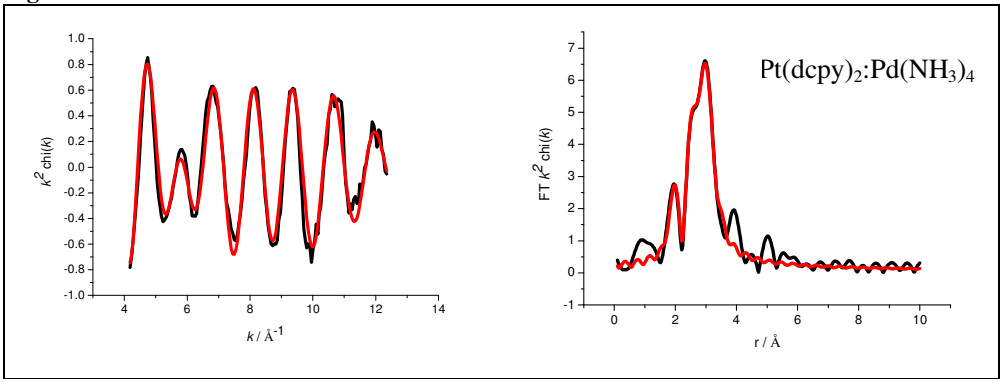

Table 3l Pt L_3

$Pt(dcpy)_2:Pd(NH_3)_4$	Pt-O	1.3 ± 0.1	1.96 ± 0.01	0.010 ± 0.001	-14.1 ± 0.8	23.82
	Pt-Pt	1.3 ± 0.2	2.70 ± 0.01	0.009 ± 0.002		
	Pt-Pd	1.2 ± 0.1	2.72 ± 0.01	0.011 ± 0.002		
	Pt-O	2.3 ± 0.2	2.76 ± 0.02	0.012 ± 0.003		
	Pt-Pt	1.3 ± 0.4	3.74 ± 0.02	0.015 ± 0.005		
	Pt-Pd	0.8 ± 0.2	3.66 ± 0.01	0.015 ± 0.005		

Table 4l Pd K

$Pt(dcpy)_2:Pd(NH_3)_4$	Pd-O	0.8 ± 0.1	2.00 ± 0.01	0.004 ± 0.002	-0.3 ± 0.8	20.34
	Pd-Pd	3.9 ± 0.2	2.73 ± 0.01	0.011 ± 0.001		
	Pd-Pt	0.9 ± 0.3	2.73 ± 0.01	0.011 ± 0.005		
	Pd-Pd	0.8 ± 0.5	3.77 ± 0.05	0.009 ± 0.006		
	Pd-Pt	1.1 ± 0.9	3.75 ± 0.04	0.011 ± 0.009		
	Pd-Pd	1.8 ± 0.7	4.76 ± 0.02	0.011 ± 0.004		

Figure 6m Pt L_3

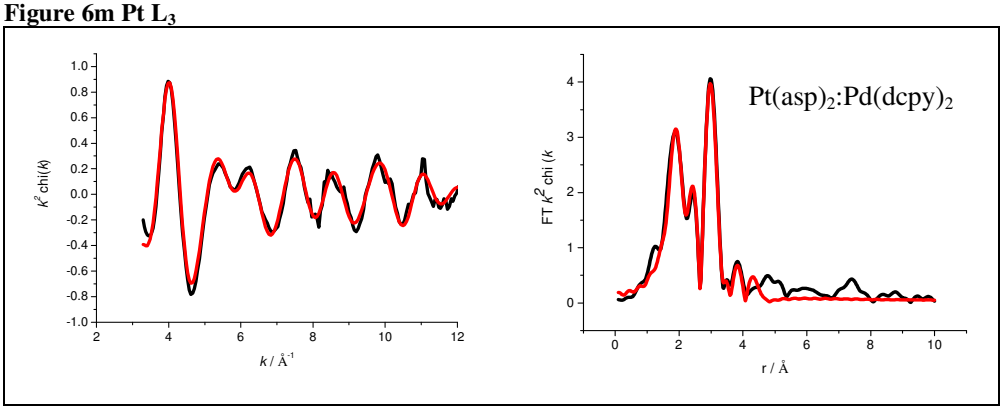

Figure 7m Pd K

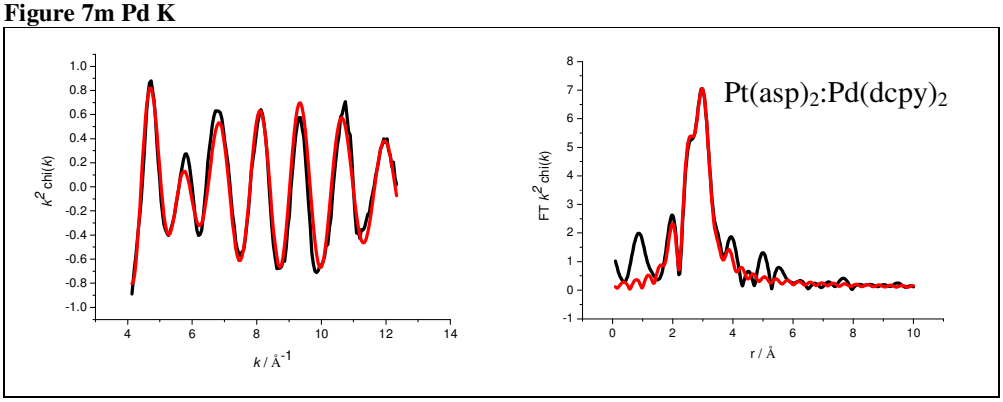

Table 3m Pt L_3

$Pt(asp)_2$:$Pd(dcpy)_2$	Pt-O	1.2 ± 0.1	1.96 ± 0.01	0.011 ± 0.002	-14.8	23.00
	Pt-Pt	0.9 ± 0.2	2.68 ± 0.01	0.007 ± 0.002	±	
	Pt-Pd	1.5 ± 0.1	2.73 ± 0.01	0.012 ± 0.002	0.8	
	Pt-O	2.3 ± 0.2	2.77 ± 0.02	0.006 ± 0.003		
	Pt-Pd	2.4 ± 0.5	3.76 ± 0.01	0.019 ± 0.004		
	Pt-Pd	1.1 ± 0.3	3.68 ± 0.02	0.021 ± 0.005		

Table 4m Pd K

$Pt(asp)_2$:$Pd(dcpy)_2$	Pd-O	0.7 ± 0.2	2.00 ± 0.02	0.003 ± 0.003	-1.1	23.80
	Pd-Pd	4.1 ± 0.2	2.74 ± 0.01	0.011 ± 0.001	±	
	Pd-Pt	0.6 ± 0.4	2.74 ± 0.05	0.014 ± 0.012	0.8	
	Pd-Pt	0.9 ± 0.6	3.73 ± 0.03	0.014 ± 0.009		
	Pd-Pd	2.2 ± 0.8	4.77 ± 0.02	0.011 ± 0.003		

Figure 6n Pt L_3

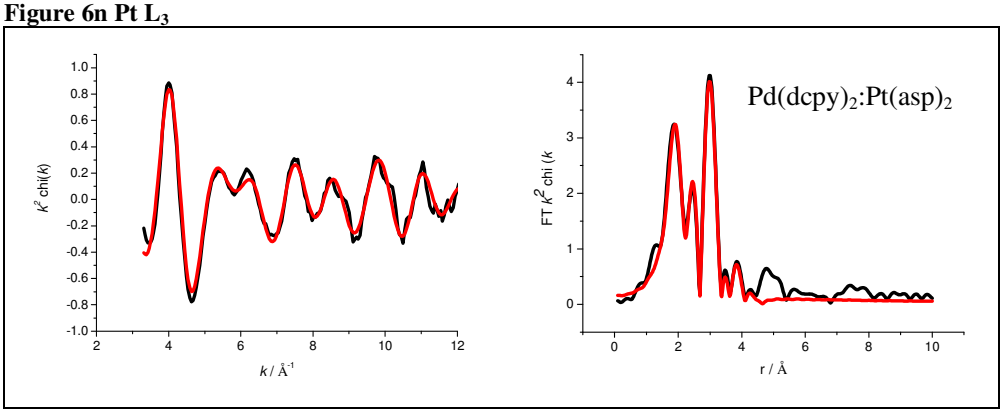

Figure 7n Pd K

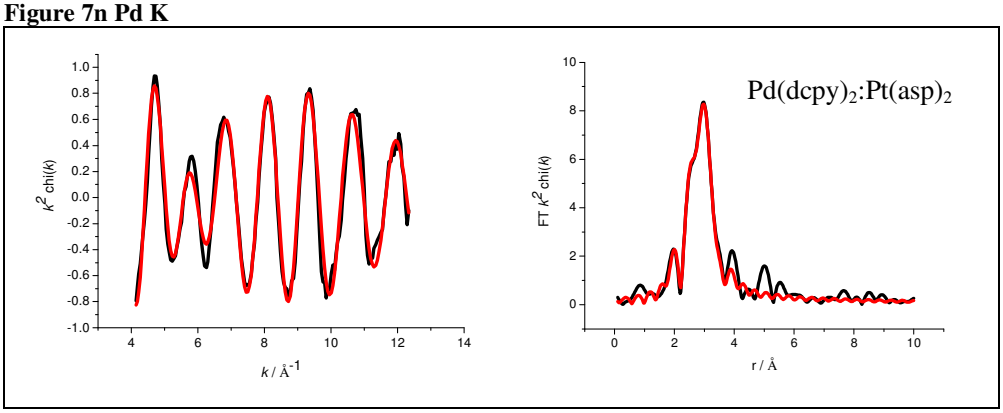

Table 3n Pt L_3

$Pd(dcpy)_2$:$Pt(asp)_2$	Pt-O	1.3 ± 0.1	1.96 ± 0.01	0.012 ± 0.002	-14.8 ± 0.8	23.35
	Pt-Pt	0.6 ± 0.3	2.97 ± 0.02	0.007 ± 0.003		
	Pt-Pd	1.7 ± 0.1	2.74 ± 0.01	0.014 ± 0.001		
	Pt-O	1.9 ± 0.2	2.75 ± 0.02	0.016 ± 0.004		
	Pt-Pt	1.2 ± 0.4	3.75 ± 0.02	0.021 ± 0.011		
	Pt-Pd	0.7 ± 0.2	3.66 ± 0.02	0.015 ± 0.005		

Table 4n Pd K

$Pd(dcpy)_2$:$Pt(asp)_2$	Pd-O	0.6 ± 0.1	2.02 ± 0.02	0.007 ± 0.004	-0.4 ± 0.1	16.57
	Pd-Pd	4.6 ± 0.2	2.74 ± 0.01	0.011 ± 0.001		
	Pd-Pd	0.8 ± 0.3	2.74 ± 0.03	0.009 ± 0.004		
	Pd-Pt	1.3 ± 0.5	3.71 ± 0.02	0.011 ± 0.004		
	Pd-Pd	2.7 ± 0.6	4.76 ± 0.01	0.011 ± 0.002		

It can be seen from the Fourier Transform data and the tables above that all samples retained a M-O neighbour between 1.95 and 2.02 Å after heating. As was discussed in Chapter Three, a M-O distance of 2.04 Å seems to correspond to oxide formation so it is reasonable to suggest that, in the case of the above samples, the ligands have not been fully removed and that the formation of the oxidised particle is not complete. The M-O coordination numbers at this distance appear to be quite small. With the exception of $[Pt(asp)_2]$:$[Pd(NH_3)_4]$ at the Pt L_3 edge, the observed M-O coordination number following mild calcination is smaller than that obtained for the dried materials (see the electronic appendix).

Fitting the Pt edge data (except $[Pt(dcpy)_2]$+$[Pd(dcpy)_2]$) required an additional low *Z* neighbour, although the coordination distances at which these neighbours were found at could not be reconciled with the 5-membered chelate model and therefore, the data indicates that any part of the ligand structure that remained was disordered.

The Pt edge data for the $[Pt(asp)_2]$:$[Pd(NH_3)_4]$ sample was fitted without the need for any metal-metal neighbours and the results are consistent with the 5-membered chelate ring remaining intact. In contrast, the Pd edge data did require the fitting of both Pd-Pd and Pd-Pt contributions although these coordination numbers are very small. Interestingly, the sample was still yellow (the colour of the dried material) following mild calcination in agreement with retention of the ligand.

In the main, the measurements at the Pd K edge of the bimetallic samples are very similar to those at the Pt L_3 edge. An M-O neighbour is detected at around 2 Å and subsequently Pd-Pd and Pd-Pt neighbours are found at increasing distances from the scattering atom. However, samples $[Pt(NH_3)_4]$+$[Pd(NH_3)_4]$, $[Pd(NH_3)_4]$:$[Pt(NH_3)_4]$ and $[Pt(dcpy)_2]$+$[Pd(dcpy)_2]$ do not display any high *Z* neighbours at the Pd K edge or, for that matter, any further low *Z* neighbours suggesting the ligand has been burned off but metal particles have not yet been formed.

The first shell of high *Z* neighbours in most of the samples was found at approximately 2.7 Å, as would be expected for a M-M bond containing Pt and/or Pd neighbours. However, in sample $[Pt(NH_3)_4]$:$[Pd(NH_3)_4]$ longer Pt-Pt and Pt-Pd distances are seen at the Pt edge. This phenomenon was seen in Chapter Three and was attributed to the metals being linked *via* a bridging oxygen atom[25]. The M-M distance measured at the Pd K edge was consistently found at expected values of R(Pd-Pd) = 2.56 Å and R(Pd-Pt) = 2.60 Å in the second and third shell.

The EXAFS of the calcined samples were measured in air and the data is available in the electronic appendix. The presence of a metal oxide layer was detected and the presence of both Pt and Pd neighbours indicating the formation of bimetallic species.

3.5.2 Calcined Al_2O_3 supported catalysts in H_2

The spectra in Figure 8 (a-n) show the experimental data (black lines) and fit (red lines) {left} and corresponding Fourier Transform {right} of bimetallic catalysts on an Al_2O_3 support and calcined and reduced under H_2. The data was obtained at the Pt L_3 edge and the data and Fourier Transforms are k^2 weighted. Figure 9 also shows the EXAFS data collected of the bimetallic samples on Al_2O_3 after they had been calcined and purged in H_2. This data is measured at the Pd K edge. All the samples were measured at room temperature. The calculated structural parameters obtained by analysis of this data are presented in Tables 5 and 6.

Figure 8a Pt L_3

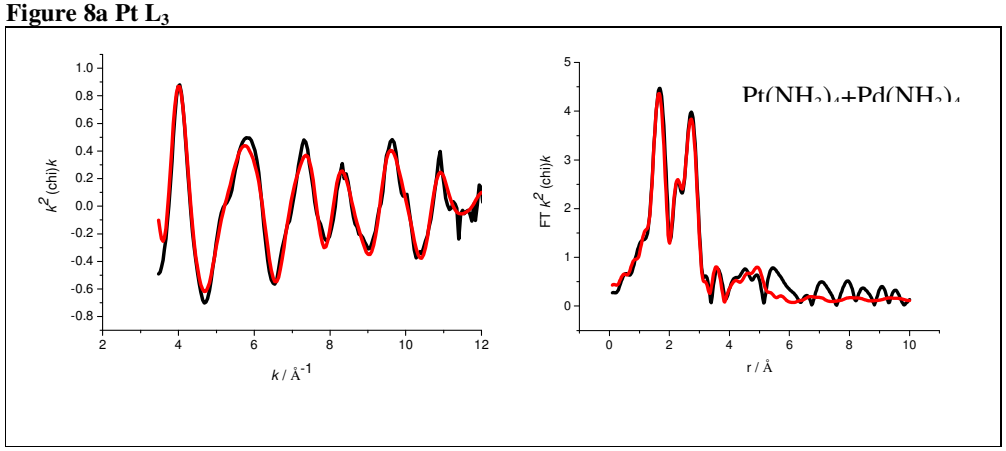

Figure 9a Pd K

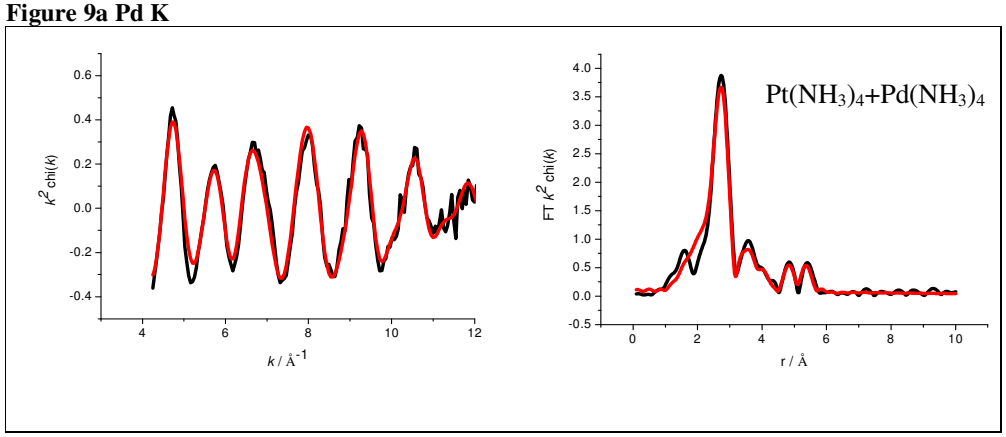

Table 5a Pt L_3

Sample	Shell	N	R / Å	$2\sigma^2$/Å^2	E_f / eV	R_{exafs} / %
$Pt(NH_3)_4$+$Pd(NH_3)_4$	Pt-Pt	3.5 ± 0.6	2.72 ± 0.01	0.025 ± 0.003	-10.5 ± 0.6	23.15
	Pt-Pd	2.3 ± 0.2	2.77 ± 0.01	0.017± 0.001		
	Pt-O	1.3 ± 0.1	1.98 ± 0.01	0.005 ± 0.001		
	Pt-Pt	7.1 ± 1.1	3.77 ± 0.01	0.029 ± 0.004		
	Pt-Pd	2.0 ± 0.4	3.68 ± 0.01	0.019 ± 0.003		
	Pt-Pt	4.8 ± 1.1	4.73 ± 0.01	0.015 ± 0.004		
	Pt-Pd	1.1 ± 0.6	4.70 ± 0.03	0.013 ± 0.008		

Table 6a Pd K

Sample	Shell	N	R / Å	$2\sigma^2/Å^2$	E_f / eV	R_{exafs} / %
$Pt(NH_3)_4$+$Pd(NH_3)_4$	Pd-Pd	2.0 ± 0.1	2.76 ± 0.01	0.013 ± 0.001	1.2 ±	23.40
	Pd-Pt	1.2 ± 0.2	2.74 ± 0.01	0.009 ± 0.001	0.9	
	Pd-Pd	1.3 ± 0.3	3.88 ± 0.03	0.002 ± 0.005		
	Pd-Pt	1.4 ± 0.4	3.62 ± 0.03	0.003 ± 0.005		
	Pd-Pd	1.6 ± 0.5	4.02 ± 0.03	0.012 ± 0.006		
	Pd-Pd	1.2 ± 0.2	4.82 ± 0.02	0.012 ± 0.004		
	Pd-Pd	1.3 ± 0.6	5.44 ± 0.02	0.011 ± 0.004		

Figure 8a Pt L_3

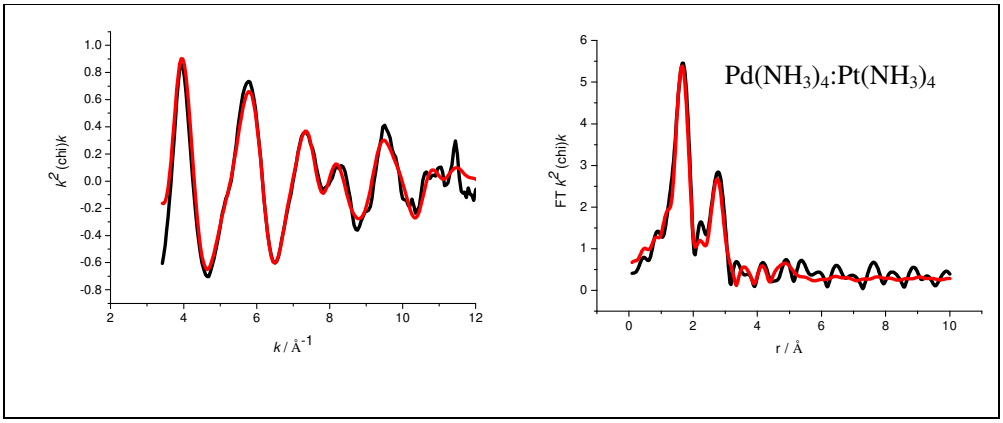

Figure 8b Pd K

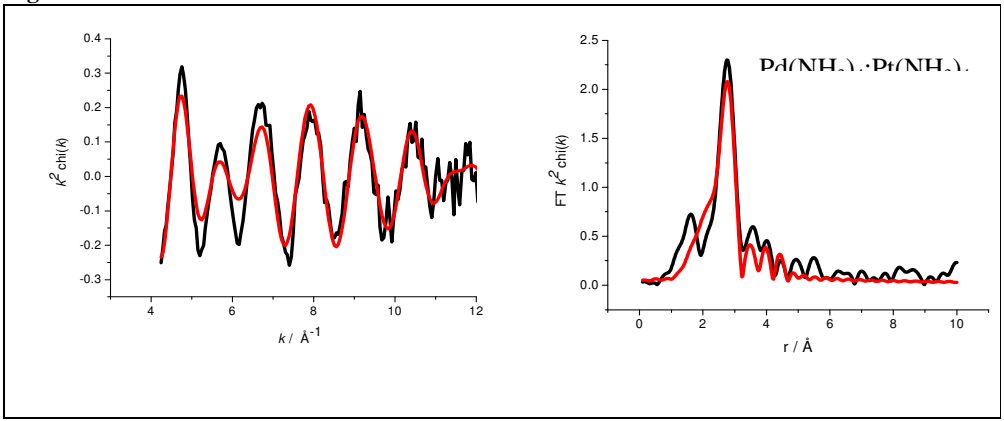

Table 5b Pt L_3

Pd(NH$_3$)$_4$:Pt(NH$_3$)$_4$	Pt-Pt	4.6 ± 0.6	2.68 ± 0.01	0.023 ± 0.002	-12.0 ± 0.8	26.23
	Pt-Pd	6.7 ± 0.9	2.93 ± 0.02	0.047 ± 0.001		
	Pt-O	1.8 ± 0.1	1.99 ± 0.01	0.004 ± 0.001		
	Pt-Pt	2.7 ± 0.8	3.88 ± 0.02	0.022 ± 0.006		
	Pt-Pt	1.9 ± 1.0	4.77 ± 0.03	0.013 ± 0.006		

Table 6b Pd K

Pd(NH$_3$)$_4$:Pt(NH$_3$)$_4$	Pd-Pd	1.1 ± 0.1	2.76 ± 0.01	0.012 ± 0.001	-3.9 ± 1.3	41.99
	Pd-Pt	1.1 ± 0.2	2.75 ± 0.02	0.012 ± 0.002		
	Pd-Pd	0.7 ± 0.3	4.07 ± 0.03	0.014 ± 0.006		
	Pd-Pt	1.1 ± 0.6	4.14 ± 0.02	0.015 ± 0.007		

Figure 8c Pt L_3

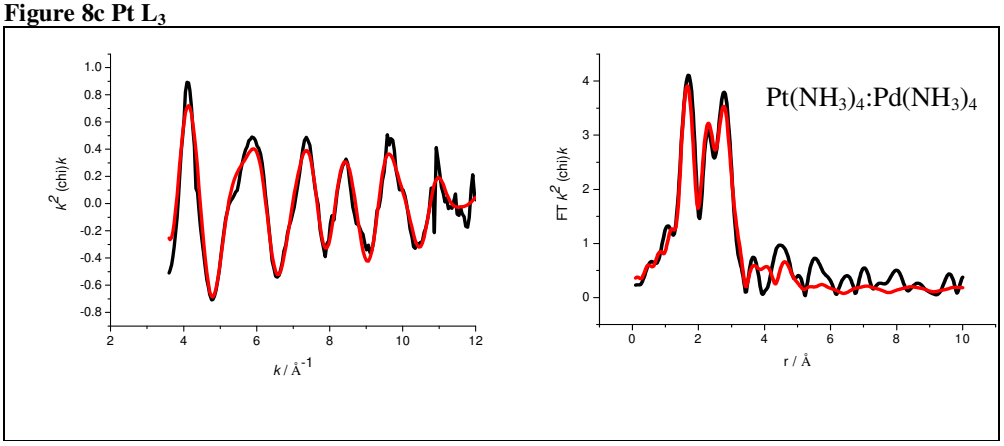

Figure 9c Pd K

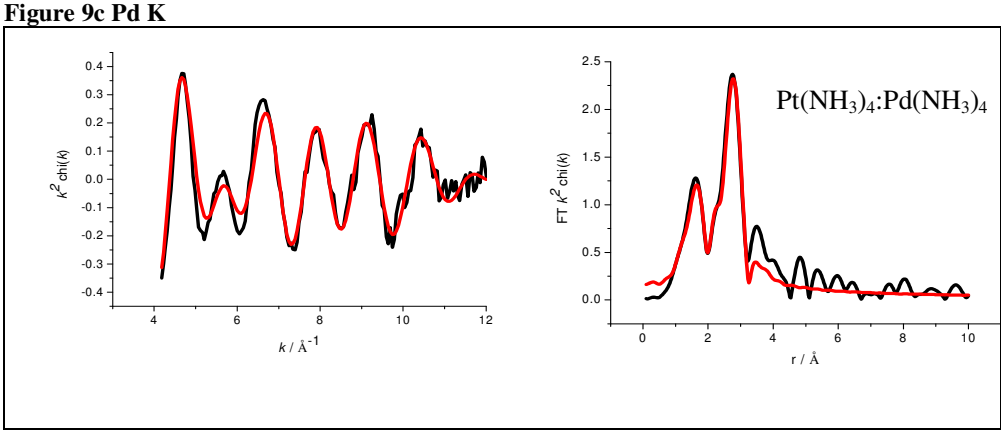

Table 5c Pt L_3

$Pt(NH_3)_4$:$Pd(NH_3)_4$	Pt-Pt	8.2 ± 1.2	2.70 ± 0.01	0.036 ± 0.003	-7.2 ± 1.2	28.75
	Pt-Pd	2.3 ± 0.3	2.76 ± 0.01	0.017 ± 0.001		
	Pt-O	0.9 ± 0.1	1.96 ± 0.01	0.003 ± 0.001		
	Pt-Pt	2.6 ± 0.8	3.79 ± 0.02	0.019 ± 0.004		
	Pt-Pt	1.7 ± 0.9	4.71 ± 0.03	0.012 ± 0.006		

Table 6c Pd K

$Pt(NH_3)_4$:$Pd(NH_3)_4$	Pd-Pd	1.7 ± 0.2	2.77 ± 0.01	0.017 ± 0.001	-5.0 ± 1.0	31.20
	Pd-Pt	1.3 ± 0.2	2.76 ± 0.01	0.016 ± 0.003		
	Pd-O	0.3 ± 0.1	2.00 ± 0.02	0.001 ± 0.002		

Figure 8d Pt L_3

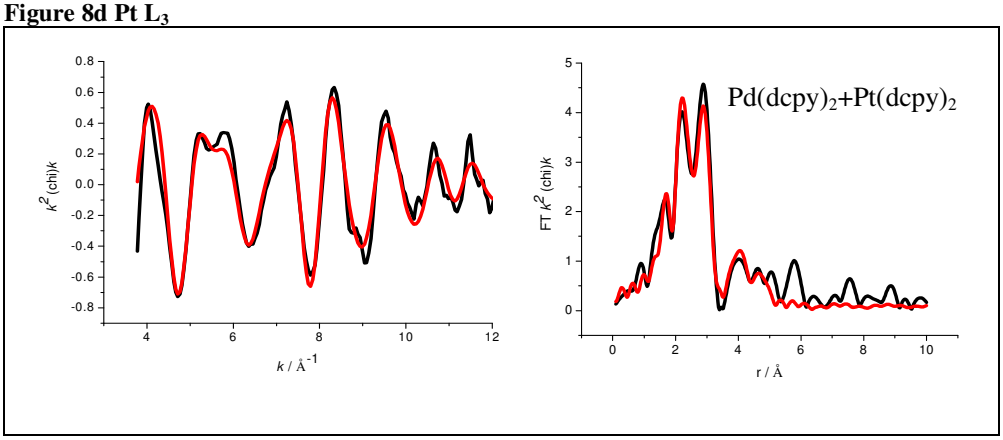

Figure 9d Pd K

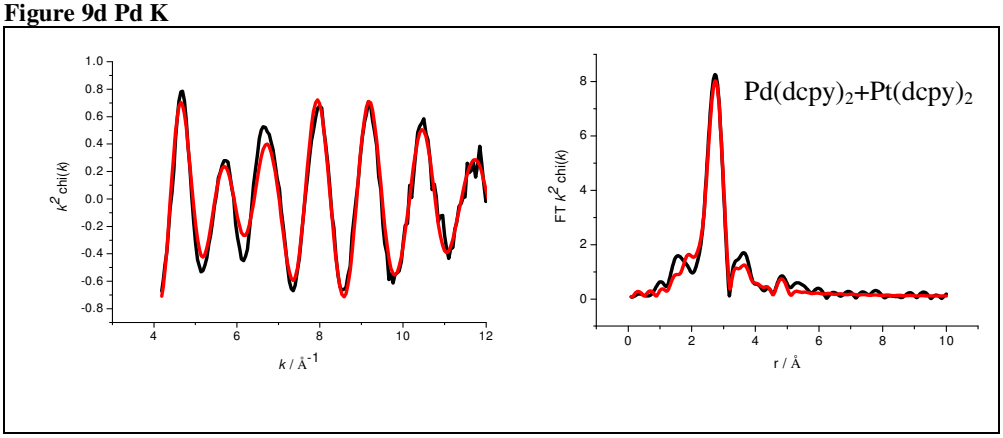

Table 5d Pt L_3

$Pd(dcpy)_2+Pt(dcpy)_2$	Pt-Pt	4.2 ± 0.3	2.75 ± 0.01	0.010 ± 0.001	-14.2 ±	28.64
	Pt-Pd	2.0 ± 0.2	2.75 ± 0.01	0.009 ± 0.001	0.9	
	Pt-O	0.6 ± 0.1	2.02 ± 0.02	0.009 ± 0.005		
	Pt-Pt	3.4 ± 1.1	3.83 ± 0.03	0.010 ± 0.006		
	Pt-Pt	1.9 ± 1.0	4.73 ± 0.03	0.010 ± 0.005		
	Pt-Pd	2.4 ± 0.8	4.08 ± 0.03	0.009 ± 0.005		

Table 6d Pd K

$Pd(dcpy)_2+Pt(dcpy)_2$	Pd-Pd	3.8 ± 0.2	2.77 ± 0.01	0.011 ± 0.001	0.0 ±	19.11
	Pd-Pt	1.7 ± 0.3	2.76 ± 0.01	0.011 ± 0.003	0.7	
	Pd-Pd	1.0 ± 0.3	3.46 ± 0.03	0.015 ± 0.010		
	Pd-Pt	1.2 ± 0.6	2.49 ± 0.04	0.015 ± 0.011		
	Pd-Pd	1.0 ± 0.7	4.86 ± 0.04	0.011 ± 0.007		

Figure 8e Pt L_3

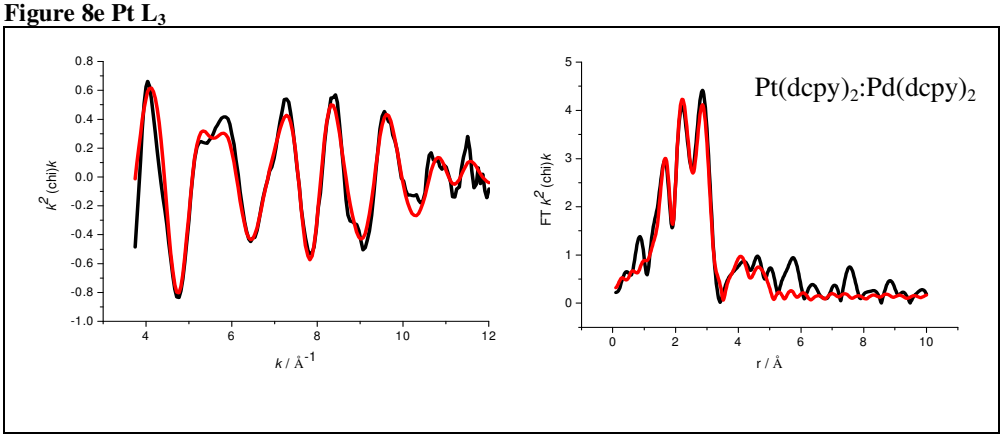

Figure 9e Pd K

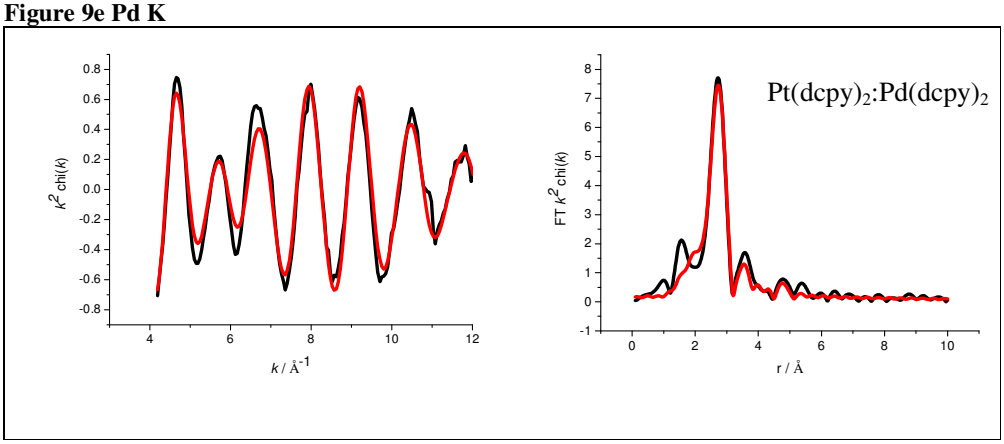

Table 5e Pt L_3

$Pt(dcpy)_2$:$Pd(dcpy)_2$	Pt-Pt	4.2 ± 0.4	2.73 ± 0.01	0.011 ± 0.001	-13.0 ± 1.0	28.82
	Pt-Pd	2.1 ± 0.2	2.74 ± 0.01	0.011 ± 0.001		
	Pt-O	0.8 ± 0..1	1.99 ± 0.01	0.007 ± 0.003		
	Pt-Pt	2.9 ± 1.1	3.79 ± 0.03	0.011 ± 0.007		
	Pt-Pd	2.2 ± 0.9	4.05 ± 0.03	0.010 ± 0.006		
	Pt-Pt	1.8 ± 1.1	4.71 ± 0.02	0.010 ± 0.006		

Table 6e Pd K

$Pt(dcpy)_2$:$Pd(dcpy)_2$	Pd-Pd	3.7 ± 0.2	2.77 ± 0.01	0.011 ± 0.001	-1.6 ± 0.7	22.93
	Pd-Pt	2.1 ± 0.3	2.75 ± 0.01	0.012 ± 0.002		
	Pd-Pd	0.5 ± 0.3	3.49 ± 0.03	0.013 ± 0.007		
	Pd-Pd	1.1 ± 0.7	4.83 ± 0.03	0.014 ± 0.008		

Figure 8f Pt L_3

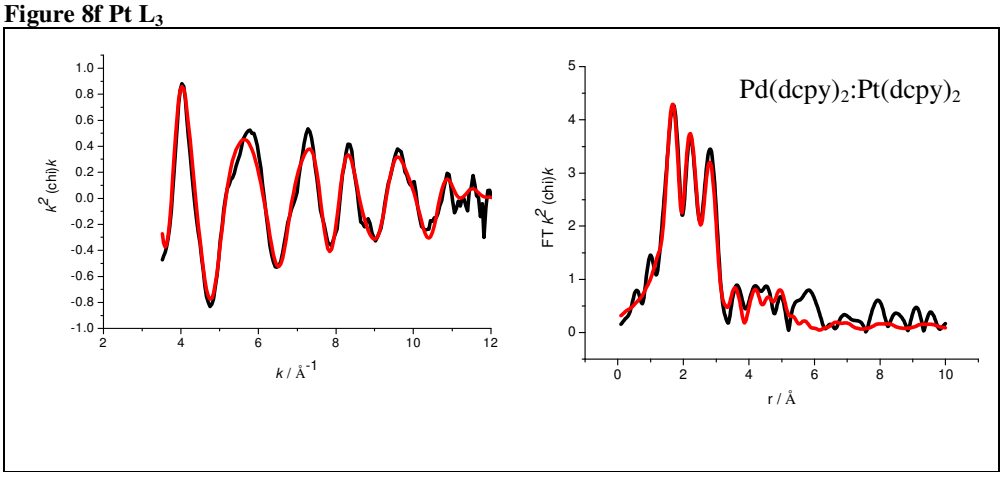

Figure 9f Pd K

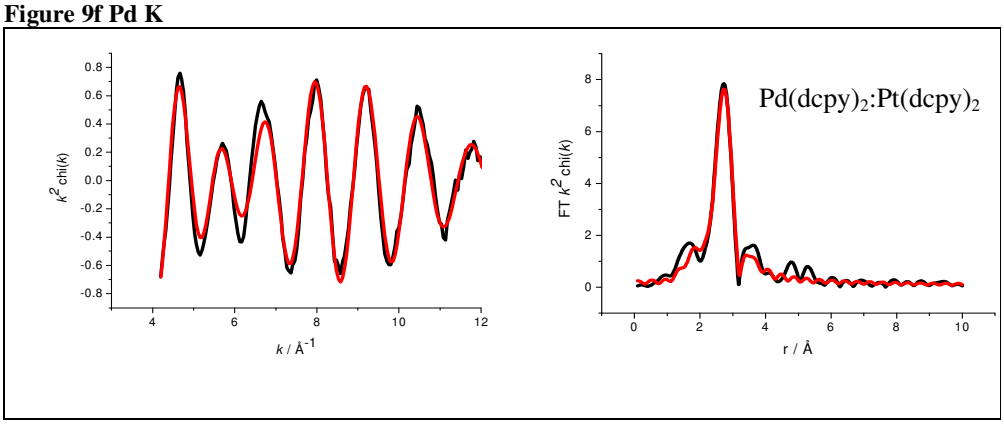

Table 5f Pt L_3

$Pd(dcpy)_2$:$Pt(dcpy)_2$	Pt-Pt	5.4 ± 0.5	2.73 ± 0.01	0.019 ± 0.001	-11.6 ±	24.08
	Pt-Pd	2.3 ± 0.2	2.74 ± 0.01	0.016 ± 0.001	0.7	
	Pt-O	1.2 ± 0.1	1.99 ± 0.01	0.005 ± 0.001		
	Pt-Pt	8.9 ± 1.6	2.80 ± 0.02	0.036 ± 0.006		
	Pt-Pd	1.1 ± 0.3	3.68 ± 0.02	0.015 ± 0.004		
	Pt-Pt	4.8 ± 1.2	4.73 ± 0.02	0.014 ± 0.003		
	Pt-Pd	1.4 ± 0.7	4.67 ± 0.03	0.014 ± 0.007		

Table 6f Pd K

$Pd(dcpy)_2$:$Pt(dcpy)_2$	Pd-Pd	3.7 ± 0.2	2.77 ± 0.01	0.011 ± 0.001	-1.3 ±	19.72
	Pd-Pt	1.7 ± 0.4	2.75 ± 0.01	0.011 ± 0.004	0.7	
	Pd-Pd	1.1 ± 0.4	3.49 ± 0.03	0.013 ± 0.006		
	Pd-Pt	1.0 ± 0.6	3.55 ± 0.04	0.015 ± 0.013		

Figure 8g Pt L_3

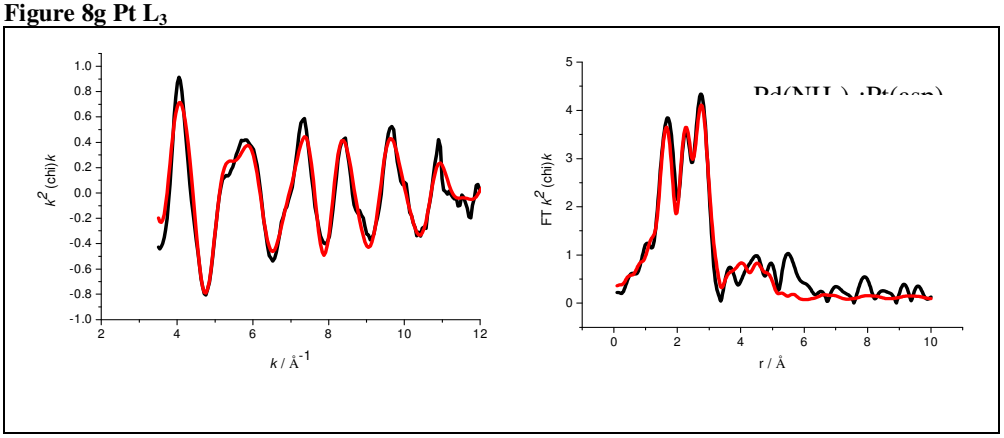

Figure 9g Pd K

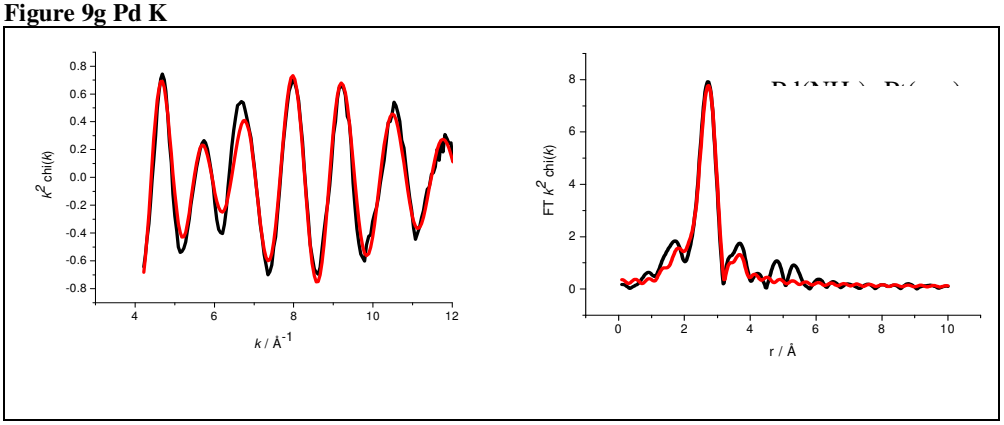

Table 5g Pt L_3

$Pd(NH_3)_4$:$Pt(asp)_2$	Pt-Pt	4.7 ± 0.6	2.72 ± 0.01	0.023 ± 0.003	-9.7 ±	25.85
	Pt-Pd	2.7 ± 0.3	2.75 ± 0.01	0.016 ± 0.001	0.9	
	Pt-O	1.1 ± 0.1	1.97 ± 0.01	0.007 ± 0.002		
	Pt-Pt	4.0 ± 1.0	3.79 ± 0.02	0.015 ± 0.006		
	Pt-Pt	2.5 ± 0.9	4.70 ± 0.02	0.012 ± 0.004		
	Pt-Pd	1.6 ± 0.6	4.06 ± 0.03	0.011 ± 0.007		

Table 6g Pd K

$Pd(NH_3)_4$:$Pt(asp)_2$	Pd-Pd	3.8 ± 0.2	2.76 ± 0.01	0.011 ± 0.001	-1.8 ±	19.65
	Pd-Pt	1.9 ± 0.4	2.75 ± 0.01	0.011 ± 0.004	0.8	
	Pd-Pd	0.8 ± 0.4	3.49 ± 0.04	0.011 ± 0.009		
	Pd-Pt	0.8 ± 0.7	3.52 ± 0.07	0.008 ± 0.010		

Figure 8h Pt L_3

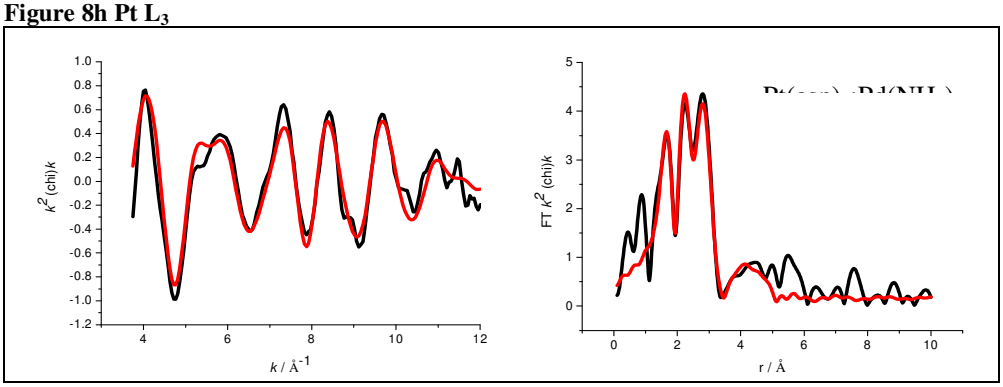

Figure 9h Pd K

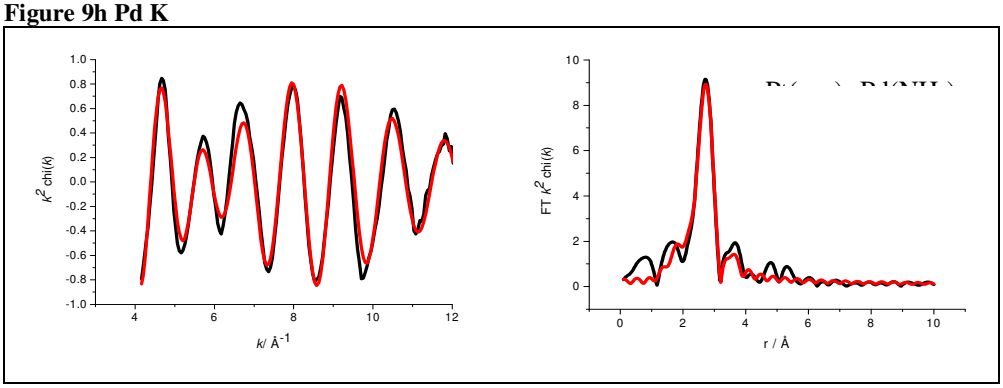

Table 5h Pt L_3

$Pt(asp)_2$:$Pd(NH_3)_4$	Pt-Pt	3.2 ± 0.4	2.74 ± 0.01	0.010 ± 0.001	-13.0 ± 1.1	34.11
	Pt-Pd	2.4 ± 0.2	2.74 ± 0.01	0.010 ± 0.001		
	Pt-O	1.3 ± 0.2	1.98 ± 0.01	0.009 ± 0.003		
	Pt-Pt	3.3 ± 1.3	3.79 ± 0.03	0.011 ± 0.007		
	Pt-Pd	1.9 ± 0.8	4.06 ± 0.03	0.008 ± 0.007		
	Pt-Pt	2.0 ± 1.3	4.68 ± 0.03	0.012 ± 0.007		

Table 6h Pd K

$Pt(asp)_2$:$Pd(NH_3)_4$	Pd-Pd	4.6 ± 0.2	2.77 ± 0.01	0.011 ± 0.001	-1.6 ± 0.7	21.56
	Pd-Pt	2.1 ± 0.4	2.76 ± 0.01	0.011 ± 0.003		
	Pd-Pd	0.6 ± 0.3	3.50 ± 0.03	0.013 ± 0.008		

Figure 8i Pt L_3

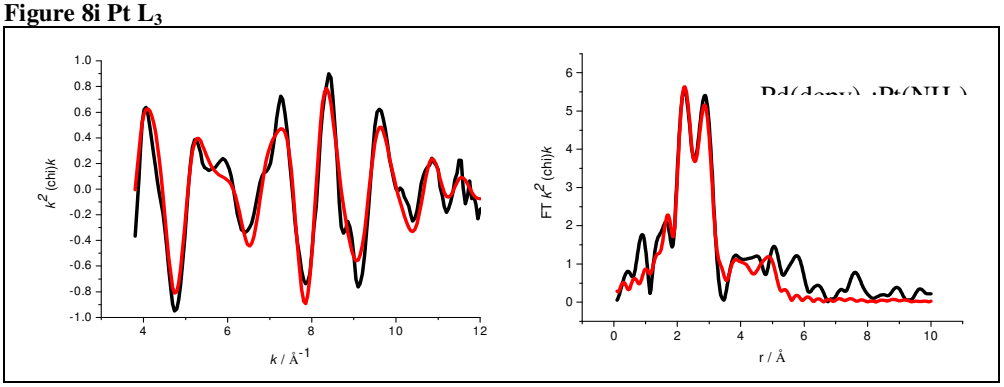

Figure 9i Pd K

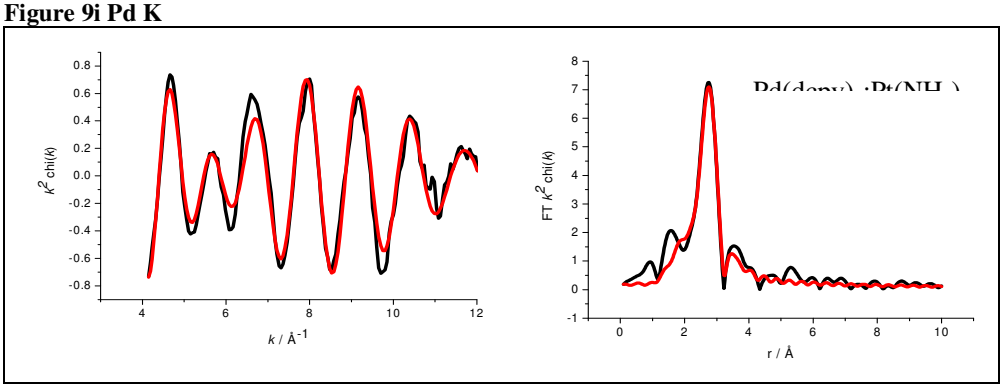

Table 5i Pt L_3

$Pd(dcpy)_2$:$Pt(NH_3)_4$	Pt-Pt	4.5 ± 0.4	2.74 ± 0.01	0.009 ± 0.001	-13.1 ± 0.9	34.82
	Pt-Pd	2.9 ± 0.2	2.74 ± 0.01	0.009± 0.001		
	Pt-O	0.4 ± 0.2	2.00 ± 0.04	0.012 ± 0.010		
	Pt-Pt	2.6 ± 1.0	3.84 ± 0.02	0.015 ± 0.005		
	Pt-Pt	5.5 ± 1.6	4.72 ± 0.02	0.010 ± 0.003		
	Pt-Pd	1.5 ± 0.8	4.69 ± 0.03	0.008 ± 0.006		

Table 6i Pd K

$Pd(dcpy)_2$:$Pt(NH_3)_4$	Pd-Pd	3.3 ± 0.3	2.77 ± 0.01	0.011 ± 0.001	-1.7 ± 0.8	23.69
	Pd-Pt	2.6 ± 0.4	2.75 ± 0.01	0.012 ± 0.003		
	Pd-Pd	0.9 ± 0.4	3.51 ± 0.02	0.010 ± 0.005		
	Pd-Pt	0.9 ± 0.8	3.58 ± 0.05	0.011 ± 0.010		

Figure 8j Pt L_3

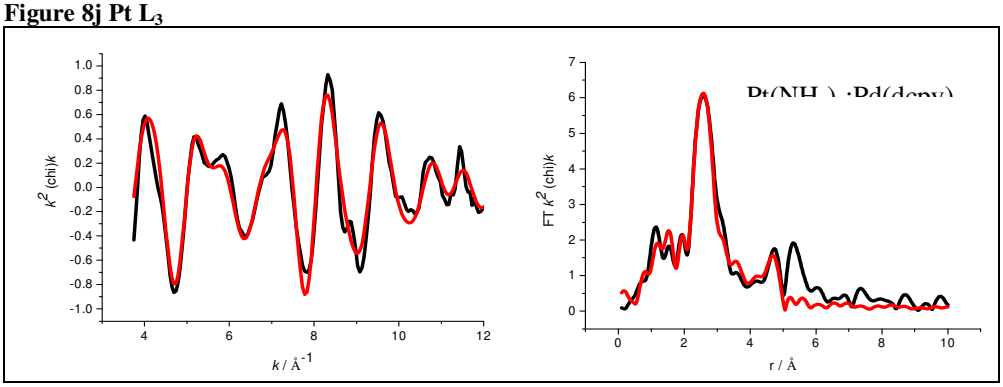

Figure 9j Pd K

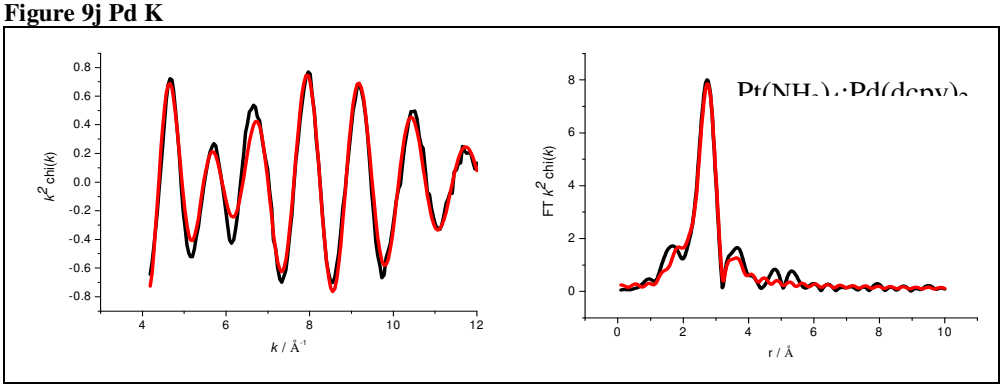

Table 5j Pt L_3

$Pt(NH_3)_4$:$Pd(dcpy)_2$	Pt-Pt	4.3 ± 0.3	2.76 ± 0.01	0.008 ± 0.001	-14.9 ± 0.9	29.10
	Pt-Pd	2.7 ± 0.2	2.75 ± 0.01	0.008 ± 0.001		
	Pt-O	0.5 ± 0.2	2.04 ± 0.03	0.013 ± 0.009		
	Pt-Pt	5.2 ± 1.4	3.82 ± 0.02	0.013 ± 0.005		
	Pt-Pd	3.2 ± 0.9	4.08 ± 0.02	0.011 ± 0.005		
	Pt-Pt	3.2 ± 1.2	4.72 ± 0.02	0.011 ± 0.003		

Table 6j Pd K

$Pt(NH_3)_4$:$Pd(dcpy)_2$	Pd-Pd	3.8 ± 0.2	2.77 ± 0.01	0.011 ± 0.001	-2.8 ± 0.7	17.53
	Pd-Pt	2.1 ± 0.3	2.75 ± 0.01	0.011 ± 0.003		
	Pd-Pd	1.0 ± 0.3	3.50 ± 0.03	0.011 ± 0.006		
	Pd-Pt	0.9 ± 0.6	3.55 ± 0.05	0.012 ± 0.011		

Figure 8k Pt L_3

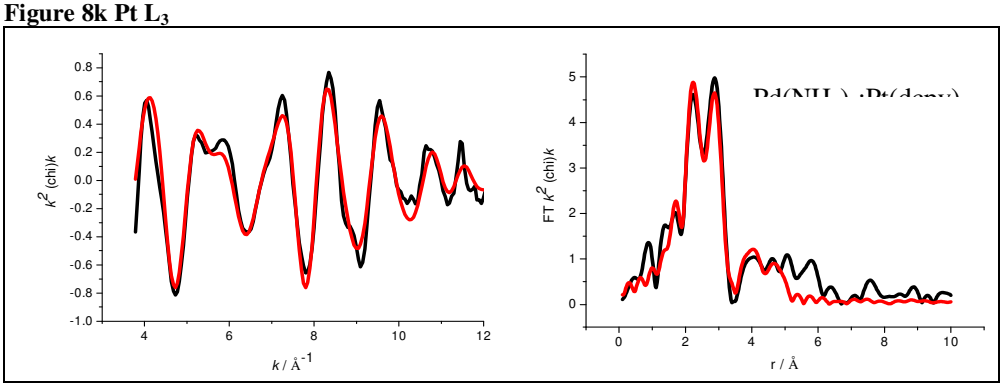

Figure 9k Pd K

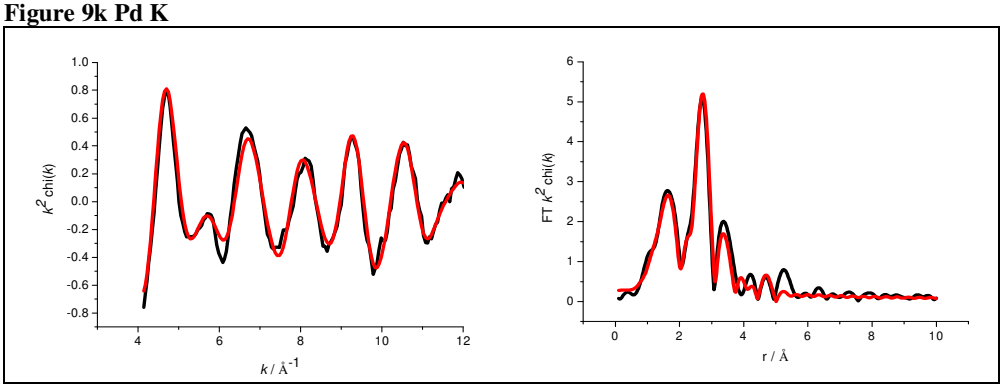

Table 5k Pt L_3

$Pd(NH_3)_4$:$Pt(dcpy)_2$	Pt-Pt	4.4 ± 0.3	2.75 ± 0.01	0.011 ± 0.001	-13.5 ± 1.0	28.93
	Pt-Pd	2.5 ± 0.2	2.75 ± 0.01	0.010 ± 0.001		
	Pt-O	0.5 ± 0.2	2.01 ± 0.03	0.012 ± 0.007		
	Pt-Pt	2.9 ± 1.2	3.82 ± 0.03	0.005 ± 0.004		
	Pt-Pd	1.9 ± 0.9	4.07 ± 0.04	0.004 ± 0.004		
	Pt-Pt	2.3 ± 1.1	4.72 ± 0.03	0.009 ± 0.004		

Table 6k Pd K

$Pd(NH_3)_4$:$Pt(dcpy)_2$	Pd-Pd	2.4 ± 0.2	2.75 ± 0.01	0.011 ± 0.001	-1.9 ± 0.7	21.68
	Pd-Pt	1.3 ± 0.3	2.74 ± 0.02	0.017 ± 0.005		
	Pd-O	1.2 ± 0.1	2.01 ± 0.01	0.008 ± 0.002		
	Pd-Pd	1.0 ± 0.2	3.42 ± 0.01	0.012 ± 0.002		
	Pd-Pd	0.9 ± 0.5	4.81 ± 0.03	0.011 ± 0.005		

Figure 8l Pt L_3

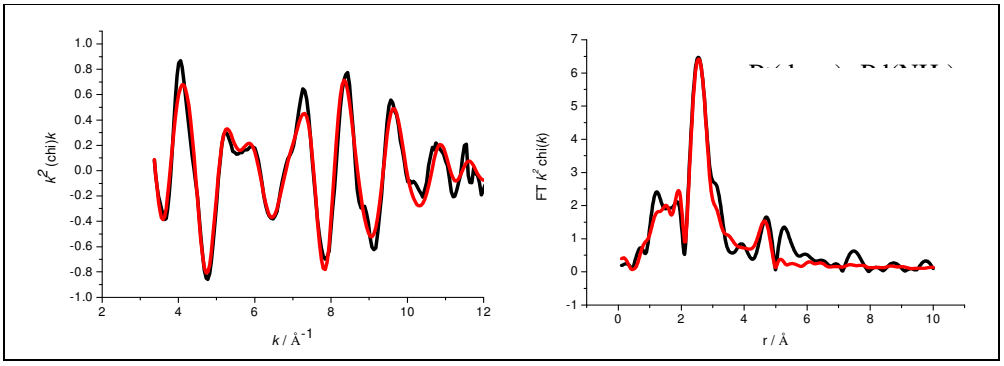

Figure 9l Pd K

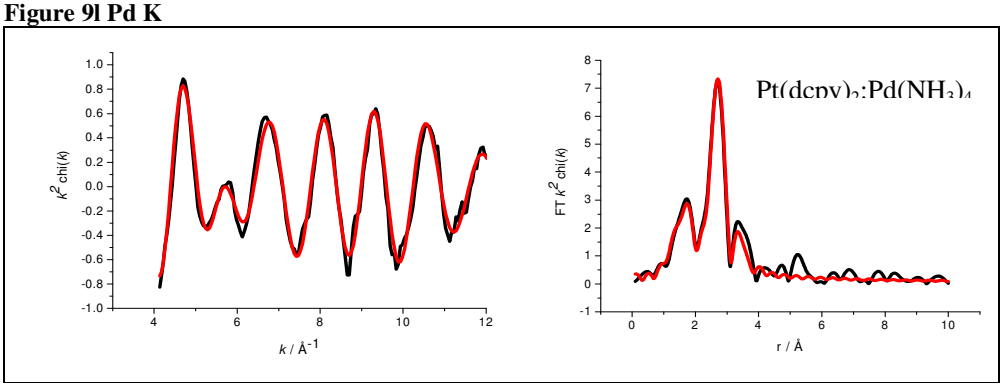

Table 5l Pt L_3

$Pt(dcpy)_2:Pd(NH_3)_4$	Pt-Pt	4.3 ± 0.3	2.74 ± 0.01	0.011 ± 0.001	-13.3 ± 0.6	25.29
	Pt-Pd	2.9 ± 0.2	2.74 ± 0.01	0.011 ± 0.001		
	Pt-O	0.7 ± 0.1	1.98 ± 0.02	0.017 ± 0.007		
	Pt-Pt	4.1 ± 1.0	3.81 ± 0.02	0.012 ± 0.005		
	Pt-Pd	2.6 ± 0.8	4.07 ± 0.02	0.011 ± 0.006		
	Pt-Pt	2.7 ± 0.1	4.69 ± 0.02	0.012 ± 0.003		

Table 6l Pd K

$Pt(dcpy)_2:Pd(NH_3)_4$	Pd-Pd	3.2 ± 0.2	2.74 ± 0.01	0.011 ± 0.001	-1.7 ± 0.7	19.73
	Pd-Pt	1.6 ± 0.4	2.71 ± 0.01	0.016 ± 0.005		
	Pd-O	1.0 ± 0.1	2.01 ± 0.01	0.007 ± 0.002		
	Pd-Pd	1.0 ± 0.2	3.43 ± 0.02	0.013 ± 0.003		

Figure 8m Pt L_3

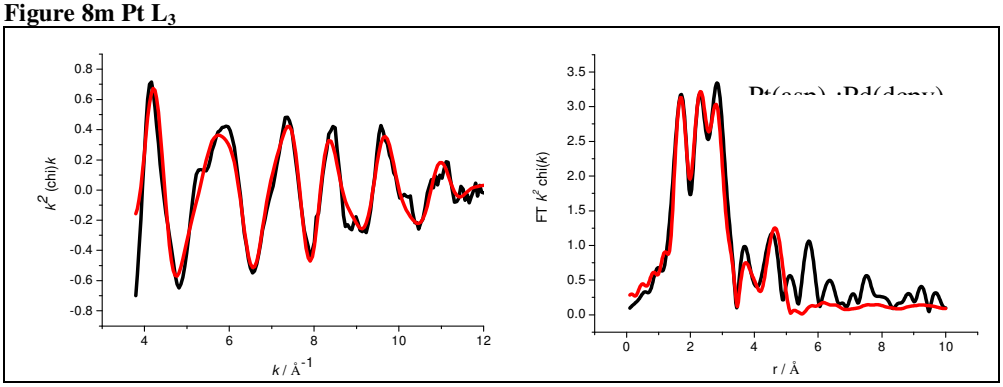

Figure 9m Pd K

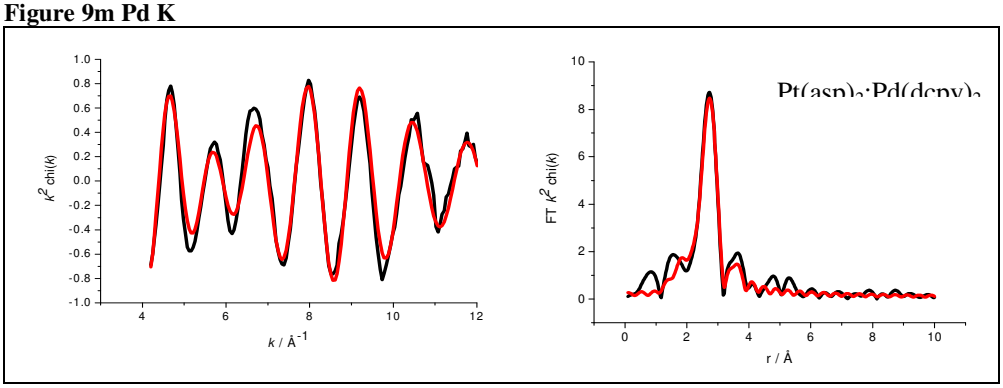

Table 5m Pt L_3

$Pt(asp)_2$:$Pd(dcpy)_2$	Pt-Pt	6.7 ± 0.8	2.69 ± 0.01	0.025 ± 0.002	-6.6 ± 1.3	30.67
	Pt-Pd	1.2 ± 0.4	2.73 ± 0.01	0.017 ± 0.004		
	Pt-O	0.6 ± 0.1	1.98 ± 0.02	0.001 ± 0.002		
	Pt-Pt	4.2 ± 1.2	4.27 ± 0.02	0.013 ± 0.004		
	Pt-Pd	1.5 ± 0.7	4.22 ± 0.04	0.011 ± 0.006		
	Pt-Pt	1.5 ± 0.7	4.79 ± 0.03	0.006 ± 0.004		

Table 6m Pd K

$Pt(asp)_2$:$Pd(dcpy)_2$	Pd-Pd	4.3 ± 0.3	2.77 ± 0.01	0.011 ± 0.001	-2.1 ± 0.8	22.26
	Pd-Pt	2.0 ± 0.4	2.75 ± 0.01	0.011 ± 0.003		
	Pd-Pd	0.7 ± 0.3	3.50 ± 0.02	0.012 ± 0.005		

Figure 8n Pt L_3

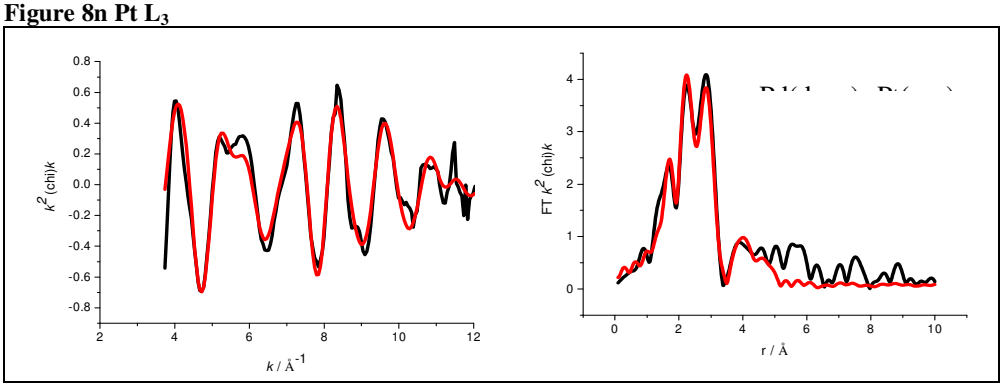

Figure 9n Pd K

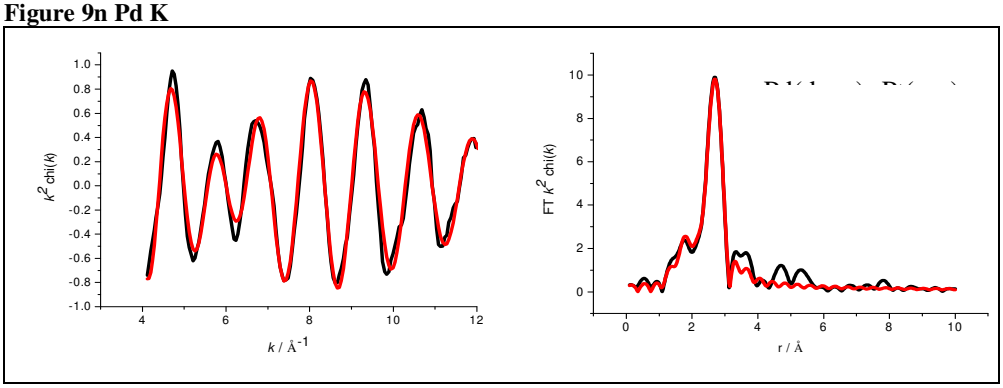

Table 5n Pt L_3

$Pd(dcpy)_2$:$Pt(asp)_2$	Pt-Pt	3.4 ± 0.3	2.74 ± 0.01	0.011 ± 0.001	-14.1 ± 1.1	30.79
	Pt-Pd	2.3 ± 0.2	2.75 ± 0.01	0.011 ± 0.001		
	Pt-O	0.7 ± 0.2	2.02 ± 0.02	0.008 ± 0.004		
	Pt-Pt	2.8 ± 1.2	3.82 ± 0.03	0.009 ± 0.006		
	Pt-Pd	1.8 ± 0.9	4.07 ± 0.03	0.007 ± 0.006		
	Pt-Pt	1.3 ± 1.1	4.70 ± 0.04	0.009 ± 0.006		

Table 6n Pd K

$Pd(dcpy)_2$:$Pt(asp)_2$	Pd-Pd	4.7 ± 0.2	2.74 ± 0.01	0.011 ± 0.001	-1.3 ± 0.7	19.03
	Pd-Pt	1.7 ± 0.4	2.73 ± 0.02	0.010 ± 0.003		
	Pd-O	0.5 ± 0.2	2.11 ± 0.03	0.013 ± 0.010		

The tables above show that when these calcined bimetallic catalyst samples are reduced, the longer Pt-O neighbour which was seen in the heated samples at the Pt L_3 edge is completely removed and, with the exception only of $[Pt(NH_3)_4]$:$[Pd(NH_3)_4]$, $[Pd(NH_3)_4]$:$[Pt(dcpy)_2]$, $[Pt(dcpy)_2]$:$[Pd(NH_3)_4]$ and $[Pd(dcpy)_2]$:$[Pt(asp)_2]$ all the Pd-O neighbours are fully removed. The low *Z* neighbours detected at the Pt edge can be found around 2.0 Å and therefore suggest that some residual ligand is present. They are, however in lower number

than is seen in the oxidised sample (see electronic appendix) implying that partial reduction has taken place. Bando et al[23] observed the retention of a metal oxide peak in Al_2O_3 supported catalysts even after reduction as opposed to SiO_2 supported catalysts (see Figure 14 and Figure 15) and concluded, therefore, that metal species on SiO_2 can be reduced more easily than those on Al_2O_3 at ambient temperature. This is due to the stronger interaction between metal atoms and Al_2O_3 compared with SiO_2. The ease of reduction of the Pd centres, in comparison, suggests that Pd experiences a change in oxidative behaviour when Pt is introduced. This is in good agreement with the XRD results, Figure 5, where both tetragonal PdO and cubic Pd were detected for some samples.

The Fourier Transforms for the data obtained at the Pt L_3 edge all showed a splitting of the peak around 2.7 Å, giving two maxima at 2.5 and 3 Å. This phenomenon is attributed to a difference in the backscattering phase shift on scattering from Pt and Pd neighbours at similar distances[17]. This interference is not seen for the metal neighbours at longer distances that give rise to the peaks in the Fourier Transform at 4 and 5 Å. No such interference was observed at the Pd K edge.

Presence of both Pt-Pt and Pt-Pd neighbours at the Pt L_3 edge and Pd-Pd and Pd-Pt neighbours at the Pd K edge indicated that the metal particles are composed of both Pt and Pd metals as opposed to a mixture of separate Pt and Pd particles, in agreement with Fujikawa et al[14] as illustrated in Figure 10.

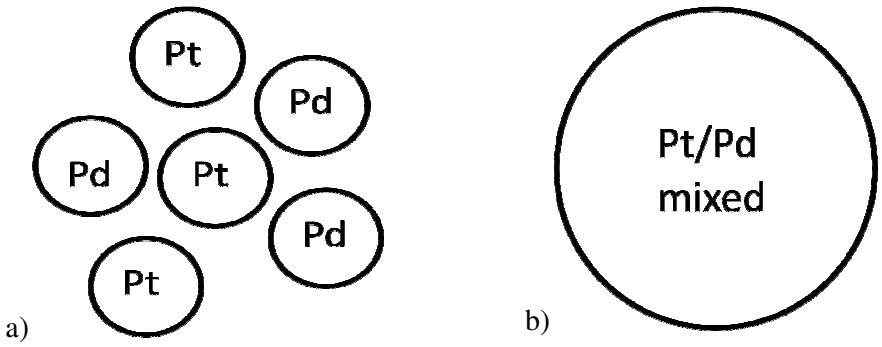

Figure 10 Diagram showing a mixture of separate Pt and Pd particles, a) and the proposed model made up of mixed Pt and Pd particles, b).

For all the samples, $N_{Pt\text{-}Pt}$ exceeds $N_{Pd\text{-}Pd}$ in agreement with studies by Hansen et al[15] and agrees with their model of a Pt-rich core surrounded by a Pd shell as shown in Figure 1.

4 Silica Supported Catalysts

4.1 Catalyst Preparation

ICP-OAS was again used to determine the composition of the prepared catalysts. As for the Al_2O_3 supported catalysts reported in Section 3, the theoretical loadings were 1.25 wt% each of Pt and Pd and the actual loadings were consistently lower as shown in Table 7.

Table 7 Precursor complexes used for preparation of bimetallic catalyst samples, method of preparation and subsequent metal wt %.

Precursor 1	Precursor 2	Preparation Method	wt % Pt	wt % Pd	Total wt %
$[Pt(NH_3)_4]$	$[Pd(NH_3)_4]$	co-impregnation	0.78	0.81	1.59
$[Pd(NH_3)_4]$	$[Pt(NH_3)_4]$	Sequential	0.91	0.96	1.87
$[Pt(NH_3)_4]$	$[Pd(NH_3)_4]$	Sequential	1.15	1.03	2.18
$[Pd(dcpy)_2]$	$[Pt(dcpy)_2]$	co-impregnation	0.99	0.93	1.92
$[Pt(dcpy)_2]$	$[Pd(dcpy)_2]$	Sequential	1.00	0.97	1.97
$[Pd(dcpy)_2]$	$[Pt(dcpy)_2]$	Sequential	0.90	0.87	1.77
$[Pd(NH_3)_4]$	$[Pt(asp)_2]$	Sequential	0.80	0.76	1.56
$[Pt(asp)_2]$	$[Pd(NH_3)_4]$	Sequential	1.00	1.05	2.05
$[Pd(dcpy)_2]$	$[Pt(NH_3)_4]$	Sequential	0.98	0.92	1.90
$[Pt(NH_3)_4]$	$[Pd(dcpy)_2]$	Sequential	0.92	0.93	1.85
$[Pd(NH_3)_4]$	$[Pt(dcpy)_2]$	Sequential	0.97	1.07	2.04
$[Pt(dcpy)_2]$	$[Pd(NH_3)_4]$	Sequential	1.08	1.00	2.08
$[Pt(asp)_2]$	$[Pd(dcpy)_2]$	Sequential	0.63	0.66	1.29
$[Pd(dcpy)_2]$	$[Pt(asp)_2]$	Sequential	0.64	0.70	1.34

The SiO_2 samples prepared, overall, had a higher actual wt % than the corresponding Al_2O_3 samples. Pt wt % ranged from 0.63 to 1.15 % and Pd wt % was in the region of 0.66 to 1.07 % for all samples. These similar percentages

confirm, as for the Al_2O_3 catalysts, that the nature of the metal complex has no effect on the overall metal loading.

4.2 Thermogravimetric Analysis

The TGA data for the SiO_2 catalysts are shown in Figure 11. The samples were measured individually from room temperature to 600 ºC to determine the temperature at which the ligands are lost when the catalyst is calcined. The results are grouped by ligand type to aid comparison. Samples $[Pd(NH_3)_4]$:$[Pt(NH_3)_4]$ and $[Pd(dcpy)_2]$:$[Pt(dcpy)_2]$, shown in panels [a] and [b] were only measured to around 400 ºC. This is because a power failure caused the furnace to halt and it was decided that in both cases, the relevant data had been collected.

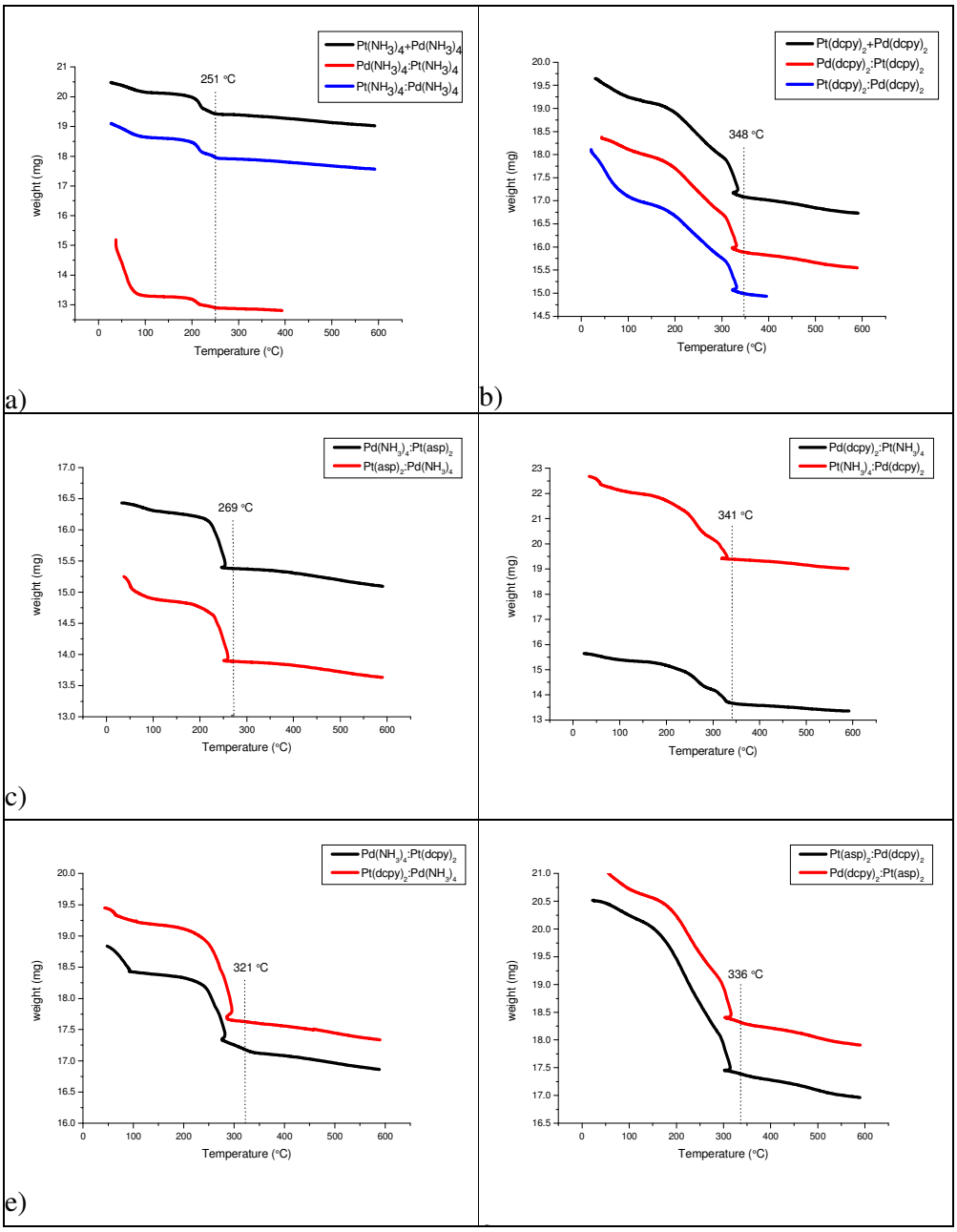

Figure 11 Weight loss (TGA) of bimetallic catalyst samples on SiO_2 during heating to 600 ºC in air. The vertical dashed lines indicate significant temperature points.

The thermogravimetric profiles of the SiO_2 supported catalysts are similar to those for the Al_2O_3 supported catalysts shown in Section 3.2.1. In both cases, the order in which the precursor is adsorbed onto the support has no effect on the temperature at which the ligands are lost. However, the SiO_2 samples lose their ligands more rapidly than the Al_2O_3 samples as can be seen by the steep drop of the curves.

4.3 TEM

The average particle sizes of the bimetallic catalysts on SiO_2 were obtained by analysing TEM images (see reports T3228A and T3228B in the electronic appendix). This measurement and the particle size distribution are presented in Figure 12. The data is grouped by ligand type to aid comparison. No suitable area was found on the sample to accurately measure the particle sizes of samples $[Pt(dcpy)_2]$:$[Pd(NH_3)_4]$ and $[Pd(dcpy)_2]$:$[Pt(asp)_2]$.

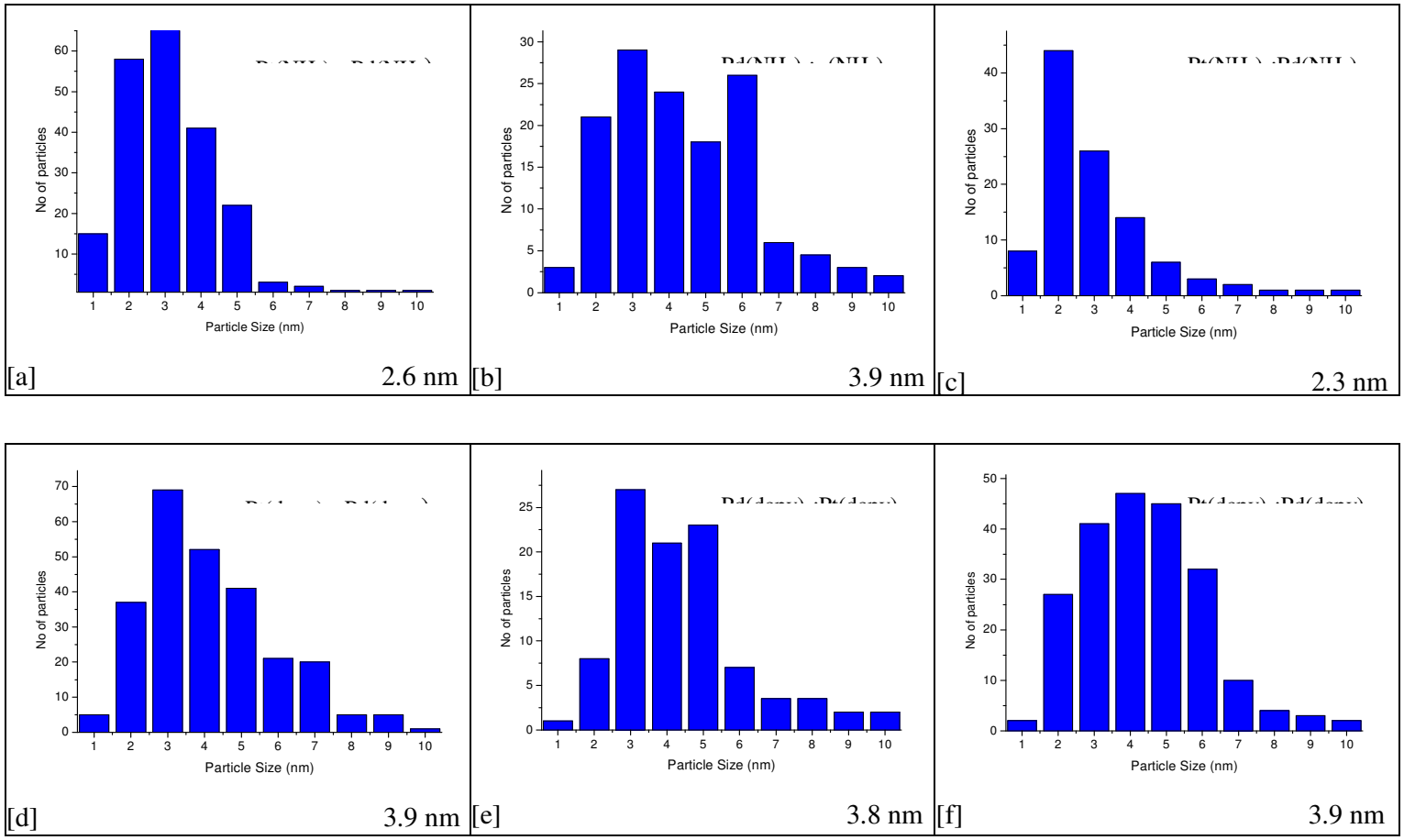

Figure 12 Particle size and distributions of bimetallic catalysts in SiO_2. All samples were analysed as calcined catalysts.

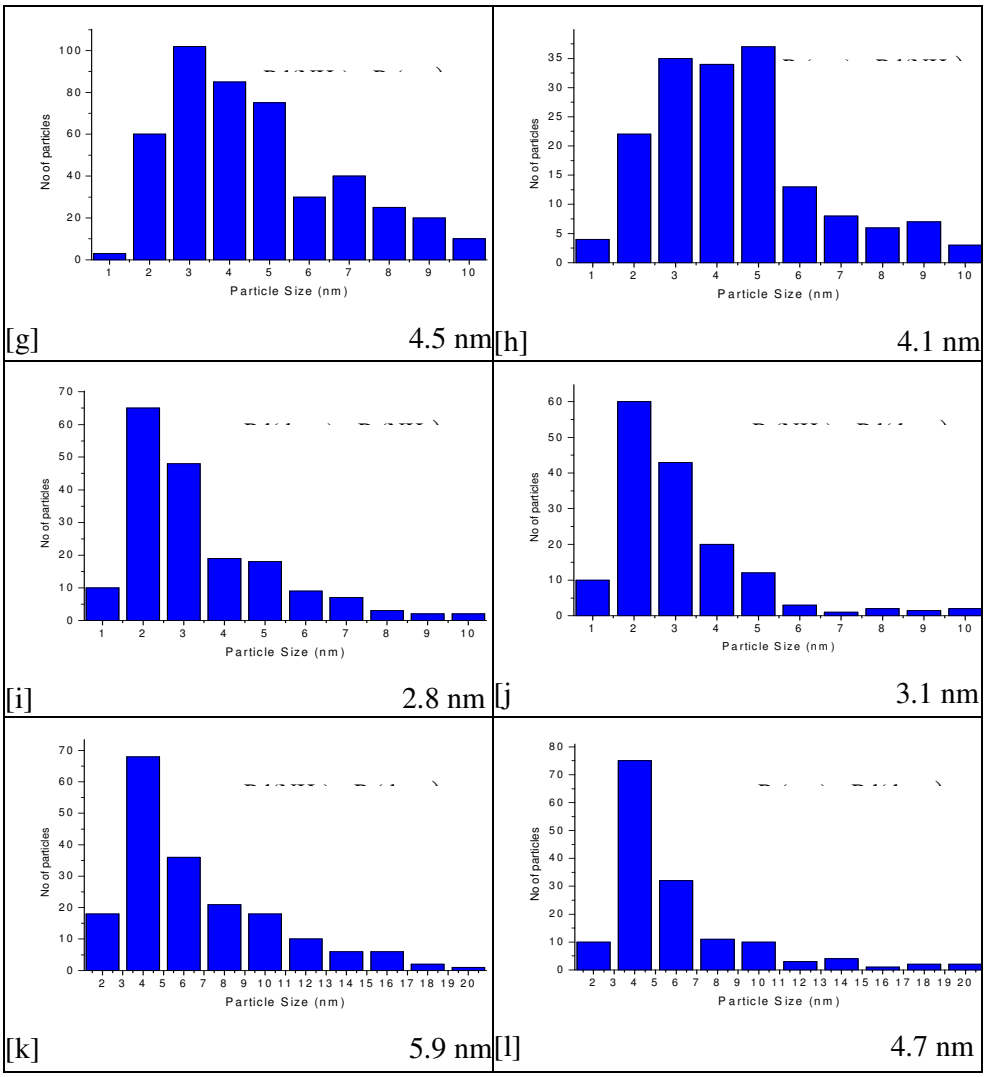

Figure 12 continued.

4.4 XRD

The XRD patterns collected in this study of the SiO_2 supported samples are presented below in Figure 13 and provide information regarding the presence of different metal and oxide phases.

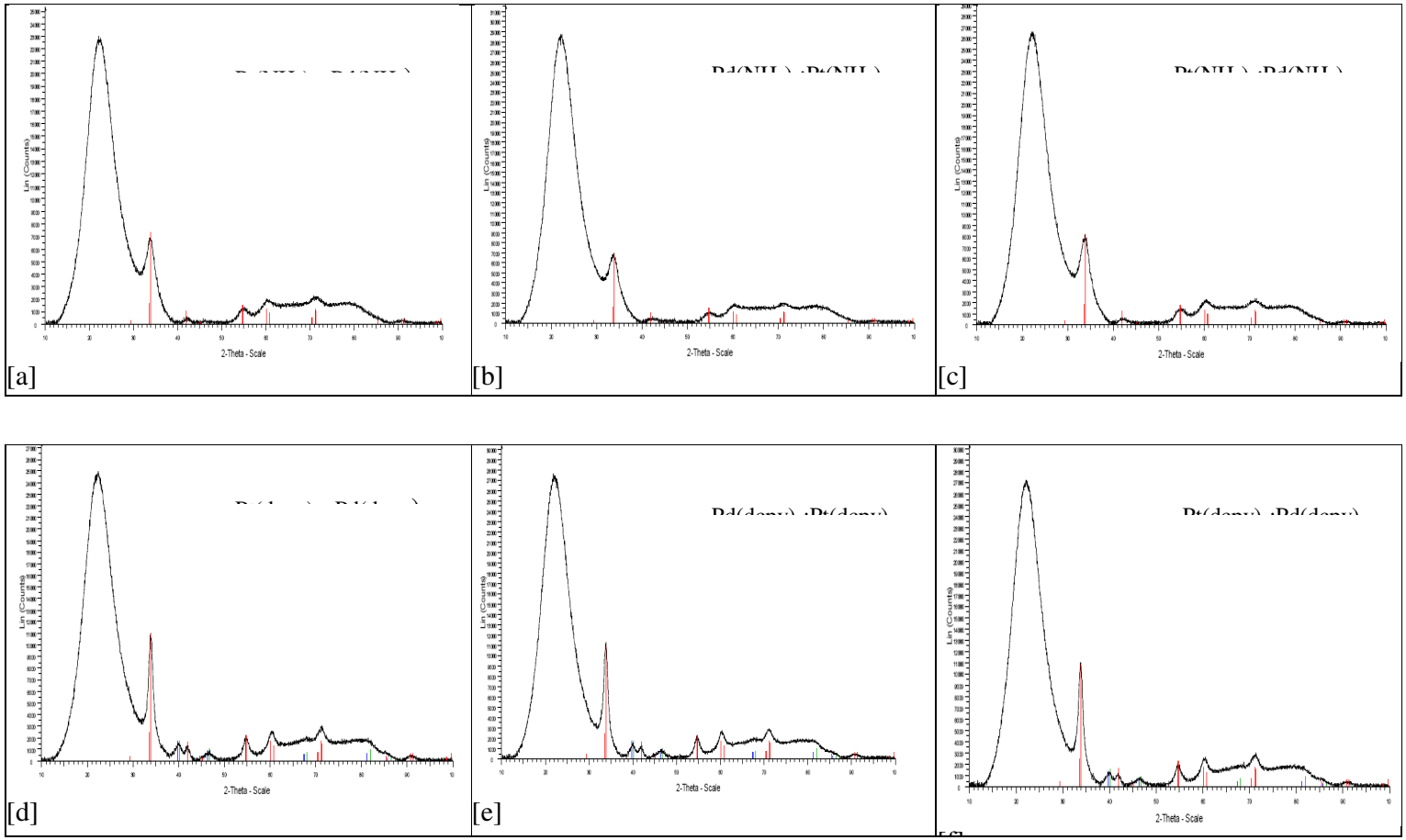

Figure 13 XRD patterns of bimetallic catalysts. All samples are calcined and supported on SiO_2. ▮ is tetragonal PdO (PDF No 00-046-1043), ▮ is cubic Pt (PDF No 00-004-0802) and ▮ is cubic Pd.

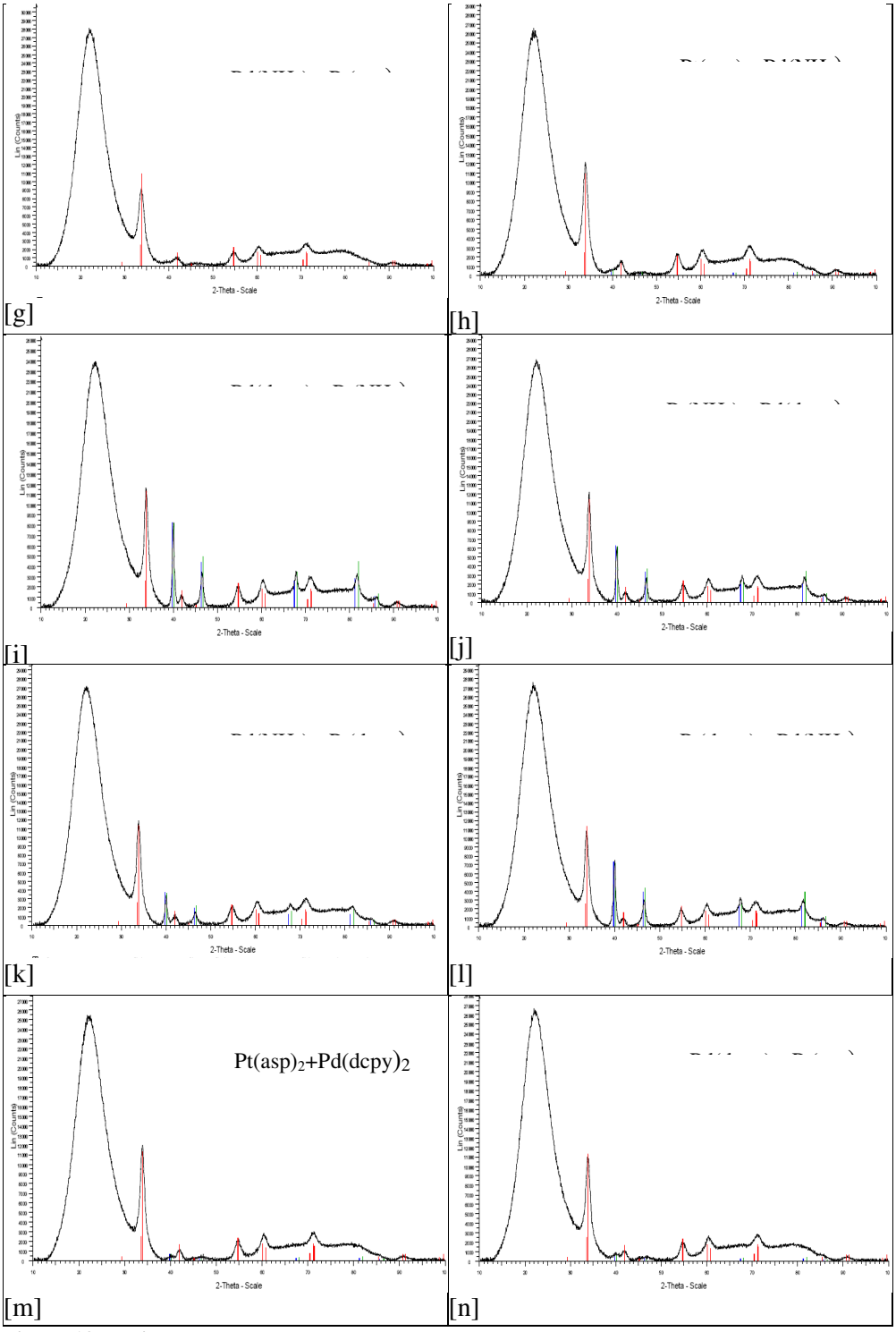

Figure 13 continued.

As with the Al_2O_3 samples measured, tetragonal Pd reflections were not detected for the $(NH_3)_4$ samples. However, in this instance the presence of cubic Pt can be seen indicating that the Pt particles in these samples are larger and less well

dispersed. This agrees with the TEM data presented in Figure 4 showing the average particle sizes of these samples to be 2.0. 1.9 and 1.6 nm respectively when supported on Al_2O_3 and 2.6, 3.9 and 2.3 nm when supported on SiO_2.

All other samples show the presence of cubic Pt, tetragonal PdO and cubic Pd indicating once more the alteration in oxidative behaviour of Pd when Pt is introduced to the system as observed by Morlang et al[2].

4.5 EXAFS

4.5.1 Calcined SiO_2 supported in H_2

The spectra in Figure 15 (a-n) show the experimental data (black lines) and fit (red lines) {left} and corresponding Fourier Transform {right} of bimetallic catalysts on a SiO_2 support and calcined and reduced under H_2. The data was obtained at the Pt L_3 edge and the data and Fourier Transforms are k^2 weighted. Figure 16 also shows the EXAFS data collected of the bimetallic samples on SiO_2 after they had been calcined and purged in H_2. This data is measured at the Pd K edge. All the samples were measured at room temperature. The calculated structural parameters obtained by analysis of this data are presented in Tables 8 and 9.

Figure 14a Pt L_3

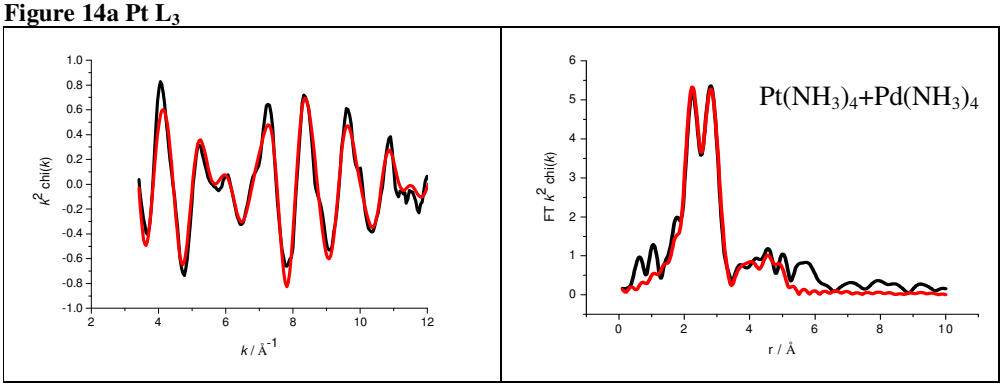

Figure 15a Pd K

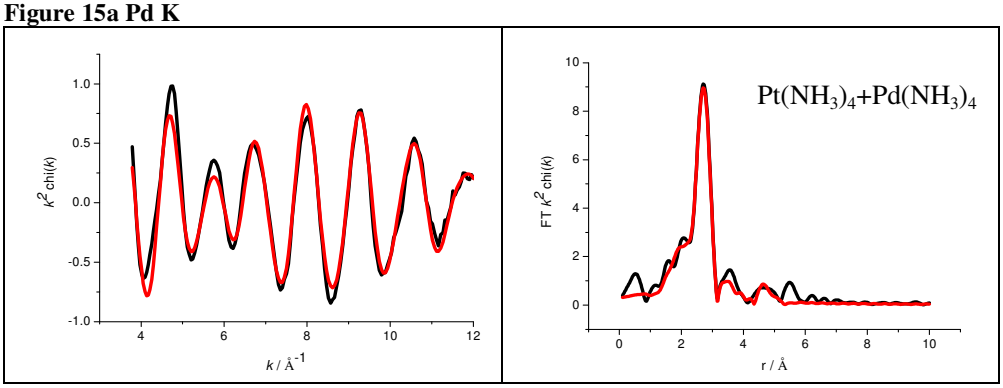

Table 8a Pt L_3

Sample	Shell	N	R / Å	$2\sigma^2$/Å^2	E_f / eV	R_{exafs} / %
Pt(NH$_3$)$_4$+Pd(NH$_3$)$_4$	Pt-Pt	4.0 ± 0.3	2.75 ± 0.01	0.011 ± 0.001	-10.5 ± 0.6	25.92
	Pt-Pd	3.4 ± 0.2	2.75 ± 0.01	0.012 ± 0.001		
	Pt-Pt	3.2 ± 1.2	3.81 ± 0.03	0.012 ± 0.006		
	Pt-Pd	1.3 ± 0.7	4.10 ± 0.04	0.008 ± 0.007		
	Pt-Pt	2.9 ± 0.8	4.72 ± 0.02	0.010 ± 0.003		

Table 9a Pd K

Sample	Shell	N	R / Å	$2\sigma^2$/Å^2	E_f / eV	R_{exafs} / %
Pt(NH$_3$)$_4$+Pd(NH$_3$)$_4$	Pd-Pd	4.3 ± 0.2	2.75 ± 0.01	0.011 ± 0.001	1.4 ± 0.6	20.94
	Pd-Pt	2.3 ± 0.3	2.75 ± 0.01	0.010 ± 0.002		
	Pd-Pd	1.7 ± 0.7	4.79 ± 0.02	0.011 ± 0.005		

Figure 15b Pt L_3

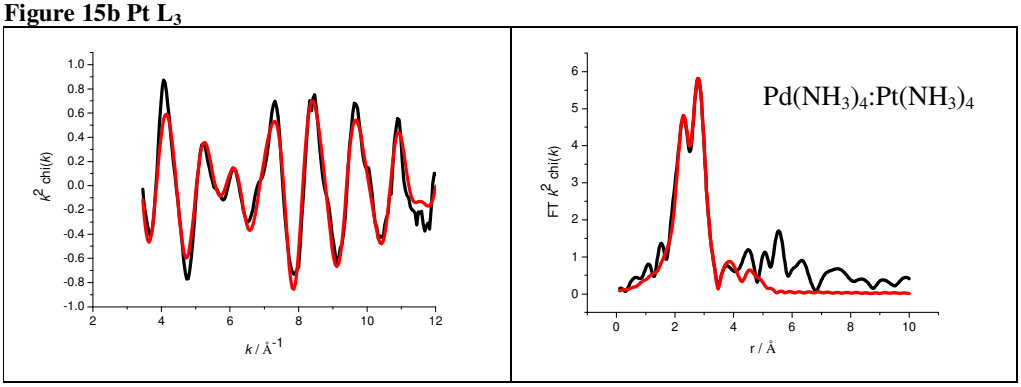

Figure 16b Pd K

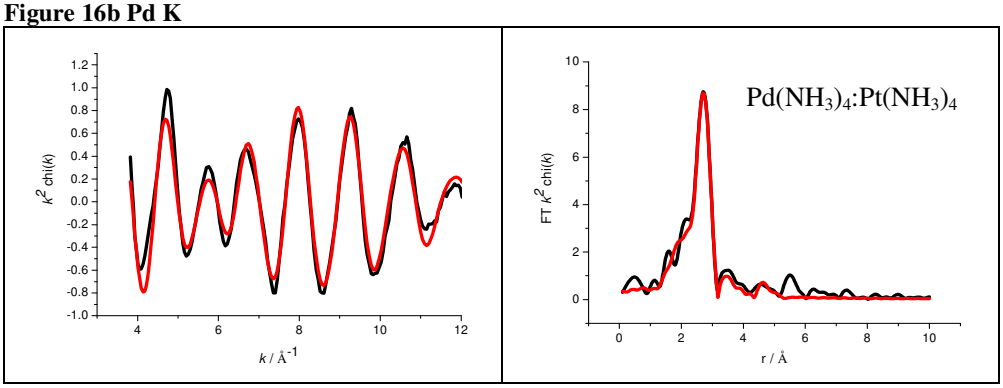

Table 8b Pt L_3

$Pd(NH_3)_4$:$Pt(NH_3)_4$	Pt-Pt	3.3 ± 0.4	2.74 ± 0.01	0.014 ± 0.002	-12.3 ± 0.7	26.46
	Pt-Pd	2.7 ± 0.3	2.75 ± 0.01	0.012 ± 0.001		
	Pt-Pd	1.4 ± 0.6	3.84 ± 0.02	0.013 ± 0.006		
	Pt-Pt	3.7 ± 1.1	4.70 ± 0.02	0.011 ± 0.003		

Table 9b Pd K

$Pd(NH_3)_4$:$Pt(NH_3)_4$	Pd-Pd	4.1 ± 2.1	2.75 ± 0.01	0.011 ± 0.001	-0.23 ± 0.6	24.70
	Pd-Pt	2.6 ± 0.3	2.75 ± 0.01	0.010 ± 0.002		
	Pd-Pd	1.4 ± 0.8	4.78 ± 0.03	0.011 ± 0.006		

Figure 15c Pt L_3

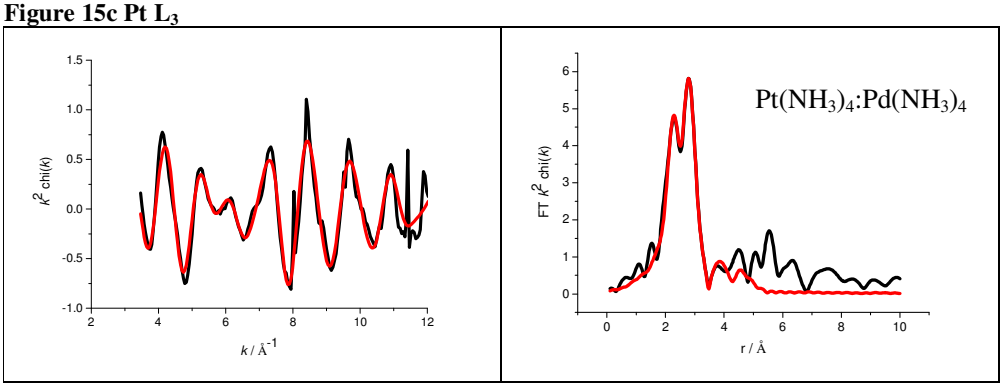

Figure 16c Pd K

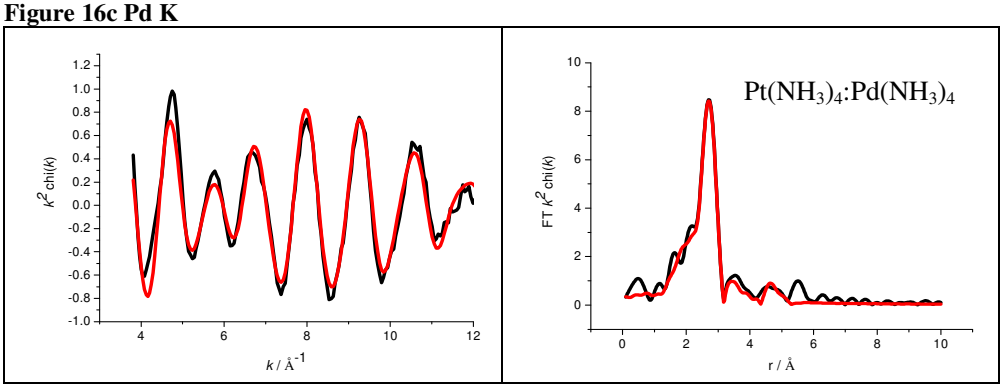

Table 8c Pt L_3

Pt(NH$_3$)$_4$:Pd(NH$_3$)$_4$	Pt-Pt	3.6 ± 0.6	2.72 ± 0.01	0.013 ± 0.003	-10.6 ± 1.3	35.92
	Pt-Pd	2.8 ± 0.4	2.75 ± 0.01	0.012 ± 0.001		
	Pt-Pt	2.0 ± 1.1	3.45 ± 0.04	0.016 ± 0.011		
	Pt-Pt	1.8 ± 1.3	3.87 ± 0.04	0.016 ± 0.010		
	Pt-Pd	1.0 ± 0.6	4.34 ± 0.05	0.015 ± 0.012		
	Pt-Pt	1.8 ± 1.4	4.70 ± 0.04	0.011 ± 0.008		

Table 9c Pd K

Pt(NH$_3$)$_4$:Pd(NH$_3$)$_4$	Pd-Pd	4.0 ± 0.2	2.75 ± 0.01	0.010 ± 0.001	0.5 ± 0.6	24.21
	Pd-Pt	2.6 ± 0.3	2.74 ± 0.01	0.009 ± 0.001		
	Pd-Pd	1.8 ± 0.8	4.78 ± 0.02	0.011 ± 0.004		

Figure 15d Pt L_3

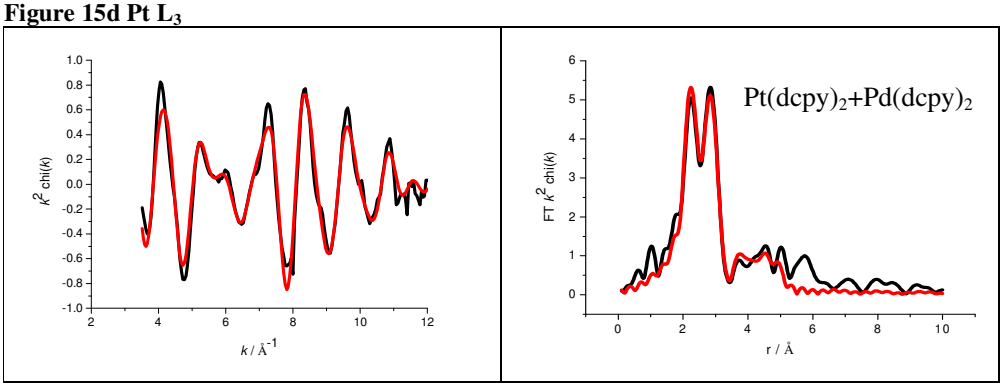

Figure 16d Pd K

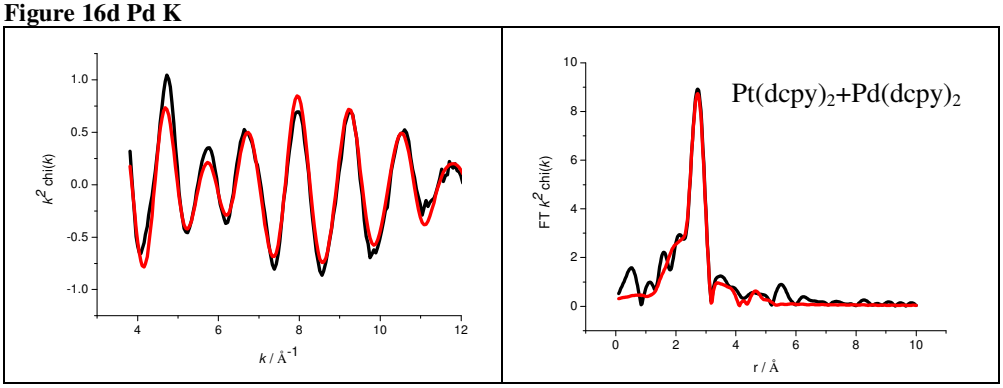

Table 8d Pt L_3

$Pt(dcpy)_2+Pd(dcpy)_2$	Pt-Pt	4.4 ± 0.3	2.74 ± 0.01	0.012 ± 0.01	-12.2 ±	25.57
	Pt-Pd	3.1 ± 0.2	2.74 ± 0.01	0.011 ± 0.001	0.7	
	Pd-Pt	3.2 ± 1.2	3.82 ± 0.03	0.008 ± 0.004		
	Pt-Pt	3.0 ± 0.9	4.72 ± 0.02	0.010 ± 0.005		
	Pt-Pd	1.5 ± 0.8	4.07 ± 0.04	0.005 ± 0.005		

Table 9d Pd K

$Pt(dcpy)_2+Pd(dcpy)_2$	Pd-Pd	4.3 ± 0.2	2.76 ± 0.01	0.011 ± 0.001	1.0 ±	24.58
	Pd-Pt	2.6 ± 0.3	2.74 ± 0.01	0.010 ± 0.002	0.7	
	Pd-Pd	0.7 ± 0.5	3.98 ± 0.04	0.017 ± 0.014		
	Pd-Pd	1.3 ± 0.8	4.80 ± 0.03	0.012 ± 0.007		

Figure 15e Pt L_3

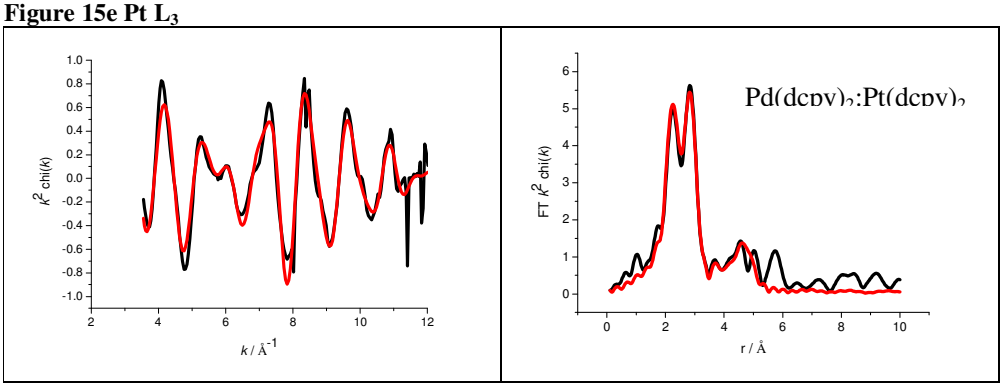

Figure 16e Pd K

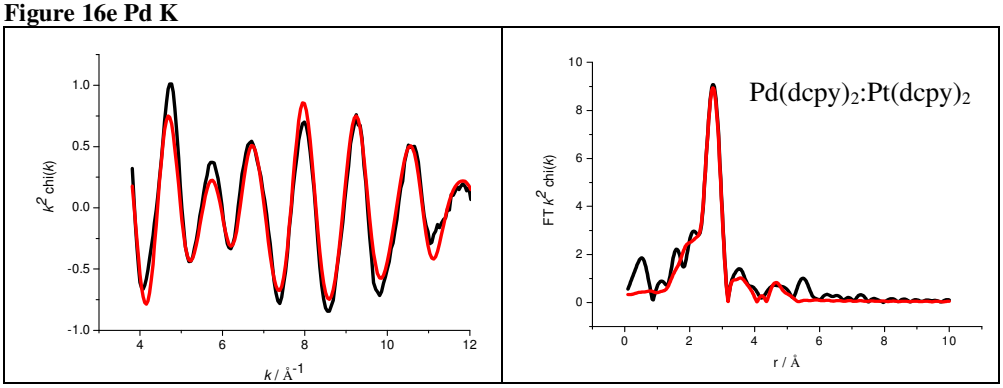

Table 8e Pt L_3

$Pd(dcpy)_2$:$Pt(dcpy)_2$	Pt-Pt	4.4 ± 0,4	2.73 ± 0.01	0.011 ± 0.001	-11.2 ± 0.9	30.04
	Pt-Pd	2.8 ± 0.2	2.74 ± 0.01	0.011 ± 0.001		
	Pt-Pt	1.2 ± 0.6	3.83 ± 0.03	0.011 ± 0.006		
	Pt-Pt	1.7 ± 0.9	4.28 ± 0.03	0.011 ± 0.005		
	Pt-Pt	3.9 ± 1.2	4.71 ± 0.02	0.010 ± 0.003		

Table 9e Pd K

$Pd(dcpy)_2$:$Pt(dcpy)_2$	Pd-Pd	4.4 ± 0.2	2.76 ± 0.01	0.011 ± 0.001	-0.8 ± 0.7	25.32
	Pd-Pt	2.5 ± 0.3	2.75 ± 0.01	0.010 ± 0.002		
	Pd-Pd	0.6 ± 0.5	3.93 ± 0.04	0.016 ± 0.014		
	Pd-Pd	1.8 ± 0.8	4.80 ± 0.02	0.012 ± 0.005		

Figure 15f Pt L_3

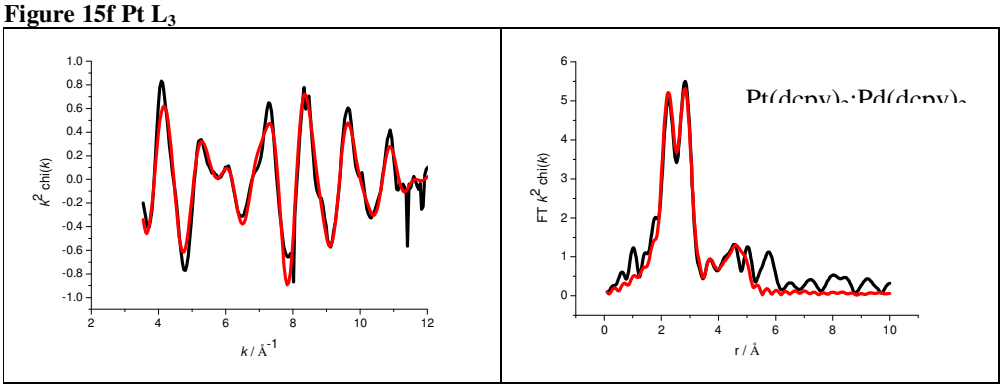

Figure 16f Pd K

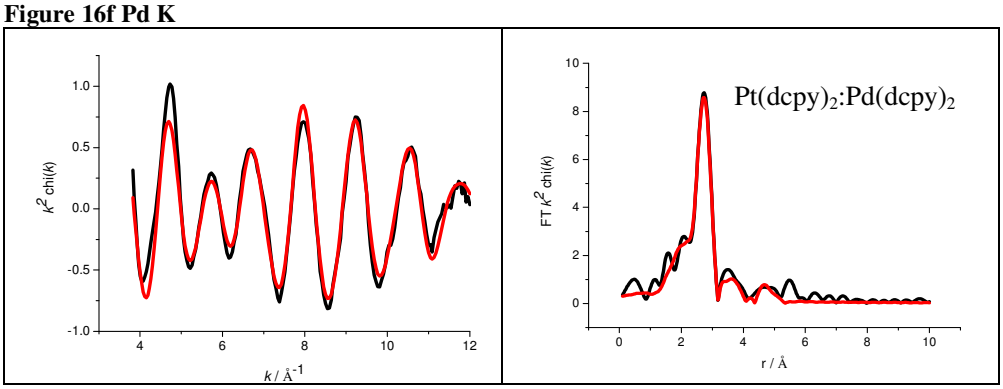

Table 8f Pt L_3

$Pt(dcpy)_2$:$Pd(dcpy)_2$	Pt-Pt	4.3 ± 0.3	2.73 ± 0.01	0.011 ± 0.001	-11.4 ±	28.24
	Pt-Pd	3.9 ± 0.2	2.74 ± 0.01	0.011 ± 0.001	0.8	
	Pt-Pt	1.4 ± 0.6	3.83 ± 0.02	0.010 ± 0.004		
	Pt-Pt	1.4 ± 0.8	4.28 ± 0.03	0.007 ± 0.004		
	Pt-Pt	3.7 ± 1.0	4.71 ± 0.02	0.010 ± 0.003		

Table 9f Pd K

$Pt(dcpy)_2$:$Pd(dcpy)_2$	Pd-Pd	4.2 ± 0.2	2.76 ± 0.01	0.011 ± 0.001	1.3 ±	22.55
	Pd-Pt	2.4 ± 0.3	2.75 ± 0.01	0.010 ± 0.001	0.7	
	Pd-Pd	1.2 ± 0.6	3.93 ± 0.03	0.020 ± 0.009		
	Pd-Pd	2.0 ± 0.8	4.80 ± 0.02	0.013 ± 0.004		

Figure 15g Pt L_3

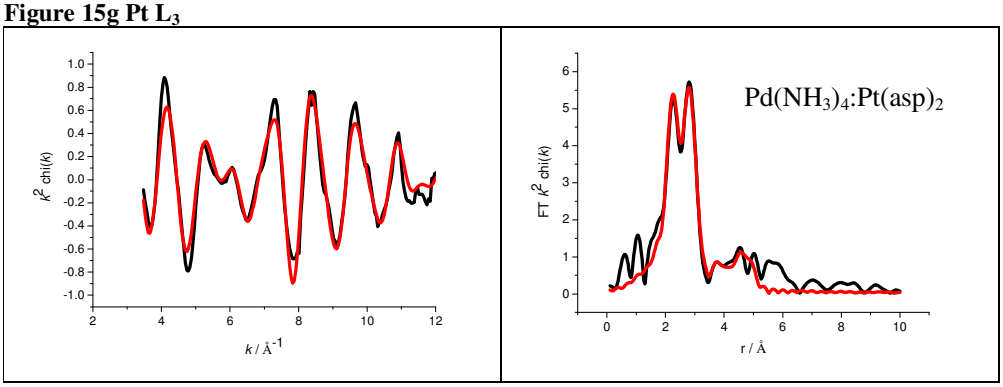

Figure 16g Pd K

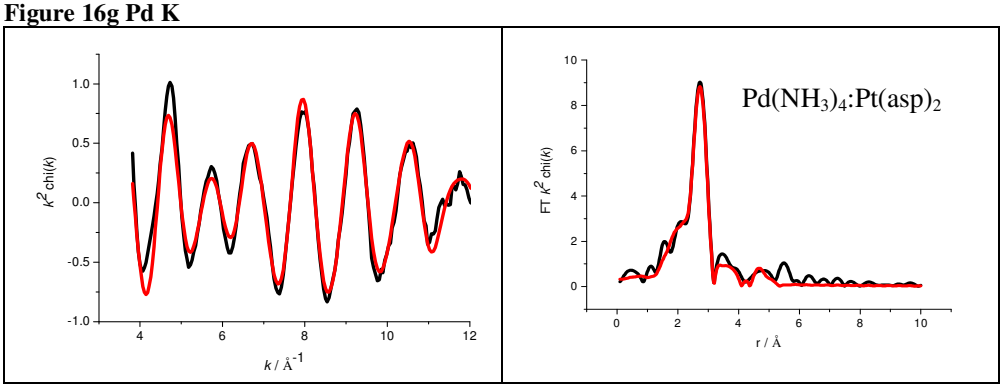

Table 8g Pt L_3

Pd(NH$_3$)$_4$:Pt(asp)$_2$	Pt-Pt	4.1 ± 0.3	2.74 ± 0.01	0.011 ± 0.001	-11.3 ± 0.7	26.92
	Pt-Pd	3.2 ± 0.2	2.74 ± 0.01	0.011 ± 0.001		
	Pt-Pt	1.6 ± 0.6	3.84 ± 0.02	0.011 ± 0.004		
	Pt-Pt	1.0 ± 0.7	4.28 ± 0.04	0.008 ± 0.006		
	Pt-Pt	3.1 ± 1.0	4.71 ± 0.02	0.009 ± 0.003		

Table 9g Pd K

Pd(NH$_3$)$_4$:Pt(asp)$_2$	Pd-Pd	4.2 ± 0.2	2.76 ±0.01	0.011 ± 0.001	-1.1 ± 0.6	21.82
	Pd-Pt	2.6 ± 0.3	2.75 ± 0.01	0.009 ± 0.001		
	Pd-Pd	0.7 ± 0.4	3.96 ± 0.03	0.016 ± 0.011		
	Pd-Pd	1.7 ± 0.8	4.81 ± 0.02	0.011 ± 0.004		

Figure 15h Pt L_3

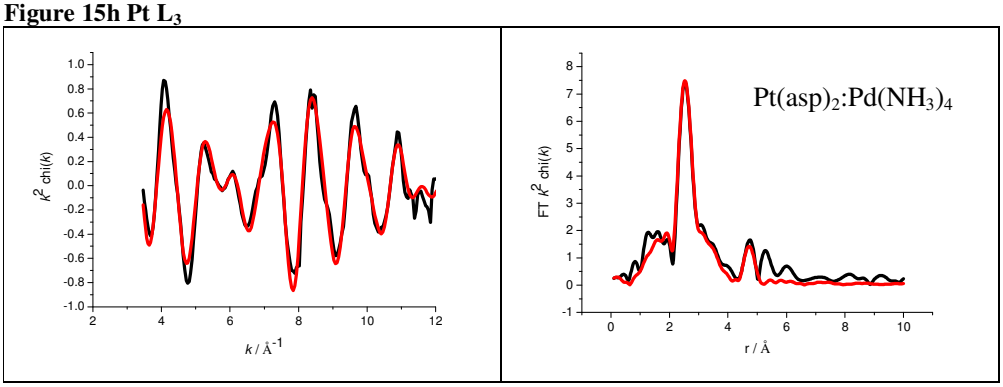

Figure 16h Pd K

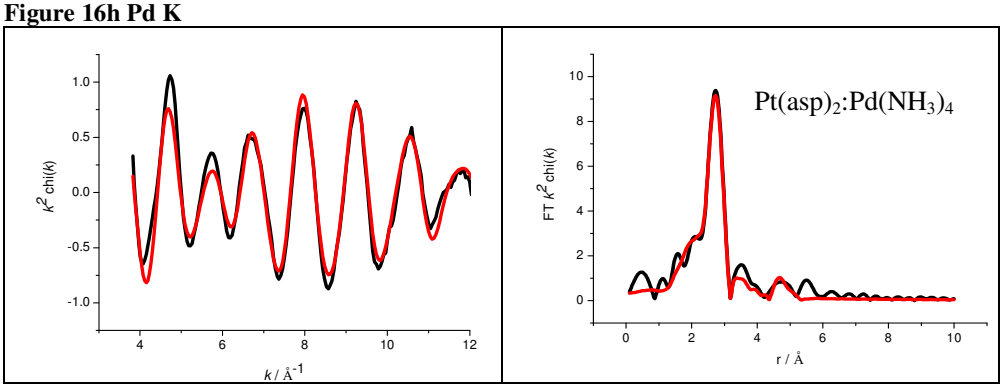

Table 8h Pt L_3

Pt(asp)$_2$:Pd(NH$_3$)$_4$	Pt-Pt	4.0 ± 0.3	2.74 ± 0.01	0.011 ± 0.001	-10.7 ± 0.6	27.37
	Pt-Pd	3.3 ± 0.2	2.74 ± 0.01	0.011 ± 0.001		
	Pt-Pt	1.4 ± 0.5	3.84 ± 0.02	0.012 ± 0.004		
	Pt-Pt	3.6 ± 0.9	4.71 ± 0.01	0.011 ± 0.002		

Table 9h Pd K

Pt(asp)$_2$:Pd(NH$_3$)$_4$	Pd-Pd	4.3 ± 0.2	2.76 ± 0.01	0.011 ± 0.001	0.3 ± 0.6	23.12
	Pd-Pt	2.7 ± 0.3	2.75 ± 0.01	0.010 ± 0.001		
	Pd-Pd	2.0 ± 0.8	4.80 ± 0.02	0.011 ± 0.004		

Figure 15i Pt L_3

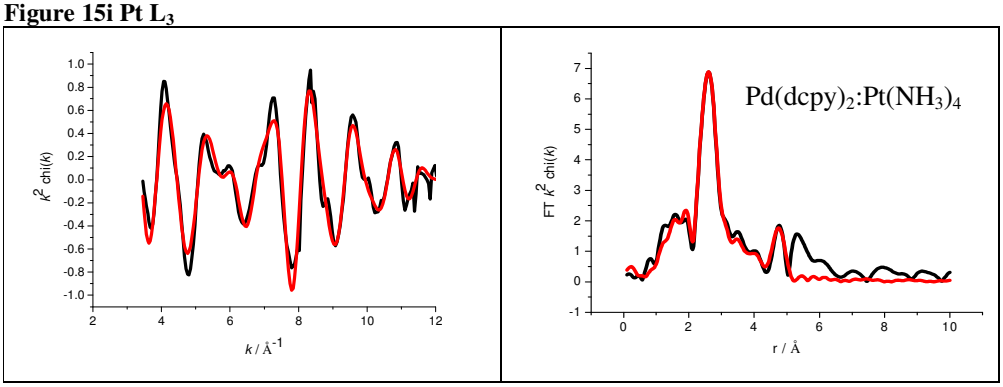

Figure 16i Pd K

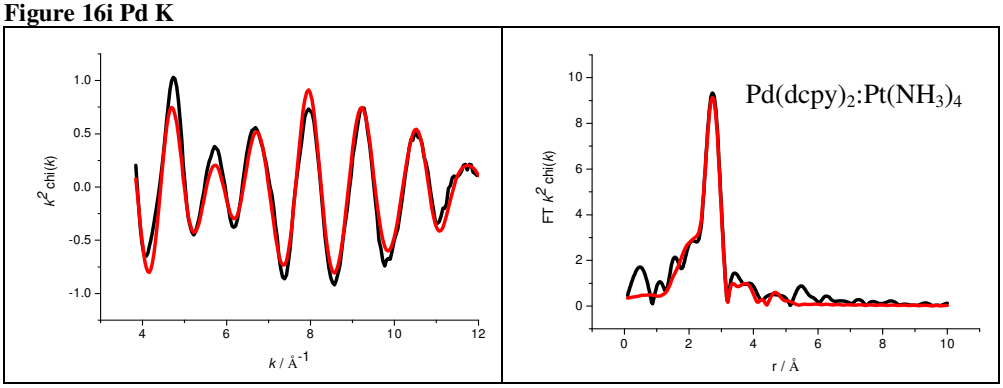

Table 8i Pt L_3

$Pd(dcpy)_2:Pt(NH_3)_4$	Pt-Pt	5.3 ± 0.3	2.74 ± 0.01	0.011 ± 0.001	-10.9 ± 0.6	29.42
	Pt-Pd	2.9 ± 0.2	2.74 ± 0.01	0.012 ± 0.001		
	Pt-Pt	2.9 ± 0.8	3.86 ± 0.02	0.014 ± 0.003		
	Pt-Pt	3.9 ± 1.0	4.73 ± 0.01	0.010 ± 0.003		
	Pt-Pd	0.9 ± 0.6	4.42 ± 0.04	0.008 ±0.005		

Table 9i Pd K

$Pd(dcpy)_2:Pt(NH_3)_4$	Pd-Pd	4.3 ± 0.2	2.76 ± 0.01	0.011 ± 0.001	1.0 ± 0.7	23.96
	Pd-Pt	2.9 ± 0.4	2.74 ± 0.01	0.010 ± 0.001		
	Pd-Pd	0.9 ± 0.5	3.96 ± 0.03	0.014 ± 0.007		
	Pd-Pd	1.2 ± 0.8	4.82 ± 0.04	0.011 ± 0.007		

Figure 15j Pt L_3

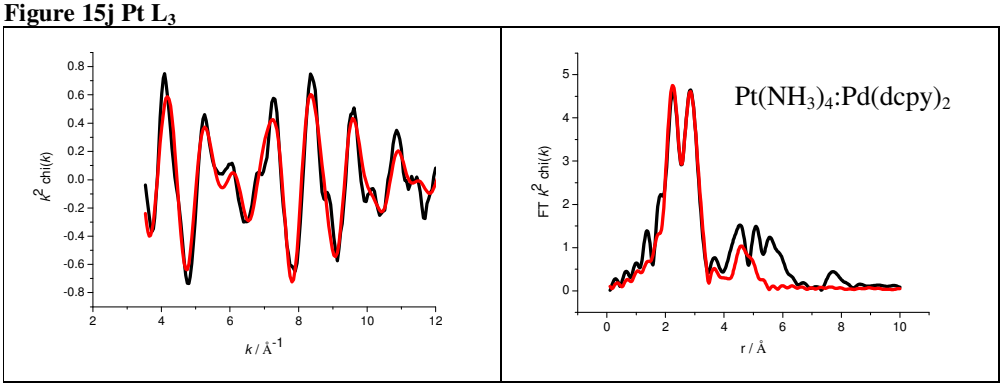

Figure 16j Pd K

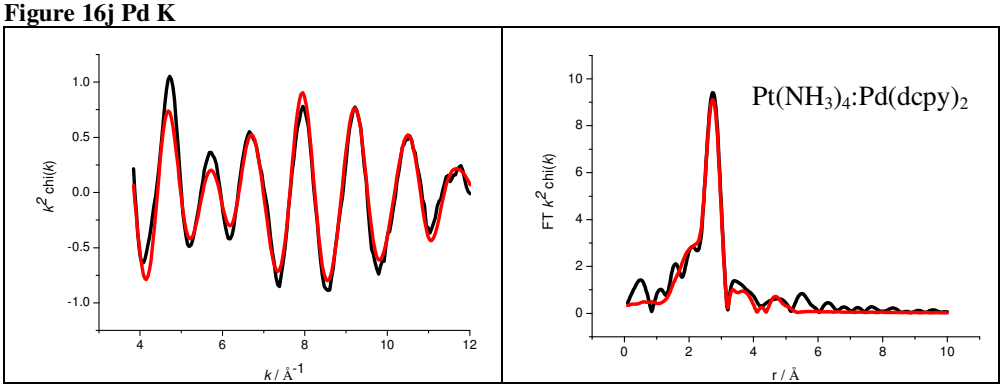

Table 8j Pt L_3

Pt(NH$_3$)$_4$:Pd(dcpy)$_2$	Pt-Pt	3.8 ± 0.4	2.75 ± 0.01	0.012 ± 0.001	-10.1 ± 0.9	36.88
	Pt-Pd	2.8 ± 0.2	2.75 ± 0.01	0.011 ± 0.001		
	Pt-Pt	1.5 ± 0.8	3.44 ± 0.03	0.018 ± 0.007		
	Pt-Pt	4.0 ± 1.2	4.71 ± 0.02	0.014 ± 0.003		

Table 9j Pd K

Pt(NH$_3$)$_4$:Pd(dcpy)$_2$	Pd-Pd	4.2 ± 0.2	2.77 ± 0.01	0.011 ± 0.001	1.1 ± 0.7	23.12
	Pd-Pt	2.8 ± 0.4	2.75 ± 0.01	0.010 ± 0.001		
	Pd-Pd	0.7 ± 0.4	3.96 ± 0.03	0.015 ± 0.010		
	Pd-Pd	1.5 ± 0.8	4.81 ± 0.03	0.011 ± 0.005		

Figure 15k Pt L_3

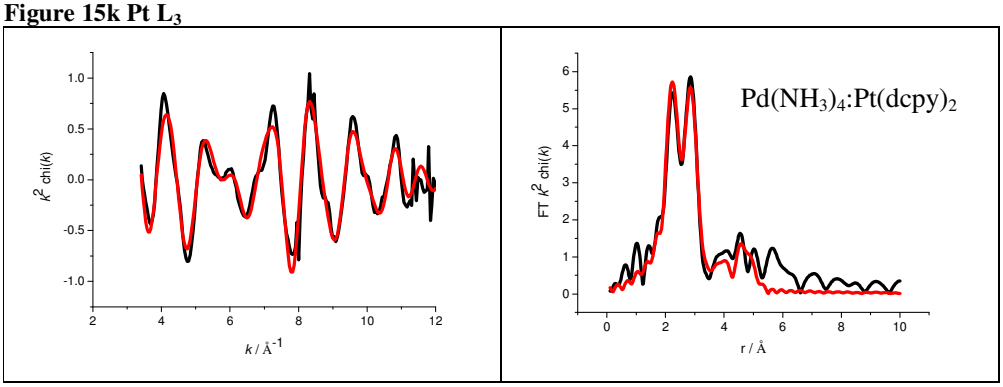

Figure 16k Pd K

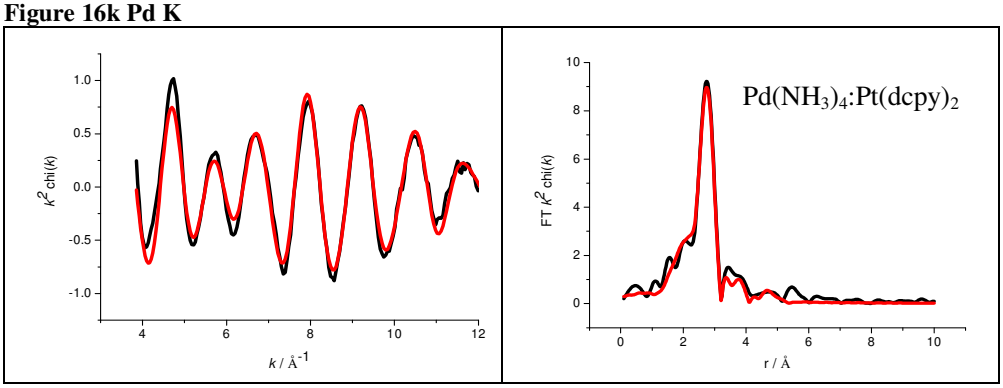

Table 8k Pt L_3

Pd(NH$_3$)$_4$:Pt(dcpy)$_2$	Pt-Pt	3.9 ± 0.4	2.75 ± 0.01	0.011 ± 0.001	-11.2 ± 0.8	34.12
	Pt-Pd	3.1 ± 0.3	2.75 ± 0.01	0.011 ± 0.001		
	Pt-Pt	1.9 ± 0.8	3.87 ± 0.02	0.012 ± 0.005		
	Pt-Pt	4.1 ± 1.4	4.72 ± 0.02	0.011 ± 0.004		

Table 9k Pd K

Pd(NH$_3$)$_4$:Pt(dcpy)$_2$	Pd-Pd	4.3 ± 0.2	2.77 ± 0.01	0.011 ± 0.001	-0.3 ± 0.7	20.23
	Pd-Pt	2.4 ± 0.3	2.75 ± 0.01	0.008 ± 0.001		
	Pd-Pd	1.8 ± 0.6	3.97 ± 0.02	0.018 ± 0.006		
	Pd-Pt	1.5 ± 0.8	4.02 ± 0.03	0.016 ± 0.009		
	Pd-Pd	1.3 ± 0.7	4.82 ± 0.03	0.013 ± 0.007		

Figure 15l Pt L_3

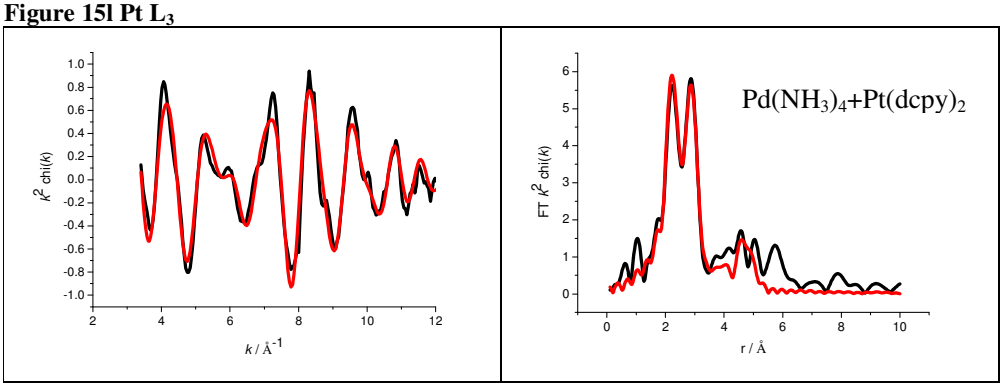

Figure 16l Pd K

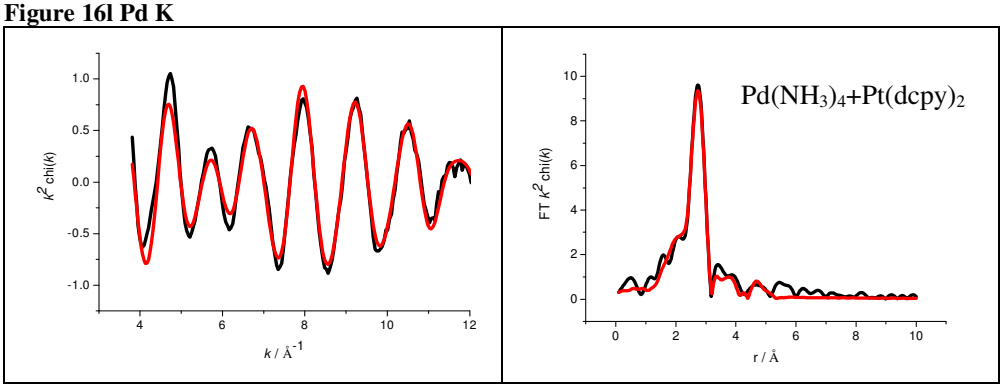

Table 8l Pt L_3

Pd(NH$_3$)$_4$+Pt(dcpy)$_2$	Pt-Pt	5.3 ± 0.3	2.75 ± 0.01	0.011 ± 0.001	-11.2 ± 0.6	29.73
	Pt-Pd	2.9 ± 0.2	2.75 ± 0.01	0.011 ± 0.001		
	Pt-Pt	1.9 ± 0.6	3.86 ± 0.02	0.014 ± 0.004		
	Pt-Pt	4.4 ± 1.1	4.73 ± 0.01	0.010 ± 0.002		

Table 9l Pd K

Pd(NH$_3$)$_4$+Pt(dcpy)$_2$	Pd-Pd	4.3 ± 0.2	2.77 ± 0.01	0.011 ± 0.001	-0.6 ± 0.6	22.11
	Pd-Pt	2.7 ± 0.3	2.75 ± 0.01	0.010 ± 0.001		
	Pd-Pd	0.9 ± 0.4	3.97 ± 0.02	0.014 ± 0.007		
	Pd-Pd	1.9 ± 0.8	4.82 ± 0.03	0.010 ± 0.004		

Figure 15m Pt L_3

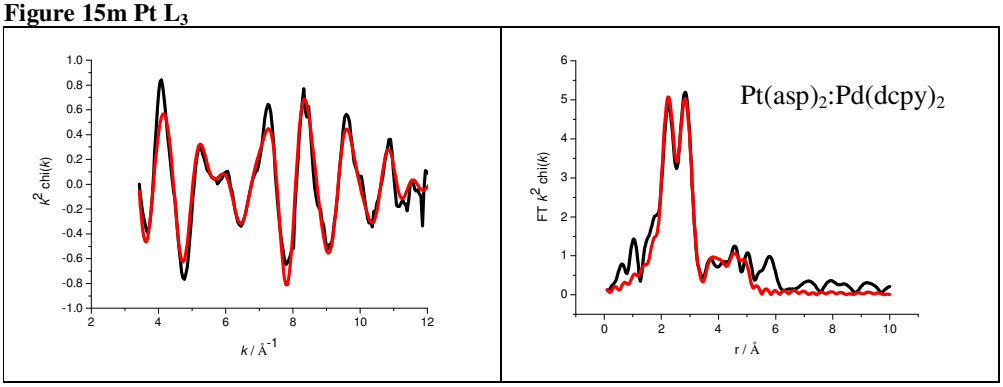

Figure 16m Pd K

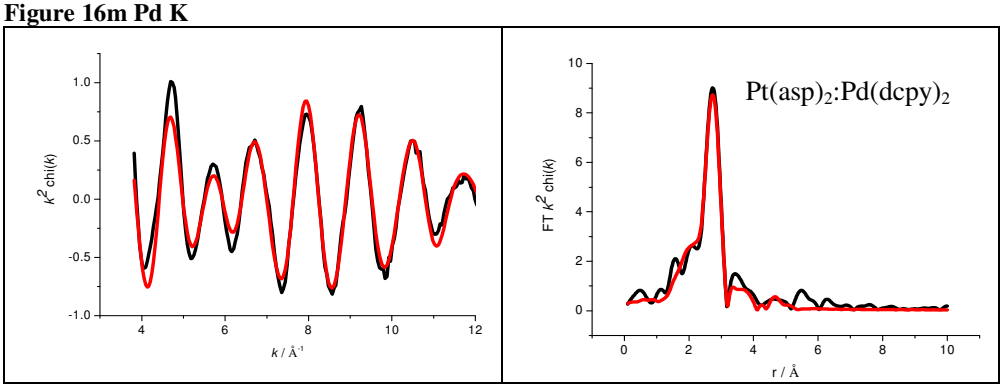

Table 8m Pt L_3

$Pt(asp)_2$:$Pd(dcpy)_2$	Pt-Pt	4.3 ± 0.3	2.75 ± 0.01	0.012 ± 0.001	-10.4 ± 0.7	27.65
	Pt-Pd	2.9 ± 0.2	2,75 ± 0.01	0.011 ± 0.001		
	Pt-Pt	2.4 ± 1.1	3.82 ± 0.03	0.006 ± 0.005		
	Pt-Pd	1.2 ± 0.8	4.07 ± 0.05	0.003 ± 0.007		
	Pt-Pd	3.1 ± 1.0	4.72 ± 0.02	0.010 ± 0.003		

Table 9m Pd K

$Pt(asp)_2$:$Pd(dcpy)_2$	Pd-Pd	4.1 ± 0.2	2.77 ± 0.01	0.011 ± 0.001	-0.6 ± 0.6	22.18
	Pd-Pt	2.6 ± 0.3	2.75 ± 0.01	0.010 ± 0.001		
	Pd-Pd	0.7 ± 0.4	3.96 ± 0.03	0.016 ± 0.011		
	Pd-Pd	1.2 ± 0.7	4.81 ± 0.03	0.012 ± 0.007		

Figure 15n Pt L_3

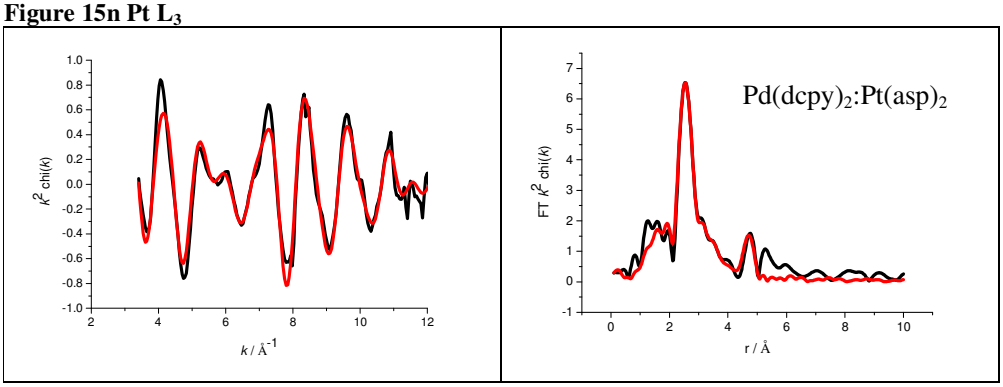

Figure 16n Pd K

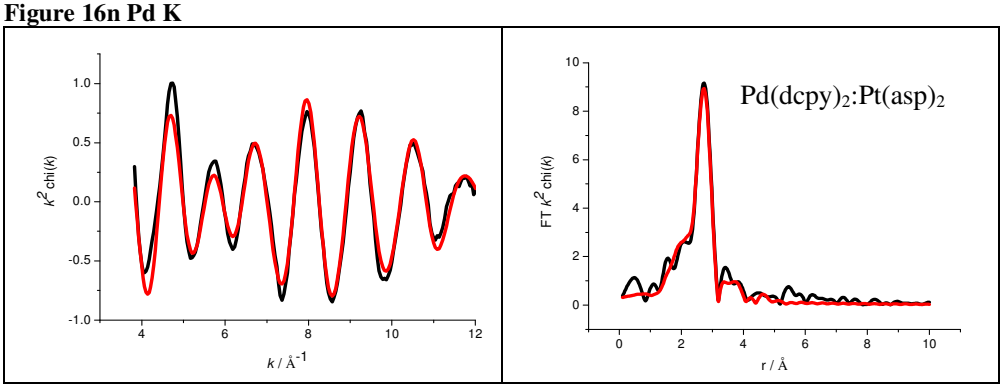

Table 8n Pt L_3

Pd(dcpy)$_2$:Pt(asp)$_2$	Pt-Pt	4.1 ± 0.3	2.75 ± 0.01	0.011 ± 0.001	-10.0 ± 0.6	28.02
	Pt-Pd	3.0 ± 0.2	2.75 ± 0.01	0.011 ± 0.001		
	Pt-Pt	2.5 ± 1.0	3.81 ± 0.03	0.006 ± 0.005		
	Pt-Pd	1.4 ± 0.8	4.07 ± 0.04	0.004 ± 0.006		
	Pt-Pt	3.1 ± 1.0	4.72 ± 0.02	0.010 ± 0.003		

Table 9n Pd K

Pd(dcpy)$_2$:Pt(asp)$_2$	Pd-Pd	4.2 ± 0.2	2.77 ± 0.01	0.011 ± 0.001	0.1 ± 0.6	21.35
	Pd-Pt	2.6 ± 0.3	2.75 ± 0.01	0.009 ± 0.001		
	Pd-Pd	0.8 ± 0.4	3.95 ± 0.03	0.013 ± 0.006		
	Pd-Pd	1.1 ± 0.7	4.82 ± 0.03	0.014 ± 0.010		

As with the Al_2O_3 samples, there is a presence of high Z neighbours in the calcined samples and both Pt and Pd are detected for all samples. The first two maxima are seen as a split peak when Pt is the scattering atom due to phase interference as discussed previously and as with the Pd K edge measurements of Pt/Pd on Al_2O_3, this phenomena is not seen at the Pd K edge for Pt/Pd on SiO_2. Low Z neighbours are not detected as they were in the Al_2O_3 samples which agrees with the analysis performed by Bando et al[23] mentioned previously who

observed no retention of a metal oxide peak in SiO_2 supported catalyst and concluded, therefore, that metal species on SiO_2 can be reduced easily at ambient temperature due to a weak interaction between metal atoms and SiO_2.

The presence of both Pt-Pt and Pt-Pd neighbours at the Pt L_3 edge and Pd-Pd and Pd-Pt neighbours at the Pd K edge indicate that the metal particles are bimetallic in nature as observed by Fujikawa et al[14]. All the samples have a larger coordination number of metals of the same type than they do Pt-Pd or Pd-Pt neighbours which disagrees with the Pt core shell model proposed in studies by Hansen et al[15] that were applicable to the Al_2O_3 supported catalysts. Relatively high N_{Pt-Pt} and N_{Pd-Pd} is consistent with the presence of pure Pt and Pd particles respectively. However, it has already been concluded above that bimetallic particles exist in the samples. Therefore, the model suggested here consists of a mixture of monometallic Pt and Pd particles and Pt/Pd bimetallic particles.

A shell of high *Z* neighbours was detected at around 4.8 Å at both the Pt L_3 and the Pd K edge. The coordination number of these neighbours was found to be less at the Pd edge than at the Pt edge however small numbers could still be detected in contrast to the Al_2O_3 samples at the Pd edge where shells in this region were difficult to fit. This could be due to the presence of monometallic particles in these samples which are not present in the Al_2O_3 supported samples.

5 Discussion

This chapter began with the adsorption of the monometallic precursor complexes outlined in Chapter Two onto Al_2O_3 and SiO_2 in Pt/Pd pairs. The pairings were chosen to vary the size and the charge of the ligands contained within the sample to monitor the effects, if any. It was seen by ICP-OAS that there was no conclusive variation in the metal uptake of samples by changing the adsorption method or order they are deposited onto the support. Thermogravimetric analysis showed that the temperature at which the metal loses its complexed ligands varies according to ligand size with the easiest ligand to lose being the

tetrammine, which is small and inorganic. However, the order in which the ligands are adsorbed onto the support has no impact on this temperature. It was noted that the SiO_2 samples had to be heated to a slightly higher temperature than the Al_2O_3 samples in order to see any weight loss.

On average, the particle sizes of the metals on Al_2O_3 are larger than those on SiO_2. TEM of the Al_2O_3 samples indicated that a different average particle size is observed, depending on the order in which the precursors were adsorbed. Generally, the average particle size was found to correlate with the particle sizes detected in the monometallic sample (Chapter Three) that was adsorbed onto the support first.

XRD of the calcined samples, as with Chapter Three, didn't detect any PtO_2 in the Pt samples indicating that any metal oxide phase is amorphous. The results showed that the introduction of Pt to a Pd catalyst changes the oxidative behaviour of Pd, which is present in both an oxidised (PdO) and metallic (Pd) form in the SiO_2 supported samples after calcining in contrast to the Pd only catalysts, which contains only tetragonal PdO. This was supported by the ease of reduction of the calcined samples when they were reduced and measured using EXAFS for SiO_2.

The EXAFS results were consistent with the results of the monometallic sample analysis, i.e. when the dried catalyst is heated, ligand is lost and metal particles start to form. During heating the EXAFS showed that the low Z neighbours present were not due to oxide formation but the remains of the ligand. The coordination number of low *Z* neighbours falls as the sample is exposed to higher temperatures representing the loss of ligands and the distance at which these neighbours are found increases implying formation of metal oxide particles. After reduction in H_2, the number of low *Z* neighbours decreases to a very small amount in Al_2O_3 supported catalysts and are impossible to detect in SiO_2 supported catalysts. The coordination number of Pt and Pd neighbours increases when the sample is calcined indicating that further heat treatment leads to metal agglomeration. The figures below illustrate the total M-M coordination numbers at both the Pt L_3 and Pd K edge for the calcined samples measured in H_2.

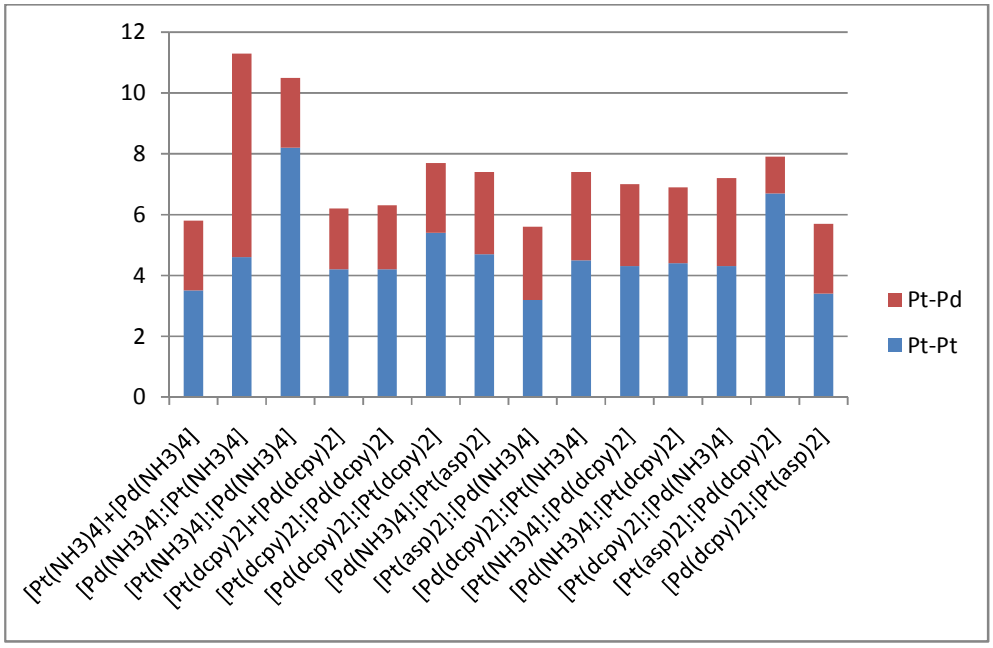

Figure 16 Histogram illustrating the number of Pt-Pt and Pt-Pd neighbours seen at the Pt L_3 edge on Al_2O_3 at ~ 2.7 Å. Samples have been calcined and reduced in H_2.

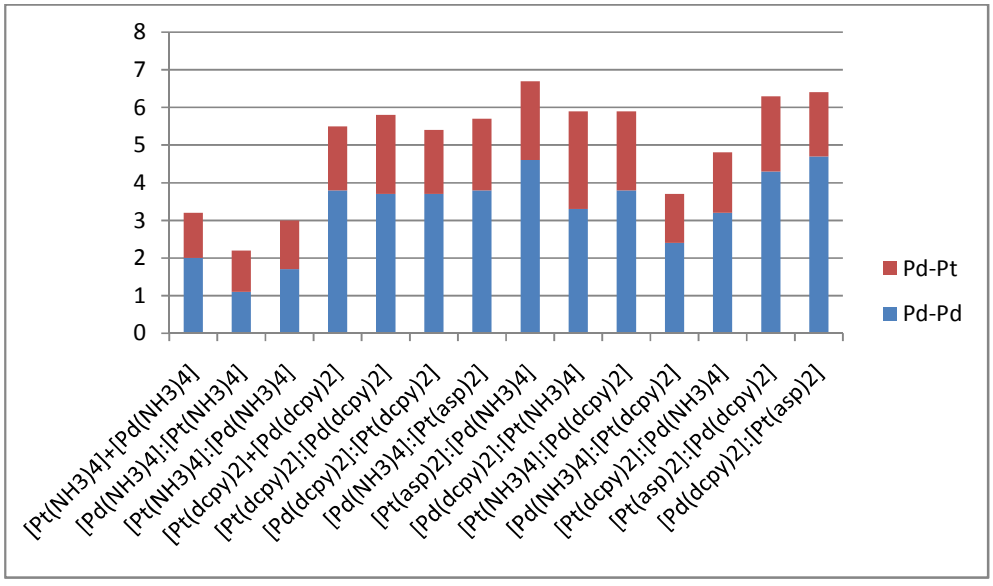

Figure 17 Histogram illustrating the number of Pt-Pt and Pt-Pd neighbours seen at the Pd K edge on Al_2O_3 at ~ 2.7 Å. Samples have been calcined and reduced in H_2.

Both Pt and Pd neighbours were found for the Al_2O_3 samples (Figure 16 and Figure 17) regardless of the scattering atom which indicates that the metal particles are bimetallic containing both Pt and Pd[14]. The data here also shows for all samples, except[$Pd(NH_3)_4$]:[$Pt(NH_3)_4$] that $N_{Pt\text{-}Pt}$ exceeds that $N_{Pd\text{-}Pd}$ which

agrees with a model in which Pd is preferentially on the surface of a PtPd bimetallic particle and leads to the conclusion that these particles are made up of a Pt rich core with an outer shell of Pd[15].

Figure 18 and Figure 19 display the same data captured from the analysis of the SiO_2 bimetallic catalysts. These results differ significantly from the Al_2O_3 results.

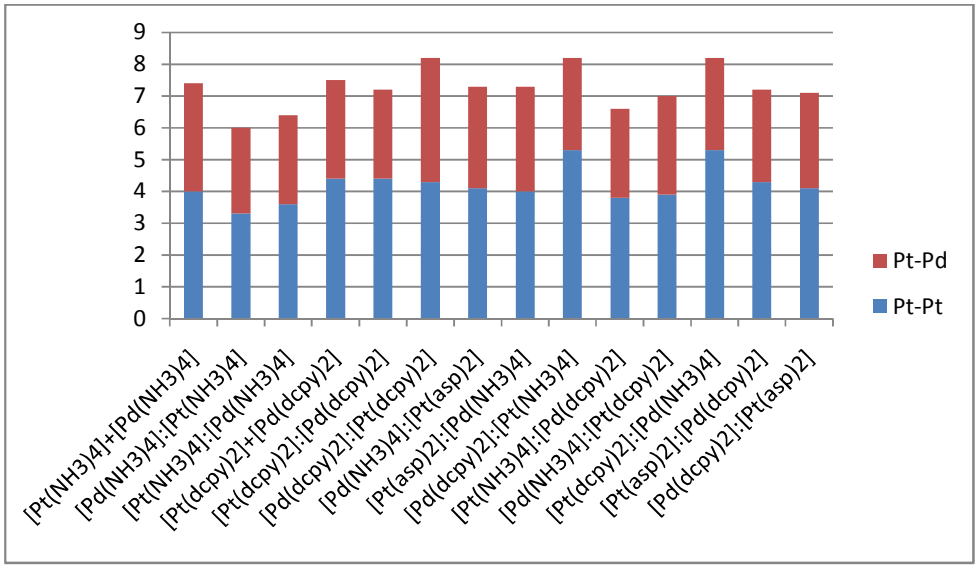

Figure 18 Histogram illustrating the number of Pt-Pt and Pt-Pd neighbours seen at the Pt L_3 edge on SiO_2 at ~ 2.7 Å. Samples have been calcined and reduced in H_2.

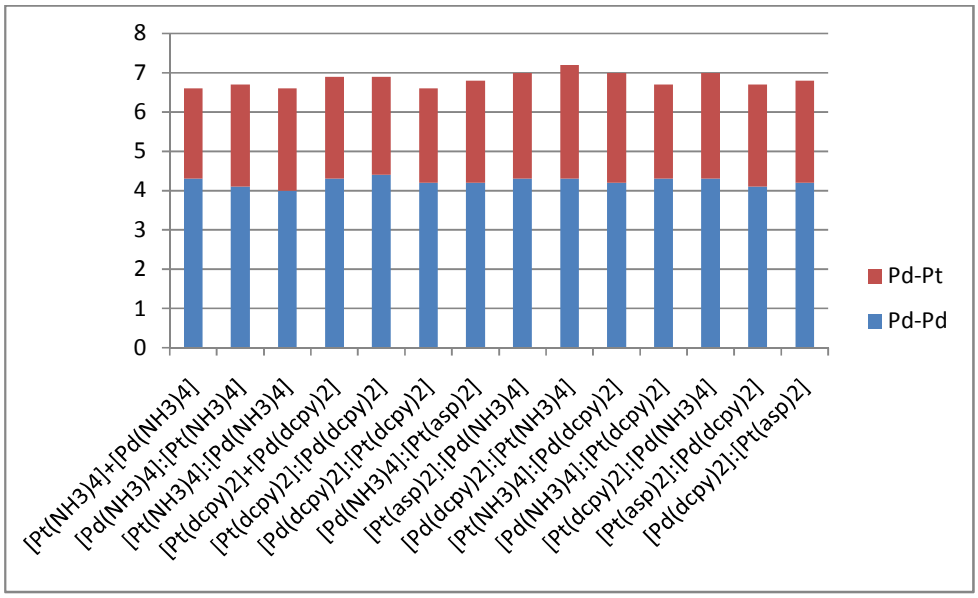

Figure 19 Histogram illustrating the number of Pt-Pt and Pt-Pd neighbours seen at the Pd K edge on SiO_2 at ~ 2.7 Å. Samples have been calcined and reduced in H_2.

The data for the SiO_2 catalysts show again, that the metal particles are bimetallic. However, in contrast to the Al_2O_3 samples, $N_{Pt\text{-}Pt}$ is generally double that of $N_{Pt\text{-}Pd}$ at the Pt L_3 edge and the $N_{Pd\text{-}Pd}$ is generally double that of $N_{Pd\text{-}Pt}$ at the Pd K edge. This disagrees with the Pt rich core shell model and instead is consistent with the presence of pure Pt and Pd particles indicating a mixture of bimetallic and monometallic metal particles in the sample.

6 References

(1) Lu, S. L.; Lonergan, W. W.; Bosco, J. P.; Wang, S. R.; Zhu, Y. X.; Xie, Y. C.; Chen, J. G. *Journal of Catalysis* **2008**, *259*, 260-268.

(2) Morlang, A.; Neuhausen, U.; Klementiev, K. V.; Schutze, F. W.; Miehe, G.; Fuess, H.; Lox, E. S. *Applied Catalysis B-Environmental* **2005**, *60*, 191-199.

(3) Chen, M.; Schmidt, L. D. *Journal of Catalysis* **1979**, *56*, 198-218.

(4) Yoshimura, Y., Toba, M., Matsui, T., Harada, M., Ichihashi, Y., Bando, K.K., Yasuda, H., Ishihara, H., Morita, Y., Kameoka, T. *Applied Catalysis A: General* **2007**, *322*, 152-171.

(5) Cooper, B. H.; Donnis, B. B. L. *Applied Catalysis A-General* **1996**, *137*, 203-223.

(6) Batista, J.; Pintar, A.; Gomilsek, J. P.; Kodre, A.; Bornette, F. *Applied Catalysis A-General* **2001**, *217*, 55-68.

(7) Chen, H. M.; Peng, H. C.; Liu, R. S.; Hu, S. F.; Jang, L. Y. *Chemical Physics Letters* **2006**, *420*, 484-488.

(8) Cho, S. J.; Kang, S. K. In *3rd Asia-Pacific Congress on Catalysis*; Elsevier Science Bv: Dalian, PEOPLES R CHINA, **2003**, p 561-566.

(9) Guczi, L., Beck, A., Horvath, A., Koppany, Z., Stefler, G., Frey, K., Sajo, I., Geszti, O., Bazn, D., Lynch, J. *Journal of Molecular Catalysis A: Chemical* **2003**, *204-205*, 545-552.

(10) Guczi, L.; Bazin, D.; Kovacs, I.; Borko, L.; Schay, Z.; Lynch, J.; Parent, P.; Lafon, C.; Stefler, G.; Koppany, Z.; Sajo, I. *Topics in Catalysis* **2002**, *20*, 129-139.

(11) Nitani, H.; Nakagawa, T.; Daimon, H.; Kurobe, Y.; Ono, T.; Honda, Y.; Koizumi, A.; Seino, S.; Yamamoto, T. A. *Applied Catalysis a-General* **2007**, *326*, 194-201.

(12) Pinxt, H.; Kuster, B. F. M.; Koningsberger, D. C.; Marin, G. B. In *11th International Congress on Catalysis*; Elsevier Science Bv: Baltimore, Maryland, **1996**, p 351-361.

(13) Ueji, M.; Harada, M.; Kimura, Y. *Journal of Colloid and Interface Science* **2008**, *322*, 358-363.

(14) Fujikawa., T., Tsuji, K., Izuguchi, H., Godo, H., Idei, K., Usui, K. *Catalysis Letters* **1999**, *63*, 27-33.

(15) Hansen, P. L.; Molenbroek, A. M.; Ruban, A. V. *Journal of Physical Chemistry B* **1997**, *101*, 1861-1868.

(16) Toshima, N.; Harada, M.; Yamazaki, Y.; Asakura, K. *Journal of Physical Chemistry* **1992**, *96*, 9927-9933.

(17) Toshima, N.; Harada, M.; Yonezawa, T.; Kushihashi, K.; Asakura, K. *Journal of Physical Chemistry* **1991**, *95*, 7448-7453.

(18) Toshima, N.; Yonezawa, T.; Kushihashi, K. *Journal of the Chemical Society-Faraday Transactions* **1993**, *89*, 2537-2543.

(19) Harada, M.; Asakura, K.; Ueki, Y.; Toshima, N. *Journal of Physical Chemistry* **1992**, *96*, 9730-9738.

(20) Mizukoshi, Y.; Fujimoto, T.; Nagata, Y.; Oshima, R.; Maeda, Y. *Journal of Physical Chemistry B* **2000**, *104*, 6028-6032.

(21) Okitsu, K.; Murakami, M.; Tanabe, S.; Matsumoto, H. *Chemistry Letters* **2000**, 1336-1337.

(22) Bando, K. K., Matsui, T., Ichihashi, Y., Sato, K., Tanaka, T., Imamura, M., Matsubayashi, N., Yoshimura, Y. *Phys. Scr* **2005**, *T115*, 828.

(23) Bando, K. K., Kawai, T., Asakura, K., Matsui, T., Le Bihan, L., Yasuda, H., Yoshimura, Y., Oyama, S.T. *Catalysis Today* **2006**, *111*, 199-204.

(24) Antoline, E., Cardellini, F. *Journal of Alloys and Compounds* **2001**, *315*, 118-122.

(25) Dou, D.; Liu, D. J.; Williamson, W. B.; Kharas, K. C.; Robota, H. J. *Applied Catalysis B-Environmental* **2001**, *30*, 11-24.

CHAPTER FIVE: CONCLUSIONS AND FUTURE WORK

This work was concerned with the characterisation of catalysts from precursor complex to active catalyst particle. A range of potential Pt and Pd catalysts were characterised in an attempt to understand the interactions occurring on the support. It is known that the chemical properties of the precious metal precursor used in catalyst preparation play an important role in the interaction of the precious metal with the support as it can influence precious metal particle size and the distribution on the surface[1].

1. Conclusions

The TEM results of the monometallic samples showed the SiO_2 supported catalysts to have an overall smaller average particle size than the Al_2O_3 samples, a feature which was seen again in Chapter Four when the bimetallic samples were analysed. TEM of the bimetallic Al_2O_3 samples implied that the first precursor to come into contact with the support would predict the particle sizes seen.

Neither XRD of the monometallic or bimetallic samples yielded a detection of PtO_2. As oxide neighbours were clearly present in all the EXAFS analysis, it was concluded that this was due to PtO_2 being amorphous in character. The XRD of the bimetallic systems detected the presence of cubic Pd when $[Pd(dcpy)_2]$ was used as a precursor. As this phase is not detectable when the monometallic sample is measured it indicates that, for this sample, the oxidative behaviour of Pd changes when Pt is introduced; a characteristic which has been previously reported[2,3].

The EXAFS data followed a similar model throughout this thesis. EXAFS analysis of the complexes indicated the presence of low *Z* neighbours at a distance which agreed with the predicted 5-membered chelate model. Once the precursor was dried onto the support, the data for the first and second shell

looked very similar indicating the preservation of the chelate structure and potentially some deterioration of the rest of the ligand. Raman spectroscopy supported the retention of the structure. In some samples the low *Z* coordination numbers decreased but this could be attributed to water loss on drying.

Heated samples were measured in Chapter Four showing that the M-O ligand bond remained intact as metal particles began to form. EXAFS of the calcined samples indicated, through an increase in bond distance, that any low *Z* neighbours present could be attributed to an oxide layer. Some catalysts showed M-M bond lengths that were longer than the literature values. However, due to the bond length shortening to the literature value once the O was removed under H_2, it was concluded that this longer bond length could be attributed to the metals bonding via a bridging O atom[4]. Reduced samples showed an increased number of M-M neighbours compared to the corresponding oxidised samples, indicating the loss of O and the growth of metal particles. Chapter Four also showed that the support plays a big part in the nature of the overall catalyst particle with the Al_2O_3 samples exhibiting the characteristics of metal particles consisting of a Pt rich core with a Pd outer shell and the SiO_2 samples consisting of a mixture of monometallic Pt and Pd particles and PtPd bimetallic particles.

The analysis of these samples could have been enhanced by the use of a surface sensitive technique such as X-ray photoelectron spectroscopy (XPS) or Low Energy Ion Scattering (LEIS). XPS can yield information on the elemental composition, oxidation state and dispersion of phases of catalysts[5]. LEIS provides quantitative information on the outer layer composition of multi-component materials[5].

Because a set of binding energies is characteristic for an element, XPS can be used to analyse the composition of samples[6]. Surface composition is the main use for XPS but dispersion can also be measured by examining intensity ratios. One of the drawbacks of this technique, however, is that a shift is sometimes seen in the peaks due to electrically insulating samples charging during measurement. As different parts of the catalyst may acquire slightly different amounts of charge, differential charging leading to broadening of peaks can

cause problems[6]. When a beam of energy impinges on a surface, the ions can scatter elastically from the surface atoms or from atoms deeper in the sample. One of the major advantages of LEIS is that atoms from below the surface can be distinguished from those in the outer layer by broadening of the peaks to lower enegies[5,6]. However, horizontal neighbours in the heavier metals range of the periodic table are not distinguishable from each other.

Part of this thesis involved work with the HOTWAXS detector on Station 9.3 at the Daresbury Laboratory. This allowed the measurement of *in situ* EXAFS and XRD and the aim was to develop an understanding of the changes in the structure during the calcining process. The HOTWAXS detector was designed to meet the requirements of good spatial resolution and parallax free detection in X-ray crystallographic studies[7]. The detector has eight gas microstrip detector modules, situated on a precision mounting plate. The modules have a complete angular range of 60 °. This is due to the modules being positioned so that the electrode design points at the sample. When X-rays enter the gas volume, the electrons formed drift to the plate surface where avalanche multiplication takes place and stimulates a pulse on the MSGC anodes[7]. The anode signals are then transmitted to low noise 16 channel charge sensitive preamplifier cards where the voltage is fed to remote discriminator cards where the signals are processed[7].

In situ HOTWAXS/EXAFS data was collected on Station 9.3 at the SRS, Daresbury Laboratory. Both Pt and Pd samples were measured so the beam energy was set accordingly to either the Pt L_3 or the Pd K absorption edge. The sample was placed in the furnace and was aligned with the kapton window to ensure penetration by the X-rays. The gas lines provide either an air or a hydrogen flow depending on the experiment. The furnace was controlled by a separate unit and was set to ramp to 500 ºC at a rate of 10 ºC per minute and to dwell at this temperature for 2 h before cooling to room temperature at a rate of 20 ºC per minute. This programme was selected to mimic the conditions normally used to calcine samples in this work.

An example of the EXAFS results collected at varying intervals during the calcination step is shown in Figure 1 and Table 1. It should be noted that the

data is slightly noisier here than the other data presented in this work as due to the *in situ* nature of the measurements, it was impossible to repeat scans.

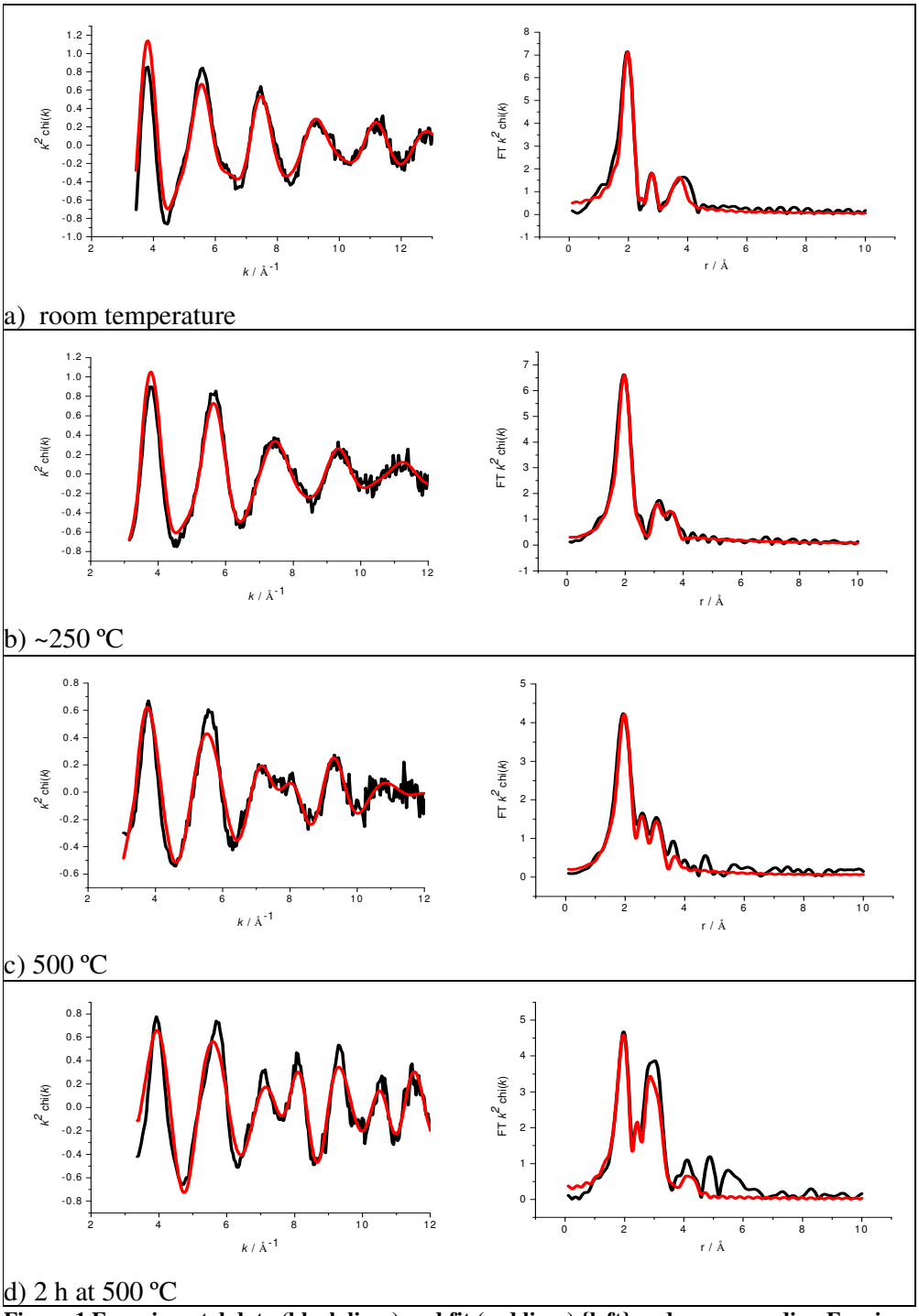

Figure 1 Experimental data (black lines) and fit (red lines) {left} and corresponding Fourier Transform {right} of $[Pt(asp)_2]$ on Al_2O_3 during calcination to 500 ºC (a-c) and after a 2h dwell at this temperature (d). Data obtained at the Pt L_3 edge in air. Data and Fourier Transforms are k^2 weighted.

Table 1 Structural parameters corresponding to spectra presented in Figure 1.

Sample	Shell	N	R / Å	$2\sigma^2/Å^2$	E_f / eV	R_{exafs} / %
$Pt(asp)_2$	Pt-O	2.3 ± 0.1	2.03 ± 0.01	0.003 ± 0.001	-16.1	32.42
before	Pt-O	0.9 ± 0.3	2.82 ± 0.02	0.001 ± 0.005	±	
heating	Pt-O	5.8 ± 1.1	3.73± 0.02	0.021 ± 0.001	0.7	
$Pt(asp)_2$	Pt-O	2.8 ± 0.1	2.02 ± 0.01	0.009 ± 0.001	-16.6	28.79
heated to	Pt-O	1.3 ± 0.3	3.06 ± 0.02	0.009 ± 0.006	±	
~ 200 ºC	Pt-O	2.7 ± 0.7	3.78 ± 0.02	0.017 ± 0.008	0.6	
$Pt(asp)_2$	Pt-O	2.1 ± 0.1	2.03 ± 0.01	0.011 ± 0.001	-17.1	37.44
heated to	Pt-Pt	0.5 ± 0.2	2.39 ± 0.02	0.011 ± 0.004	±	
500 ºC	Pt-Pt	0.7 ± 0.2	2.76 ± 0.02	0.011 ± 0.003	0.8	
	Pt-Pt	0.7 ± 0.3	3.17 ± 0.03	0.014 ± 0.006		
$Pt(asp)_2$	Pt-O	1.9 ± 0.1	2.01 ± 0.01	0.009 ± 0.001	-15.0	36.33
heated to	Pt-Pt	2.3 ± 0.3	2.78 ± 0.01	0.011 ± 0.001	±	
500 ºC for 2h	Pt-Pt	1.4 ±0.6	3.95 ±0.02	0.012 ± 0.005	1.1	

The data collected shows that the sample measured before heating consists of only low *Z* neighbours with distances which correlate with the 5-membered chelate model confirming, as throughout this work, that the ligand has remained intact during adsorption onto the support. When the sample is heated, the 1st shell of O atoms is retained at 2.02 Å, however, the other neighbouring low Z neighbours are detected at slightly longer distances before. This could correlate with the breaking up of the ligand. Once the sample has been heated to 500 ºC, high *Z* Pt neighbours can be detected but only in very small numbers. The importance of the dwell at this high temperature can be seen by looking at the sample subjected to this treatment as here, the number Pt particles has increased and the distances at which they are found is in agreement with the literature values.

The figure below shows the change in Pt-O and Pt-Pt coordination number, taking the first shell of each type of atom in each instance during heating of the sample.

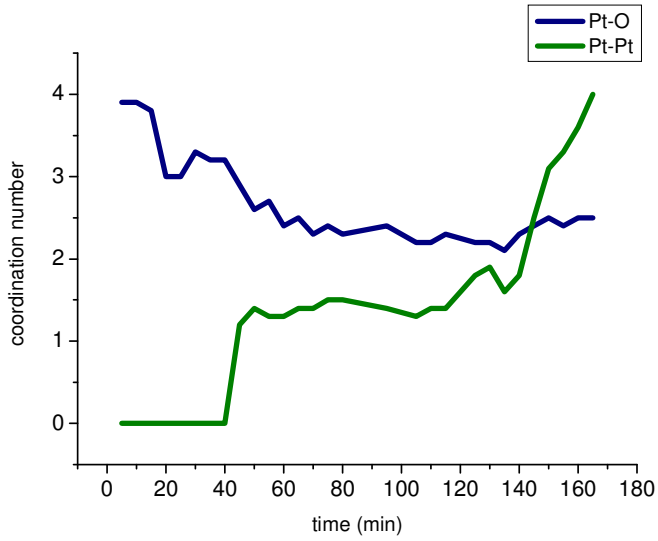

Figure 2 Graph showing the change in Pt-O and Pt-Pt coordination number over time during the calcination step. The catalyst measured was $[Pt(asp)_2]/Al_2O_3$ in air.

This graph shows a decrease in the number of O atoms from around 4 to 2 during heating where the coordination number plateaus probably due to a stable metal oxide layer on the surface of the Pt particle. The number of Pt neighbours detected sits at zero until a sharp rise to around 1.2 is seen after 45 minutes of heating. This number then continues to rise suggesting some agglomeration and it would be expected that it would continue to increase should the sample be held at a high temperature for any longer.

The data above has shown how useful *in situ* characterisation of the catalysts could have been. Unfortunately, there was severe misalignment issues with the XRD part of the HOTWAXS detector when these samples were measured rendering the data impossible to interpret.

The combination of Diffuse Reflectance Infrared Spectroscopy (DRIFTS) with dispersive EXAFS (EDE) and Mass Spectrometry (MS) has been outlined by Newton *et al*[8] to address structure, functionality and reactivity of a sample at high time resolution. These methods would be of real interest to studies such as those described in this work to examine the real time formation of the particles and the evolution of their structures under operating conditions. This

combination of techniques has been used recently to probe how NO(g) reacts with Al_2O_3 supported, metallic Rh nanoparticles[9] and to examine structure-performance relationships of Rh and RhPd alloy supported catalysts[10].

Another way in which the conclusions of this study could have been enhanced significantly would be the possibility to test the catalysts. Unfortunately, due to reorganisation at the Johnson Matthey Technology Centre, the testing rig was dismantled and this was not possible. Any further work should involve testing in order to correlate the behaviour of the precursors in this work with their overall catalytic activity. As was mentioned in the introduction, Rhodium (Rh) is also a good candidate for diesel oxidation. This study could therefore be furthered by similar characterisation of Rh monometallic and bimetallic catalysts. Investigations into any effects that may occur if the precursor itself is bimetallic may also be of interest.

This study was concerned primarily with diesel oxidation catalysts. The basic prerequisite of an oxidation catalyst is that there is a good dispersion of metal with a particle size below 10 nm[11]. Pd acts as a stabilising agent against sintering processes of Pt particles and conserves the catalytic activity[12]. However, the authors explain this as being due to the formation of a PdO protective coating on the metallic particles. This implies that if the sample is made up of a mixture of monometallic and bimetallic particles as seen in Chapter Four for the SiO_2 supported samples, the Pd would not act as a stabiliser in this way leading to the conclusion that despite them being less dispersed, the Al_2O_3 supported bimetallic samples would be better diesel oxidation catalysts.

2. References

(1) Dawody, J.; Skoglundh, M.; Wall, S.; Fridell, E. *Journal of Molecular Catalysis A-Chemical* **2005**, *225*, 259-269.

(2) Morlang, A.; Neuhausen, U.; Klementiev, K. V.; Schutze, F. W.; Miehe, G.; Fuess, H.; Lox, E. S. *Applied Catalysis B-Environmental* **2005**, *60*, 191-199.

(3) Chen, M.; Schmidt, L. D. *Journal of Catalysis* **1979**, *56*, 198-218.

(4) Dou, D.; Liu, D. J.; Williamson, W. B.; Kharas, K. C.; Robota, H. J. *Applied Catalysis B-Environmental* **2001**, *30*, 11-24.

(5) Niemantsverdriet, J. W. *Spectroscopy in Catalysis - An Introduction*; Wiley: Weinheim, **2000**.

(6) Moulijn, J. A.; Leeuwen, P. W. M. N. v.; Staten, R. A. v. *Catalysis: An Intergrated Approach to Homogeneous, Heterogenoeous and Industrial Catalysis*; Elsevier: Amsterdam, **1993**.

(7) Bateman, J. E., Derbyshire, G.E., Diakun, G., Duxbury, D.M., Fairclough, J.P.A., Harvey., I., Helsby, W.I., Lipp, J.D., Marsh, A.S., Salisbury, J., Sankar, G., Spill, E.J., Stephenson, R., Terill, N.J. *Nuclear Instruments and Methds in Physics Research A* **2007**, *580*, 1526-1535.

(8) Newton, M. A.; Dent, A. J.; Fiddy, S. G.; Jyoti, B.; Evans, J., In *2nd International Congress on Operando Spectroscopy*; Elsevier Science Bv: Toledo, SPAIN, **2006**, p 64-72.

(9) Newton, M. A.; Dent, A. J.; Fiddy, S. G.; Jyoti, B.; Evans, J. *Physical Chemistry Chemical Physics* **2007**, *9*, 246-249.

(10) Dent, A. J.; Evans, J.; Fiddy, S. G.; Jyoti, B.; Newton, M. A.; Tromp, M. *Faraday Discussions* **2008**, *138*, 287-300.

(11) Schmitt, D., Fuess, H., Klein, H., Neuhausen, U., Lox, E.S. *Topics in Catalysis* **2001**, *16/17*, 355.

(12) Haass, F., Fuess, H. *Advanced Engineering Materials* **2005**, *7*, 899.